Fundamental Properties of Atoms and Molecules on Surfaces

a Combined STM and Shot-Noise Study

Daniela Rolf

Dissertation
zur Erlangung des Grades eines
Doktors der Naturwissenschaften

am Fachbereich Physik
der Freien Universität Berlin

Berlin, 2018

Diese Arbeit entstand in der Arbeitsgruppe von Prof. Dr. Katharina J. Franke am Fachbereich Physik der Freien Universität Berlin.

Berlin, 30.10.2018

Erstgutachterin: Prof. Dr. Katharina J. Franke
Zweitgutachter: Prof. Dr. Martin Wolf
Datum der Disputation: 19.12.2018

Abstract

In this thesis, two different projects are presented that concentrate on complementary aspects of nanoscopic systems. Not only "conventional" scanning tunneling microscopy (STM) is utilized to study the fundamental properties of atoms and molecules, but in order to detect the fluctuations of the tunneling current, a high-frequency amplifier setup is employed.

In the first part, Fe-5,10,15,20-tetra-pyridyl-porphyrin molecules were investigated on a Au(111) surface. Due to the flexibility of this molecule, several different islands of the Fe-TPyP molecule self-assemble on the surface. By means of non-contact atomic force microscopy (nc-AFM), we could show that the molecules in the different arrangements also exhibit differences in the intramolecular distortions. Moreover, using scanning tunneling spectroscopy (STS), the magnetic properties of the molecules in the different structures were compared. We showed that the intramolecular distortions influence the ligand field that is acting on the central Fe atom, such that transverse magnetic anisotropy is introduced in the system. Eventually, a spin crossover was observable, which might be ascribed to large intramolecular distortions. Furthermore, an exceptionally large number of additional inelastic excitations were observable in the differential conductance spectra of the Fe-TPyP molecules between 20 meV and 150 meV in some of the molecular arrangements, whereas no signatures of these inelastic excitations were observable on others. By means of high-resolution electron energy loss spectroscopy (HREELS), we could identify these features as excitations of molecular vibrations. By comparing the energy position of the corresponding electronic orbitals that are involved in the excitation process, the differences in the intensity of the vibrations between the different structures could be explained in a simple co-tunneling picture.

In the second part of this thesis, the optimization and testing of a complementary measurement technique is described. Here, not the DC current but the current fluctuations, *i.e.*, the shot noise, allow to gain insight into the transport properties of a system. Due to electron correlations, the shot noise of a system contains information about the effective charge e^* of the charge carriers, such that fractional charges, Cooper-pair tunneling and spin-polarized transport can be identified from the current fluctuations. As shot-noise measurements require the signal detection at high frequencies, in the order of several hundreds of kHz, a high-frequency amplifier setup has been included into the STM system. A preamplifier is mounted directly at the STM head, where it is working at cryogenic temperatures. A second amplifier is then installed outside the vacuum chamber to further enhance the signal. The characteristics of these amplifiers and the main steps towards achieving a working shot-noise setup are explained in detail in this thesis. Moreover, test measurements were performed on Au adatoms that were created on the Au(111) surface by tip identation. Comparison of our experimental shot noise data with literature shows that the amplifier setup is fully functional and exhibits the necessary sensitivity to detect the tiny current fluctuations. Finally, an outlook on first measurements of the shot noise of cobalt adatoms on the Au(111) surface will be given. As single Co atoms on Au(111) have shown to exhibit distinct magnetic properties depending on their adsorption site, it is an interesting system for shot-noise measurements.

Kurzfassung

In der vorliegenden Dissertation werden zwei komplementäre Methoden der Rastertunnelmikroskopie verwendet um die Eigenschaften von nanoskopischen Systemen zu untersuchen.

Der erste Teil befasst sich mit den Eigenschaften von Fe-5,10,15,20-Tetra-Pyridyl-Porphyrin Molekülen auf einer Au(111) Oberfläche. Aufgrund der Flexibilität der Fe-TPyP Moleküle bilden sich verschiedene Adsorptionsstrukturen aus. Mittels Rasterkraftmikroskopie konnten wir zeigen, dass die Moleküle in den verschiedenen Strukturen Unterschiede in ihrer intramolekularen Verzerrung aufweisen. Jene Verzerrungen beeinflussen das Ligandenfeld, welches auf das zentrale Eisenatom wirkt. Daher zeigten die Moleküle in den verschiedenen Anordnungen auch unterschiedliche inelastische Anregungen, welche auf die Unterschiede in der magnetischen Anisotropie zurückzuführen sind. Mittels Rastertunnelspektroskopie wurde bei einigen Molekülen sogar eine Änderung des Spinzustandes beobachtet, der eventuell durch eine besonders starke Verzerrung erklärt werden kann. Desweiteren zeigen Moleküle in einigen Strukturen eine ungewöhnlich große Zahl an zusätzlichen inelastischen Anregungen im Bereich von 20 meV bis 150 meV. Mittels hochaufgelöster Elektronenenergieverlustspektroskopie (HREELS) konnten jene Stufen als Anregung von molekularen Vibrationen identifiziert werden. Durch Vergleich der energetischen Lage jener Molekülorbitale, die bei der Anregung der Vibrationen involviert sind, konnten die unterschiedlichen Intensitäten der Vibrationen in den Spektren durch die Wahrscheinlichkeit des Co-tunnels erklärt werden.

Im zweiten Teil der Arbeit werden die entscheidenden Schritte der Optimierung einer komplementären Messmethode beschrieben, bei der nicht der mittlere Strom, sondern das Stromrauschen betrachtet werden. Das sogenannte Schrotrauschen entsteht dadurch, dass der Strom aus einzelnen Ladungsträgern besteht. Aufgrund der unterschiedlichen Korrelationen dieser Ladungsträger in einem System lässt sich aus dem Schrotrauschen eine Aussage über die effektive Ladung e^* der Ladungsträger treffen, sodass Effekte wie das Cooper-Paar Tunneln in Supraleitern oder spin-polarisierter Transport nachgewiesen werden können. Da die Detektion des Schrotrauschens Messungen bei hohen Frequenzen im Bereich einiger Hundert kHz bedarf, wurden zwei spezielle Hochfrequenzverstärker in das Rastertunnelmikroskop (STM) integriert. Der erste Verstärker befindet sich dabei direkt am Kopf des STM und arbeitet bei kryogenen Temperaturen. Ein zweiter Nachverstärker befindet sich außerhalb der Vakuumkammer und sorgt für eine weitere Verstärkung. Die genauen Charakteristika beider Verstärker und die Hauptarbeitsschritte zum Erreichen eines funktionierenden Aufbaus werden im zweiten Kapitel beschrieben. Um den Aufbau auf seine Funktionsfähigkeit zu überprüfen wurden Testmessungen auf einzelnen Au Atomen auf einer Au(111) Oberfläche durchgeführt. Ein Vergleich mit der Literatur zeigte hier, das der Verstärkeraufbau in der Lage ist das Schrotrauschen einzelner atomarer Kontakte zu messen, und über die benötigte Sensitivität verfügt. Zuletzt wird ein Ausblick auf erste Messungen des Schrotrauschens von Cobalt Atomen auf Au(111) gegeben. In frühere Messungen von Cobalt Atomen wurde eine Abhängigkeit der magnetischen Eigenschaften vom Adsorptionsplatz des Cobalt Atomes festgestellt. Mittels Messungen des Schrotrauschen wollen wir daher herausfinden, ob sich diese Unterschiede auch in den Rauschspektren nachweisen lassen.

List of Abbreviations

AFM	Atomic force miscroscopy
ARPES	Angle-resolved photoemission spectroscopy
CMOS	Complementary metal-oxide semiconductors
CBM	Conduction-band maximum
DFT	Density functional theory
DOS	Density of states
DSP	Digital signal processor
EA	Electron affinity
Fe-TPyP	Iron-5,10,15,20-tetra-pyridyl-porphyrin
FFT	Fast Fourier transform
FWHM	Full width at half maximum
HWHM	Half width at half maximum
HREELS	High-resolution electron energy loss spectroscopy
HOMO	Highest occupied molecular orbital
IETS	Inelastic electron tunneling spectroscopy
IP	Ionization potential
LDOS	Local density of states
LEED	Low-energy electron diffraction
LUMO	Lowest unoccupied molecular orbital
MCBJ	Mechanically-controlled break junction
NEXAFS	Near-edge X-ray absorption fine structure
nc FM-AFM	Non-contact frequency-modulated atomic force microscopy
NDR	Negative differential resistance
PSD	Power spectral density
PDOS	Projected density of states
STM	Scanning tunneling microscopy
STS	Scanning tunneling spectroscopy
TSP	Titanium sublimation pump
TMDC	Transition-metal dichalcogenides
UHV	Ultra-high vacuum
VBM	Valence-band minimum
WKB	Wenzel-Kramer-Brillouin
XMCD	X-ray magnetic circular dichroism
ZFS	Zero-field splitting

Contents

CHAPTER I

Introduction

"When we get to the very, very small world – say circuits of seven atoms – we have a lot of new things that would happen that represent completely new opportunities for design" — this quote by Richard Feynman during his famous lecture at the annual meeting of the American Physical Society at Caltech in 1959 paved the way for the reasearch field of nanotechnology [1]. Nowadays, almost 60 years later, nanotechnology is a well established research field, which is evolving at a rapid speed. The term *"nanotechnology"* was first used in 1974 by N. Taniguchi [2] from the Tokyo University of Science and referred to processing methods such as thin-film deposition and ion-beam milling, which are needed for the production of increasingly smaller semiconductor structures. This process of down-scaling of already existing structures is commonly referred to as top-down approach. Despite the advantage of its feasability in terms of large scale production, the size of the functional units has reached a plateau in the last years. By means of lithography and mechanical printing techniques, only structures down to 10 nm can be produced from microscopic wafers. In the recent years, the size of the complementary metal-oxide semiconductors (CMOS), the standard technology for constructing integrated circuits, has reached a half-pitch value of 20 nm, corresponding to half the distance between two identical components. A further downscaling of semiconductor technology seems to be limited by fundamental physical effects that can occur at such small lengthscales, such as tunneling of electrons between the source and drain electrode of a transistor.

An alternative path towards small functional devices is the bottom-up approach, where single atoms or molecules are used as building blocks for the construction of functional units. This general concept of molecular engineering was already mentioned in 1956 by A. von Hippel, who suggested the use of single atoms as building blocks of electronic devices to tailor the desired properties [3]. Despite the lack of an existing measurement technique to perfom any real experimens at that time, in 1974, A. Aviram and M. A. Ratner made the first specific proposal for a molecular device. They theoretically discussed the use of a single organic molecule as a rectifier, which impelled the field of molecular electronics [4]. At the same time, K. E. Drexler developed the concept of molecular nanotechnology [5, 6] and proposed the idea of so-called *"assemblers"*, tiny machines that can built structures atom by atom, which might be used to fabricate even the most complex objects.

With the development of suitable measurement techniques such as the scanning tunneling microscope (STM), the realization of experiments at the single molecule level became possible in the decade that followed. The first measurements of the electronic properties of a molecular wire were performed in 1996 by means of STM [7]. Shortly after, in 1997, mechanically controlled break junction (MCBJ) experiments enabled the measurement of the current-voltage characteristic of a single molecule for the first time [8]. In the same year, a field-effect transistor was built from a single carbon nanotube, whose conductance properties were tunable by a gate voltage that was applied through an attached metal electrode [9]. Shortly afterwards, a consecutive study repeated these measurements, which were performed at 5 mK before, at room temperature [10], which is a major step with regard to transferring the technology from the lab environment to real-life conditions. In 2007, a monolayer of bistable rotaxane molecules was used for data storage, achieving an ultra-dense memory circuit with 10^{11} bits/cm^2 [11]. In 2009, an organic molecule was used in a field-effect transistor geometry to prove the concept of molecular orbital gating, as revealed by tunneling spectroscopy [12]. In 2011, the *"nano car"* attracted a lot of attention, where STM measurements confirmed the controlled unidirectional motion of a molecule by its four rotary motor functional units upon sequential electronic and vibrational excitation [13]. Five years after the first reports on molecular transistors, the first single-atom transistor was built [14]. Using a combination of scanning tunnelling microscopy and hydrogen-resist lithography, M. Fuechsle, et al. have placed an individual phosphorus dopant atom within an epitaxial silicon device architecture with a spatial accuracy of one lattice site. By means of transport measurements, they confirmed the existence of discrete quantum levels with the system's charging energy close to the bulk value. In 2016, another study by F. E. Kalff, et al. managed to outperform the data storage density of the aforementioned rotaxane device of 10^{11} bits/cm^2 by more than three orders of magnitude by rearranging vacancies on a chlorinated Cu(100) surface [15]. In 2016 the Nobel prize in chemistry has been awarded to J.P. Sauvage, Sir J. Fraser Stoddart and B. L. Feringa for their pioneering work on molecular machines [16], underlining the importance of this research field.

However, despite all the scientific achievements in the last 20 years, molecular nanotechnology has still not been realized on the industrial scale. In order to utilize single molecules for operations that are currently performed by larger-scale silicon-based devices, a deeper understanding of the molecular properties and electron transport on the molecular scale is required. The prerequisite for the use of a molecular system as a component in a functional circuit is a suitable choice of the molecule. Here, chemical synthesis allows to design molecules with the desired properties by, *e.g.*, modifying the functional endgroups of an organic compound. To get larger-scale structures, these molecules should reliably form self-assembled structures upon deposition on a substrate. To use a molecule in nanotechnology, it is required to posses tunable properties. One approach is described by the term molecular switches, where the idea is to use external influences like light, an electric field or tunneling electrons to induce reversible modifications on the molecule, *e.g.*, the rotation of a functional endgroup or the opening of a chemical bond. Another approach to use molecules as functional units is termed spintronics and aims at utilizing the atomic or molecular spin state to store information. The idea is as follows: according to Hund's rules, the unpaired electrons in an atom sum up to a total spin. In an isotropic environment, all directions of the spin projection in space are equally favourable. In the presence of magnetic anisotropy, however, certain directions are energetically more favourable, which splits the different spin directions in energy. In order to get a functional device, two degenerate ground states are required, seperated by an energy barrier that hinders the spins from spontaneous flippings. This anisotropy can be controlled by the choice of the surface or the ligand of a molecule.

Even after overcomming all these challenges in finding a proper compound with tunable properties, it has to be deposited on some kind of surface and contacted by metal electrodes in order to use the molecular building block in any device. However, upon adsorption, the electronic structure of the molecule will be affected, which can strongly alter all molecular properties. It was not without reason that H. Kroemer stated *"the interface is the device"* when expressing the importance of the transition region for the functionality of a device during his nobel lecture in the year 2000 in Stockholm [17]. This especially holds true for submonolayers of molecules, when all the molecules are in contact with the substrate. Therefore, a deep understanding of the interface between organic molecule and metal electrodes is essential. The investigation of molecules adsorbed on a substrate is possible with many different measurement techniques, such as X-ray magnetic circular dichroism (XMCD), near edge X-ray absorption fine structure (NEXAFS), high-resolution electron energy loss spectroscopy (HREELS) or scanning tunneling microscopy (STM).

The goal of this thesis is to contribute to the understanding of the fundamental processes occuring for atoms and molecules adsorbed on a metal surface. Therefore, low-temperature scanning tunneling microscopy (STM) was chosen as an experimental tool, since it does not only constitute an ideal instrument for studying the adsorption geometry of molecules on a substrate with atomic precision, but simultaneously allows to obtain insight into the electronic structure of a compound. Moreover, by means of scanning tunneling spectroscopy (STS), also magnetic and vibrational excitations can be probed, allowing to draw conclusions about the spin state of the molecular adsorbates.

In chapter III, the properties of a porphyrin molecule are investigated on a Au(111) surface. As metallo-porphyrins fullfill a variety of tasks in biology, *e.g.*, as catalists, molecular transporters or energy transducers in photosynthesis [18], they are also of interest for molecular electronics. Due to their flexibility in terms of the central metal atoms or functional endgroups at their macrocycle, a variety of porphyrin derivates exist. In this thesis, Fe-5,10,15,20-tetra-pyridyl-porphyrin (Fe-TPyP) is investigated, consisting of a porphin core with a central Fe atom and four rotatable pyridyl groups attached to it. On the Au(111) substrate, Fe-TPyP molecules can adapt different adsorption geometries due to the flexibility of their pyridyl end groups. More precisely, depending on the rotational angle of the pyridyl groups, different distortions of the macrocycle occur due to steric hindrance between adjacent hydrogen atoms. For the investigated three structures of Fe-TPyP on Au(111), the changes in molecular geometry induced changes in the electronic structure and even altered the magnetic ground state of the molecules. Moreover, only some structures showed pronounced signals of vibrational excitations, whose origin could be confirmed by means of HREELS measurements that were performed in the group of P. Tegeder, whereas no vibrational signatures were detectable in other structures. In chapter III, the properties of the molecules in the different structures are introduced at first and the cause of the aforementioned differences is analyzed. Moreover, to decouple the molecules from the substrate, Fe-TPyP is studied on a single layer of MoS_2 grown on the Au(111) surface. Due to the band gap of MoS_2, weaker hybridization effects occur between the Fe-TPyP and the surface, leading to changes in the molecular properties.

In chapter IV, a very different approach to study the properties of a system is followed, which bases on shot-noise measurements. Therefore, not the DC component of the tunneling current is regarded, but its fluctuations. In contrast to the DC component, the level of current fluctuations allows to gain insight into the transmission channels that are involved in the transport process and give complementary information about the electron-electron and electron-phonon interaction processes during the tunneling events. The shot-noise power spectral density S is given by

$$S_{\mathrm{I}} = 2eG_0V\sum_{i=1}^{N}\tau_i(1-\tau_i),$$

with G_0 corresponding to the quantum of conductance and τ_i to the transmittivity of each transmission channel. In case of non-negligible interaction between the tunneling electrons, which is usually the case for higher transmission probabilities, the shot noise is partially suppressed, which is expressed by the Fano factor F. This Fano factor depends on internal electron-electron and electron-phonon interaction processes. Therefore, fundamental aspects such as spin-polarized transport, fractional charges or Cooper-pair tunneling can be identified from the current fluctuations. Shot-noise measurements hence give complementary information about the properties of single atoms and molecules, which are typically not accessible with conventional STS.

In order to detect the shot noise in the tunneling current, a complex technical setup is required. It consists of a high-frequency low-temperature pre-amplifier, which is installed inside the cryostat at the STM head and a post-amplifier, which is positioned outside the UHV chamber. In the first experimental part of the chapter, the steps towards achieving a working shot-noise amplifier setup are discussed, as many modifications were necessary to detect the tiny current fluctuations. Moreover, test measurements on Au adatoms are presented, which are created on a Au(111) surface by controlled tip indentation. As the transport through Au-Au contacts on the single-atom level is well understood, it is a suitable system to characterize and test the shot-noise setup in terms of its functionality and sensitivity. Finally, an outlook on first measurements on single cobalt atoms will be given. As Co atoms exhibit signatures of the Kondo effect, the transport properties should differ from the trivial spin-degenerate transport.

As all the measurents in this thesis were performed with a combined STM-AFM, an introduction to the basic principles of scanning tunneling microscopy, as well as a theoretical discription of the tunneling junction will be given in chapter II. Moreover, the working principle of atomic force microscopy will be explained in sec. C of chapter II. In sec. D, an introduction to the experimental details of the STM will be given, covering also the properties of the employed Au(111) sample.

CHAPTER II

Theoretical Background and Experimental Details

In the past century, a variety of spectroscopic techniques has been developed in order to characterize surfaces and surface structures, ranging from low-energy electron diffraction (LEED) to angle-resolved photoemission spectroscopy (ARPES). Being only sensitive to periodic structures in reciprocal space, they were restricted to simple and ordered structures. A milestone in surface science was the development of scanning tunneling microscopy by G. Binning and H. Rohrer in 1981 [19, 20], which opened the possibility to analyze samples in real space. With a spatial resolution on the atomic scale, which is far beyond the optical limit, the STM allows to gain insight into the structure of individual surface atoms, defects or single adsorbates. Moreover, by means of scanning tunneling spectroscopy (STS), insights into the electronic properties of a specimen depending on its local environment can be obtained.

Since the first studies in the early years of the STM, which focussed on topographic images of coinage metal and silicon surfaces, the field has progressively evolved over the last two decades. One big breakthrough was inelastic electron tunneling spectroscopy (IETS), which utilizes the signal of the inelastic transport path to detect intramolecular vibrations [21] and spin-flip excitations

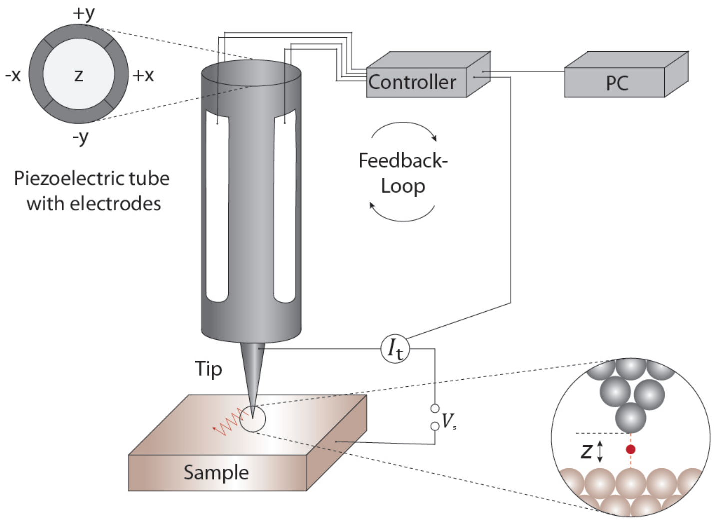

Figure 2.1. Working mechanism of an STM. The tunneling gap z is varied by the controller by means of a feedback loop such that the tunneling current I is kept constant for a given sample bias voltage V. The tip position is controlled by means of piezoelecric elements (see sketch in upper left corner for top view of the piezo tube). The red arrow at the sample surface indicates the movement of the tip, during the recording of an image. The inset on the bottom right shows a magnified view on the tunneling junction.

[22]. Employing magnetic fields, IETS is widely used to determine the spin state of single atoms and molecules depending on their local environment on the surface. In more recent developments, the STM is combined with other techniques to obtain complementary information that was not accessible on the atomic scale before. In 2014, a combination of STM measurements with X-ray magnetic circular dichroism (XMCD) allowed to get chemical sensitivity on individual adatoms, which until then was not possible with STM alone [23]. In 2015, the transport mechanisms through different adatoms were studied by means of shot noise measurements, allowing to identify spin-degenerate transport for some species and spin-polarized channels for others [24]. Moreover, in 2017, the dipole-dipole interactions between individual Fe atoms of variable distance were examined by combining STM with electron spin resonance (ESR) [25].

Despite all these advancements regarding STM, due to its main observable being the tunneling current, it is restricted to conducting samples, only. Another related measurement technique — the atomic force microscopy — which has been invented in 1985 only a few years after the STM, has managed to overcome this obstacle, while still providing atomic resolution. It is based on a small tip attached to a cantilever which is oscillating at a high frequency. Relying on the interactive forces between a tip and the molecules and not on the tunneling current, it allows to obtain complementary information about a specimen, ranging from the determination of forces between the tip and molecular moieties to local variations in the work function of the underlying substrate. By utilizing appropriate sensors, the advantages of both measurement techniques can be combined.

In this chapter, the theory of STM and AFM will be introduced. In sec. A, the basic concepts of STM will be discussed and an introduction into the theoretical description with the Tersoff-Hamann model will be given. Furthermore, the concept of scanning tunneling spectroscopy will be explained, which allows to probe the local density of states (LDOS) of a sample. Moreover, an overview over the spectral features that arise due the above-mentioned inelastic electron tunneling will be given. In sec. C, the working principle of the AFM will be discussed, as well as the relevant forces that play a role in the tip-sample interaction. Finally, in sec. D, some experimental details of the combined STM-AFM setup will be presented.

A. Working Principle of an STM

The fundamental principle underlying the STM is the tunneling effect. In contrast to classical objects, electrons posses a non-vanishing probability of tunneling through a small potential barrier. The centerpiece of an STM is a sharp metal tip, which is placed at a certain distance z — usually in the range of a few Ångström — above a conducting sample surface (see fig. 2.1). Upon application of a bias voltage V between sample and tip, a shift in the chemical potentials between both leads is induced. The vacuum gap between tip and sample constitutes an energy barrier, which — in a classical picture — can not be overcome by the electrons. Due to the quantum-mechanical nature of the electrons, however, there is a finite probability of the electrons to tunnel from the tip to the sample through the vacuum barrier. The resulting tunneling current I that flows between both leads depends on the tip and sample materials and on the applied bias voltage. A short derivation of the tunneling current in dependence of these parameters will be given in the next section.

To obtain a topographic image of a sample, the STM tip is moved laterally line by line across the surface. Here, the precise positioning of the tip on the sample is realized by means of piezo-electric elements. As shown in fig. 2.1, the tip is connected to a piezo element which contains five segments. Four of these form two opposing pairs in the x- and y direction and allow for a lateral movement of the tip upon application of a DC voltage to the opposing segments. Moreover, the central segment

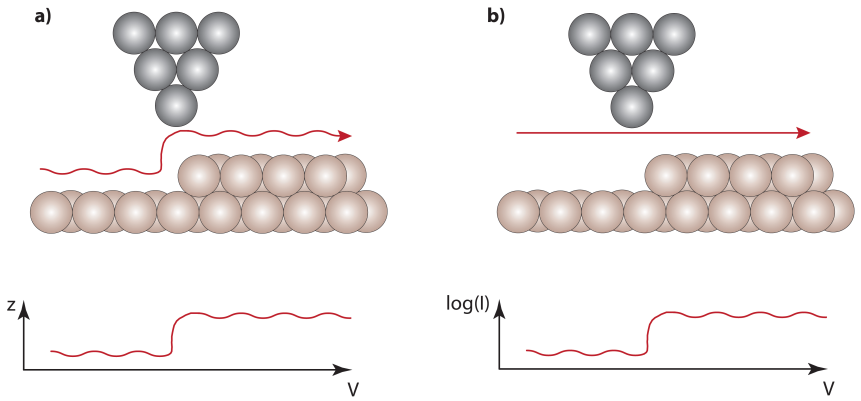

Figure 2.2. Different scanning modes of an STM: **a)** in the constant-current mode, current and voltage are kept constant, whereas the tip-sample distance gives information about the surface topography. **b)** in the constant-height mode, the current varies during the scan, as the tip-sample distance and the voltage are fixed.

allows to directly control the tip-sample distance z.

There are two main operating modes to obtain topographic images of the sample surface: the constant-current mode and the constant-height mode (see fig. 2.2). In the constant-current mode, the tip-sample distance is regulated by an electrical feedback loop in such a way, that an initially set current value is kept constant during the scan. Here, the exponential dependence of the tunneling current on the distance z allows for a precise feedback control. At each measurement point, the piezo-voltage that is needed to reach the feedback current is recorded. The obtained values are converted into an image, which corresponds to the apparent height of the surface structure, containing information about both the electronic and geometric properties of the sample. Alternatively, in the constant-height mode, the variations in the tunneling current I can be plotted, while the tip-sample distance z is held constant at an initially set value. As for this scanning mode the feedback loop is disabled, only sufficiently flat surface areas can be scanned to avoid tip crashes at step edges and adsorbates. Moreover, the measurement conditions have to be very stable to measure in the constant-height mode, as even small thermal drifts can lead to a drifting of the tip out of the tunneling range or into the surface during the scan of an image.

1. Tersoff and Hamann Model

In the previous description of the operating modes of the STM, we have seen that the tunneling current plays a major role in obtaining information about the surface properties. In order to get a mathematical expression for the dependence of the tunneling current I on the bias voltage V and tip-sample distance z, the STM junction is considered from a theoretical point of view.

In thermal equilibrium and without application of an external bias voltage, the chemical potentials of the tip and sample are aligned and — assuming the same work functions for tip and sample — no net current is flowing across the junction. Upon application of an external voltage V, the chemical potentials μ_t and μ_s of tip and sample are shifted by eV with respect to each other, as depicted in fig. 2.3. In the following derivation, we follow the convention of tunneling from the occupied states of the tip to the unoccupied states of the sample in case of positive applied bias voltages. The total tunneling current I that flows under the application of a certain bias voltage eV can be obtained by evaluating the sum over all combinations of initial states ψ_μ and final states ψ_ν of the electron within the corresponding bias window, under consideration of a weighting factor, which expresses the tunneling probability for each pair of states. J. Tersoff and D. R. Hamann developed a theoretical description by assuming the tip and sample to be two independent systems with non-orthogonal eigenstates ψ_μ and ψ_ν. For a tunneling process from the initial state ψ_μ at energy E_μ to the final state ψ_ν at energy E_ν, the tunneling current according to first-order pertubation theory in Bardeen's formalism is given by [26, 27]

$$I(V) = \frac{2\pi e}{\hbar} \sum_{\mu\nu} f(E_\mu)[1 - f(E_\nu)]\delta(E_\mu - E_\nu + eV)|M_{\mu\nu}|^2, \tag{2.1}$$

with $M_{\mu\nu}$ being the tunneling matrix element. The absolute square $|M_{\mu\nu}|^2$ hence corresponds to the tunneling probability. Energy conservation during the tunneling process and Pauli principle are taken into account by the δ function and Fermi-Dirac distribution function $f(E)$, respectively. J. Bardeen has shown that the tunneling matrix element $M_{\mu\nu}$ can be expressed as [27]

$$M_{\mu\nu} = -\frac{\hbar^2}{2m_\mathrm{e}} \int \mathrm{d}\vec{S}[\psi_\mu^* \nabla \psi_\nu - \psi_\nu \nabla \psi_\mu^*]. \tag{2.2}$$

This expression corresponds to the current operator (the term in parenthesis) integrated over any arbitrary surface $\vec{S}$ lying entirely within the tunneling gap that separates the two sides. To evaluate this integral, the assumption of asymptotic spherical s-wave functions at the very last atom of the tip[1] has to be made, as proposed by J. Tersoff and D. R. Hamann [26]. Moreover, the semiclassical WKB approximation is used, which approximates the non-constant tunneling barrier by the simplified case of a rectangular energy barrier at the average barrier height of $eV/2$, as is sketched in blue in fig. 2.3. Under these simplifications, the expression for the matrix elements can be modified to [29, 30]

$$|M_{\mu\nu}|^2 \propto e^{-2z\sqrt{\frac{2m_\mathrm{e}}{\hbar^2}}\sqrt{\Phi_\mathrm{av} - E + \frac{eV}{2}}}, \tag{2.3}$$

with Φ_av corresponding to the average work function of sample and tip. In this expression for the tunneling matrix, only the energy of the corresponding state is of importance and not its nature. The same approach can also be made for the tunneling current in eq. 2.1 by first summing up all states at the same energy, which gives the local density of states of tip and sample ρ_t and ρ_s, respectively. Performing the integration over the energy yields

$$I(V) = \frac{2\pi e}{\hbar} \int \mathrm{d}E_\mu \int \mathrm{d}E_\nu \rho_\mathrm{t}(E_\mu)\rho_\mathrm{s}(E_\nu) f(E_\mu)[1 - f(E_\nu)]\delta(E_\mu - E_\nu + eV)|M_{\mu\nu}|^2. \tag{2.4}$$

By removing one of the integrals, the evaluation of the δ function simplifies this equation to

$$I(V) = \frac{2\pi e}{\hbar} \int_0^{eV} \mathrm{d}E\, \rho_\mathrm{t}(E_\mathrm{F} + E - eV)\rho_\mathrm{s}(E_\mathrm{F} + E) f(E_\mathrm{F} + E - eV)[1 - f(E_\mathrm{F} + E)]|M_{\mu\nu}|^2. \tag{2.5}$$

Moreover, some simplification can be made due to the experimental conditions. As the temperature broadening is usually smaller than the spectroscopic resolution, the Fermi distribution function can be considered in the limit of vanishing temperature, resulting in a step function. Hence, eq. 2.5

---

[1] Note that the Tersoff-Hamann model has proven to be an adequate approach for systems where the approximation of a flat and featureless tip is sufficient [26]. However, in systems were the tunneling electrons predominantly show non-s-wave character, *e.g.*, p- or d-wave character, the differing character of the contributing orbitals has to be regarded [28].

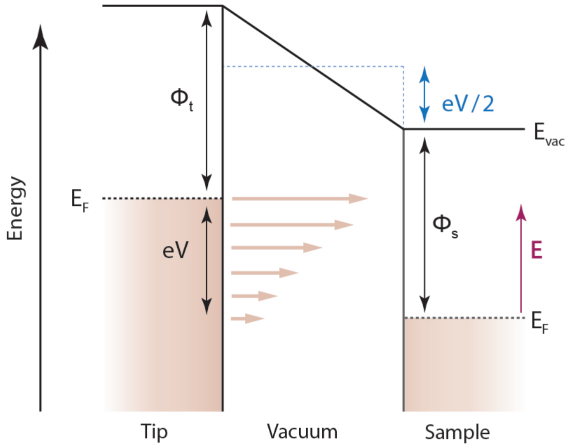

Figure 2.3. Schematic energy diagramm for the case of tunneling from the tip to the sample after a bias voltage of eV has been applied. Φ_t and Φ_s are the work functions of tip and sample, respectively. The potential treated in the WKB-approximated case (see text for explanation) is marked with the blue dotted lines. The red line indicates the energy window, which is being considered in the derivation.

simplifies to

$$I(V) = \frac{2\pi e}{\hbar} \int_0^{eV} \mathrm{d}E\, \rho_\mathrm{t}(E_\mathrm{F} + E - eV)\rho_\mathrm{s}(E_\mathrm{F} + E)|M_{\mu\nu}|^2. \tag{2.6}$$

The most fundamental properties of the tunneling current are already captured in this short derivation. Combined with eq. 2.3, eq. 2.6 exhibits the already mentioned exponential dependence of the tunneling current on the tunneling gap z. This is the basis for the precise control of the tip-sample distance, as the retraction of the tip by 1 Å typically reduces the current by one order of magnitude. The same dependency is also responsible for the high lateral resolution, as the contributions from the very last atom of the tip dominate the tunneling current. The next atoms of the tip that are further away from the sample have an exponentially smaller contribution and can therefore often be neglected. Furthermore, eq. 2.6 contains the dependence of the tunneling current on the DOS of tip and sample. Hence, the measurement data is always a convolution of topographic information and electronic properties of the system under investigation. While the variation of the LDOS is small for clean metal surfaces, it will have non-negligible effects on the data for molecular adsorbates, where electronic resonances strongly vary in the considered energy window. Therefore, in the next part, scanning tunneling spectroscopy will be introduced, which uses the dependence of the tunneling current on the LDOS of a specimen. Moreover, the theory only accounts for purely elastic processes. In case of inelastic contributions, a more generalized theory as developed by N. Lorente and M. Persson must be used [31]. The effect of inelastic processes on the tunneling current will be discussed in sec. 4.

B. Scanning Tunneling Spectroscopy

Besides the capapility of capturing topographical information about a surface with atomic resolution, the STM can also be utilized to perform spectroscopic measurements locally on the sample, giving insight into the LDOS of a sample by means of scanning tunneling spectroscopy. Its main working principle and some details about its technological implementation will be presented in the following part.

1. Theoretical Consideration

The dependence of the tunneling current on the LDOS of both the tip and the sample is evident from eq. 2.6. However, as the integral is considered, all states between the Fermi level and the applied bias voltage contribute to the total current. To regard only the contribution at one specific bias voltage, we consider the derivative of the current with respect to the bias voltage

$$\begin{aligned}\frac{\mathrm{d}I}{\mathrm{d}V} &\sim \rho_\mathrm{t}(E_\mathrm{F})\rho_\mathrm{s}(E_\mathrm{F}+eV)|M_{\mu\nu}|^2\\ &+\int_0^{eV}\mathrm{d}E\,\rho_\mathrm{t}(E-eV)\rho_\mathrm{s}(E)\frac{\mathrm{d}|M_{\mu\nu}|^2}{\mathrm{d}V}\\ &+\int_0^{eV}\mathrm{d}E\,\rho_\mathrm{s}(E)\frac{\mathrm{d}\rho_\mathrm{t}(E')}{\mathrm{d}E'}|M_{\mu\nu}|^2.\end{aligned} \tag{2.7}$$

For small bias voltages ($eV \ll \Phi$) and constant tip-sample distances, $|M_{\mu\nu}|^2$ is assumed to be constant such that the second term of eq. 2.7 can be neglected [27]. Moreover, in case of an STM tip without sharp features in the DOS around E_F, as is usually the case for metallic tips, ρ_t can be treated as constant as well, which also cancels the last term. This simplifies eq. 2.7 to

$$\frac{\mathrm{d}I}{\mathrm{d}V} \sim \rho_\mathrm{t}(E_\mathrm{F})\rho_\mathrm{s}(E_\mathrm{F}+eV)|M_{\mu\nu}|^2 \sim \rho_\mathrm{s}(E_\mathrm{F}+eV). \tag{2.8}$$

Accordingly, the differential conductance is directly proportional to the LDOS of the sample near the Fermi energy, for small voltages that allow the tunneling probability to be treated as constant. At higher voltages, however, the dependence of the tunneling probability on the sample bias voltage has to be regarded [32], as will be discussed later on.

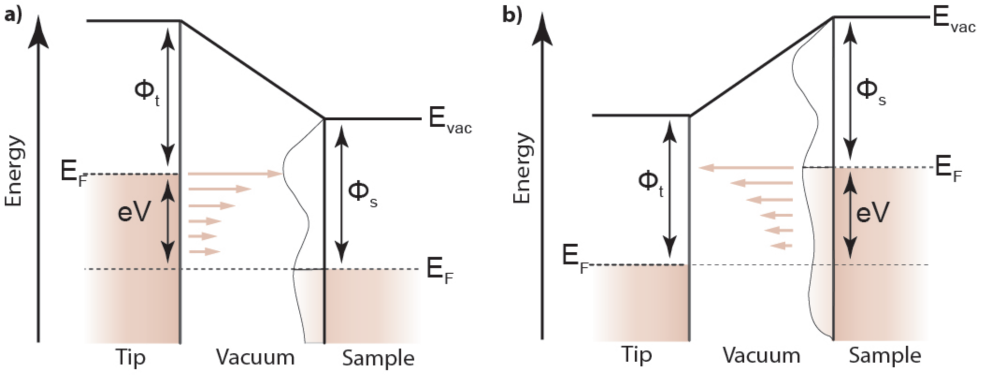

Figure 2.4. Energy level diagram of an STM junction including a non-constant sample DOS. **a)** A positive bias voltage is applied, leading to tunneling of electrons from the tip into unoccupied states of the sample. **b)** A negative applied bias voltage induces a tunneling current of electrons from the occupied states of the sample into the tip. States within the energy window eV contribute to the tunneling. The different length of the arrows indicates the dependence of the tunneling probability on the respective height of the tunneling barrier and also regards the DOS of the sample.

In order to get information about the LDOS of a sample, the tip is placed at a fixed position on the sample and a spectroscopic curve is recorded. Therefore, one of the three parameters I, V and z is recorded in dependence of another, while the third one is held constant. The two most common operating modes — the $I(V)$ mode and $I(z)$ mode — will be briefly discussed in the following.

Constant-Height Mode

In the constant-height mode, the feedback loop is disabled and the tip stays at a certain tip-sample distance, whose value is determined by the feedback parameters throughout the measurement. Under the above-discussed conditions of small bias voltages and a flat DOS of the tip ρ_t, the density of states of the sample ρ_s can be directly obtained from the derivative of the current with respect to the bias voltage (see eq. 2.8).

In fig. 2.4, the dependence of the tunneling current on ρ_t is depicted. For the length of the arrows, not only the exponential dependence of the tunneling probability on the respective height of the tunneling barrier is taken into account, but also the DOS of the sample. At energies where the sample shows an enhanced number of available states, also the contributions to the tunneling current are larger.

In experiment, $\mathrm{d}I/\mathrm{d}V$ spectoscropy is performed to determine the energetic positions of orbitals of adsorbed molecules. Here, typical energy scales are in the order of several eV, such that to detect the lowest occupied or highest unoccupied molecular orbital (HOMO and LUMO, respectively), spectra of up to 1 eV to 3 eV are recorded. In this energy window, however, the above made assumption of $eV \ll \Phi$ can no longer be made, such that the tunneling matrix can no longer be treated as constant. This effect superimposes an exponential background to the spectra, which causes a shift of the maxima to higher energies. Moreover, relative peak intensities are distorted, such that peaks at higher energies are enlarged, due to the reduced effective barrier height. These effects can be empirically compensated by multiplying with the factor V/I

$$\frac{V}{I}\frac{\mathrm{d}I}{\mathrm{d}V} \sim \rho_s(E_F + eV), \tag{2.9}$$

as proposed by J. A. Stroscio [29, 33]. However, the normalization might enhance the noise level especially at small bias voltages, and is therefore applied only rarely.

Constant-Current Mode

A more suitable method to obtain the specta at higher energies is to measure in a different mode, the constant-current mode. Here, the current is kept constant by a feedback loop and the tip height is adjusted while the bias is swept. This mode is superior at larger bias voltages, as the retraction of the tip prevents the sample from destruction from too high currents and electric field strengths. However, also in the constant-current mode, the peak position of the molecular resonances is altered, since the changing tip height leads to variations in the tunneling matrix. Moreover, the constant-current mode is not suitable to record spectra close to E_F, as in order to maintain a constant current value, the tip crashes into the substrate at too low bias voltages. As a conclusion, neither of the two operational modes is favourable over the other. Instead, the operational mode should be adjusted to the measurement conditions and the regarded energy window. One has to keep in mind, however, that the line shapes and peak positions can alter significantly between different operation modes [34].

In the STM experiment, the differential conductance is not obtained by recording the current as a function of voltage and differentiating it afterwards, but it is measured directly. This is realized by the use of a lock-in amplifier, whose working principle will be introduced in the following section.

2. Lock-in Amplifier

Lock-in detection is a commonly used technique for the purpose of accurately measuring small signals and bases on a principle called phase-sensitive detection (PSD). A lock-in amplifier reduces the signal-to-noise ratio to such an extend that it allows to measure signals that are superimposed by noise several orders of magnitude larger than the actual signal [35]. In order to use the lock-in amplifier, a small sinusoidal voltage $V_{\mathrm{mod}}\sin(\omega_{\mathrm{mod}}t)$ with modulation frequency ω_{mod} has to be added to the DC bias voltage V. The lock-in amplifier then operates as a band pass filter, centered at the reference frequency ω_{ref}, which only passes signals within a very narrow bandwidth $\Delta\omega$, whereas signals at other frequencies are filtered out [35].

Working Mechanism

In order to understand the principle behind the lock-in detection technique in case of $\mathrm{d}I/\mathrm{d}V$ measurements, the tunneling current at a voltage of $V + V_{\mathrm{mod}}\sin(\omega_{\mathrm{mod}}t)$ will be considered. Under the assumptions made above in sec. 1, *i.e.*, a constant tip density of states ρ_{t} and a tunneling probability independent from the voltage in the considered region $eV \ll \Phi$, the tunneling current as derived in eq. 2.6 in sec. 1 reads

$$I(V + V_{\mathrm{mod}}\sin(\omega_{\mathrm{mod}}t)) \propto \int_0^{eV+eV_{\mathrm{mod}}\sin(\omega_{\mathrm{mod}}t)} \rho_{\mathrm{s}}(E)\mathrm{d}E. \tag{2.10}$$

For a fixed V and a sufficiently small V_{mod}, the tunneling current $I(V + V_{\mathrm{mod}}\sin(\omega_{\mathrm{mod}}t))$ can be expanded as a Taylor series around V, resulting in

$$I(V + V_{\mathrm{mod}}\sin(\omega_{\mathrm{mod}}t)) \propto I(V) + \underbrace{\frac{\mathrm{d}I}{\mathrm{d}V}V_{\mathrm{mod}}\sin(\omega_{\mathrm{mod}}t)}_{\text{1st harmonic}} + \underbrace{\frac{\mathrm{d}^2I}{\mathrm{d}V^2}V_{\mathrm{mod}}^2\sin^2(\omega_{\mathrm{mod}}t)}_{\text{2nd harmonic}} + \mathcal{O}(3). \tag{2.11}$$

The first term, often referred to as the zero-order component, is proportional to the tunneling current and shows no time dependence. The 1^{st} harmonic term in eq. 2.11 is proportional to the differential conductance and hence to ρ_{s}, the LDOS on the sample. This signal can be extracted by a lock-in amplifier by the following method: The lock-in amplifier takes the input signal and an external reference signal of frequency ω_{ref}. These two signals are mixed in the phase sensitive detector, which acts as a linear multiplier and constitutes the central component of a lock-in amplifier. From the trigonomentric product identities $\sin(\alpha)\sin(\beta) = {}^{1}\!/_{2}\left[\cos(\alpha-\beta)-\cos(\alpha+\beta)\right]$, one obtains an output signal consisting of two components at frequencies $[\omega_{\mathrm{mod}} - \omega_{\mathrm{ref}}]$ and $[\omega_{\mathrm{mod}} + \omega_{\mathrm{ref}}]$ [35]

$$\begin{aligned} I_{\text{lock-in}} \propto\, & I(V)V_{\mathrm{ref}}\sin(\omega_{\mathrm{ref}}t + \phi_{\mathrm{ref}}) \\ & + \frac{1}{2}V_{\mathrm{mod}}V_{\mathrm{ref}}\frac{\mathrm{d}I}{\mathrm{d}V}\cos([\omega_{\mathrm{mod}} - \omega_{\mathrm{ref}}]t + [\phi_{\mathrm{mod}} - \phi_{\mathrm{ref}}]) \\ & - \frac{1}{2}V_{\mathrm{mod}}V_{\mathrm{ref}}\frac{\mathrm{d}I}{\mathrm{d}V}\cos([\omega_{\mathrm{mod}} + \omega_{\mathrm{ref}}]t + [\phi_{\mathrm{mod}} + \phi_{\mathrm{ref}}]) \\ & + \mathcal{O}(2). \end{aligned} \tag{2.12}$$

Here, V_{ref} is the amplitude of the reference signal and ϕ_{ref} and ϕ_{mod} correspond to the phase of the reference signal and modulation signal, respectively.

In the following step, the multiplied signal is passed through a low pass filter, which performs an integration over the signal form. Hence, in case of $\omega_{\mathrm{mod}} \neq \omega_{\mathrm{ref}}$ all components oscillate in time and

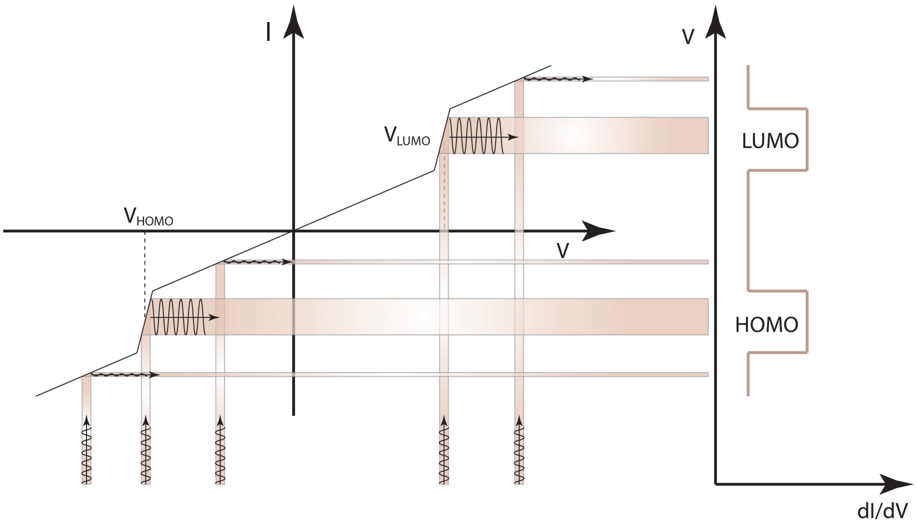

Figure 2.5. Working mechanism of a lock-in amplifier. A sinusoidal voltage is added to the DC bias voltage. Due to the bias modulation, the current value also oscillates between $I(V-V_{\mathrm{mod}})$ and $I(V+V_{\mathrm{mod}})$. In regions of higher slope, *i.e.*, close to molecular resonances, the amplitude of this current oscillation is larger, leading to an enhanced $\mathrm{d}I/\mathrm{d}V$ signal amplitude. Figure in analogy to [36].

cancel out during the integration procedure. This also applies to contributions from noise signals, as they usually have a frequency different from the reference frequency, which makes using a lock-in amplifier very favourable. However, if $\omega_{\mathrm{mod}} = \omega_{\mathrm{ref}}$, the signal with frequency $[\omega_{\mathrm{mod}} - \omega_{\mathrm{ref}}]$ is a DC signal, which does not cancel out, such that the integration leads to the filtered PSD output

$$I_{\text{lock-in}} \propto \frac{1}{2} V_{\mathrm{mod}} V_{\mathrm{ref}} \frac{\mathrm{d}I}{\mathrm{d}V} \cos(\phi_{\mathrm{mod}} - \phi_{\mathrm{ref}}). \tag{2.13}$$

Depending on the bandwidth $\Delta\omega$ of the low pass filter, not only signals at frequency ω_{ref} can pass, but all signals with frequencies within $\Delta\omega$. Furthermore, the phase difference in eq. 2.13 is usually adjustable. By means of a phase-locked loop, the reference signal is locked to the external signal in order to achieve a matching of the phases, which maximizes the output signal.

A schematics of the working principle is depicted in fig. 2.5. A sinusoidal AC voltage of constant amplitude (vertical wiggles) is added to the DC voltage. The bias modulation induces an oscillation of the current between $I(V-V_{\mathrm{mod}})$ and $I(V+V_{\mathrm{mod}})$ (horizontal wiggles). In regions of a larger slope of the $\mathrm{d}I/\mathrm{d}V$ signal, the amplitude of these current oscillations is large, which results in a larger $\mathrm{d}I/\mathrm{d}V$ signal amplitude. In regions where the $I(V)$ curve is flatter, the induced current oscillations are smaller, such that the $\mathrm{d}I/\mathrm{d}V$ signal is also reduced.

By means of the lock-in technique it is also possible to measure the second harmonic contribution by choosing a reference signal with twice the frequency of the output modulation $\omega_{\mathrm{ref}} = 2\omega_{\mathrm{mod}}$. It is proportional to the second derivative of the current with respect to the voltage and becomes of relevance for very small signals, *e.g.*, vibrations or spin excitations, which are often hard to detect in the $\mathrm{d}I/\mathrm{d}V$ signal.

The possibility to measure the $\mathrm{d}I/\mathrm{d}V$ signal directly without ramping the bias voltage allows to record ρ_{s} at a specific energy eV with spatial resolution in a so-called $\mathrm{d}I/\mathrm{d}V$ map. In contrast to the topography image, which includes contributions from all states between the Fermi energy E_{F} and $E_{\mathrm{F}} + eV$, the resulting image only reflects the DOS of the sample ρ_{s} at that specific energy. For the recording of a constant-current $\mathrm{d}I/\mathrm{d}V$ maps or constant-current spectra, the feedback loop has to be activated. Therefore, the modulation frequency has to be above the cut-off frequency of the feedback loop in order to avoid a modulation of the tip height due to the modulation signal of the lock-in amplifier.

From eq. 2.13 one can see that the output signal of the lock-in amplifier is proportional to the amplitude of the modulation signal V_{mod}. Accordingly, in order to get a high signal intensity, a large modulation amplitude seems favourable. However, the modulation voltage induces a broadening of the spectral features, which is proportional to the modulation amplitude. Hence, a compromise between high signal intensity and induced broadening has to be made.

3. Molecular Adsorbates on the Surface

In the previous parts, we discussed how STS allows to study the electronic properties of a system. In order to correctly interpret the obtained data, some characteristic properties of this technique with respect to molecular adsorbates should be regarded.

One major aspect that has to be considered is that STS bases on electrons tunneling into or out of a neutral molecule. Therefore, in a first consideration, the energetic position of the resonance, which is observed in the spectra, does not correspond to the lowest unoccupied molecular orbital (LUMO) and highest occipied molecular orbital (HOMO) of the molecule, but rather to its anionic and cationic states, the electron affinity level (EA) and ionization potential (IP), respectively. The probed peaks should hence be higher in energy than the actual HOMO and LUMO states. On the other hand, this effect is counteracted by the influence of the underlying metal surface. Due to the coupling of the molecule to the substrate, the near-by electron sea of the metal will screen the electric field of the additional charge by creating an image charge [37]. This reduces the Coulomb repulsion E_C within the molecule, which induces a shift of the electronic levels closer to the HOMO and LUMO (see fig.

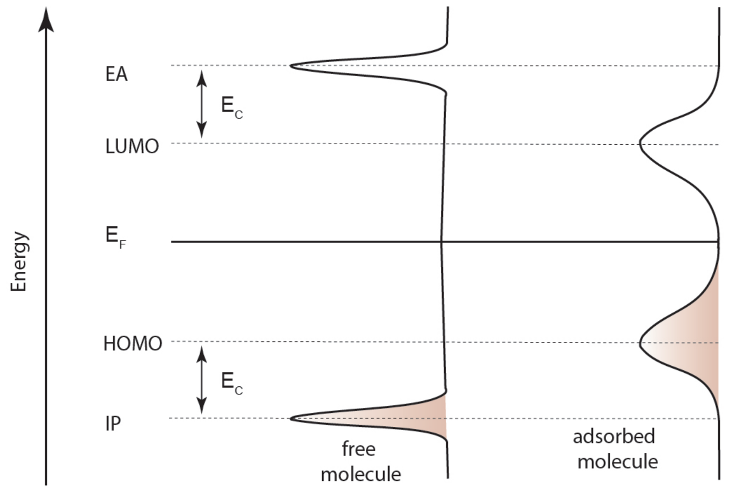

Figure 2.6. Schematics of the shifting of molecular levels due to adsorbtion on a metal surface. The free molecule shows energetically sharp and localized peaks at the energetic positions of the electron affinity level (EA) and ionization potential (IP). Due to the screening by the metal surface, the Coulomb respulsion energy E_C is reduced and the energy levels of the adsorbed molecule shift towards the HOMO and LUMO. Moreover, due to the strong coupling and the associated reduction of lifetime of the corresponding states, energetic level broadening occurs.

2.6.

The coupling to the surface does not only lead to a shifting of the probed peaks, but the effect of life-time broadening also comes into play, as due to the coupling of the molecule to the surface, tunneling electrons can quickly relax from the molecule into the metal. Assuming typical life times in the order of 10^{-15} s, a broadening of the energetic states of up to hundreds of meV is induced.

Moreover, a third effect influencing the electronic structure can occur, if charges are transferred between the surface and a molecule permanently. This charge transfer may cause a total realignment of the electronic molecular levels, and might lead to the formation of surface dipoles, band bendings and changes in the local work function [37].

4. Inelastic Electron Tunneling Spectroscopy

In the previous parts, only elastic tunneling processes were considered, where the intial and final states of the electron are at equal energies. In this case and under some assumptions, the measured $\mathrm{d}I/\mathrm{d}V$ signal reflects the LDOS of the molecule, as depicted in fig. 2.7a. However, besides the elastic transport path, tunneling electrons can also excite vibrational degrees of freedom or induce spin-flip processes [38–40], which is investigated by means of inelastic electron tunneling spectroscopy (IETS). In these inelastic processes, energy is transferred from the electron onto the system or vice versa during the tunneling process.

A typical shape of the current-voltage characteristics that includes inelastic processes is schematically depicted in fig. 2.7b. The $I(V)$ curve shows kinks at characteristic energies, which can be explained as follows: Each excitation has a certain energy $\hbar\omega$. For energies of the tunneling electron below $\hbar\omega$, no excitation can occur and the transport takes place only elastically. In case of the electron energy exceeding the excitation energy ($eV \geq \hbar\omega$), a new transport channel opens up [38], which can be taken by a certain number of all electrons with sufficient energy. Hence, the $I(V)$ curve shows an increased slope above the energy $\hbar\omega/e$. This difference in slope will be visible as a step in the $\mathrm{d}I/\mathrm{d}V$ curve or a peak in the $\mathrm{d}^2I/\mathrm{d}V^2$ spectrum, respectively. As inelastic processes take place independently of the tunneling direction, the feature in the spectrum can be seen at both positive and negative bias but with opposite sign. This property can be used to verify whether an observed feature in the spectrum originates from inelastic excitations [38].

As mentioned, there are two possible excitations that can be probed with IETS: spin excitations and vibrational excitations. In case of spin excitations, the symmetry breaking at the surface or by the molecular ligand field induces a lifting of the degeneracy of the different spin directions of the molecular spin, which are seperated by the magnetic anisotropy energy. A tunneling electron can then induce spin excitation processes for energies exceeding the level splitting, caused by this magnetic anisotropy. Due to the strong electron-spin coupling, spin exitations usually imply a rather large change of conductance of up to 100 % [41].

For vibrational excitations, on the other hand, the process is slightly more complex. There is indeed a positive contribution to the conductance originating from the opening of an additional inelastic transport channel, however, also the elastic transport path is affected. The contribution of the elastic path to the conductance is negative, due to exchange processes between the incident electrons and the electrons of the Fermi gas [42, 43]. Depending on the ratio between these two contributions, the IETS signal can either show a step in the $\mathrm{d}I/\mathrm{d}V$, be flat or even exhibit an inverted feature [44]. In any case, the excitation probability depends on the strength of the electron-vibron coupling. As it is much smaller than the electron-spin coupling strength, the change of conductance due to the excitation of vibrations in general is much smaller than the spin-excitation amplitudes and typically ranges in the order of 1 % to 10 % [41, 45, 46]. As the steps in the $\mathrm{d}I/\mathrm{d}V$ curve are hence rather small,

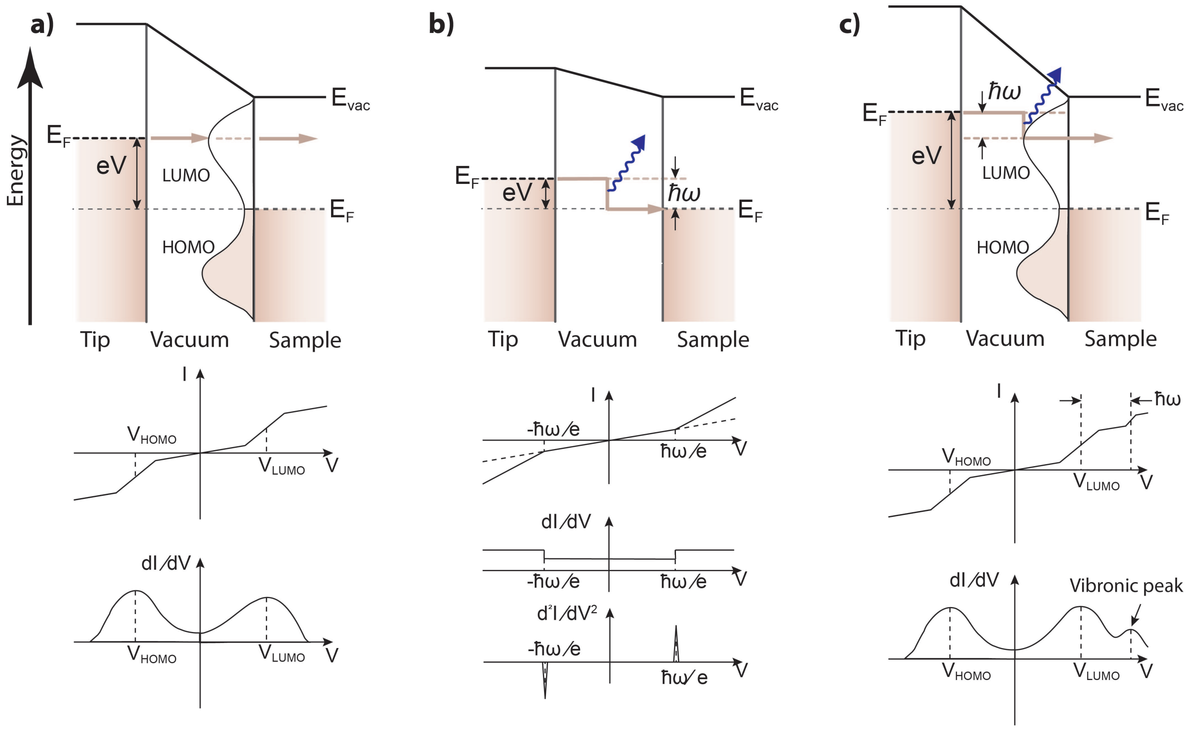

Figure 2.7. Schematics of the different tunneling processes that are observable in STS: **a)** Elastic tunneling process, with the dI/dV signal directly reflecting the LDOS of the sample. **b)** Inelastic tunneling process: The tunneling electrons excite a vibration with energy $\hbar\omega$ in the molecule. This creates an additional inelastic transport channel, leading to an increase of the differential conductance. Due to this effect being rather small, it is best oberserved in the d^2I/dV^2 signal. **c)** Vibronic tunneling process: The electron tunnels elastically through an electronic molecular resonance, after having excited a vibration with energy $\hbar\omega$ in the molecule.

vibrational features can be determined more easily from the d^2I/dV^2 curve. Moreover, it has been shown that in many systems only some vibrational modes have a sufficiently large coupling to be observed at all. Certain vibrational modes are totally quenched, due to the adsorbtion of the molecule on the surface [38, 40, 47].

In addition to the described inelastic processes, tunneling can take place through vibronic levels, *i.e.*, vibrational excitations of electronic resonances. Here, an electron with energy eV slightly above the resonance energy E_r can enhance its tunneling probability, by depositing the excess energy to reach E_r into vibrational excitations (see fig. 2.7 c). These vibrational modes will be visible in the dI/dV signal as resonant peaks at multiple energies of $\hbar\omega$ at the shoulder of the corresponding resonance [48, 49].

C. Atomic Force Microscopy

In the previous section, the working principle of the STM has been discussed. As all information in scanning tunneling microscopy is obtained from the tunneling current, this measurement technique is restricted to metals and semiconducting samples only. However, only a few years after the invention of the STM, in 1985 G. Binning, C. F. Quate and Ch. Gerber proposed a related measurement technique referred to as atomic force microscopy (AFM), which is also suitable for the investigation of non-conducting substrates [50]. In contrast to STM, where a metallic tip is mounted on a stiff tip holder (see sec. D for more details), in AFM the tip is mounted on a small tuning fork, which acts as an harmonic oscillator with an eigenfrequency f_0, typically in the order to 15 kHz to 40 kHz. When the tip is brought to close proximity to the sample, the oscillation frequency f changes due to the interaction between the tip and the sample. From this change of the eigenfrequency of the tuning fork, complementary information about the substrate can be obtained.

There are two main operational categories in AFM: the static mode, also referred to as contact mode, and the dynamic mode, referred to as non-contact mode [51]. As the name suggeset, in the contact mode, the tip is in contact with the surface while it is dragged across the sample. To obtain information about the sample, either the deflection of the cantilever due to forces between the tip and the substrate are measured directly, or the feedback signal is recorded that is needed to keep the cantilever at a fixed position. In the non-contact (nc) mode, on the other hand, the cantilever is oscillating with an eigenfrequency f_0 at a certain distance from the sample. An external feedback loop is driving this oscillation. For the non-contact mode, two different feedback modes can be utilized: the amplitude modulation (AM) and the frequency modulation (FM) modes. In the frequency modulation mode, the cantilever is driven to oscillate at its eigenfrequency at a constant oscillation amplitude. The change of the eigenfrequency due to the interaction of the tip with the sample are used to characterize the forces. In the amplitude modulation mode, the tip is driven by a constant driving amplitude to oscillate at a fixed frequency close to its eigenfrequency. In the AM-AFM mode, changing forces between tip and sample are detected by the change of the resulting oscillation amplitude.

The measurements in this thesis were performed with a combined STM-AFM in the non-contact frequency-modulated AFM (nc FM-AFM) mode. The use of very stiff cantilevers with spring constants around $k_0 = 1800\,\mathrm{N\,m^{-1}}$ allow for very small oscillation amplitudes in the order of 30 pm, which enables simultaneous STM and AFM measurements. In the following parts, the theoretical working principle of AFM will be introduced and the main forces contributing to the AFM signal will be briefly discussed.

1. Theory of AFM: The Harmonic Oscillator

The motion of the cantilever in a dynamic AFM can be described by the equations of motions of an harmonic oscillator, whose only degree of freedom is the displacement of the cantilever z in the direction perpendicular to the surface. The corresponding equation is given by [52]

$$z(t) = A_0 \cdot \cos\left(2\pi f_0 t\right), \tag{2.14}$$

with A_0 being the oscillation amplitude. The resonance frequency f_0 is defined by the spring constant k_0 and the effective mass m^* of the cantilever as

$$f_0 = \frac{1}{2\pi}\sqrt{\frac{k_0}{m^*}}. \tag{2.15}$$

Under the influence of external forces, *e.g.*, originating from tip-sample interactions, the oscillator experiences a pertubation, which affects the effective spring konstant k^*. For oscillation amplitudes A_0 that are small compared to the tip-sample distance z, the effective spring constant for a given tip-sample interaction F_{ts} can be expressed as [53]

$$k^* = k_0 - \frac{\partial F_{\mathrm{ts}}}{\partial z}. \tag{2.16}$$

This leads to a modification of the resonance frequency to

$$f^* = \frac{1}{2\pi}\sqrt{\frac{k_0 - \frac{\partial F_{\mathrm{ts}}}{\partial z}}{m^*}}. \tag{2.17}$$

The shift of the frequency Δf from its unperturbed eigenfrequency is hence given by

$$\Delta f = -\frac{f_0}{2k_0}\frac{\partial F_{\mathrm{ts}}}{\partial z}, \tag{2.18}$$

which is directly proportional to the gradient of the tip-sample force.

2. Different Forces Relevant for Atomic Force Microscopy

As mentioned above, information about the surface in AFM is obtained from the shift of the eigenfrequency of the cantilever as a result of the tip-sample interaction. There are several forces playing a role for this interaction, each with a particular strength and distance dependence. The most relevant ones that will be described in the following are the chemical forces, the Van der Waals forces and the electrostatic forces. Moreover, there are magnetic forces, which play a role in case of magnetic tips and samples. However, as they are only relevant for certain systems and are typically small compared to the other forces, they will not be considered here.

Van der Waals Forces

Van der Waals forces arise due to the interaction between electric dipole moments of molecules and atoms [54]. Typically, they are divided into three categories of Van der Waals interactions. The Keesom force describes interactions between two permanent dipoles. The Debye force treats the case of one permanent dipole that is acting on a polarizable molecule by inducing a dipole moment. The third category - the London dispersive force - describes instantaneously induces dipoles between two molecules without permanent dipole moment. The van der Waals potential E_{vdW} is rather short ranged, as it decays with $E_{\mathrm{vdW}} \propto -1/z^6$, where z denotes the distance between the corresponding atoms. The van der Waals force is a rather weak force and acts only attractively. However, it plays a non-negligible role in AFM, as a real tip does not consist of a single apex atom but all the macroscopic tip atoms contribute to an overall van der Waals background. The approach of H. C. Hamaker calculates the resulting van der Waals force for a spherical tip of radius R at a distance z from an infinite flat surface plane [55]

$$F_{\mathrm{vdW}}(z) = -\frac{HR}{6z^2}, \tag{2.19}$$

with H being the material-dependent Hamaker constant. Thus, by reducing the tip radius R, the van der Waals background can be reduced.

Chemical Forces

The chemical force consists of two components with an attractive and a repulsive part. It is often modelled by a Lennard-Jones potential, which describes the potential energy of two atoms as a func-

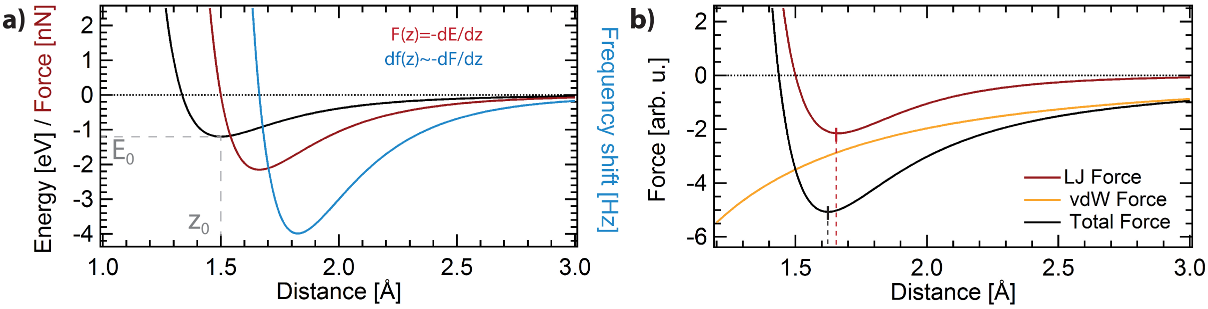

Figure 2.8. Lennard-Jones force as a function of distance. **a)** Lennard-Jones potential (black) and Lennard-Jones force (red) as a function of distance between two atoms. The distance z_0 denotes the bond distance and E_0 the corresponding binding enery. The blue curve corresponds to the frequency shift, which is proportional to the derivative of the force. **b)** Shift of the Lennard-Jones force (red) under the influence of an additional Van der Waals force (yellow).

tion of their distance z [56]

$$E_{\mathrm{LJ}}(z) = E_0\left[\left(\frac{z_0}{z}\right)^{12} - 2\left(\frac{z_0}{z}\right)^{6}\right], \tag{2.20}$$

where E_0 denotes the binding energy and z_0 the bond distance. The first term in eq. 2.20 represents the repulsive component of the force, which stems from the Pauli repulsion. At close proximity of the atoms, the electronic wavefunctions will start to overlap. Due to the fermionic character of the electrons, however, they may no longer occupy the same energetically lowest level, but have to occupy higher lying orbitals, which increases the total energy of the system. The second term in eq. 2.20 arises due to attractive van der Waals forces. In contrast to the earlier discussed van der Waals background of the macroscopic tip, this term only takes into account the interactions of the very last atom of the tip apex.

A sketch of the Lennard-Jones potential for a binding energy of $E_0 = 1.2\,\mathrm{eV}$ and a bond distance of $z_0 = 1.5\,\text{Å}$ is depicted in fig. 2.8a in black. The red curve shows the corresponding force — in the following referred to as the Lennard-Jones force — that can be obtained from the derivative of the Lennard-Jones potential

$$F_{\mathrm{LJ}}(z) = -\frac{\partial E_{\mathrm{LJ}}(z)}{\partial z} = 12 \cdot \frac{E_0}{z_0}\left[\left(\frac{z_0}{z}\right)^{13} - \left(\frac{z_0}{z}\right)^{7}\right]. \tag{2.21}$$

The blue curve corresponds to the frequency shift, which is proportional to the derivative of the Lennard-Jones force.

Figure 2.8b shows the Lennard-Jones force together with a non-negligible van der Waals backgound of the macroscopic tip. Due to the $F_{\mathrm{vdW}} \propto -{}^{1}/_{z^2}$ decay of the van der Waals background of the tip (yellow curve), the van der Waals force plays a crucial role at larger tip-sample distances. In contrast, the influence of the chemical force predominates at smaller distances (red curve). Therefore, in order to obtain high-resolution images in AFM, it is necessary to scan at a close tip-sample distance. The sum of both the Lennard-Jones force and a macroscopic van der Waals backgound is shown in black with its minimum shifted to smaller distances with respect to the red curve, as indicated by the dashed lines.

Electrostatic Forces

The third category of relevant forces, the electrostatic forces are the most long-ranged ones. In AFM, they can result from a potential difference between tip and sample, which can be either intrinsic to the system (*i.e.*, due to a difference in the work function of the materials) or induced by the application of an external voltage V. In a simple picture, the tip and sample can be treated as a capacitor, whose energy is given by

$$E_{\text{Cap}} = {}^{1}\!/_{2} \cdot C \cdot V^{2}, \tag{2.22}$$

with C corresponding to the capacitance of the system, which depends on the tip-sample distance z. The effective electrostatic potential $V = V_{\text{bias}} + V_{\text{LCPD}}$ consists of the applied bias voltage and the local contact potential difference. The force is given by the gradient of the potential energy

$$F_{\text{electr}} = \frac{1}{2} \cdot \frac{\partial C}{\partial z} \cdot V^{2}. \tag{2.23}$$

As the term ${}^{\partial C}\!/_{\partial z} < 0$, the resulting electrostatic force is always attractive. From the dependence in eq. 2.23, one can see that the electrostatic force depends quadratically on the applied bias voltage V_{bias}. When ramping the bias voltage, the force describes an inverse parabola, whose vertex (*i.e.*, its absolute minimum) corresponds to the local contact potential difference that is needed to compensate the acting electrostatic forces resulting from differences in the work functions of the tip and sample materials. This method to determine the local variations of the work function is referred to as Kelvin probe force microscopy (KPFM).

D. Experimental Set-up

The measurements presented within this thesis were performed using two different low-temperature STM's under UHV conditions: a Createc machine working at 4.5 K and a Specs Joule-Thomson (JT) STM, which can reach temperatures of 1.1 K. Their general working principles and main components are very similar, however, the designs of their STM heads is different for both machines. As most measurements were performed on the Createc machine, its characteristics will be described in more detail. Afterwards, only some comments on the working principle of the JT circuit will be made. Moreover, some details about the experimental realization, *i.e.*, the sample preparation and the mainly used Au(111) crystal, will be introduced in the following.

To maintain a clean surface without unwanted contamination, all measurements were performed under UHV conditions. Therefore, a set of pumps, *i.e.*, two ion pumps, a turbomolecular pump, a titanium-sublimation pump (TSP) and a cold trap are installed at the UHV chamber to maintain a low pressure. In order to reduce the mobility of the adsorbates on the surface and enhance the energy resolution of the spectra, liquid nitrogen and liquid helium are used to cool down the system. Therefore, the STM head is attached to a bath cryostat, which further acts as an efficient pump, allowing for even better pressures inside the STM chamber.

The UHV chamber itself consists of two parts: the preparation chamber and the STM chamber (see fig. 2.9a). In the preparation chamber, the sample cleaning by means of multiple cycles of sputtering and annealing as well as the sample preparation through deposition of the molecules or atoms takes place. Therefore, it is equipped with a Ne-sputter gun and multiple slots for molecular and metal evaporators. Furthermore, a mass spectrometer is installed. The preparation chamber is separated by a gate valve from the STM chamber. The transfer of the sample between the preparation- and the

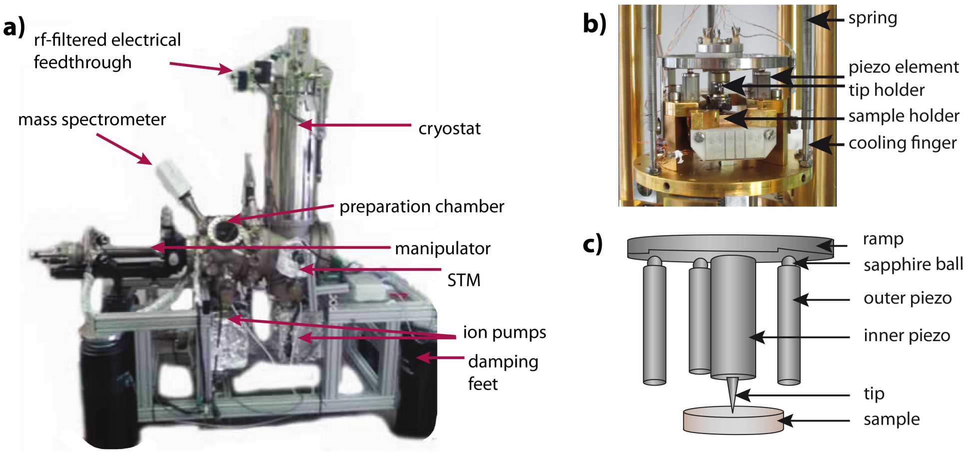

Figure 2.9. Image of the Createc STM setup: **a)** The UHV chamber consisting of the preparation chamber, the STM chamber, a manipulator and a cryostat. Picture slightly modified from [57]. **b)** Photograph of the STM head. The crystal sample is mounted onto a sample holder, which is positioned inside the STM. The latter is hanging on Eddy-Current damped springs in order to reduce vibrations. Picture slightly modified from [57]. **c)** Schematics of the Besocke-type STM head. The tip is mounted onto a ramp, standing on three piezo elements. Application of a sawtooth voltage pulse to the piezo elements leads to the rotation of the ramp, which controls the movement of the tip.

STM chamber is done by a sample manipulator, which can be independently moved along all three axes and rotated freely. It furthermore allows for the pre-cooling of the sample before the transfer into the STM chamber or heating of the sample during the annealing cycles or molecule deposition, respectively. The reachable temperatures are in the range of 80 K to 1000 K.

The Createc machine has a scanning head with a design proposed by K. Besocke [58], where the movement of the tip is realized by means of piezo elements. Therefore, a three-fold segmented copper ramp is standing on three piezo elements with sapphire spheres on top, as shown in fig. 2.9c. By applying sawtooth-shaped voltage pulses to certain electrodes of the piezo elements, a lateral movement or rotation of the ramp plate can be induced, leading to a change of the tip position in both horizontal and vertical direction. Here, a maximal lift height of 0.6 mm can be obtained. Another piezo element in the center of the ramp is directly connected to the tip and allows for its precise control on the surface, independent from the other piezo elements. The entire STM head is hanging on Eddy-Current damped stainless steel springs, in order to reduce vibrations. Further damping in the low-frequency regime during data acquisition is achieved by lifting the entire chamber onto pneumatic feet. Moreover, the Createc machine is a combined STM-AFM system, which allows to perform non-contact frequency-modulated AFM (nc FM-AFM) measurements simultaneously to normal STM measurements. Therefore, the central STM tip can be exchanged by a qplus tuning fork sensor [59], which can be attached to the main piezo elements with magnets. Both, the STM tips and the tip used for the tuning fork sensors are made of tungsten (W) and were chemically etched in order to assure their microscopically sharp end. Furthermore, the machine contains a low-temperature high-frequency amplifier, which is attached to the cooling fingers of the STM. As it is a central component of the shot-noise measurements, it will be described in detail in chapt. IV.

The Specs JT-STM, on the other hand, is designed for the purpose of obtaining temperatures below 4.5 K, which is typically the limit that can be reached with lHe bath cryostates. To achieve lower temperatures, a Joule-Thomson cooler is integrated into the setup, consisting of a system of capillaries, which are filled with He gas. By means of adiabatic gas expansion inside the JT pot, the STM can be cooled down to 1.1 K by using He^4 or to even lower temperatures with the rare He^3 gas. More-

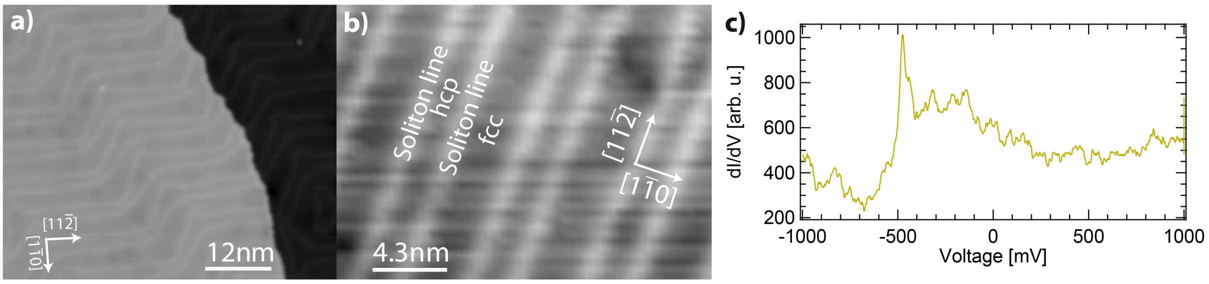

Figure 2.10. Characteristics of the Au(111) surface: **a)** STM topography showing two terraces of clean Au(111). **b)** Zoom into the herringbone reconstruction. The hcp and fcc areas are separated by 0.2 Å higher soliton lines. Topographies were recorded at 500 mV. **c)** $\mathrm{d}I/\mathrm{d}V$ spectrum recorded on the clean the gold surface showing the onset of the Au(111) surface state at −490 mV.

over, the JT-STM contains a set of superconducting coils, which can generate homogeneous magnetic fields of up to 3 T perpendicular to the sample surface.

The STM is controlled by a digital signal processor (DSP), which is connected to a computer. STM images were taken using the STMAFM 3.1 software from Createc and analyzed by means of the Nanotec-software WSxM 5.0 [60]. STS spectra were recorded with the Stanford Research SR830 DSP Lock-in Amplifier and furthermore evaluated with Igor Pro [61] and SpectraFox 9.01.0.0 [62].

1. Substrates and Preparation Methods

For the investigation of single molecules on a substrate and in order to allow them to self-assemble in ordered islands, a well-defined atomically clean substrate is required. The low-index surfaces of the coinage metals (Au, Ag, Cu) are a suitable choice, as they are well characterized and form large flat terraces. Moreover, they are relatively easy to clean by means of repeated cycles of sputtering and annealing. Therefore, nobel gas atoms like Ne are ionized and accelerated with approx. 1.5 keV towards the sample surface. Afterwards, the sample is annealed to 800 K for some minutes, to smoothen the surface and obtain large flat terraces.

The Au(111) Surface

The substrate used throughout this thesis is a Au single crystal, which was grown and polished in the (111)-direction. Due to its low reactivity, it does exhibit a rather weak interaction with molecular adsorbates and it is a suitable choice to maintain a clean surface. The bulk structure of gold exhibits a face-centered cubic (fcc) symmetry. On the surface, however, a reconstruction occurs, leading to alternating regions of fcc and hexagonally closed packed (hcp) arrangements (see fig. 2.10a). So-called soliton lines with corrugations of 0.2 Å seperate the corresponding areas. These lines, aligned along the [11$\bar{2}$]-direction, rotate periodically around 120°, leading to the formation of the characteristic zig-zag structure, also known as the herringbone reconstruction, as depicted in fig. 2.10a and b. Moreover, the Au(111) surface features a Shockley-type surface state at −490 mV [63]. Together with the soliton lines, observation of the latter can help to assure having a clean STM tip during measurements.

CHAPTER III

Spin- and Vibrational Excitations in Different Configurations of Fe-TPyP on Au(111) and MoS_2

In the field of spintronics, data is stored in the spin state of systems as small as single atoms. The functionality of spintronic devices depends crucially on the survival of the spin on a surface. By placing a single magnetic atom on a metal substrate, exchange scattering with the conduction electrons of the underlying substrate can lead to a total screening of the spin, referred to as the Kondo effect [64]. One way to protect the spin system from such screening is to embed it into a molecular complex. A suitable choice for such a complex are porphyrins, which constitute a class of well-investigated molecules, because of their versatility in terms of self-assembly and electronic and magnetic properties [65–73]. Due to the chemical flexibility with respect to the functional endgroups, the variety of porphyrins seems infinite. Numerous studies on porphyrins have been performed with different central metal atoms on different metal substrates, showing that by a suitable choice of metal center and surface, the magnetic and electronic properties of the complex can be tailored [74–76]. In this chapter, we investigate Fe-5,10,15,20-tetra-pyridyl-porphyrin (Fe-TPyP) molecules adsorbed on

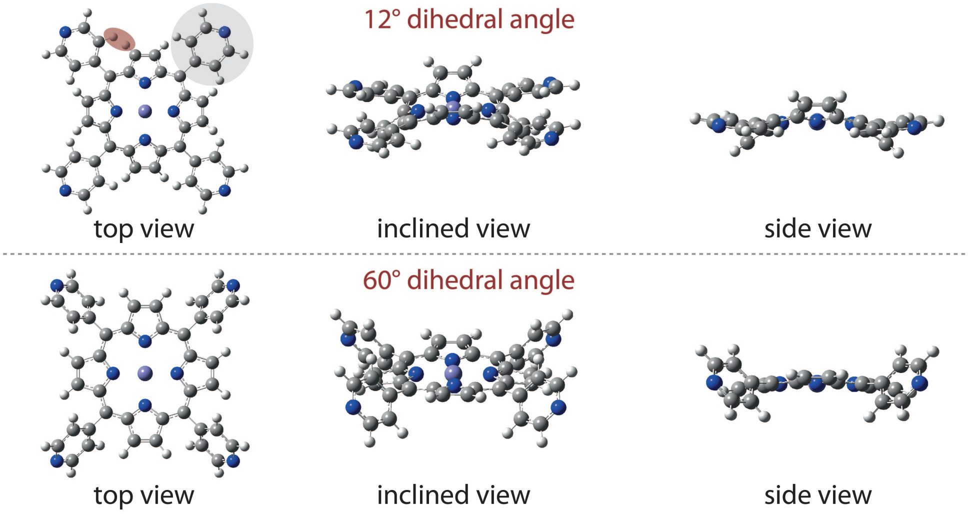

Figure 3.1. Schematics of the Fe-TPyP molecule (C=grey, N=blue, H=white, Fe=violet). Steric repulsion of neighbouring hydrogen atoms (red elipse) induces a rotation of the pyridyl groups (grey circle), leading to a deformation of the macrocycle. Top: for small dihedral angles, the pyridyl groups remain rather flat, which induces a larger saddle-shape distortion of the porphin core. Bottom: higher rotational angles of the pyridyl groups, in contrast, allow for the macrocycle to remain flat.

a Au(111) substrate. The structure of Fe-TPyP is shown in fig. 3.1. The TPyP macrocylce consists of a porphin core, with four pyridyl groups (marked by the grey circle) attached to it. In the gas phase, the pyridyl groups are rotated by 90° with respect to the flat macrocycle. On the surface, in contrast, a maximized interaction with the substrate would be obtained for completely flat pyridyl moieties. Steric hindrance between adjacent hydrogen atoms of the pyridyl groups and the porphin macrocylce (marked by the red elipse), however, disables a complete flattening of the pyridyl groups, such that a distortion of the macrocycle is induced. Two extreme cases of this distortion with dihedral angles of 12° and 60°, which characterizes the rotation of the pyridyl groups, are depicted in fig. 3.1. For smaller dihydral angles (top), the pyridyl groups are rotated less strongly, which, to avoid steric repulsion, induces a saddle shape distortion of the porphin core. This is sketched in an inclined view and side view, to demonstrate the up- and down bending of the opposing pyrrole groups, respectively. For larger dihedral angles, *i.e.*, 60° as shown in the bottom, the rotation of the pyridyl groups allows for the macrocycle to stay in a rather flat geometry, and only small saddle-shape distortions are expected. These conformational changes of the molecular macrocycle due to adsorption on a surface can strongly influence the electronic and magnetic properties of the molecule, as has been shown in many studies on tetra-phenyl-porphyrins (TPP) [65, 68, 72, 77, 78] and tetra-pyridyl-porphyrins (TPyP) [69, 70, 73, 79, 80].

In this chapter, we show that one molecular system on one and the same surface can have different magnetic and electronic properties, caused by small changes in the adsorption geometry. Therefore, we investigate spin- and vibrational excitations on Fe-TPyP molecules adsorbed on a Au(111) substrate. Several different intermolecular arrangements were observed, which are accompanied by different intramolecular distortions. By employing low-temperature scanning tunneling spectroscopy on the molecules in the different arrangements, we show that these intramolecular distortions also affect the magnetic properties of the molecules. Moreover, the different hybridization of the electronic states of the molecules leads to slight changes in the energy position of the molecular orbitals, which has also has an impact on the vibrational signatures.

In the first three sections, the individual adsorption structures will be introduced seperately. After the corresponding magnetic and vibrational properties were explained for each structure, a comparison between the different arrangements will be drawn that helps to understand the impact of the ligand deformations on the properties of the central Fe atom. Moreover, by annealing the Fe-TPyP molecules on the Au(111) sample to elevated temperatures, some intramolecular bonds in the Fe-TPyP complex could be broken and a flat species of Fe-TPyP derivatives were formed. Their properties will be briefly analyzed in sec. F. Finally, to go one step further, the Fe-TPyP molecules were also investigated on a decoupling molybdenum disulfide (MoS$_2$) single-layer, which was grown on the Au(111) substrate.

A. Magnetic Anisotropy

The magnetic properties of atoms and molecules arises from unpaired electron spins. The ground-state configuration of these electrons is described by Hund's rules. According to the first Hund's rule, the total spin $|\vec{S}|$ of a system is maximized due to the parallel alignment of the individual spins, resulting from exchange interactions. According to Hund's second rule, in case of several available orbitals, those levels are filled first that lead to a maximization of the total orbital angular momentum $|\vec{L}|$. The third Hund's rule then describes how both momenta $|\vec{S}|$ and $|\vec{L}|$ couple to a total angular momentum $|\vec{J}|$ by aligning either in a parallel or anti-parallel way. If the spin system is in an isotropic environment, *i.e.*, in the gas phase, there is no preferrential orientation of the magnetic moment in space.

However, if the atom is inserted in an anisotropic environment as present in a molecular complex or on a surface, the rotational symmetry is broken and certain directions in space become energetically favourable. In the following, the influence of an anisotropic environment on the magnetic moment of a magnetic 3d transition metal atom will be introduced.

1. Crystal Field Splitting

An anisotropic environment has several effects on a spin system. The most apparent one is a shifting of the energetic position of certain orbitals, due to their different spatial distribution. To understand this effect, fig. 3.2b illustrates the d-level arrangement for a 3d transition-metal element. In an isotropic environment (left), all five 3d levels are energetically degenerate. By embedding the atom in an octahedral crystal field with six atoms placed along the Cartesian axes (middle), the degeneracy of the d levels is partially lifted. Those orbitals that point directly towards the ligand atoms, namely the $d_{x^2-y^2}$ and the d_{z^2} orbitals, shift up in energy as they experience the strongest Coulomb repulsion (see fig. 3.2a). Those orbitals that extend in between the Cartesian axes, *i.e.*, the d_{xz}, d_{yz} and d_{xy} orbitals,

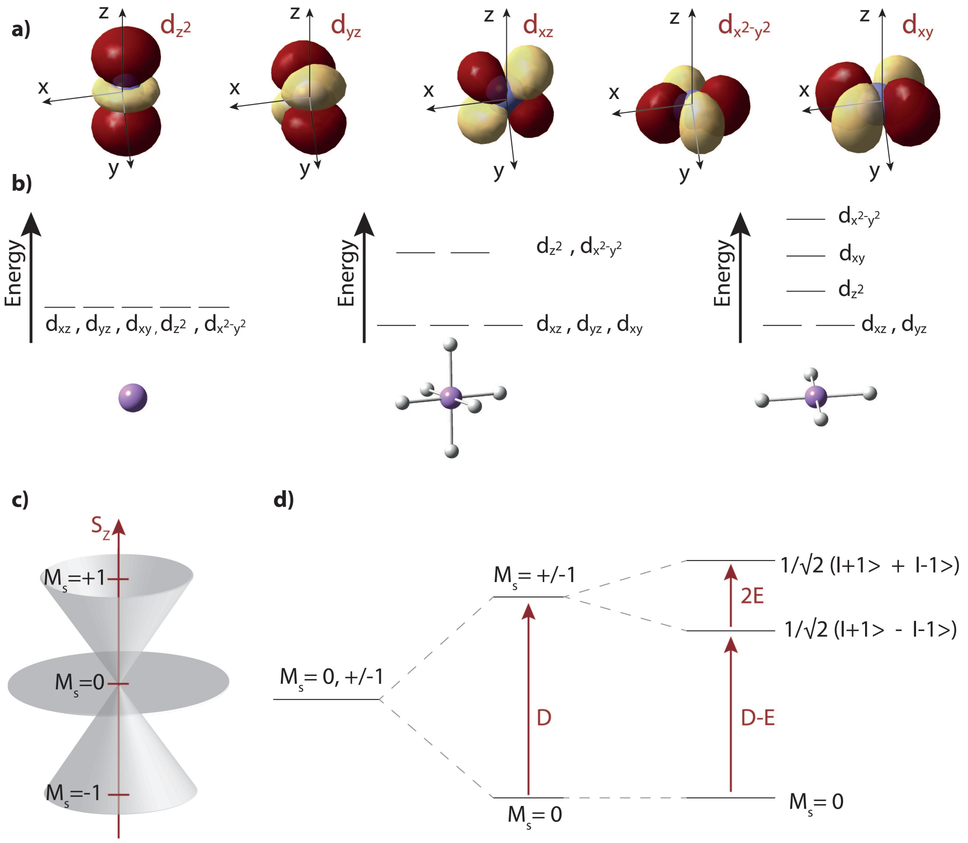

Figure 3.2. **a)** Spatial distribution of the 3d orbitals. **b)** Lifting of the degeneracy of the 3d levels in different crystal fields. Left: isotropic environment with all five levels degenerate. Middle: Octahedral cystal field, with a splitting of the d levels into two subsets. Right: A square-planar ligand field, leaving only the d_π orbitals degenerate. **c)** Schematic illustration showing the different directions of the spin projection M_S in space. **d)** Sketch of the effect of the magnetic anisotropy on a spin system. Due to an axial anisotropy D, the different levels $M_S = 0$ and $M_S = \pm 1$ are split in energy. An additional transverse anisotropy E induces a mixing of the $M_S = \pm 1$ states, which leads to the formation of new levels $|+\rangle$ and $|-\rangle$ that are split in energy.

have less overlap with the neighbouring atoms and are hence energetically favoured. This lifting of the degeneracy of the d levels is called crystal-field splitting. The crystal field splitting competes with Hund's first rule to maximize the spin, as the energy splitting of the d levels is usually in the same order of magnitude as the spin-pairing energy. Thus, the symmetry and magnitude of the crystal field can determine whether an atom lies in the high-spin or low-spin state.

On the right side of fig. 3.2b, the d-level splitting in an environment of even lower symmetry is sketched. In a square-planar symmetry, only four atoms are surrounding the central atom, leading to a further lifting of the degeneracy. In this case, the d_{z^2} does no longer point directly at the ligand atoms and hence shifts down in energy. Moreover, the degeneracy between the d_{xz}, d_{yz} and d_{xy} orbitals is broken, and only the d_{π} levels (d_{xz} and d_{yz}) form the degenerate lowest-lying state.

2. Magnetocrystalline Anisotropy and Spin-Orbit Coupling

In the previous section, we have discussed how the crystal field leads to a lifting of the degeneracy of the d levels, which affects the total spin state of the system. To understand how magnetic anisotropy emerges in a system, we do not only have to consider the spin momentum of the atom but also its orbital angular momentum. The d levels mentioned above are linear combinations of the 3d orbitals that solve the Schrödinger equation ($3\mathrm{d}_{-2}$, $3\mathrm{d}_{-1}$, $3\mathrm{d}_{0}$, $3\mathrm{d}_{1}$, $3\mathrm{d}_{2}$). The linear combinations are formed by a superpositon of the orbitals with opposite orbital angular momentum, *e.g.*, $3\mathrm{d}_{-2}$ and $3\mathrm{d}_{+2}$, such that the resulting orbitals no longer exhibit imaginary parts. This results in the five d orbitals d_{xz}, d_{yz}, d_{xy}, d_{z^2} and $\mathrm{d}_{x^2\text{-}y^2}$, which all exhibit a vanishing orbital angular momentum $\mathrm{l} = 0$. Hence, also the total angular momentum of the ground state of a 3d transition metal atom is usually quenched.

However, by second order pertubation effects, a finite orbital angular momentum L is restored, by the admixture of the different atomic orbitals via virtual excitation processes. This orbital angular momentum couples to the total spin moment via spin-orbit coupling, leading to a preferred direction of the spin in space. This results in a finite magnetocrystalline anisotropy.

In a simple spin model, the splitting of the different spin directions due to magnetic anisotropy can be described by the spin Hamiltonian

$$\mathscr{H}_{\mathrm{S}} = D\hat{S}_{\mathrm{z}}^2 + E(\hat{S}_{\mathrm{x}}^2 - \hat{S}_{\mathrm{y}}^2). \qquad \mathbf{3.1}$$

Here, $\hat{S}_{\mathrm{x}}^2$, $\hat{S}_{\mathrm{y}}^2$ and $\hat{S}_{\mathrm{z}}^2$ denote the spin components in x, y and z direction, respectively. The axial anisotropy constant D describes the splitting of the 2S+1 sublevels that correspond to a spin state S, according to their absolute projection in z direction. In case of a spin 1 system (see fig. 3.2d), the three different spin projections $\mathrm{M_S} = 0$ and $\mathrm{M_S} = \pm 1$ are split in energy by D according to the absolute value of their spin projection. The three different projections of the spin are depicted in fig. 3.2c. Depending on the sign of D, it is either favourable to have a high-spin projections ($D<0$), known as easy-axis anisotropy or low spin projections ($D>0$), referred to as easy-plane anisotropy. Since this splitting occurs without an external magnetic field, it is referred to as zero-field splitting (ZFS).

The second term in equ. 3.1 describes the case of an additional transverse anisotropy E. This component induces a mixing of the $\mathrm{M_S} = \pm 1$ states, which leads to the formation of new levels $|+\rangle = 1/\sqrt{2}(|+1\rangle + |-1\rangle)$ and $|-\rangle = 1/\sqrt{2}(|+1\rangle - |-1\rangle)$ that are split by an energy 2E. Typically, the coordinate system chosen to describe D and E deviates from Cartesian coordinates, as by convention [81] the axis are chosen such that $|D|$ is maximized and E positive, leading to values where $E < 1/3|D|$.

B. Densely-Packed Structure of Fe-TPyP on Au(111)

After in the previous section, the physics leading to magnetic anisotropy in single atoms and molecules has been introduced, in the following, we want to investigate the properties of the molecular Fe-TPyP system. As mentioned in the introduction, different structures were observable for Fe-TPyP on Au(111). In this section, we will examine the properties of the first structure, in the following referred to as the densely-packed arrangement. For the preparation of densely-packed self-assembled islands, the Fe-5,10,15,20-tetra-pyridyl-porphyrin complex[1] was evaporated from a commercial Knudsen-cell evaporator at 410 °C, with the sample held at room temperature. Upon deposition, the molecules get dechlorinated, with the central Fe atom changing its oxidation state from +3 to +2. The measurement in this section were all performed at 4.8 K.

1. Adsorption Structure of Densely-Packed FeTPyP on Au(111)

Deposition of a submonolayer of Fe-TPyP molecules onto the Au(111) substrate at room temperature leads to the formation of self-assembled densely-packed islands (see fig. 3.3). Due to their high mobility on the surface, the molecules form a two-dimensional structure that expands over several hundreds of nanometers. The observation of the characteristic herringbone reconstruction of the Au(111) surface through the molecular overlayer indicates a rather weak interaction between the molecules and the underlying surface. The orientation of the molecules inside the island is shown in fig. 3.3b. The molecules adapt an ordered structure of alternating rows, which is built up by a unit cell of 1.4 nm × 2.7 nm, containing two molecules. From the topographical images, the breaking of the four-fold symmetry of the molecules is apparent. Upon adsorption, the pyridyl groups, which are perpendicular in gas phase, are flattened due to the interaction with the substrate. Due to steric hindrance of the adjacent hydrogen atoms, this flattening induces one pair of opposing pyrrole rings to bend up while the other pair bends down, leading to a saddle-shaped configuration of the Fe-TPyP molecules. A schematic view of the molecular distortion is depicted in fig. 3.3c, with the red ellipses marking the part of the pyridyl legs that protrudes the most. As the pyridyl groups rotate away from the upper pyrroles and towards the lower pyrroles, the molecular topography is no longer of fourfold symmetry, but shows rather twofold symmetric molecules of rectangular shape. Such a saddle-shape distortion upon adsorption has already been described for many M-TPP and M-TPyP systems [70, 72, 73, 79, 82–85]. Note that in the structure model that is overlaid in the topographic images (*e.g.*, fig. 3.3b), the rotation of the pyridyl legs is difficult to illustrate. Therefore, it is indicated by moving the entire pyridyl legs towards the position of its most protruding site.

The observed molecular structure on the Au(111) surface as well as the size of the unit cell coincides with the arrangement of Fe-TPyP on Ag(111), where a unit cell size of 1.39 nm × 2.74 nm was reported [69, 79]. In their paper, W. Auwärter, et al. [79] found that the dihedral angle, by which the pyridyl groups rotate out of the plane, is about 60°. This rather strong pyridyl rotation leads to a weak distortion of the inner macrocycle. Due to the similarity between the molecular arrangements on Au(111) and Ag(111) and the similar lattice constants of the two substrates, it seems reasonable to assume a similar distortion of the porphyrin macrocyle on Au(111).

To confirm this geometry, constant-heigth Δf maps were recorded at different tip-sample distances with a functionalized Cl tip. Figure 3.4a shows the topography of an island of Fe-TPyP and fig. 3.4b-d the corresponding Δf maps. In the map with the largest tip-sample distance (see fig. 3.4b), a strong contrast originating from the pyridyl moieties can be observed, indicating them to be the

---

[1] The molecules were synthesizes by C. Czekelius from the Heinrich-Heine Universität Düsseldorf.

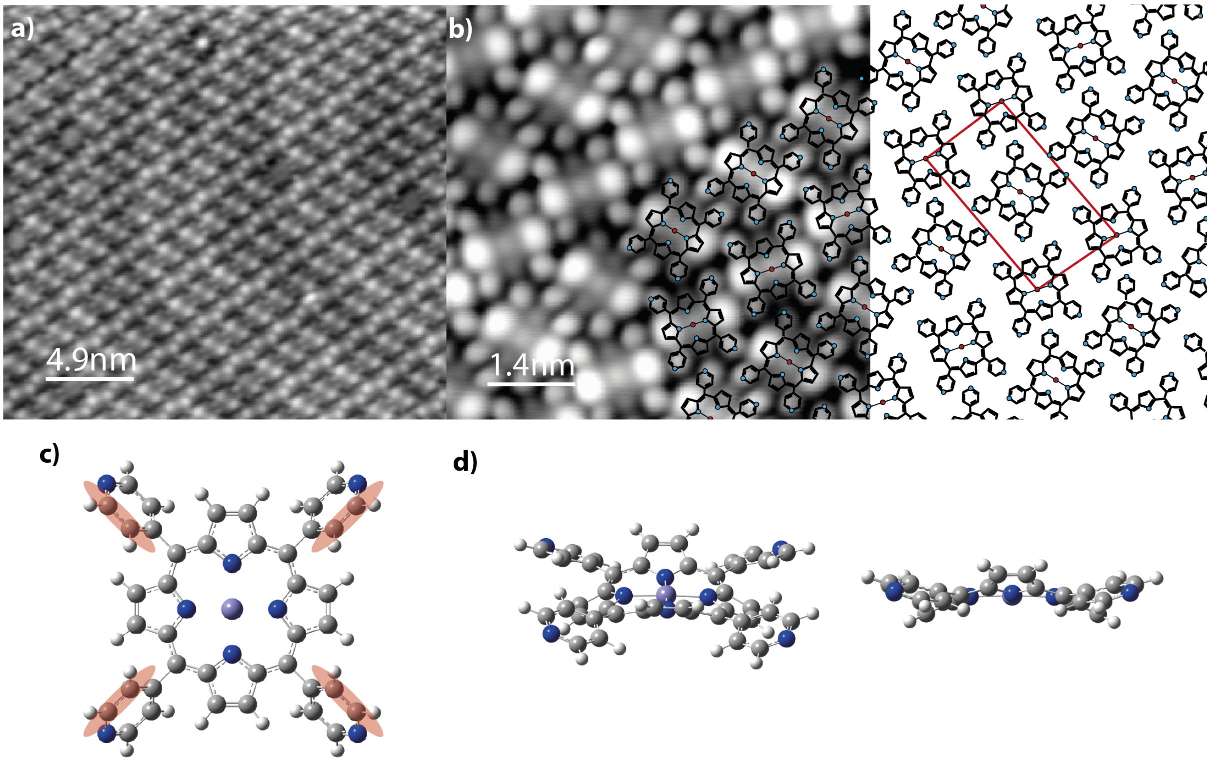

Figure 3.3. a) STM topography showing the regular, densely-packed arrangement of Fe-TPyP molecules on a Au(111) surface after deposition at room temperature. The characteristic herringbone reconstruction of the underlying substrate can still be seen. Topographies recorded at 310 pA, 300 mV. **b)** Close-up view showing the molecular arrangement inside the layer. A molecular model is overlaid to indicate how the pyridyl groups determine the optimal arrangement. The red lines show the unit cell of the molecular arrangement of 1.4 nm × 2.7 nm, containing two molecules. Topographies recorded at 200 pA, 200 mV. **c)** Structure model of Fe-TPyP showing the asymmetric rotation of the pyridyl legs. The red ellipses mark the parts of the pyridyl groups that stick out the most. **d)** Side view (right) and inclined view (left) of the molecular deformation towards a saddle-shaped structure. The rotation of the pyridyl groups can be seen, with a simultaneous up- and down-tilting of the pyrrole groups, respectively.

most protruding molecular group. When approaching further (fig. 3.4c,d), the upper pyrrole groups can be observed, which confirms the slight saddle-shaped distortion of the molecule. To conceive an idea of the strength of the molecular deformations with respect to the rotational angles of the pyridyl groups, simulations of the Δf maps were performed for several molecular geometries. Therefore, the dihedral angles that define the rotation of the pyridyl legs with respect to the surface plane were manually varied and fixed during the DFT minimization process. For each structure, simulations of the Δf maps were performed with a Cl tip at different tip-sample distances by using the simulation program of P. Hapala, et al. [86], which is based on the force field between a flexible tip and the molecules [87, 88]. The best results, shown in fig. 3.4e were achieved for a rotational angle of 45°.

2. Electronic Properties of Densely-Packed FeTPyP

In the next step, we want to study the electronic properties of the densely-packed Fe-TPyP molecules. In fig. 3.5, dI/dV spectra of an Fe-TPyP molecule are compared to the spectra of an unmetallated TPyP molecule, which can be found in a small amount within the molecular island. In fig. 3.5b the

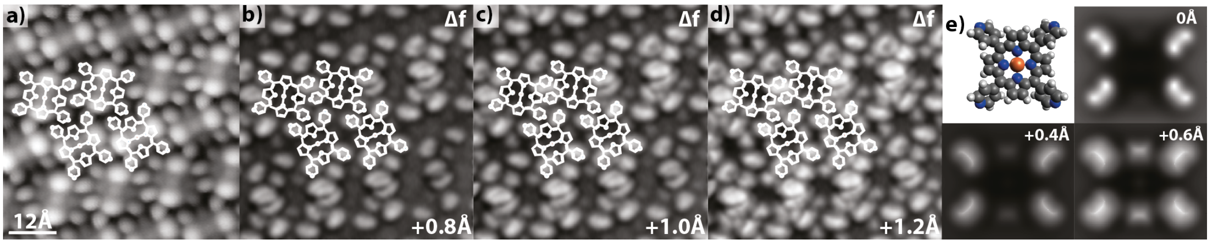

Figure 3.4. AFM images of Fe-TPyP. **a)** Topography and **b-d)** constant-height Δf maps recorded at different distances with a functionalized Cl tip. In constrast to the topographic appearance, where the pyrrole groups appear highest, the Δf maps indicate that the pyridyl legs are the molecular moieties that protrude the most. Topography recorded at 150 pA, 230 mV. For the Δf maps, the tip position with respect to this setpoint is indicated in the respective images. **e)** Simulated Δf map for a rotational angle of the pyridyl moities of 45° with respect to the surface, which yielded the best agreement to the experimental data.

unmetallated molecule (red) shows an onset of a resonance at −1.05 V and a double peak at 1.30 V and 1.45 V. To ensure the quality of the tip, the yellow spectrum corresponds to a reference spectrum recorded on the bare Au(111) surface. It features a Shockley-type surface state at −490 mV [89], which is visible as a peak in the $\mathrm{d}I/\mathrm{d}V$ spectrum. The $\mathrm{d}I/\mathrm{d}V$ spectrum on the metallated FeTPyP molecule (black) exhibits the same resonances as the unmetallated molecule at positve bias voltages, but the lower peak is shifted by approx. 50 mV in energy towards the Fermi level. The localization of these electronic resonances on the molecule can be seen in fig. 3.5e, where maps of the differential conductance are shown, which were recorded at 1.3 V and −1.3 V in the constant-height mode. The state at 1.3 V is localized on the organic macrocycle of the molecule with its main weight on the pyridyl legs and exhibits a nodal plane along the upper pyrrole rings. Its shape resembles the shape of the LUMO orbital as found in other theoretical and experimental studies [68, 82]. Hence, the double peak at positive bias voltages can be associated with the LUMO and LUMO+1 of the TPyP macrocycle, which are energetically degenerate for the isolated molecule [74, 79, 90]. Upon adsorption on a surface, the saddle deformation of the Fe-TPyP and TPyP molecules induces a lifting of the degeneracy between the LUMO and LUMO+1 orbitals, which leads to a splitting of these levels.

The $\mathrm{d}I/\mathrm{d}V$ map recorded at −1.3 V shows that the states at negative energies on the contrary are more localized at the molecular centre and can be assigned to the HOMO orbital. This localization of the HOMO and LUMO is in agreement with studies on CoTPP on Au(111) [82], where they find that the HOMO originates from hybridized d states of the central metal atom with porphyrin states and is hence more localized in the center of the molecule, whereas the LUMO predominantly keeps its porphyrin character and is localized on the organic macrocycle.

3. Inelastic Spin Excitations on FeTPyP

In fig. 3.5c, spectra on Fe-TPyP and TPyP are shown in a smaller energy range around the Fermi level. Here, an additional V-shaped feature can be observed on Fe-TPyP between −200 mV and +200 mV, with two steps at approx. ±8 mV around E_F (see fig. 3.5d). These steps indicate inelastic tunneling processes that occur at the energy of the step. The asymmetric lineshape and high broadening of the steps beyond thermal resolution and modulation effects resembles the spectra found on Fe-OEP on Au(111) [91]. They assigned the steps to inelastic spin excitations corresponding to an intermediate spin state of $S = 1$. An intermediate spin state is typical for Fe^{2+} in square-planar ligand fields and has been oberved on other Fe-porphyrins [71, 92–95]. Due to the agreement in line shape and the similar coordination geometry of the Fe atom inside the molecular complex, the assumption of a spin of $S = 1$

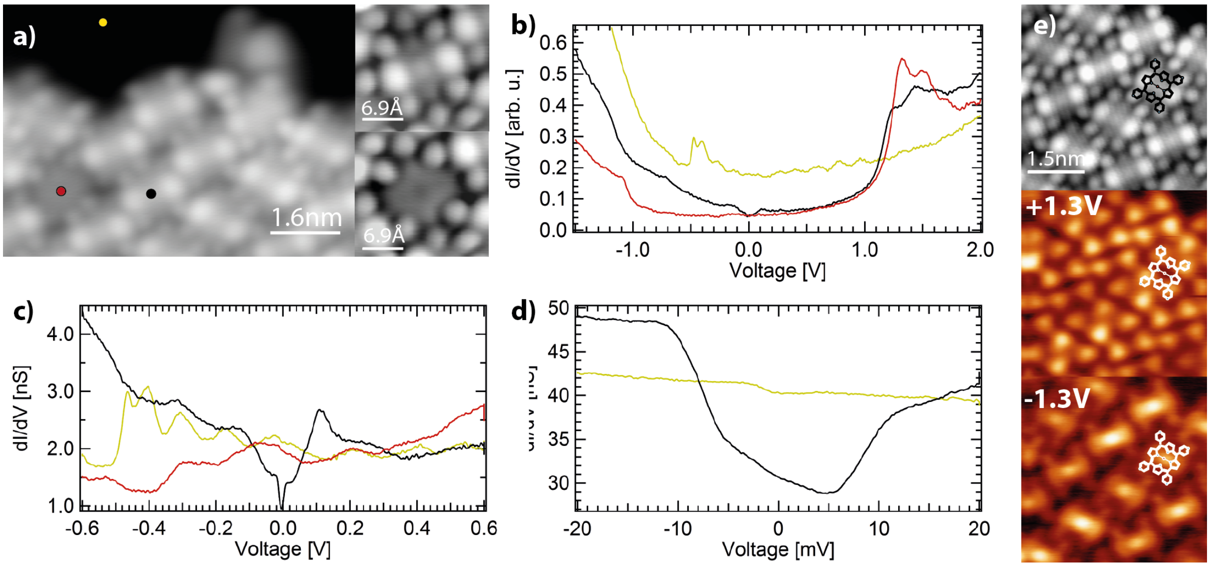

Figure 3.5. Tunneling spectroscopy recorded on different molecules. **a)** Topography, showing the edge of a molecular island. The metallated Fe-TPyP molecules can be seen, as well as a darker molecule, corresponding to an unmetallated TPyP molecule. Right: Close-up images showing the metallated Fe-TPyP and the unmetallated TPyP molecules, respectively. **b)** dI/dV spectra recorded on Fe-TPyP (black) and TPyP (red) as well as a reference spectrum recorded on Au(111). Feedback opened at 2 V, 1 nA at $V_{\mathrm{mod}} = 10$ mV. **c)** Spectroscopy showing a step-like feature for Fe-TPyP around E_{F}. Feedback opened at 500 mV, 1 nA at $V_{\mathrm{mod}} = 4$ mV. **d)** Close-up view of the steps around the Fermi level, recorded in the center of an Fe-TPyP molecule. Feedback opened at 50 mV, 2 nA with $V_{\mathrm{mod}} = 0.5$ mV. **e)** Topography (top) and constant-height dI/dV maps recorded at the LUMO and HOMO energies of the Fe-TPyP molecules, respectively. Topography recorded at 500 pA, 200 mV. For the dI/dV maps, the tip was retracted by 2 Å with respect to this setpoint ($V_{\mathrm{mod}} = 10$ mV).

also for FeTPyP on Au(111) seems reasonable.

The origin of these spin excitations lies in the molecular ligand field. Its fourfold symmetry acts on the d levels of the central Fe^{2+} atom and shifts those levels up in energy that point towards the N sites. For FeTPP and Fe-TPyP molecules, multiple possibilities for the d-level fillings with almost the same energy and resulting total spin have been reported [71, 96, 97]. Two possibilities of the resulting d-level occupation of Fe^{+2} with its electron configuration of [Ar]3d^{6}4s^0 are depicted in fig. 3.6b, both for an intermediate spin state. The $^3A_{2g}$ configuration on the left was reported for FeTPP in bulk [98]. Here, the $d_{x^2\text{-}y^2}$ orbital remains unoccupied, as it lies highest in energy due to the direct overlap with the neighbouring N atoms. The d_{xz} and d_{yz} states are both singly occupied and the orbitals that are least affected by the ligand field, the d_{z^2} and d_{xy} states, are both doubly occupied. Another possible configuration was reported for FeTPP on Au(111) [71] and is shown on the right. In the ^3E_g configuration, the d_{z^2} orbital shifts above the d_{xz} and d_{yz} states. Therefore, the latter share three electrons, whereas the d_{z^2} orbital is the second highest in energy and only singly occupied. Due to the multiconfigurational character of Fe^{2+}, the different d-level occupations are very close in energy. Therefore, depending on the exact adsorption geometry of the molecule and the length of the Fe-N bonds, the level occupation could be any of the possibilities or even a mixture of these.

To determine the step position, the spectrum in fig. 3.6a was fitted[2] under the assumption of a spin state of $S = 1$. In a first approximation, the step energy only depends on the axial anisotropy

---

[2] The program used to fit this spectrum was the software by Markus Ternes [99], which is based on a scattering model that takes into account higher-order scattering terms.

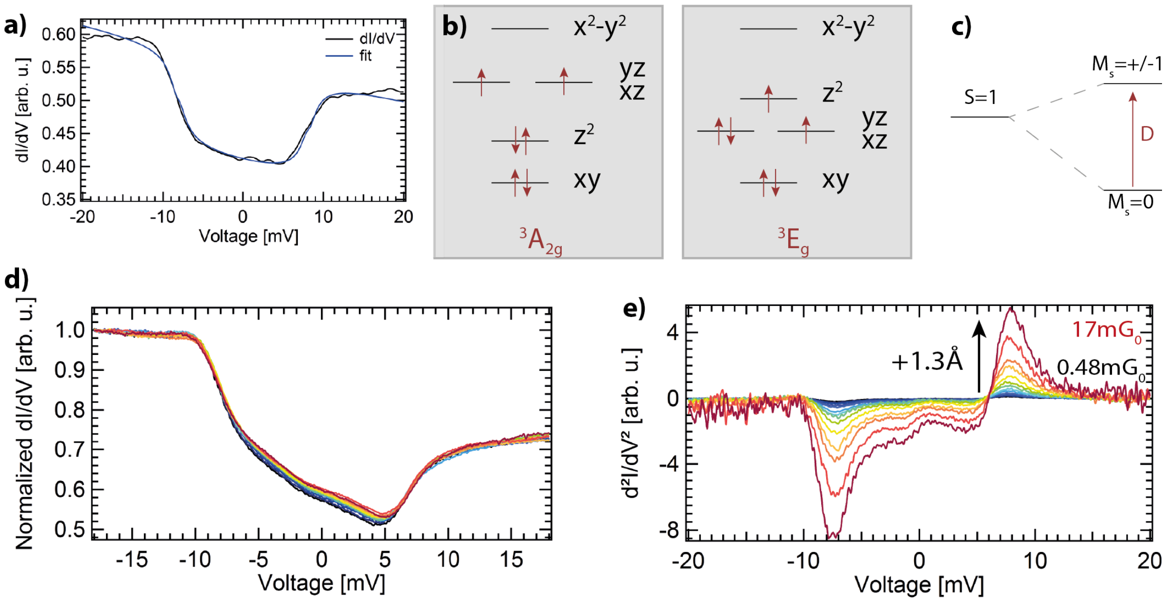

Figure 3.6. Distance-dependent spectra recorded in the center of an Fe-TPyP molecule. **a)** $\mathrm{d}I/\mathrm{d}V$ spectrum (black) and corresponding fit curve (blue) under the assumption of a $S = 1$ system with axial anisotropy $D > 0$. Feedback opened at 50 mV, 2 nA with $V_{\mathrm{mod}} = 0.5$ mV. **b)** Two possible occupation schemes of the d levels of the cental Fe atom, resulting in a spin-state of $S = 1$. **c)** Schematic level splitting of the $M_{\mathrm{S}} = \pm 1$ and $M_{\mathrm{S}} = 0$ levels with a non-negligibe axial anisotropy D. The transition from the ground state to the first excited state can be seen as steps in the $\mathrm{d}I/\mathrm{d}V$ signal at ≈ 8.2 mV. **d,e)** Distance dependence of the normalized $\mathrm{d}I/\mathrm{d}V$ and $\mathrm{d}^2I/\mathrm{d}V^2$ signal, respectively. In total 14 spectra are shown, each approached by additional 0.1 Å.

constant D and the transverse anisotropy constant E, which is described by the spin Hamiltonian:

$$\mathscr{H}_{\mathrm{S}} = D\hat{S}_{\mathrm{z}}^2 + E(\hat{S}_{\mathrm{x}}^2 - \hat{S}_{\mathrm{y}}^2). \tag{3.2}$$

The best fit result was obtained with an axial anisotropy $D = 8.2\,\mathrm{meV}$ and no transverse anisotropy $E = 0$. The corresponding fit curve is shown in blue. For a non-vanishing axial anisotropy, the $S = 1$ triplett is split into two subsets $M_{\mathrm{S}} = \pm 1$ and $M_{\mathrm{S}} = 0$ due to spin-orbit coupling. Hence, the steps in the differential conductance indicate spin excitations between these different spin projections. The corresponding transition is shown in fig. 3.6c, exemplarily for the case of a positive D anisotropy. In case of D> 0, the $M_{\mathrm{S}} = 0$ state is the ground state and transitions occur to the higher-lying $M_{\mathrm{S}} = \pm 1$ doublett. The step energy of ≈ ± 8.2 mV around E_{F} is then a direct measure of the axial anisotropy constant D. The reverse level arrangement occurs for a negative D value. The experimental values for D determined for different molecules are spread by approx. 0.4 meV around the average value of 8.2 meV, which indicates a similar distortion of all molecules. This value is in agreement with other axial anisotropy constants of $D = 7.4\,\mathrm{meV}$ reported for FeTPP [71] and $D = 6\,\mathrm{meV}$ for FeOEP on Au(111) [91].

Figure 3.6d shows the dependence of the spectral shape of the $\mathrm{d}I/\mathrm{d}V$ signal on the tip height. For a better comparison, the $\mathrm{d}^2I/\mathrm{d}V^2$ signal is shown as well in fig. 3.6c, where the steps of the $\mathrm{d}I/\mathrm{d}V$ signal appear as peaks and dips at the corresponding energies (see sec. 4 in chapt. II), respectively. The black curve was recorded at a setpoint of 2 nA at 50 mV. Towards the red spectrum, the tip is approached successively by 1.3 Å in steps of 0.1 Å, leading to an increase in signal intensity. Even with this high increase in conductance from 0.48 mG_0 to 17 mG_0 during the approach, neither the step position, nor its broadening and shape are influenced.

Delocalization of the Spin Excitations

Figure 3.7 shows the variation of the spectral shape across an Fe-TPyP molecule. The spectral evolution along the up-tilted pyrroles in an energy window of ±200 meV is shown in fig. 3.7a. The black spectrum corresponds to the Fe site, showing the most symmetric spectrum with peaks at −125 mV and 125 mV. When moving the tip towards the upper pyrrole rings, the intensity of the resonance at negative energies decreases, whereas the peak at positive energies is enhanced. This goes along with a slight down-shifting of the peak to 115 mV, while a shoulder at 70 mV appears. At the position of the upper pyrrole, the resonance at −125 mV has completely vanished. Along the direction of the lower pyrroles, in contrast, the signal intensity of all features decreases towards the edge of the molecule (see fig. 3.7b). This localization of the resonances at −125 mV and 125 mV can also be seen in the dI/dV maps in fig. 3.7e. The top image shows the topography of a molecular island. The central and bottom images show maps of the differential conductance at −125 mV and 125 mV, respectively. The localization of the resonance at negative bias voltages in the centre of the molecule agrees well with the line spectra, as does the predominant localization of the positive bias resonance on the upper pyrrole groups. As the unmetallated TPyP molecules do not exhibit any features in their dI/dV spectrum around E_F (red curve in fig. 3.5d), it seem reasonable that the d levels of the Fe center are responsible for the resonances in the spectra.

Similar spectral shapes and the localizations of resonances have also been observed for FeTPP on Au(111) [71]. With the help of DFT calculations of an adsorbed FeTPP molecule (see fig. 3.8b,c), C. Rubio Verdú, et al. identify the tunneling path at the Fe site to take place predominantly via the d$_{z^2}$ orbital, which has its main component below the Fermi level and might account for the resonance at −125 mV. At the pyrrole sites, on the contrary, the dominating transport channel is a hybridized state

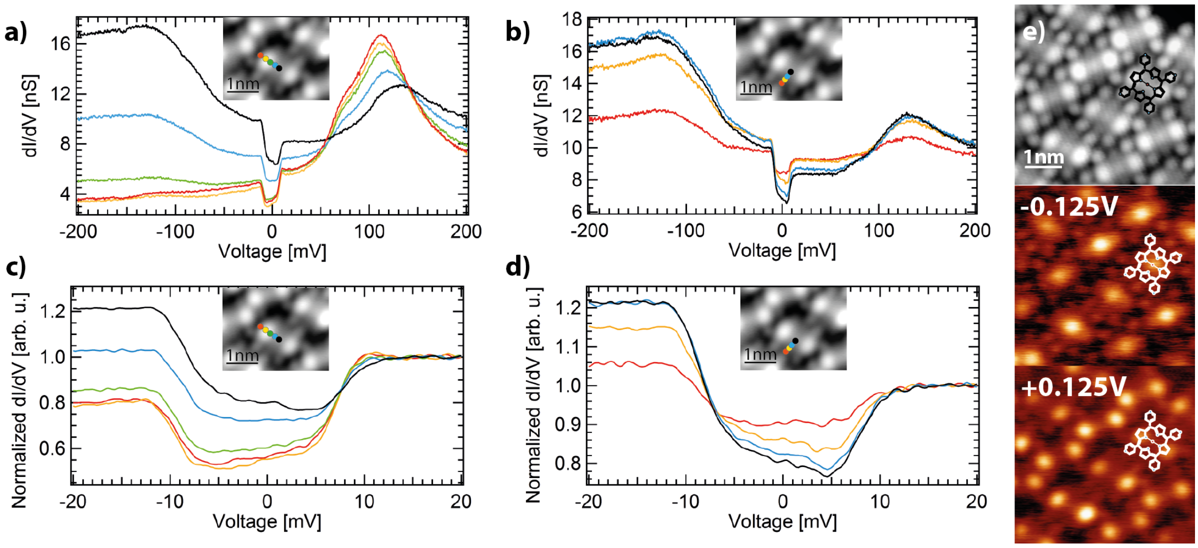

Figure 3.7. Spectra around E_F, showing the localization of the spin excitations on the molecule. **a,b)** Spectra along the upper/lower pyrrole rings, respectively. The resonance at −125 mV has a decreasing intensity towards the edge of the molecule, whereas the peak at 125 mV is more pronounced on the upper pyrroles. **c,d)** Localization of the spin excitations on the molecule. Normalized intensities are shown, to allow for a better comparison of the signals. Feedback for all spectra opened at 200 mV, 2 nA with $V_{mod} = 1$ mV. **e)** Topography and constant-height dI/dV maps at characteristic energies for the Fe-TPyP molecules. Topography recorded at 500 pA, 200 mV. For the dI/dV maps, the tip was retracted by 1 Å with respect to this setpoint ($V_{mod} = 10$ mV).

between the d_{yz} Fe orbital and a ligand state, with the main weight of the resulting orbital above the Fermi level. This orbital could be responsible for both, the state at 125 mV and the shoulder at 70 mV, as due to the interaction with the surface, the PDOS corresponding to the d_{yz} is not localized at one specific energy, but might exhibit several distinct maxima (see fig. 3.8b). A sketch of the corresponding orbitals is shown in fig. 3.8a. The upper image shows the hybrid orbital along the upper pyrroles and the lower image corresponds to the d_{z^2} orbital. Although the spin density is mostly located on the Fe center, the mixing of the ligand states with Fe states allows for the spin excitations to be excited not only in the center of the molecule, but also along the upper pyrroles [71, 100].

The evolution of the spin-excitation spectra over the molecule is shown in fig. 3.7c and d. From the center towards the lower pyrroles, the signal intensity gradually decreases. Along the upper pyrroles, on the contrary, the steps in the dI/dV signal show a similar intensity as in the center, but with a reverse asymmetry: while in the center, the step height at negative bias voltages is slightly enhanced, the reverse situation occurs at the upper pyrroles. The step position, however, is the same across the molecule, indicating that it is indeed the same spin excitation that takes place at different parts of the molecules.

This asymmetry in step height can not be described by the simple model we used in equ. 3.2, as it neglects spin-electron interactions. Instead, the tunneling event has to be described as a scattering process, such that two scattering terms have to be added: an exchange scattering term $\mathscr{J}$ that accounts for spin-spin interaction between the tunneling electron and the molecular spin, where angular momentum can be transferred. The second term is a potential scattering term $\mathscr{U}$, which describes charge scattering at the localized states and does not affect the spin state of the system.

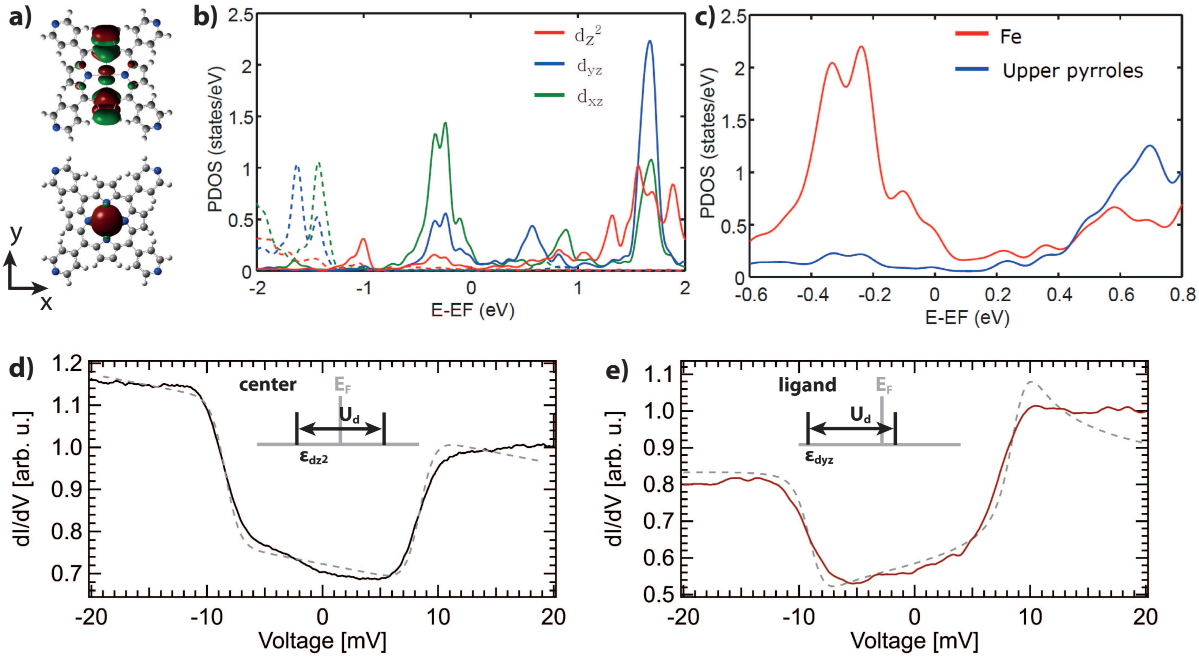

Figure 3.8. **a)** DFT simulations of the hybrid orbitals between the organic ligand and the Fe center. Used parameters in the Gaussian programm [101]: b3pw91-6-31g* for C,N,H, and LanL2dz with ECP for Fe. The dihedral angle was fixed to 25°. **b,c)** Spin-polarized DOS of FeTPP/Au(111) projected on the Fe d orbitals. Graphics taken from [71]. **d,e)** Fits of the dI/dV spectra recorded in the center (left) and on the ligand (right), respectively. Feedback opened at 50 mV, 2 nA with $V_{\mathrm{mod}} = 0.5$ mV. Insets: Sketch of the ratio between the energy of the singly-occupied level ϵ_d and the Coulomb energy U_d for the center and the ligand of the molecule.

This term is responsible for a breaking of the electron-hole symmetry [99]. A physical picture of this parameter $\mathscr{U}$ is given by the Anderson impurity model [102]. By using the Schrieffer-Wolff transformation [103], the higher energy scale of the Anderson impurity model can be related to the scattering parameters $\mathscr{J}$ and $\mathscr{U}$ via the formula:

$$\frac{\mathscr{U}}{\mathscr{J}} = 1 + 2\frac{\epsilon_\mathrm{d}}{U_\mathrm{d}}, \tag{3.3}$$

where ϵ_d denotes the energy of the singly-occupied state and U_d the Coulomb energy. In case of electron-hole symmetry, the potential scattering term $\mathscr{U}$ vanishes and the Coulomb energy U_d is $-2\epsilon_\mathrm{d}$. If there is a finite $\mathscr{U}$, the electron-hole symmetry is broken and either the hole-like or electron-like excitations are favoured.

This scenario is sketched in fig. 3.8d and e for the center and the ligand of the Fe-TPyP molecule. In the center, the step height at negative bias voltages is only slightly enhanced and hence the fit results in a ratio of $\epsilon_{\mathrm{dz}^2}/U_\mathrm{d} \approx -0.5$ for the transport through the dominating $\mathrm{d}_{\mathrm{z}^2}$ orbital. At the upper pyrroles of the ligand, on the other hand, the transport predominantly takes place via a different path, namely the d_yz state. Here, the step height at positive bias voltages is higher, which results in a ratio of $\epsilon_\mathrm{dyz}/U_\mathrm{d} \approx -0.9$. As this ratio deviates from the electron-hole symmetry point of $\epsilon_\mathrm{dyz}/U_\mathrm{d} = -0.5$, the electron-like excitations are favoured. Hence, despite the fact that the spin excitation both at the center and on the ligand of the molecule corresponds to an excitation of the total spin of the system, the different transport paths at both sites and their corresponding potential scattering terms can explain the different spectral shapes, even in the simplified picture of the Anderson impurity model.

C. Distorted Structures of Fe-TPyP on Au(111)

In the last section, we have studied the densely-packed structure of Fe-TPyP molecules on the Au(111) substrate and found delocalized spin excitations along the upper pyrroles of the saddle-shaped molecules. Now, we want to investigate a second arrangement of the very same Fe-TPyP molecules also on the Au(111) substrate. To obtain the second molecular structure, similar preparation conditions were met as for the densely-packed structure. The Fe-5,10,15,20-tetra-pyridyl-porphyrin complex was also evaporated from a commercial Knudsen cell evaporator at 410 °C, with the sample held at room temperature. In contrast to the measurement on the densely-packed structure, some of the measurements in this section were performed at 1.1 K, as will be indicated in the respective figure caption.

1. Adsorption Structure

Figure 3.9 shows the formation of locally-ordered structures that also extend over several tens up to hundreds of nanometers. In fig. 3.9a, some parts of the island consist of the bare Fe-TPyP molecules, whereas brighter protrusions can be seen in between the molecules at other sites. The molecular arrangement inside one area of the molecular island without bright protrusions is shown in fig. 3.9b.

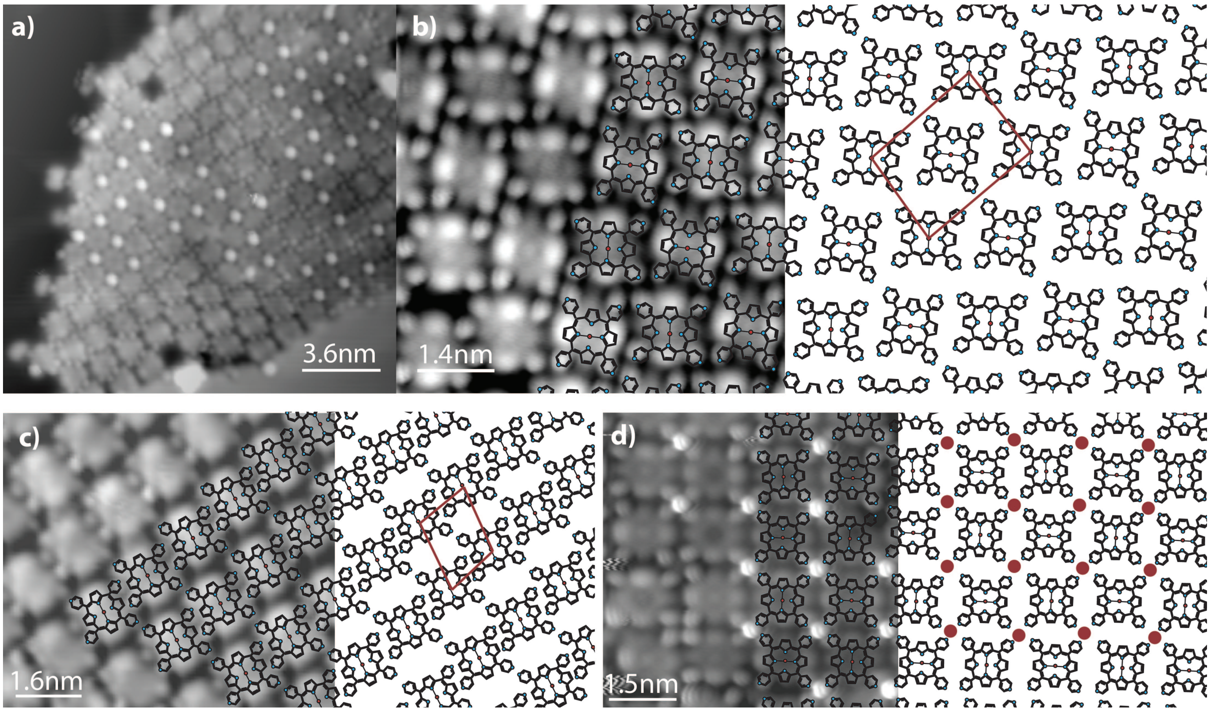

Figure 3.9. STM topography of the surface after deposition of the Fe-TPyP molecules. **a)** Overview of a typical island, showing close-packed molecules and some parts with brighter protrusions in between. **b)** Molecular arrangement in the areas of the Fe-TPyP molecules without bright protrusions. The distorted staggered orientation of the molecules is indicated by the overlaid structure model. An alternating arrangement of the molecules can be observed from the orientation of the upper pyrroles of the molecules, as indicated by the horizontal lines of the structure model. **c)** Alternative molecular arrangement of the Fe-TPyP molecules in lines of parallel molecules. **d)** Square arrangement of Fe-TPyP in the areas with bright protrusions. The red circles in the structure model indicate the positions of possible adatoms.

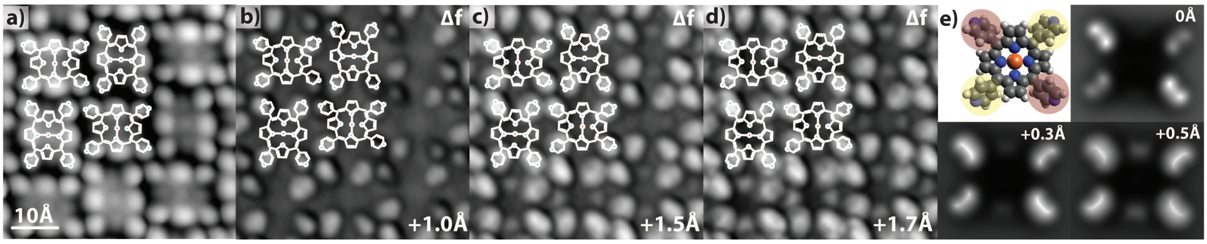

Figure 3.10. AFM images of the distorted staggered structure of Fe-TPyP. **a)** Topography and **b-d)** constant-height Δf maps recorded at different distances with a functionalized Cl tip. The Δf maps indicate an asymmetric distortion of the pyridyl legs, with two diagonal moities protuding more than the other two. **c,d)** Upon closer approach, the saddle deformation of the molecule can be observed, as two opposing pyrrole groups become visible. Topography recorded at 200 pA, 200 mV. For the Δf maps, the tip position with respect to this setpoint is indicated in the respective images. **e)** Simulated Δf maps for three different tip-sample distances. The different colours of the pyridyl groups of the molecular structure model indicate two different rotational angles.

The molecules arrange in an alternating way, such that the upper pyrrole groups of neighbouring molecules are oriented perpendicular to each other, as can be seen in the overlaid structure model. The size of the unit cell containing two molecules (see red rhomboid in fig. 3.9b) is 2.2 nm × 2.0 nm. In fig. 3.9c and d, two alternative arrangements of the molecules can be seen, which coexist in the same preparation. In fig. 3.9c, the structure consists of lines of parallel molecules that are aligned next to each other. A similar packing in lines was observed for FeTPP on Au(111) [71]. The unit cell of this arrangement is 1.4 nm × 1.8 nm and contains only one molecule.

Figure 3.9d shows an area of molecules including the above mentioned protrusions. In this arrangement, the molecules form square-like structures, with the pyridyl legs pointing directly towards the bright protrusions. The origin of these bright protrusions can not be identified so easily. One possible explanation is chlorine that desorbs from the Fe-TPyP molecules upon deposition of the molecules, and which might be coordinating in between the molecules. Another explanation can be found by comparing to experimental findings from V. Iancu, et al. [66]. In their study, they metallate TPyP molecules on a Au(111) substrate with Cr and Co atoms and find similar bright protrusions on many sites. They assign them to different numbers of Cr adatoms at the molecular junction. Since in our study only metallated molecules were evaporated, the existence of such a quantity of single Fe atoms on the substrate seems unlikely. Hence, desorbed chlorine appears to be the most reasonable explanation.

To further ananalyze the adsorption geometries of the molecules in the different arrangements, we investigated all three structures with the AFM. In the following, the corresponding constant-height Δf maps of the structures will be shown.

Distorted staggered Arrangement

Figure 3.10 depicts the topography of the distorted staggered phase of Fe-TPyP, together with the corresponding Δf maps. At higher tip-sample distances (see fig. 3.10 b), the protruding pyridyl groups can be seen. In contrast to the Δf maps of the densely-packed structure, in this arrangement two diagonally opposing pyridyl groups are higher than the other two, such that the molecule does no longer exhibit a symmetry axis along the pyrrole groups. When approaching further (see fig. 3.10c,d), one can see that also in this phase, the Fe-TPyP molecules obtain a saddle shape configuration, with two opposing pyrrole groups bend up while the other two are bend down towards the surface. To conceive an idea of the strength of the asymmetry of the rotational angles of the pyridyl groups, also

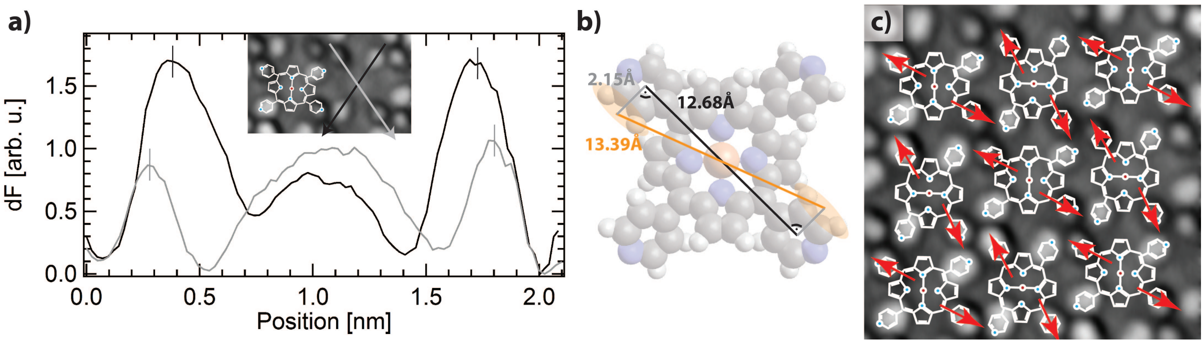

Figure 3.11. **a)** Line profile across the two diagonal axes of an Fe-TPyP molecule. The Δf signal on the pyridyl legs along one diagonal are higher than along the other diagonal. Moreover, the distance between the pyridyl moieties differs. **b)** Sketch of the maximal theoretical apparent length difference for pyridyl groups of different rotational angles. For completely perpendicular pyridyl groups (black line), the distance between the pyridyl groups is minimized. For any flatter arrangement of the pyridyl groups, the rotation of the H atoms of the pyridyl groups away from the diagonal will increase the length (orange line). **c)** Constant-height Δf map, showing the intermolecular arrangement of the FeTPyP molecules. The red arrows indicate the lower pyridyl groups, which coordinate to the pyridyl groups of the neighboring molecule, thus introducing a small diagonal intramolecular distortion.

for this structure, Δf maps were simulated for different manually-distorted DFT minimized molecular structures. The best result are shown in fig. 3.10e for rotational angles of 44° and 49°, respectively.

Figure 3.11a shows a line profile across the four pyridyl legs of an FeTPyP molecule. The grey line corresponds to the lower pyridyl groups and the black line to the upper moieties, respectively. Next to the different intensity of the Δf signal, which arises from the different height of the corresponding groups, a clear difference in the distance between opposing pyridyl legs can be observed along the two diagonals. The lower pyridyl groups are further apart than the upper ones. From basic geometry arguments, a certain length difference is expected due to the different rotational angle, as the most protruding H atoms of the pyridyl groups - which are responsible for the contrast in the Δf maps - are no longer aligned with the center of the pyridyl rings. Figure 3.11b shows a sketch of this apparent length difference. The black line corresponds to the minimal distance of 12.68 Å between opposing pyridyl moieties, which is obtained for the theoretical case of the pyridyl groups being perpendicular to the surface plane. In case of a flattening of the pyridyl groups, the opposing direction of the rotation of the pyridyl legs induces an increase of the measured distance, as indicated by the orange line. For the theoretical case of almost flat pyridyl legs, this would correspond to a distance d of

$$d = \sqrt{(12.68\,\text{Å})^2 + (2.15\,\text{Å})^2} = 13.39\,\text{Å}. \tag{3.4}$$

Hence, the maximal apparent length difference that can arise due to different rotational angles of the pyridyl groups is 0.7 Å. For the nine molecules in fig. 3.10, the average length difference amounts to 2.5 Å, which can not be explained by different rotational angles. Instead, an asymmetric distortion of the molecules might account for the length difference.

From the Δf maps, also the intermolecular arrangement of the molecules can be understood. In the distorted staggered structure, neighboring molecules are rotated by 90° with respect to the direction of their saddle shape. Due to this orientation, the pyridyl legs can interact in an egde-to-face fashion, thereby contributing to a stabilization of the molecular arrangement. The edge-to-face orientation of the pyridyl groups is sketched in fig. 3.11c. The red arrows mark the flatter pair of pyridyl rings, for which an the elongation has been oberved. As observable from the overlaid structure model,

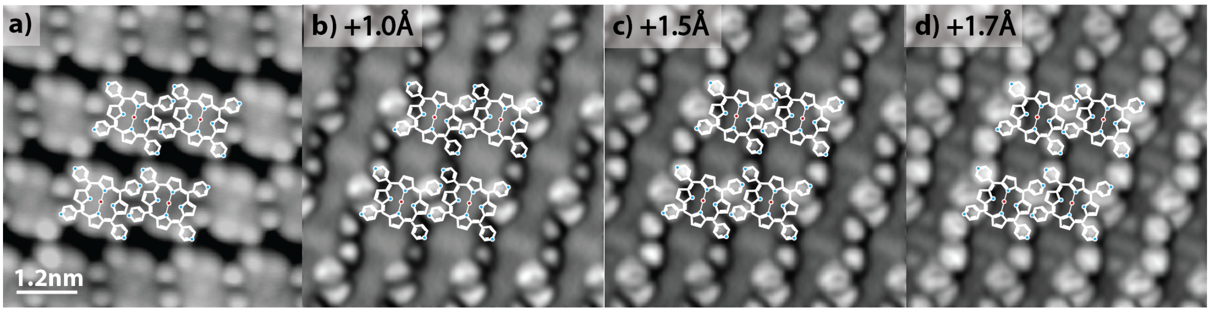

Figure 3.12. AFM images of the line structure of Fe-TPyP. **a)** Topography and **b-d)** constant-height Δf maps recorded at different distances with a functionalized Cl tip. The Δf maps indicate an asymmetric distortion of the pyridyl legs, with two diagonal moities protruding more than the other two. **c,d)** Upon closer approach, the saddle deformation of the molecule can be observed, as two opposing pyrrole groups become visible. Topography recorded at 160 pA, 230 mV. For the Δf maps, the tip position with respect to this setpoint is indicated in the respective images.

the flatter pyridyl groups point towards the upstanding pyridyl group of the neighboring molecule. By introducing a small diagonal distortion within the molecules, the distance between the neighboring pyridyl groups is reduced, such that the intermolecular structure is stabilized.

Line Arrangement

A topography of the Fe-TPyP molecules in the line structure is shown in fig. 3.12. Similarly to the maps on the distorted staggered structure, the Δf maps at larger tip-sample distances (see fig. 3.12b) indicate an asymmetrically distorted structure of the molecules with two pyridyl groups exhibiting a stronger rotation than the other two. Also in this structure, the alternating rotation of the pyridyl legs along the molecular lines is stabilized by the edge-to-face coordination of neighbouring molecules. In between the lines, the larger molecular distance allows for the pyridyl groups of neighbouring molecules to have the same rotational angle. Furthermore, when approaching the tip to smaller tip-sample distances (see fig. 3.12d), the molecular geometry still resembles the one in the distorted staggered structure, as also for this structure the saddle shape becomes visible. Moreover, also the molecules in the line structure exhibit an asymmetric distortion, as the length between opposing pyridyl groups is different along both diagonal axes. For this structure, however, a slightly smaller average length difference of 1.3 Å can be determined for the molecules shown in fig. 3.12.

Hence, considering the geometry of the individual molecules in the distorted staggered and the line structure, similar properties are expected for the molecules in both arrangements, despite the differences in the intermolecular arrangements.

Adatom-Mediated Arrangement

Finally, the last of the three oberved structures, the adatom-mediated structure is analyzed. In fig. 3.13, an area is shown that exhibits bright protrusions on almost all spots between the molecules. However, there are two neighbouring spots, where these protrusions are missing. Due to the large height of the bright protrusions, no Δf maps could be recorded that resolved both the protrusions and the structure of the molecules simultaneously. Instead, Δf maps were recorded at the spot indicated by the white rectangle, where the bright protrusions are missing. The topography of this small area is shown in fig. 3.13b. A small difference in the appearance between the upper and lower molecular junctions, *i.e.*, the spot where the pyridyl legs of the four neighbouring molecules are meeting, is visible. The pyridyl legs in the upper junction appear slightly farther apart than in the lower one.

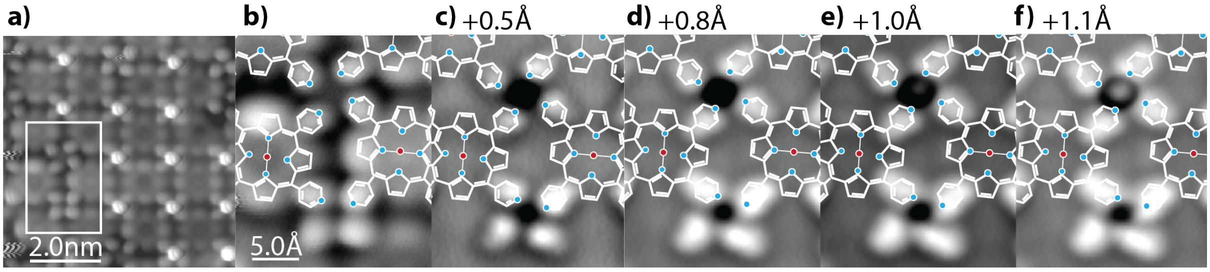

Figure 3.13. AFM images of the adatom-mediated structure of Fe-TPyP. **a)** Topography of an island exhibiting bright protrusions on all but two spots. **b)** Close-up view of the area marked by the white rectangle in a). **c-f)** constant-height Δf maps recorded at different distances with a functionalized Cl tip. The Δf maps indicate the presence of an adatom in the middle of the upper four pyridyl legs. Topographies recorded at 160 pA, 230 mV. For the Δf maps, the tip position with respect to this setpoint is indicated above the respective images.

Moreover, in the upper junction, the pyridyl legs are pointing directly towards each other, whereas in the lower junction they are more staggered.

To further analyze the difference between both spots, constant-height Δf maps were recorded, as shown in fig. 3.13c-f for various tip-sample distances. Upon tip approach (see fig. 3.13f), a bright spot appears in the center of the pyridyl legs in the upper junction, which indicates the presence of an adatom, probably originating from the Au surface. Moreover, in the upper junction, the adatom seems to influence the molecular arrangement such that the pyridyl legs point directly towards each other. In contrast, in the lower junction, the pyridyl groups are coordinating in an edge-to-face fashion as has been observed also in the distorted staggered structure, and no adatom can be oberved in the Δf maps in between the molecules.

Due to the large height of the bright protrusions, it is not possible to analyze the Δf maps of the molecules in this structure in terms of their intermolecular arrangement or intramolecular distortions. The distance between the bright protrusions is equal along the different directions, however, the pyridyl groups might still exhibit a slight length difference. Therefore, a comparison of the intramolecular geometry with the molecules in the distorted staggered arrangement and line structure is not possible.

2. Adatom-Mediated Molecular Structure

As seen in fig. 3.9a, the self-formed islands can either consist of the Fe-TPyP molecules only, or they might be coordiated by bright protrusions in between the molecules. In the following, both of these structures will be investigated individually. At first, the electronic and magnetic properties of the adatom-mediated molecules next to those bright protrusions will be studied. In the second part, in sec. 3, the properties will be compared with those of the molecules in the distorted staggered arrangement without neighbouring protrusions.

Electronic Properties of FeTPyP

Figure 3.14 shows $\mathrm{d}I/\mathrm{d}V$ spectra recorded on Fe-TPyP molecules inside one part of a molecular island. For comparison, spectra on an Fe-TPyP molecule (black) and on non-metallated TPyP (red) as well as the reference spectrum on the bare Au(111) surface are depicted in fig. 3.14a. As observed for the densely-packed structure, also the Fe-TPyP molecules in this packing exhibit the characteristic double resonances at 1.05 V and 1.24 V, corresponding to the LUMO and LUMO+1 orbitals. For this structure, the LUMO and LUMO+1 of the metallated molecules are shifted towards the Fermi level by

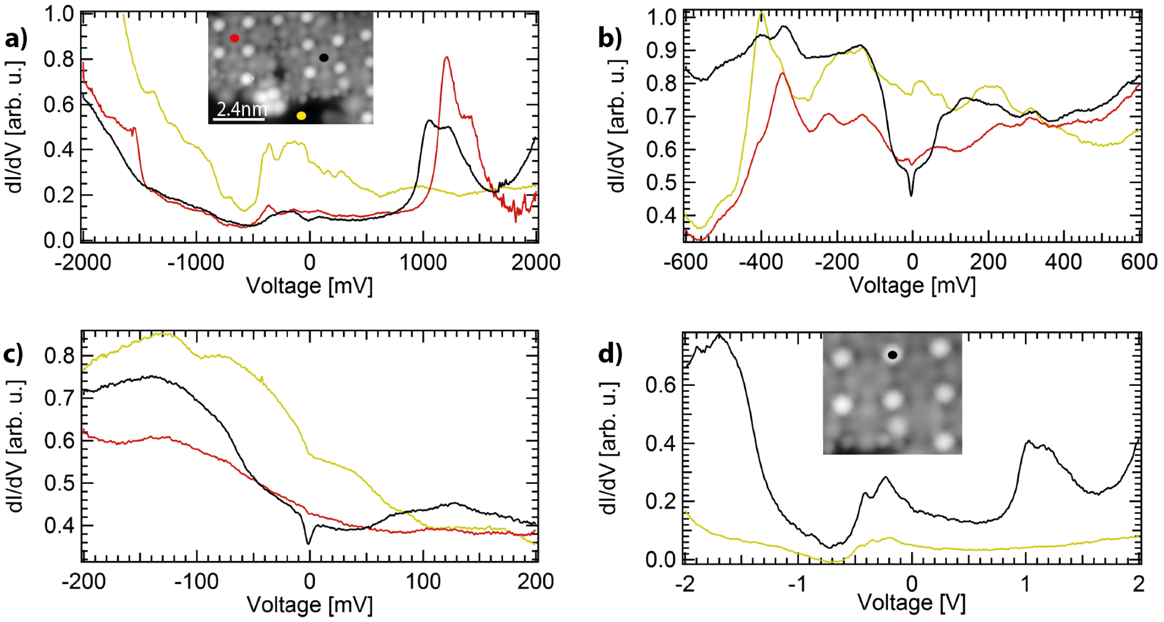

Figure 3.14. Spectra recorded on different sites within an island of the adatom-mediated structure of Fe-TPyP with bright protrusions. **a)** dI/dV spectra recorded on Fe-TPyP (black), unmetallated TPyP (red) and on Au(111) (yellow). Feedback opened at 2 V, 1 nA with V_{mod} = 10 mV. **b,c)** Spectra recorded between ±600 mV and ±200 mV, respectively. Feedback opened at 0.5 V, 2 nA with V_{mod} = 4 mV and 200 mV, 2 nA with V_{mod} = 1 mV. **d)** Spectrum taken on the protrusions, showing the Au(111) surface state at −490 mV and porphyrin states at 1 V. Feedback opened at 0.5 V, 2 nA with V_{mod} = 4 mV.

approx. 200 mV, with respect to the non-metallated TPyP and the molecules in the densely-packed structure. This shift of both the LUMO and LUMO+1 states to the Fermi level indicates a stronger hybridization of the molecular orbitals with the underlying substrate [82].

In fig. 3.14b and c, the dI/dV spectra at a smaller energy range of ±600 mV and ±200 mV are shown, respectively. In this energy window, the non-metallated molecule is featureless and only shows the surface state of the underlying Au(111) substrate. The Fe-TPyP molecule on the other hand, shows a V-shaped feature between ±150 mV with a smaller dip close to E_F, resembling the spectra on the densely-packed molecules. The characteristics of this dip, and whether it can also be assigned to spin excitations, will be closely examined in the next section. Before looking at the properties of the molecule, however, we want to check for the nature of the brighter protrusions in between. Spectra of the differential conductance recorded on these bright protrusions are shown in fig. 3.14d. The spectra show two main peaks at around −500 mV and 1 V. Comparison to spectra recorded on the underlying Au substrate allows to assign the peak at −500 mV to the Au(111) surface state that can also be probed through the protrusions. The peak at 1 V matches with the double peak structure of the LUMO and LUMO+1 of the porphyrins and hence either corresponds to the probing of the molecular orbitals of the underlying porphyrin groups through the bright protrusions or indicates the formation of a hybrid state. As a conclusion, there are no electronic states detectable that originate from the bright protrusions themselves and that differ from the pure molecular properties.

Magnetic Properties: Spin-Crossover Between Type II and Type I Molecules

Upon taking dI/dV spectra between ±200 mV around the Fermi level on several molecules within one island, two types of molecules can be spectroscopically identified. The first type - *type II* - ex-

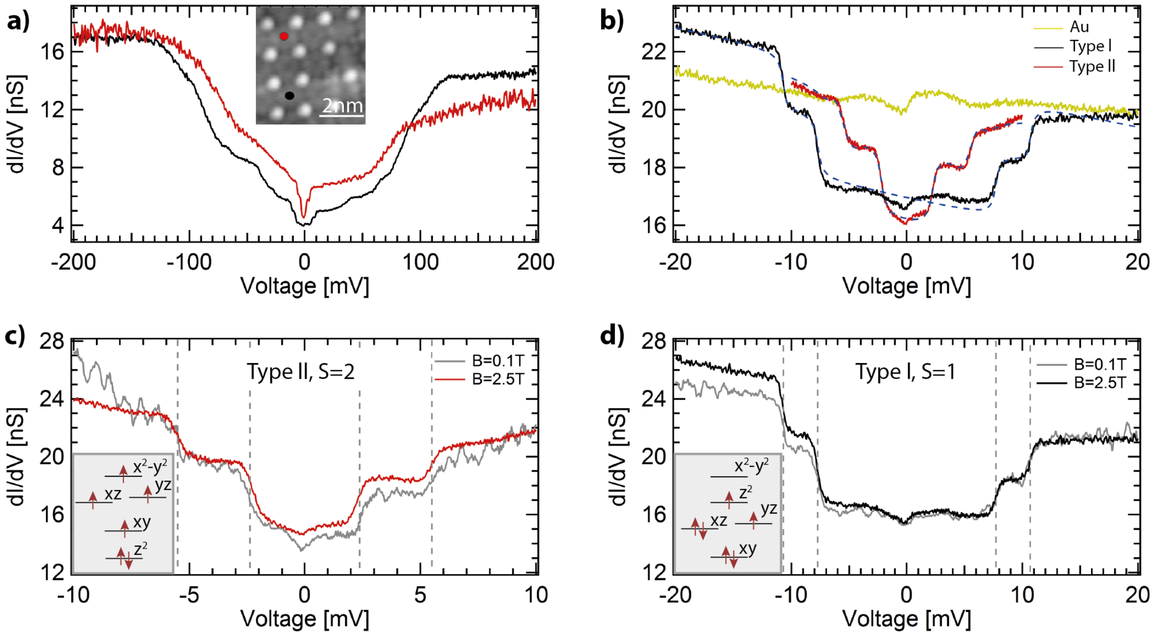

Figure 3.15. Spectra recorded on two metallated Fe-TPyP molecules within an island of the adatom-mediated structure. **a)** Two different spectral shapes can be observed around the Fermi level. Feedback opened at 200 mV, 2 nA with $V_{\text{mod}} = 0.25$ mV, $B = 0.5T$. All spectra were recorded at 1.1 K. **b)** Close-up view of the inelastic steps around E_{F}, with a type II molecule in red, and a type I molecule in black. Feedback opened at 1 nA, 50 mV with $V_{\text{mod}} = 0.25$ mV, $B = 2.5T$. **c,d)** Comparison of the step positions of the type I/type II molecule, respecively, at $B = 0.1T$ and $B = 2.5T$. No shift of the steps can be seen for either of the two molecules.

hibits one narrower dip at E_{F} and no further steps (see fig. 3.15a, red). The other type - *type I* - has a wider dip at E_{F} and some more steps at higher energies (black). From the topographic images and energetic positions of the LUMO and LUMO+1 resonances, no difference between these two types of molecules could be observed. Moreover, there was no regular pattern of the two types, in contrast to findings of Mn-TPyP on Cu(111) [73], where two distinct saddle geometries were identified due to steric repulsion between neighbouring molecules. Moreover, symmetry considerations with respect to the underlying substrate did not allow to assign different adsorption sites to the two molecular species. Furthermore, the high extend of the neighbouring protrusions between the molecules did also not allow to investigate a possible difference between the two types by means of Δf maps.

Figure 3.15b shows $\mathrm{d}I/\mathrm{d}V$ spectra on both types of molecules at ±20 mV around E_{F}. With this higher resolution, both types of molecules exhibit two steps in the differential conductance each, which can be identified as inelastic excitations. The tiny dip right at the Fermi level in both spectra, however, seems to be an artefact from the tip, as it is also observable on the Au reference spectrum (yellow). The energies of the step positions varies for the two types of molecules. Whereas the steps on the type II molecule are at ±2.2 mV and ±5.4 mV, the steps on the type I molecule are higher in energy at ±7.4 mV and ±10.6 mV.

Also for this structure, the steps in the differential conductance are assigned to spin excitations. In the densely-packed structure, a spin state of $S = 1$ with only axial anisotropy $D = 8.2$ meV and a vanishing transverse anisotropy $E = 0$ was found to be responsible for the observation of one step in the $\mathrm{d}I/\mathrm{d}V$ spectra. For the present structure, the obervation of two steps in the spectra can only be modelled in a spin 1 system under the assumption of a non-vanishing transverse anisotropy $E \neq 0$. The corresponding fit for the type I molecule is depicted in fig. 3.15b for anisotropy parameters of

$D = 8.0\,\text{meV}$ and $E = 1.6\,\text{meV}$ (grey dashed line) and does nicely reproduce the experimental curve. The presence of a transverse anisotropy can be explained by the intramolecular distortions, which reduce the ligand field symmetry from D_{4h} to D_{2h}. As a consequence, the degeneracy between the d_{xz} and d_{yz} levels is lifted, which induces a transverse anisotropy component $E \neq 0$ to the system. Note that the saddle-shape deformation as observed in all structures already reduces the molecular symmetry as it breaks the fourfold rotational symmetry of the macrocycle. However, the positions of the N atoms with respect to the Fe center remain essentially unchanged, such that the ligand field still exhibits D_{4h} symmetry. The asymmetric distortions of the molecules in the distorted staggered structure occurs in addition to the saddle deformation and leads to a displacement of the N atoms, such that the ligand field is reduced.

Fitting of the spectra of the type II molecule, however, leads to fit results that contradicted the assumption of a spin 1 system. As mentioned in sec. A, the D and E anisotropy constants are usually expressed in such a way that $|D|$ is maximized and E positive. This can usually be achieved by a suitable choice of the coordinate system. For this specra, however, all expressions of D and E contained combination of D and E, where $E < 1/3|D|$ cannot be fulfilled. Therefore, the assumption of a spin state of $S = 1$ for the type II molecules in this structure seems unlikely.

Instead, a second option to explain the two steps on the type II molecule is to describe the system with a high-spin state of $S = 2$. The corresponding fit of the spectrum of the type II molecule (red) with a spin $S = 2$ model is shown in fig. 3.15b by the grey dashed line. Within the $S = 2$ description, a good fit result can be obtained. Moreover, the values of the anisotropy constants of $D = 3.5\,\text{meV}$ and $E = 0.5\,\text{meV}$ for the type II molecule agree with the above mentioned criteria. Additonally, the interpretation of a high-spin state for Fe-TPyP matches with the findings of B. Liu, et al. who investigated Fe-TPyP molecules also on Au(111), but in a chain-like arrangement [67]. They performed on-surface metallation, with their final metallation product showing a similar spectral shape as the spectra presented in this chapter. Their proposed d-level occupation, resulting in the high-spin state is $(d_{z^2})^2$, $(d_{xy})^1$, $(d_{xz})^1$, $(d_{yz})^1$, $(d_{x^2\text{-}y^2})^1$. A higher spin state is usually favoured for elongated Fe-N bonds, as the influence of the ligand field is weakened and the system approaches the free-spin regime, where Hund's first rule of a maximized spin dominates in the determination of the spin state. Hence, a stronger distortion of the type II molecules might be responsible for the spin crossover.

To confirm the magnetic origin of the steps in the differential conductance, dI/dV spectra were recorded at different magnetic fields perpendicular to the surface. In fig. 3.15c and d, dI/dV spectra recorded at 0.1 T and 2.5 T are depicted for the type I and type II molecules, respectively. For neither of the two structures, a shift of the step position with increasing B field is visible up to fields of 3.0 T (not shown here). On the first glance, the absence of a shift of the step position with higher B fields seems to contradict the interpretation of a magnetic origin of the steps. To estimate the expected shift of the steps, we make use of the relation

$$\Delta E = g\mu_B B M_S, \tag{3.5}$$

with μ_B denoting the Bohr magneton and g the gyromagnetic ratio, which is g=2 in case of a free spin. The shift should therefore be in the order of 350 µV at 3.0 T, which is in the order of the thermal broadening at the measurement temperature of 1.1 K. Moreover, in case of a non-negligible transverse anisotropy in the system, the resulting intermixing of the states of opposite spin projection would counteract the splitting of the levels with increasing B-field and the corresponding Zeeman shift would be smaller. Hence, the absence of a shift does not allow to interpret the origin of the steps as non-magnetic. Since the quality of the spectra is better at higher B-fields and no effect of a B-field on the molecular properties could be observed, in the rest of the chapter, spectra recorded at $B = 0.5\,\text{T}$ will be shown, if not stated otherwise.

3. Distorted Staggered Structure of FeTPyP Molecules

In the last section, the electronic and magnetic properties of the adatom-mediated molecules next to the bright protrusions have been studied. Two types of molecules were observed inside the islands that exhibited a spin state of $S = 1$ for the type I molecules and $S = 2$ for the type II molecules. However, no clear difference between these two types of molecules could be found with respect to their geometry, their adsorption site on the underlying Au(111) substrate, their higher lying electronic resonances or their proximity to the brighter protrusions. Although there were no electronic states detectable on the bright protrusions themselves, it is still interesting to see, if and to what extend they might have influenced the properties of the neighbouring molecules. Therefore, in this section, the same measurements will be shown on islands of Fe-TPyP molecules in the distorted staggered arrangement.

Comparison Between the Structures

To characterize the electronic and magnetic properties of the distorted staggered Fe-TPyP molecules, spectra were taken on different molecules within the island. Also here, two types of molecules were oberved. In fig. 3.16a, spectra are shown at ±200 mV around the Fermi level. Two different spectral shapes can be identified as shown in red and black: one with a narrow dip around E_F and one with a wider dip and more steps at higher energies. To allow for a direct comparison, the spectra of the structure with protrusions are also shown in faint red and black. The agreement between the lineshapes of the red and faint red and black and grey spectra, respectively, indicates the same spectroscopic fingerprint on both structures. To varify if also the spin properties of the molecules in both structures are the same, fig. 3.16b depicts the same spectra in an energy window of ±20 mV around E_F. Also here, the agreement between the curves for both the type I and the type II molecules can be confirmed. Hence, there is no sign of any influence of the bright protrusions on the molecular properties. Therefore, due to the similarity of the molecular properties, it seems likely that also the molecules in the adatom-mediated structure exhibit an asymmetric intramolecular distortion. Moreover, also the measurements on the line structure showed similar electronic and magnetic fingerprints (not shown here to avoid redundancy), as expected due to the similar molecular geometry as determined from the Δf maps. As the molecules in all three structures show the same electronic and magnetic properties, all measurements from now on will be shown only on the Fe-TPyP molecules in the distorted staggered structure.

Note that for the adatom-mediated structure, no difference in the topography or constant-height Δf maps between the type I and the type II molecules could be observed. Also from the constant-

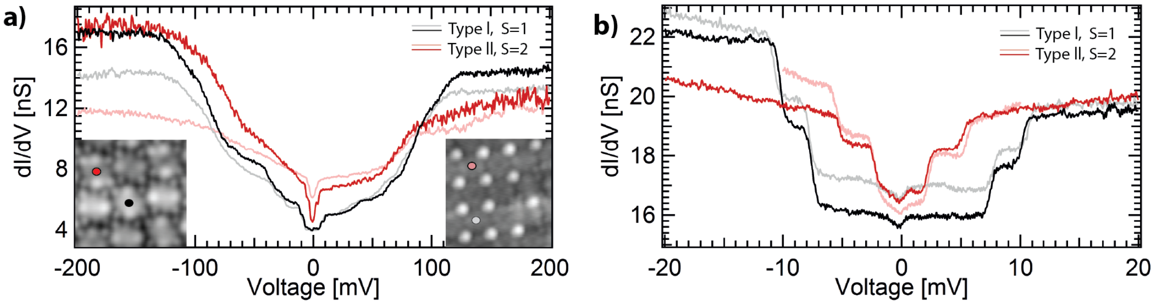

Figure 3.16. a,b) Comparison between the molecules in the distorted staggered and adatom-mediated arrangements. In both structures, two molecular species are present, which show the same spectral fingerprints. Feedback opened at a) 200 mV, 2 nA with $V_\mathrm{mod} = 0.25\,\mathrm{mV}$ to $0.50\,\mathrm{mV}$, $B = 0.5T$ and b) 50 mV, 1 nA with $V_\mathrm{mod} = 0.25\,\mathrm{mV}$, $B = 2.5T$.

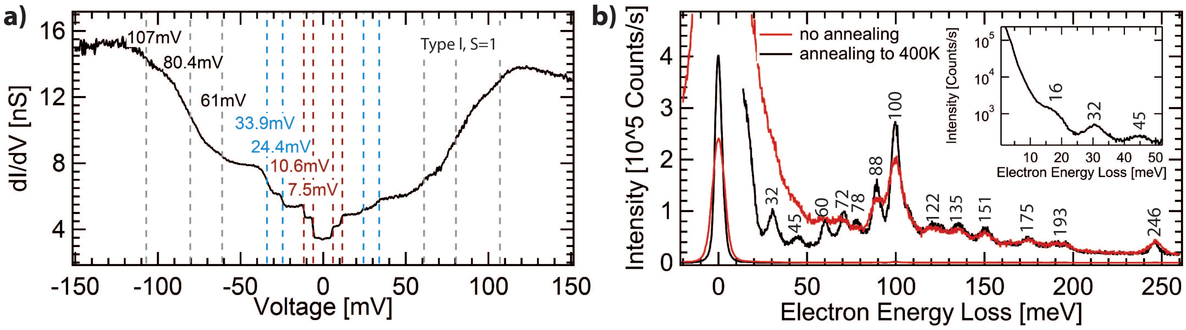

Figure 3.17. Vibrational excitations of Fe-TPyP. **a)** dI/dV spectrum, showing a variety of steps symmetrically around the Fermi level. The step positions are indicated by the dashed lines, with the red lines indicating the spin excitations. Feedback opened at 200 mV, 2 nA with $V_{\text{mod}} = 0.5$ mV, $B = 0.5T$. **b)** HREELS spectrum recorded for the sample before annealing (red) and after annealing to 400 K (black), showing the energy of molecular vibrations. The inset shows the low-energy region of the annealed sample, confirming the absence of vibrational excitations below 16 meV. Spectra recorded at 55° incident angle with respect to the surface normal. The resolution of the spectra amounts to a FWHM of 4.7 meV (black) and 7.9 meV (red).

height Δf maps of the distorted staggered structure shown in sec. 1, no geometric difference between the two types is apparent. On the first glance, this seems to contradict the above made assumptions of elongated Fe-N bonds in the type II molecules, which were assumed to exhibit an $S = 2$ magnetic ground state. However, only very small changes in the Fe-N bond length are required for the Fe to undergo a spin crossover. DFT calculations indicate that changes of the Fe-N bond length in the order of several pm are suffcient to alter the ground state of Fe porphyrins [104–106]. However, changes of such a length scale are beyond the resolution of our measurements. Another possible explanation is the elongation of the Fe-N bonds in the direction towards the surface due to stronger interactions of the Fe atom with the substrate. In the constant-height Δf maps, however, the Fe atom can not be imaged on either of the two types of molecules, as it lies below the molecular plane on both structures. Therefore, the discrepancy between both types of molecules can only be determined from spectroscopy.

Vibrational Excitations of Type I FeTPyP Molecules

As described above, two types of molecules coexist within the molecular islands. Type II molecules with only two steps around E_F and type I molecules with higher lying excitations. In this section, the origin of these higher lying steps of the type I molecules will be examined. Figure 3.17a shows a spectrum of a type I molecule. Several steps are visible in the spectrum: two steps at 7.5 mV and 10.6 mV (see dashed red lines), two sharp steps of similar intensity at 24.4 mV and 33.9 mV (blue lines) and several steps with weaker intensity at 61 mV, 80 mV and 107 mV. The two innermost steps were already identified erlier to result from inelastic spin-flip excitations. For the higher-lying steps, however, a magnetic origin is rather unlikely, as magnetic anisotropy constants in the order of several tenth of meV would be necessary, which is far beyond values typically found for transition-metal complexes with a quenched orbital angular momentum [67, 107, 108]. Instead, the steps in the dI/dV spectrum might result from the excitation of molecular vibrations.

In order to determine the origin of the multitude of steps in the dI/dV spectra, high-resolution electron energy loss spectroscopy (HREELS) measurements were performed in the group of P. Tegeder. By means of inelastic electron scattering, HREELS allows to detect vibrational excitations in molecules. Depending on the incident angle of the electron beam and the corresponding analyzer

Table I. Assignment of the peaks in the HREELS spectra to steps in the dI/dV signal, together with their calculated energy from DFT calculations (b3pw91/genecp) for dihedral angles of 25° and 60°, respectively. All energies are given in meV. The symbols ν, δ, γ and τ denote stretching, in-plane wagging, out-of-plane wagging and torsion modes, respectively.

HREELS [meV]	IETS	DFT (25°/60°)	Mode Description
16	24.4	17 / 18	symmetric buckling / asymmetric buckling
32	33.9	30 / 30	Butterfly mode, Fe-tapping / sym. ν (Pyrrole)
45	-	-	-
60	61.0	59 / 59	N-tapping / τ(Pyrrole)
72	-	-	-
78	80.4	82 / 83	δ(C-C-C) / γ(C-H)
88	-	-	-
100	107	109 / 108	γ(C-H) / δ(C-H)
122	-	-	-
135	-	-	-
151	-	-	-

angle, the signal does either result from dipole or collisional scattering of the electrons. In our setup, an incident angle of 55° with respect to the surface normal and an equal analyzer angle of 55° was chosen, such that the signal of both collisional and dipole scattering is detected. The corresponding HREELS spectra are depicted in fig. 3.17b, with the red curve corresponding to measurements after molecule deposition at room temperature, whereas the black curve was measured after the sample was post-annealed to 400 K for 5 min. Due to the high intensity of the zero loss peak, the magnified spectra (factor of 200) are also depicted in order to resolve the vibrational signals. Both, for the sample preparation without post-annealing and the sample after annealing, several peaks are observable at similar energies. However, the signal-to-noise ratio of the annealed sample (black) is much better than before the annealing, with an energy resolution of around 4.7 meV FWHM for the black and 7.9 meV for the red spectra, respectively. The better signal quality of the annealed sample indicates a more homogeneous surface arrangement. Despite the difference in signal intensity, the peak energies for both preparations coincide and the same vibrational modes are present for the sample before and after annealing. In the STM topographies, we oberved different structures of FeTPyP on the surface, which all emerged under identical preparation conditions.

From the HREELS measurements, one can not know, which of the different structures is probed on the surface. Therefore, HREELS spectra were acquired for multiple sample preparations. However, the spectra and the corresponding peak positions remained unchanged between different preparations.

The inset of fig. 3.17b shows the HREELS spectrum for small excitations energies. The shoulder on the left corresponds to the elastically scattered electrons. Three vibrational modes are detectable at 16 meV, 32 meV and 45 meV. The absence of peaks at energies below 16 meV corroborates the interpretation of the lowest two steps in the dI/dV spectra to result from spin-flip excitations.

In tab. I, the higher lying step energies in the dI/dV spectra are compared to peak energies from the HREELS measurements of the annealed sample. With the help of DFT calculations[3] of an isolated Fe-TPyP molecule, the corresponding vibrational modes can be identified. For the DFT calculations, two dihedral angles of 25° and 60° were compared and the corresponding energies and vibrational modes are given for both angles. Since the calculations were performed neglecting the surface, no

---

[3] DFT calculations were performed with Gaussian[101] using hybrid orbitals between the organic ligand and the Fe center. Used parameters: b3pw91-6-31g* for C,N,H, and LanL2dz with ECP for Fe.

certain assignment of the vibrational modes can be made, however, general trends for the vibrations can be observed. At higher energies, the vibrational modes constitute of in-plane and out-of-plane wagging modes of the C-H and C-C-C bonds, as in the case of the vibrations at 80 meV and 107 meV. Since they are delocalized over the entire molecule, their exact energetic position does not so crucially depend on the conformation of the molecule such that the DFT energies agree very well with the experimental values. The vibrational modes at lower energies, on the other hand, correspond to symmetric and antisymmetric buckling and stretching modes of the pyrrole groups. Since these modes deform the pyrrole groups and hence also the Fe-N distance of the molecule, their energy depends much stronger on the exact conformation of the molecule on the surface.

Multiple molecular vibrations at similar energies were also observed by N. Ohta, et al. [95] on double layer FePc molecules on Ag(111). They observed a variety of vibrational modes and an overall similar lineshape of the $\mathrm{d}I/\mathrm{d}V$ signal in a region of 150 meV around E_F.

Delocalization of the Vibrational- and Spin Excitations

Up to now, the spin- and vibrational excitations were identified in the center of the molecule. For Fe-TPyP in the densely-packed structure, the delocalization of the molecular orbitals allowed to excite spin excitations also on the upper pyrroles of the molecule. Therefore, in the following, we want to investigate if the same occurs also for Fe-TPyP in this structure. Figure 3.18 shows spectra recorded across two Fe-TPyP molecules: the three left images (see fig. 3.18a, c and e) correspond to a type I molecule, the three right images (see fig. 3.18b, d and f) to a type II molecule.

For simplicity, we first want to investigate the local changes of the spectral shape of a type II molecule, which did not exhibit signs of vibrational exitations. In fig. 3.18b, the spectra in the range of ±200 mV are shown along the upper pyrroles of a type II Fe-TPyP molecule. Similar to the case of the densely-packed structure, also on the type II molecules, an asymmetry across the molecule can be seen: the signal intensity at negative bias voltages decreases towards the upper ligand of the molecule (red curve), whereas the signal intensity at positive bias is enhanced. Along the lower pyrrole (see fig. 3.18d), the signal intensity at both bias polarities fades out. As described in more detail in sec. B.3, this can be explained by the localization of the corresponding resonances. Whereas the dominant transport channel in the center of the molecule is the d_{z^2} orbital, having its main weight below the Fermi level, the predominant path at the ligand, the hybridized d_{yz} orbital, lies above E_F. Hence, also the signal intensity at positive bias is enhanced on the upper pyrroles, whereas the highest signal intensity at negative bias is in the central part of the molecule.

Figures 3.18a and c show similar spectra across a type I molecule. Overall, the same localization trend of the resonances over the molecule is observable. However, for this type, also the intensities of the inelastic steps varies across the molecule (see red curve in fig. 3.18a). Along the upper pyrroles, no vibrational modes are obervable at negative bias voltages such that the only two visible steps correspond to spin excitations. At positive bias voltages, on the contrary, the situation is more complicated as the intensity of certain vibrational modes is strongly enhanced, whereas other modes are not visible.

In sec. B, we explained how the delocalization of spin excitations could be explained by the extended hybrid d_{yz} orbitals on the ligand. Since the obervation of vibrational modes follows a similar localization as the above described d_{yz} and d_{z^2} orbitals, it is reasonable that also the vibrational excitations are mediated over these states. At negative bias voltages, the d_{z^2} orbital in the center is the dominant path for the virtual excitations whereas at positive bias, the hybrid d_{yz} orbital on the ligand mediates the excitation. As the vibrational excitations and spin excitations take place via the same states, the very same localization on the molecule is expected. Therefore, the obervation of spin excitations at negative bias voltages on the ligand of the molecule with a simultaneous non-existence

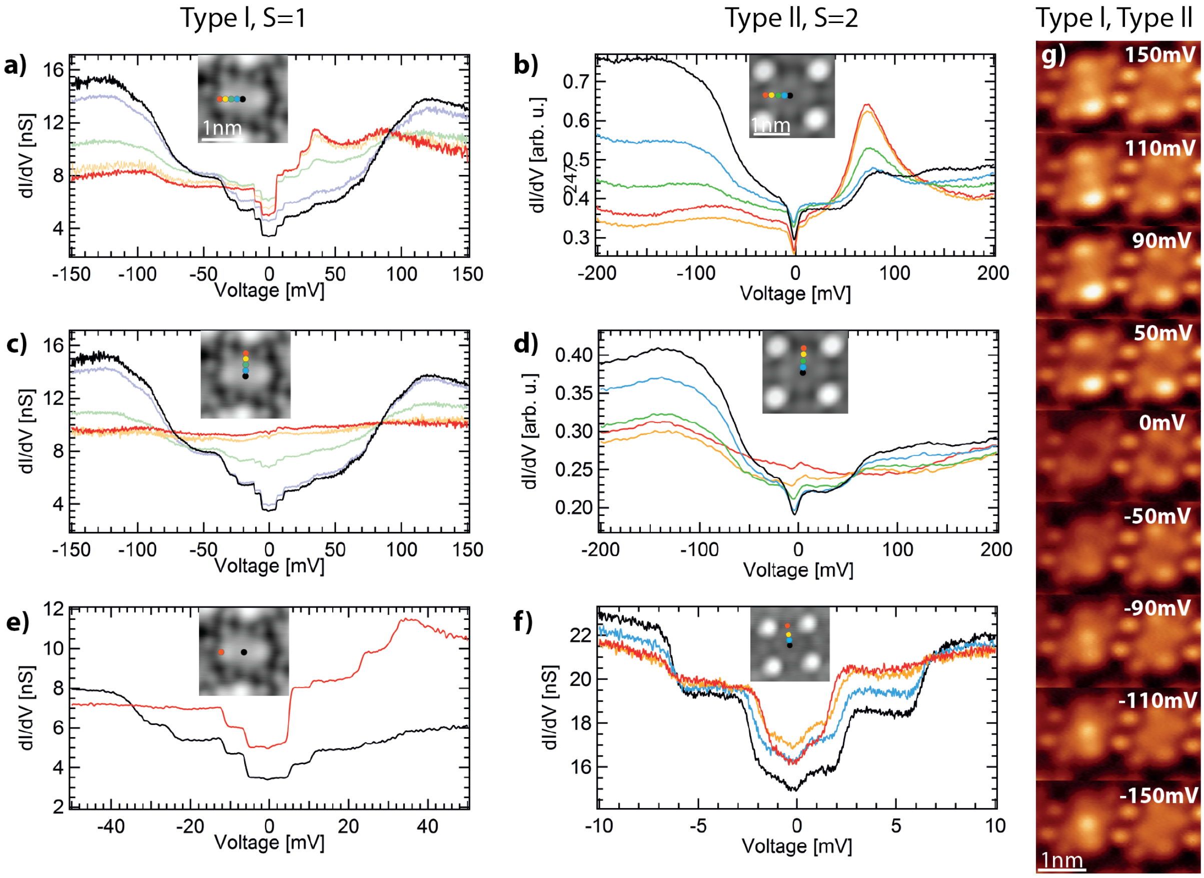

Figure 3.18. Spectra on different parts of the molecule. **a,c)** Spectra recorded along the upper/lower pyrroles of a type I Fe-TPyP molecule. The spectra exhibit an asymmetric lineshape at the upper pyrroles, whereas the signal intensity decreases towards the lower pyrroles. Feedback opened at 200 mV, 2 nA with $V_{\mathrm{mod}} = 0.5\,\mathrm{mV}$, $B = 0.5T$. **b,d)** Spectra recorded along the upper/lower pyrroles of a type II Fe-TPyP molecule, exhibiting the same signal localization as for the type I molecule. Feedback opened at 200 mV, 2 nA with $V_{\mathrm{mod}} = 1\,\mathrm{mV}$, $B = 0T$ at 4.8 K. **e,f)** Spectra around E_F recorded along the upper pyrroles of a type I/type II molecule. **g)** Constant-height dI/dV maps recorded on a type I (left) and type II (right) Fe-TPyP molecule at characteristic energies around E_F with a modulation of $V_{\mathrm{mod}} = 5\,\mathrm{mV}$.

of vibrational signatures at negative bias seems to contradict the interpretation of the same state mediating these two excitations in a virtual process. Since there should be a vanishing DoS of the d_{z^2} orbital at the ligand, in a strict picture no excitations at all should be observable at negative bias. At the upper pyrroles, however, the d_{yz} has some weight also at negative bias. Its tail overlapping the Fermi level might allow for the spin transitions to occur, while the overlap with the higher-lying vibrational excitations is too low, especially regarding the much lower excitation cross section of vibrations compared to magnetic transitions [109–111].

The general trend of the localization of the vibrational excitations on the molecules can be seen in the dI/dV maps, as shown in fig. 3.18g for bias voltages between 150 mV to −150 mV. The left molecule corresponds to a type I molecule and the right one to a type II molecule, respectively. Overall, the same features can be seen for both types of molecules. Whereas at positve bias voltages (top), the intensity on the upper pyrroles is predominant, at negative bias voltages (bottom), the center shows the highest intensity. Overall, the dI/dV maps agree very well with the maps recorded on the densely-packed structure (see fig. 3.7).

Note that for all bias voltages, the type II molecule shows less intensity in the center than the type I molecule. This might either result from an electronic effect, *i.e.*, the d_{z^2} orbital, which is responsible for the intensity in the center of the type I molecule might be shifted down in energy away from E_F and might hence not be accessible in the tunneling process. Such a down shifting of the d_{z^2} is in agreement with the level occupation for a $S = 2$ state, as proposed in sec. 2. The other possibly is a geometric effect, with the Fe center being lowered towards the surface. This would also reduce the overall tunneling probability into the Fe-center for all bias voltages. Both these explanations are in agreement with the previous interpretations.

Asymmetry in the Step Height of the Spin Excitations

In the previous paragraph, we explained why the spin- and vibrational excitations are also visible on the ligand of the Fe-TPyP molecule. Certain vibrational modes were even enhanced on the upper pyrroles at positive bias voltages. Upon taking a closer look at the evolution of the spin excitations across the molecule, also here, a change can be observed for both, the type I and type II molecules. This is depicted in a smaller energy window in fig. 3.18e for the type I molecule. From the center (black) towards the ligand (red), no clear change of the step height of the two innermost steps can be seen at negative bias voltages. At positive bias, however, the first step at 7.7 mV is strongly enhanced on the ligand, whereas the second step at 10.7 mV is weakened.

The asymmetry in the step height for positive and negative bias voltages was previously explained for the densely-packed structure (see sec. B.3) in terms of an additional potential scattering term $\mathcal{U}$, which breaks the electron-hole symmetry. However, even under consideration of non-vanishing potential scattering, the asymmetry in the step height for steps at the same bias polarity can not so easily be understood in a simple $S = 1$ picture. In this framework, the steps correspond to excitations from the $|0\rangle$ to the $|+\rangle$ and $|-\rangle$ states, with $|\pm\rangle = 1/\sqrt{2}(|+1\rangle \pm |-1\rangle)$ (see fig. 3.2d). As the states $|+\rangle$ and $|-\rangle$ are superpositions of the same states, also the transition matrix element from $|0\rangle$ to both states should give the same intensity. Hence, for both bias polarities, a similar step height for the first and the second step is expected.

The same holds for the type II molecules. Figure 3.18f shows spectra on the type II molecules in the center (black) and on the ligand (red). On the ligand, the step height of the first step is equal to the step height in the center. The second step, however, almost vanishes. Although for the type II molecule this trend is the same for both bias polarities, the asymmetric changes in signal intensity between the first and second step cannot be captured in a simple spin-excitation framework, either.

Distance-Dependent Shifts of the Spin- and Vibrational Excitations

In the previous parts, we have seen, how small changes in the ligand field of a magnetic atom can influence the anisotropy parameters and even the total spin state. Now, we utilize this observation to try and tune the ligand field in a controlled way. One way to influence the ligand field acting on the central Fe atom is by approaching the central Fe atom with the tip. The tip acts as an additional ligand to the Fe center, which influences the spin state of the system and might even induce an overall deformation of the molecule. A series of dI/dV spectra recorded in the center of a type I Fe-TPyP molecule at different tip heights is shown in fig. 3.19a. From an initial setpoint (red curve) of 250 pA at 50 mV, the tip is consecutively approached by 190 pm (black curve) in steps of 10 pm. Upon approaching, the four innermost steps around E_F, *i.e.*, two steps resulting from spin excitations and the two lowest vibrational excitations, all shift to higher energies.

To understand the influence of the tip on the molecular properties, we first focus on the shift of the two innermost steps. The position of the steps in the dI/dV spectra can be expressed in terms of the axial anisotropy parameter D and the transverse anisotropy E. The changes of both anisotropy

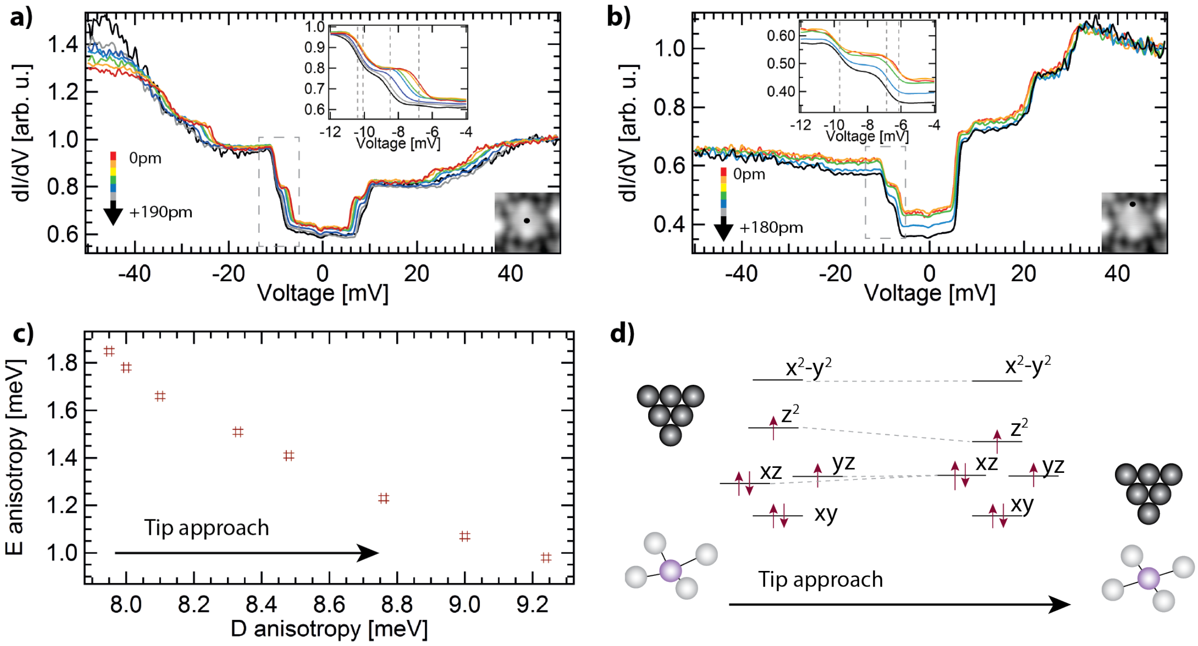

Figure 3.19. Distance-dependent steps recorded **a)** in the center and **b)** on the ligand of the molecule. The spectra are normalized to allow for a direct comparison of the step positions. The tip-sample distance is varied from the feedback position at 50 mV, 250 pA with $V_{\mathrm{mod}} = 0.5$ mV by approaching the tip by up to 190 pm. **c)** Change of the transverse anisotropy E as a function of the axial anisotropy D upon approaching. With decreasing molecule-tip distance, the axials anisotropy D increases whereas E decreases. **d)** Proposed level-shifting due to the molecular deformations. The reduced level splitting between the d_{z^2} and the d_{xz} and d_{yz} orbitals induces an increase of D.

constants are depicted in fig. 3.19c. A tip approach leads to an increase of the axial anisotropy D while the transverse anisotropy E is reduced. This interplay of the anisotropy parameters leads to the case, where the innermost steps shifts to higher energies, whereas the outer steps hardly move at all.

These changes in D and E can be understood when considering the response of the molecule, as a result of the tip approach. Without a surface, the Fe atom is located in the central plane between the four N atoms of the pyrrole groups. Due to the attraction of the underlying Au substrate, however, the Fe atom is expected to be slightly below the porphyrin plane [72, 92].

There are two main options of what may happen when the tip approaches the molecule. When the tip approaches the center of the molecule, the central Fe atom might be pulled up into the central plane. As this would go along with a reduction of the Fe-N bond length, the splitting between all the d levels is expected to increase. Moreover, the increasing Fe-surface distance will lower the energy of the d_{z^2} orbital. Since the magnetic anisotropy results from admixture of the ground state with excited states, a smaller splitting between the d_{z^2} and the d_{xz} and d_{yz} orbitals will lead to a stronger mixing of the levels and hence an increase of D, in agreement with the experimental data. Upon further approach, the Fe atom would start to cross the molecular plane, which should go along with a reduction of D, as the influence of the tip reverses the previous lowering of the energy of the d_{z^2} orbital [92]. This regime, however, was not reached in our experiment, but has been observed in measurements on Fe-TPyP on Pb(111) [112]. The trend of the E anisotropy, however, can not so easily be explained by the lifting of the central Fe atom, as the change of the Fe-N bond length should shift the responsible d_{xz} and d_{yz} orbitals in a uniform way. Therefore, this model does not explain the decreasing E anisotropy that occurs upon tip approach.

Another scenario, which might explain the decreasing E anisotropy, is the overall lifting of the molecule due to the attractive forces of the tip. Also for this scenario, the lifting of the molecule would go along with a smaller splitting between the d_{z^2} and the d_{xz} and d_{yz}, as the weakened Fe-surface bond would relax the Fe atom back into the molecular plane, which would also here account for the decreasing D anisotropy. Moreover, the lifting of the molecule would most likely be accompanied by a relaxation of the molecular macrocycle. As in gas phase, the molecular macrocycle is flat and the pyridyl legs are rotated by 90°, the lifting of the molecule would probably lead to a weakened deformation of the molecular macrocycle, which would account for the decreasing E anisotropy that was observed in experiment. A lifting of the molecule upon tip approach has recently been reported for FeTPP on Au(111) [113], where they observed similar intra-molecular relaxations, which led to the change of the magnetic properties of the molecules.

Following these arguments, the second option of an overall lifting of the molecule seems to be the appropriate model to explain the experimental findings.

The same approach series was also recorded on the upper pyrrole group of the Fe-TPyP molecule. In fig. 3.19b, a similar shifting trend can be observed, as in the center of the molecule: the inner step shifts much faster to higher energies than the outer step, resulting in an increasing D value with a simultaneous reduction of E. Since the approach on the upper pyrrole of the molecule will most likely not act directly on the Fe atom, the change of the anisotropy parameters also on the ligand can be more easily explained by an overall lifting of the molecule from the substrate.

Moreover, this interpretation can be cross-checked with the shift of the vibrational excitations. Upon approaching, also the two lowest vibrational modes at 24 meV and 34 meV shift to higher energies. As mentioned above (see sec. 3), these vibrations can be assigned to buckling and butterfly modes of the macrocycle of the Fe-TPyP molecule. As both of these modes describe motions perpendicular to the surface, the tip is expected to have a rather strong effect on the energy of the vibrational excitations. Thus, also the shift towards higher energies seems reasonable, as the presence of the tip hinders the molecular vibrations.

Charging Effects on Type I Molecules

In the previous sections, we have analyzed the low-energy properties of the Fe-TPyP molecules. Another interesting phenomenon is occuring at higher energy scales and has been neglected so far. In fig. 3.14a in sec. 2, we studied the electronic properties of Fe-TPyP and observed a shift of the LUMO and LUMO+1 resonances towards the Fermi level, as a consequence of hybridization with the surface. However, what is not visible in fig. 3.14a is that all the type I molecules exhibited either oscillations in the dI/dV signal at higher energies between 1 V to 3 V or negative differential resistance (NDR) features, where an increasing voltage causes a decreasing current. An exemplary set of the different features that can arise is presented in fig. 3.20a. The yellow spectrum on the bottom shows the Au reference spectrum, ensuring the quality and stability of the tip. The other spectra were all recorded in the center of different type I molecules. As can be seen from this comparison, the oscillatory behaviour does mostly occur at the onset of the LUMO (black spectrum) or HOMO resonances (red and orange spectra), respectively. Only in some occasions, an NDR dip is visible at smaller absolute energies (blue spectrum). Each of these features is characteristic for the corresponding molecule, *i.e.*, it has never occurred that, *e.g.*, a molecule showing an NDR suddenly exhibited oscillations in the dI/dV spectrum. Apart from these features, the spectra in the rest of the energy window look ordinary, with the characteristic V-shaped dip around E_F. There are numerous mechanisms causing NDR on single molecules [114–121], however, a mechanism is required that can explain the occurance of all the different types of features in the dI/dV spectra.

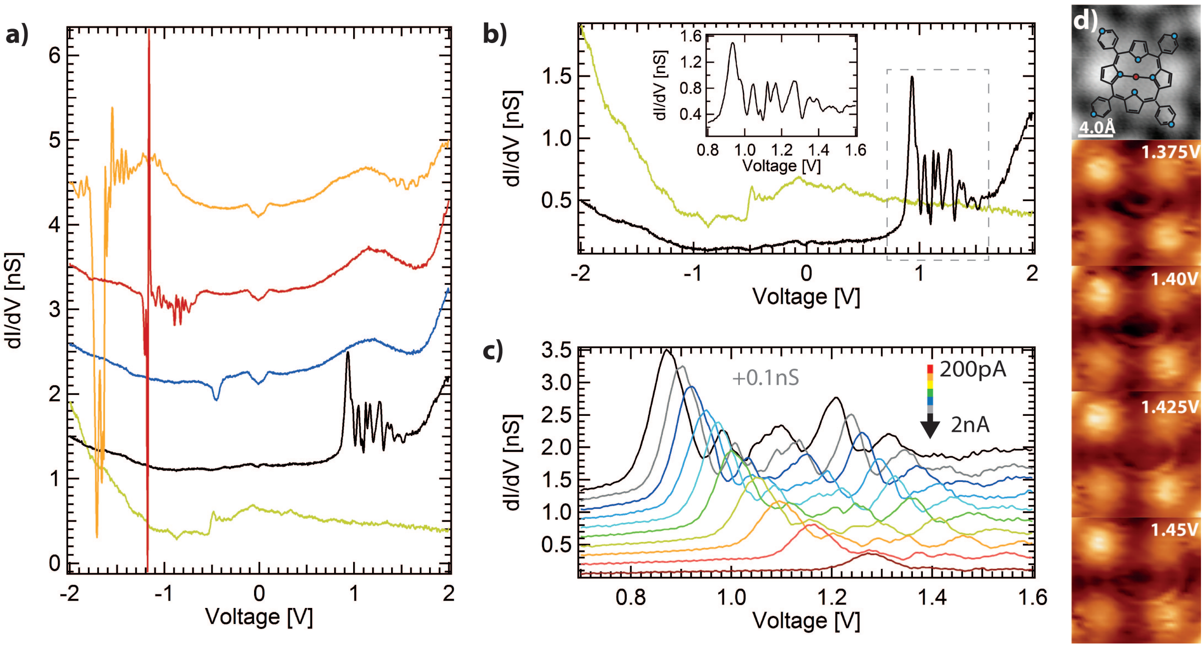

Figure 3.20. **a)** Overview of different spectra in the range of −2 V to 2 V on different type I molecules. Different features ranging from NDR's to oscillations can be observed. Feedback opened at 1 nA, 2 V with $V_{\mathrm{mod}} = 5\,\mathrm{mV}$. Spectra are offset by 1nS for clarity. **b)** Black spectrum of fig. a). The oscillatory part is shown as an inset. **c)** Distance dependent shift of the oscillations towards the Fermi level. **d)** Constant-height $\mathrm{d}I/\mathrm{d}V$ maps recorded on one molecule, showing the increase of the radius of the charging rings at higher bias voltages. The bright protrusions corresponds to the position of the pyridyl groups such that the rings start in the center of the molecule. Maps recorded at a setpoint of 140 pA, 800 mV with $V_{\mathrm{mod}} = 10\,\mathrm{mV}$.

The black spectrum with the oscillations at positive energies is depicted again in fig. 3.20b and c. It will exemplarily be chosen to investigate the physical effects behind all these features. One hint for a possible explanation for these spectral shapes can be obtained from constant-height $\mathrm{d}I/\mathrm{d}V$ maps. A set of maps recorded on one molecule is shown in fig. 3.20d for voltages in the range of the oscillations. In the $\mathrm{d}I/\mathrm{d}V$ maps, one can observe ring-like variations of the intensity, whose radius increases with higher bias voltages. Comparison to literature [120, 122–126] suggests these features to arise from charging effects, where the ring in the $\mathrm{d}I/\mathrm{d}V$ spectra corresponds to the transition from one to the other charge state.

In literature, the occurance of charging effects is typically related to the transport through double-barrier tunneling junctions [120, 121]. Figure 3.21 shows sketches of the energy level alignment for different regimes in the transport through such a double-barrier tunneling junction. In fig. 3.21a the situation with zero applied bias is shown. The Fermi level of tip and sample are aligned and the HOMO and LUMO orbital fully occupied and unoccupied, respectively. Under application of a small bias voltage (fig. 3.21b), the Fermi level of the tip shifts with respect to the molecular resonances. However, due to the small barrier between molecule and sample, the molecular resonances also shift with respect to the sample states. As a consequence of this shift, at some threshold, the LUMO orbital becomes accessible in the transport and visible in the spectra as a broad peak. Upon further increase of the bias (fig. 3.21c), the reduced coupling of the molecular states to the sample allows for the HOMO level to be pulled up above the Fermi level of the sample, which induces a partial emptying of the HOMO. As a consequence, also the HOMO becomes accessible for transport. As due to the different tunneling barriers, the hopping of the electron from the molecule to the sample is much faster than

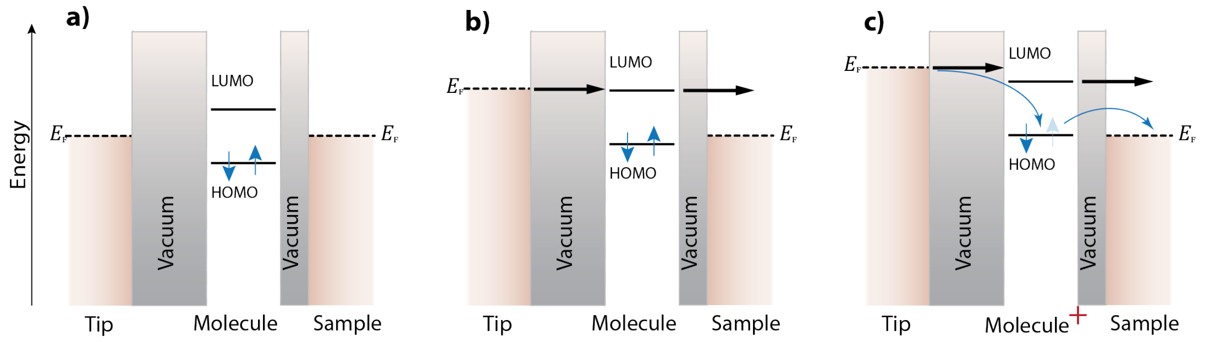

Figure 3.21. Tunneling through a double barrier junction at positive bias voltages. **a)** For zero applied bias, the Fermi levels of sample and tip are aligned and no transport takes place. **b)** Upon application of a positive bias voltage, transport can occur through the LUMO orbital of the molecule. **c)** Upon further increase, the HOMO resonance is shifted up in energy above the Fermi level of the sample, inducing a partial emptying of the HOMO level. This is accompanied by the accessibility of an additional transport path.

the filling of the level by a tip electron, the molecule is in a positive charge state, which leads to an abrupt increase in the conductance, as electron transport is facilitated. An interference between the transport channels through the HOMO and LUMO might account for the oscillatory behaviour in the $\mathrm{d}I/\mathrm{d}V$ traces [127]. Note that depending on the exact coupling to the leads and the energy level spacing, also the reversed process of first emptying the HOMO and then tunneling through the LUMO might occur.

One way to validate this explanation is by examining the distance dependence of the oscillations. In case of charging, a smaller molecule-tip distance would reduce the barrier between the two and couple the molecular resonances more strongly to the Fermi level of the tip. Hence, smaller bias voltages would be sufficient to shift the LUMO and HOMO levels in energy. This exact behaviour has been observed on this molecules, as can be seen in fig. 3.21c, when the tip was approached consecutively and the oscillations shifted towards the Fermi level.

For the oscillatory feature at positive bias, a consistent explanation could be found that reproduces the experimental results and is in agreement with literature. In the following, we want to check if the same arguments also describe the other features. Therefore, we try to explain the NDR feature (blue curve in fig. 3.20a in the framework from above. Figure 3.22a shows again the corresponding dip in the $\mathrm{d}I/\mathrm{d}V$ spectrum. At first, the distance dependence of the NDR position is examined. The shift of the NDR with decreasing tip-molecule distance is depicted in fig. 3.22b. With approaching tip (red to black), the spectra shift to higher absolute energies, and away from the Fermi level. This is unexpected in a charging picture, because the electric field increases with decreasing tip-sample distance, and hence, charging should be possible at lower voltages [121, 125].

Despite of this curiosity, we will nontheless consider the transport through a double barrier junction at negative bias voltages at first, and then try to understand this opposite shifting behaviour with the electric field. The double-barrier transport sketches for negative bias voltages are shown in fig. 3.22c-e, in analogy to the ones discussed above. At zero bias voltage, the Fermi level of tip and sample are aligned. At intermediate bias voltages, the HOMO state will be the first accessible transport channel, where first one electron hops off to the tip and then an electron from the surface can occupy the resulting unoccupied level. As the first hopping process is slower than the second one, the molecule will be neutral. If the bias voltage is further increased (see fig. 3.22e), also the LUMO orbital will contribute to the transport. This time, however, the electrons can quickly occupy the LUMO state and tunnel only slowly through the barrier into the tip, which leaves the molecule in a negatively-

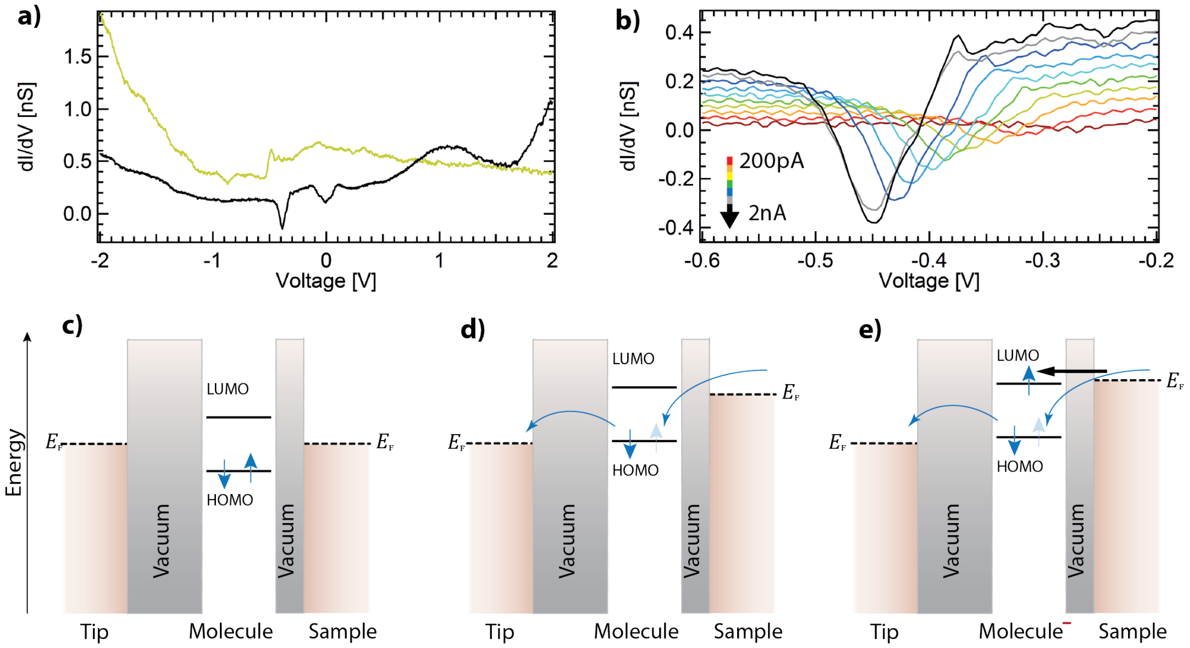

Figure 3.22. Tunneling through a double barrier junction at negative bias voltages. **a)** NDR feature of one of the Fe-TPyP molecules. **b)** Distance-dependent shift of the NDR away from E_F with increasing fields. Feedback opened at varying currents with $U = 2\,\mathrm{V}$, $V_{\mathrm{mod}} = 5\,\mathrm{mV}$. **c)** For zero applied bias, the Fermi level of sample and tip are aligned and no transport takes place. **d)** Upon application of a negative bias voltage, transport can occur through the HOMO orbital of the molecule. **e)** Upon further increase of the bias voltage, the molecular resonances are shifted up in energy above the Fermi level of the tip, inducing a partial filling of the LUMO orbital. This leaves the molecule in a negative charge state, which induces a reduced differential conductance.

charged state. This leads to a blocking of the tunneling current, resulting in an NDR dip in the $\mathrm{d}I/\mathrm{d}V$ spectra. As the tunneling through the HOMO and LUMO might occur here at similar voltages as well, interference effects are also reasonable to account for the variety in the spectral shapes.

The described mechanism can explain the occurring NDR features in the $\mathrm{d}I/\mathrm{d}V$ spectra, however, it does not capture the unexpected behaviour of an increasing NDR onset at smaller tip-sample distances, as the smaller tunneling barrier should allow the LUMO orbital to be occupied more easily. However, this behaviour can be explained in case of a variable barrier between sample and molecule. In case that the molecules slightly lift of the surface during the tip approach, the barrier between molecule and sample would increase, which would shift up the features in absolute energy. As a similar effect of an increasing molecule-sample distance upon tip approach has already been observed when studying the impact of the tip on the magnetic anisotropy parameters of the molecule, this picture seems appropriate to explain the curious shifting behaviour.

The previous explanations discussed the general occurance of charging rings and NDR effects in the $\mathrm{d}I/\mathrm{d}V$ spectra. In this description, however, we did not identify the electronic resonances that are involved in this process. The HOMO and LUMO orbitals of the Fe-TPyP molecules, as they are referred to in sec. 2 (see fig. 3.14a), are located at approx. $\pm 1\,\mathrm{eV}$ around E_F. Assuming a reasonable coupling strength between the molecule and the surface, it is not possible to shift this HOMO level by about 1 eV up to the Fermi level at moderate bias voltages around 2 V. Therefore, it seems more likely, the the Fe d states, which are situated at approx. $\pm 100\,\mathrm{mV}$ around E_F account for the HOMO orbital in the first consideration and the LUMO state in the second explanation, respectively.

D. Disordered Adatom-Mediated Structure of Fe-TPyP on Au(111)

In the previous sections, two adsorption geometries of Fe-TPyP on Au(111) were observed and their electronic and magnetic properties were analyzed. We saw the formation of densely-packed islands of the Fe-TPyP molecule and an asymmetrically distorted structure. In this chapter, we will examine a third structure of Fe-TPyP on Au(111), which is prepared analogously to the densely-packed structure and asymmetrically distorted structure by evaporating at room temperature. However, for this preparation, a different evaporator was used.

A topography of the structure of the Fe-TPyP molecules on the surface is depicted in fig. 3.23a and shows the formation of rather unordered molecular islands. From the analysis of the adsorption angles in fig. 3.23c, the orientation of the molecules in multiples of angles of 15° with respect to the symmetry directions of the Au(111) substrate becomes apparent. Moreover, also in this arrangement, the pyridyl groups of neighbouring molecules are pointing at each other, as can be seen in fig. 3.23b by the overlaid structure model. As the opposing arrangement of the N-lone pairs is energetically not favourable, this orientation corroborates the interpretation of atoms at the linking positions. Furthermore, in this structure, the molecules appear more blurry than the ones in the densely-packed structure or the distorted structure, which might indicate a stronger hybridization of the molecules with the substrate. This interpretation is supported by the constant-height Δf map shown in fig. 3.23e. The map showing a single Fe-TPyP molecule (see fig. 3.23d for topography) indicates that in this molecular structure, the pyrrole groups are the highest molecular moiety, in contrast to previous structures, where the pyridyl legs were protruding the most. To analyze what may cause the pyridyl legs to adapt a flatter geometry, the preparation conditions may give a hint. In contrast to

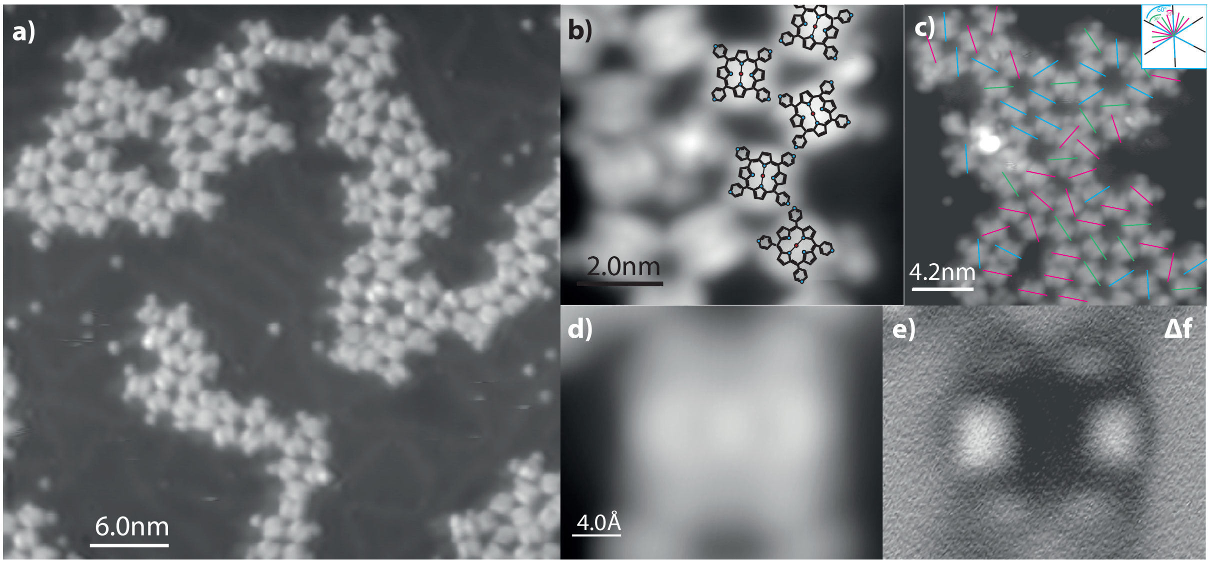

Figure 3.23. Disordered adatom-mediated structure of Fe-TPyP molecules on Au(111). **a)** Topography showing the formation of rather unordered Fe-TPyP molecules on the substrate. **b)** Close-up view of a molecular island, indicating the orientation of the pyridyl groups. **c)** Analysis of the orientation in multiples of 15° of the Fe-TPyP molecules on the substrate. **d)** Topography and **e)** constant-height Δf map of a single Fe-TPyP molecule. In contrast to previous structures, the pyrrole groups of this molecule are the highest moiety. During the recording of the Δf map, the tip was retracted by 0.35 Å with respect to the setpoint of 140 pA, 300 mV.

the previous preparations, a different evaporator was utilized to obtain this structure. Several preparations under similar conditions all resulted in the same structure, however, after a while, the surface became more contaminated during evaporation. As this structure was only obtained with this one particular evaporator, it seems likely that some kind of contaminant from the evaporator was involved in the formation of this structure, and induced a flattening of the pyridyl legs. However, the origin of this contaminant is unclear. Nontheless, despite the uncertainty of the nature of the additional constituents of this molecular structure, in the following, the properties of these Fe-TPyP molecules will be examined.

At first, we want to investigate the electronic properties. Figure 3.24a shows a $\mathrm{d}I/\mathrm{d}V$ spectrum recorded in the center of an Fe-TPyP molecule (black) and a reference spectrum on Au (yellow). Two pronounced resonances can be identified: the HOMO resonance at −1.3 V and the LUMO and LUMO+1 peaks at 750 mV and 820 mV with an additional shoulder at 540 mV. The LUMO and LUMO+1 onset of these molecules is even more down-shifted than the ones of the asymmetric structure, indicating an even stronger hybridization with the substrate due to the flatter pyridyl legs. Figure 3.24b depicts a series of $\mathrm{d}I/\mathrm{d}V$ maps that were recorded at the energies of the HOMO and LUMO resonances and at the higher-lying state at 2 V. In agreement to maps on the densely-packed structure, the HOMO orbital is more localized in the center of the molecule, whereas the LUMO is more delocalized at the organic macrocycle. The state at 2 V even shows the highest contributions at the pyridyl legs of the molecule.

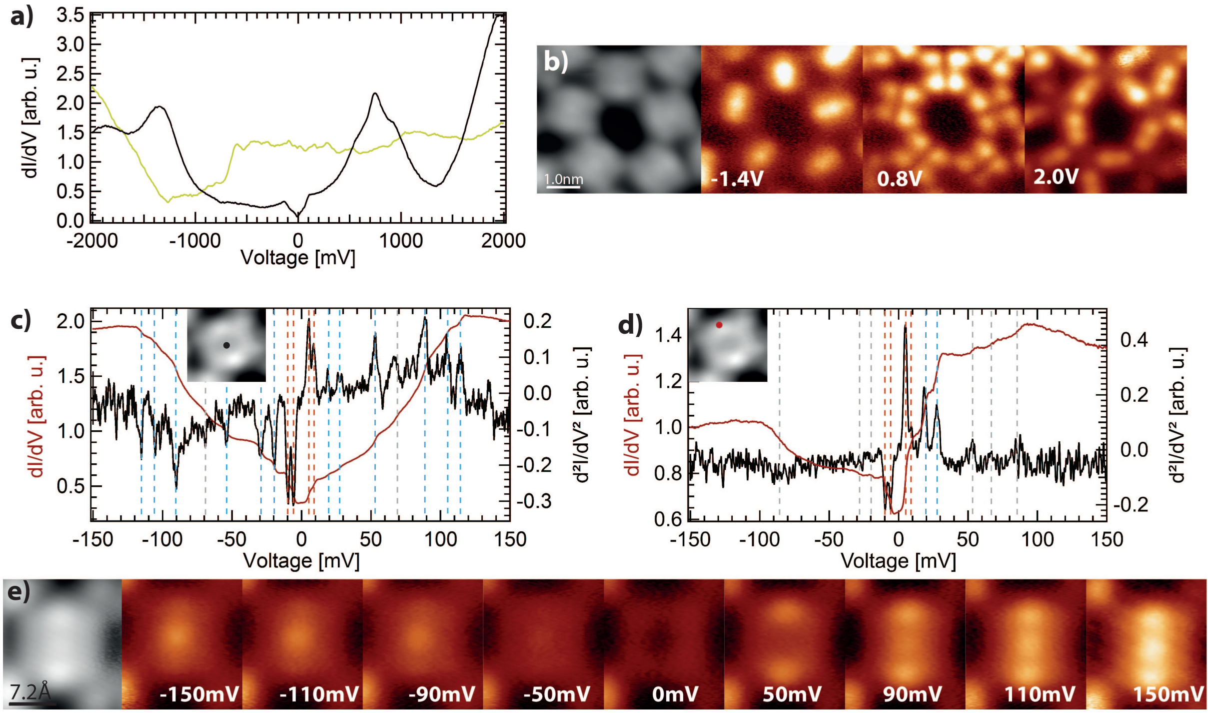

Figure 3.24. Electronic properties of the Fe-TPyP molecules in the disordered adatom-mediated structure. **a)** $\mathrm{d}I/\mathrm{d}V$ spectrum recorded in the center of the molecule, showing the LUMO, LUMO+1 and HOMO resonances. Feedback opened at 2 V, 1 nA with V_mod = 10 mV. **b)** Topgraphy and constant-height $\mathrm{d}I/\mathrm{d}V$ maps (V_mod = 10 mV) recorded at the energies of the resonances in a). **c)** $\mathrm{d}I/\mathrm{d}V$ (red) and $\mathrm{d}^2I/\mathrm{d}V^2$ (black) spectra recorded in the center of an Fe-TPyP molecule, showing several steps that are symmetric around the Fermi level. Feedback opened at 150 mV, 3 nA with V_mod = 1 mV. **d)** $\mathrm{d}I/\mathrm{d}V$ (red) and $\mathrm{d}^2I/\mathrm{d}V^2$ (black) spectra recorded on the upper pyrrole of an Fe-TPyP molecule (same feedback parameter as in c). **e)** Topgraphy and constant-height $\mathrm{d}I/\mathrm{d}V$ maps recorded at several characteristic energies (V_mod = 5 mV).

Table II. Assignment of the peaks in the HREELS spectra to steps in the $\mathrm{d}I/\mathrm{d}V$ signal of the distorted staggered structure and the disordered adatom-mediated arrangements of Fe-TPyP, together with their calculated energy from DFT calculations (b3pw91/genecp) for dihedral angles of 25° and 60°, respectively. All energies are given in meV. The symbols ν, δ, γ and τ denote stretching, in-plane wagging, out-of-plane wagging and torsion, respectively.

HREELS	**IETS (ord.)**	**IETS (disord.)**	**DFT (25°/60°)**	**Mode**
16	24.4	21	17 / 18	symmetric buckling / asymmetric buckling
32	33.9	30.5	30 / 30	Butterfly mode, Fe-tapping / sym. ν (Pyrrole)
45	-	-	-	-
60	61.0	54	59 / 59	N-tapping / τ(Pyrrole)
72	-	69	73 / 68	γ(C-H) / δ(C-H)
78	80.4	-	82 / 83	δ(C-C-C) / γ(C-H)
88	-	90	92 / 93	γ(C-H) / δ(C-H)
100	107	104	109 / 108	γ(C-H) / δ(C-H)
122	-	115	114 / 115	δ(C-N / δ(C-H))
135	-	-	-	-
151	-	-	-	-

Moreover, also the molecules in this arrangement exhibit a dip-like feature around the Fermi level. A close-up view of this feature is shown in fig. 3.24c. As for the type I molecules of the asymmetrically distorted structure, also these molecules exhibit a variety of steps in the $\mathrm{d}I/\mathrm{d}V$ signal at energies ranging from 7 meV to 115 meV. To allow for a better analysis of the step positions, in addition to the $\mathrm{d}I/\mathrm{d}V$ signal, also the $\mathrm{d}^2I/\mathrm{d}V^2$ signal is recorded simultaneously and plotted in black. By comparing the step position in the $\mathrm{d}I/\mathrm{d}V$ signal with the peak/dip positions in the $\mathrm{d}^2I/\mathrm{d}V^2$ signal, ten inelastic excitations can be identified, as marked by the dashed lines. Due to the similarity of this spectrum, with the ones of the type I molecules of the distorted structure, it seems reasonable that the steps in the spectra have the same origin. Hence, the two innermost steps marked by the red dashed lines at 6 meV and 9 meV are assigned to result from inelastic spin excitations. The blue dashed lines indicate vibrational excitations that are clearly resolvable and the grey lines correspond to molecular vibrations that are only faintly distinguishable.

The similarity of the spectral shape is also observed on the ligand of the Fe-TPyP molecules, as plotted in fig. 3.24d. The $\mathrm{d}I/\mathrm{d}V$ spectrum shows the exact same trends as the one on the type I molecules of the distorted staggered structure. The two lowest vibrational modes are strongly enhanced at positive bias voltages, whereas they are hardly visible at negative bias polarity. Moreover, the higher-lying vibrational modes have a much weaker intensity at both bias polarities. Due to the similarity between the spectral shapes at the high and low energy scale with the spectra on the distorted staggered structure, the general character of the Fe-TPyP molecules seems to be maintained. Hence, a strong modification of the molecular properties by the aforementioned contaminant from the evaporator can be excluded and the latter most likely only alters the molecular adsorption geometry.

The step energies that are observable in the $\mathrm{d}I/\mathrm{d}V$ signal are listed in tab. II, together with the energies determined from the HREELS measurements (see sec. C) and the ones observed on the type I molecules of the distorted staggered structure. The lower energy modes between 20 mV and 60 mV are in agreement for both structures. At higher energies, however, more steps are apparent in the disordered adatom-mediated structure.

The localization of the steps at positive energies can be seen in constant-height $\mathrm{d}I/\mathrm{d}V$ maps, as shown in fig. 3.24e. In general, the same observations as on the densely-packed molecules and the ones in the distorted staggered arrangement can be made. At negative bias voltages, the signal intensity is highest in the center of the molecule. At positive bias voltages, however, the observations are slightly different on the different structures. Whereas on the densely-packed structure and distorted staggered structure, the signal intensity is always higher on the upper pyrrole groups than in the center of the molecules, in the adatom-mediated structure, the same signal intensity is obtained in the center and on the ligand above 110 mV. Only below 110 mV, the signal on the upper pyrroles is stronger than in the center.

E. Comparison of the Different Adsorption Structures of Fe-TPyP on Au(111)

In sec. B, sec. C and sec. D, three different structures of Fe-TPyP on Au(111) were characterized. The similar localization of the molecular resonances on the molecules in all three arrangements emphasizes the similarities between all three investigated structures. However, the different magnetic properties also indicates that there are differences between the molecules in the different arrangements. Moreover, on two structures, vibrational excitations were observable, which were absent for the other two types of molecules. To understand how the molecular properties are altered in the different structures, in this section, a direct comparison of the properties of the molecules in all three adsorption geometries is made.

Similar preparation conditions were chosen to obtain the different structures, with the sample held at room temperature during the deposition of molecules. However, due to the conformational degrees of freedom of the Fe-TPyP molecules, different intermolecular configurations can emerge, which are influencing the intramolecular distortions. The corresponding adsorption geometries for the three observed structures are depicted in fig. 3.25 for a the densely-packed structure, b the distorted staggered structure and c the disordered adatom-mediated structure.

In the densely-packed arrangement, all molecules show the same spectral features. In the distorted staggered structure, two different types of molecules were observed. By studying the occurance of the type I and type II molecules within the islands, no correlation between the arrangement of type I and type II molecules and the symmetry properties of the underlying substrate could be observed. Hence, it seems unlikely that the different types result from different adsorption sites on the Au(111) substrate but are rather assigned to slightly different molecular distortions. The third

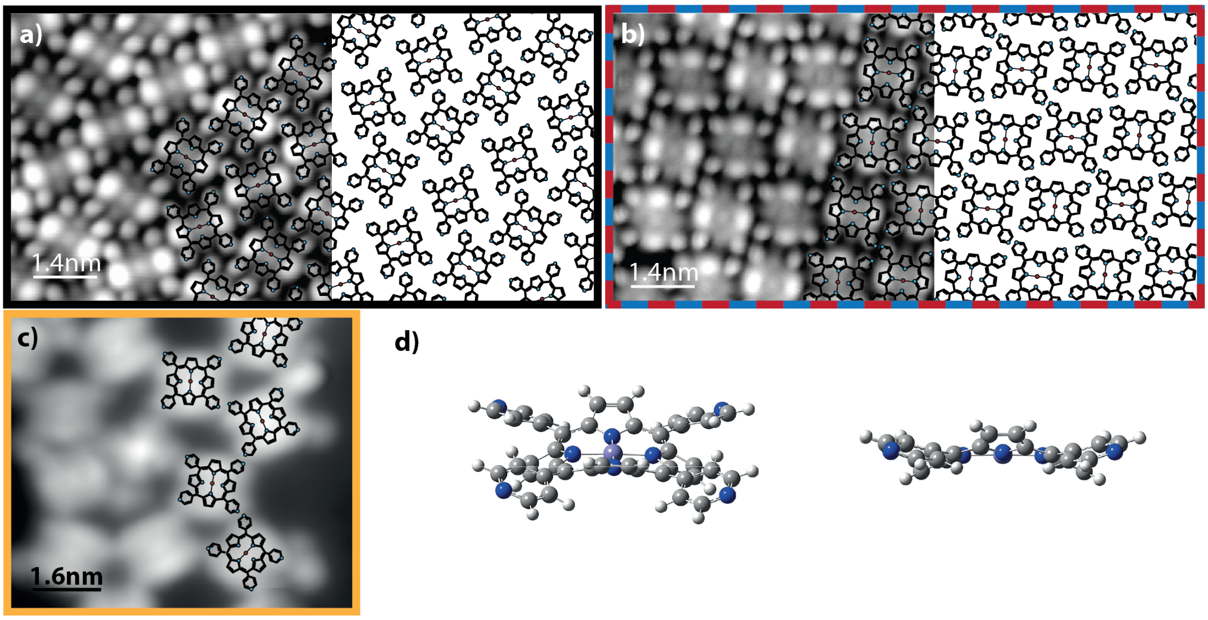

Figure 3.25. Topography, showing the adsorption geometries of the three observed arrangements of **a)** the densely-packed structure; **b)** the distorted staggered structure and **c)** the disordered adatom-mediated structure. The colour of the boxes around the images corresponds to the spectral colours in figs. 3.27, 3.28 and 3.29. Images recorded at a) 0.2 V, 200 pA; b) 0.23 V, 160 pA; c) 0.44 V, 93 pA. **d)** Sketches of the saddle deformation of the Fe-TPyP macrocycle. Exemplarily, a dihedral angle of 25° was chosen.

structure, the disordered adatom-mediated structure, was observed, when preparing with a different evaporator. In this structure, a more random orientation of the molecules was found, with some kind of species that was codeposited during the evaporation process presumably coordinating between the Fe-TPyP N lone pairs of the pyridyl groups. However, its nature remains unclear. Due to the similarity of the electronic and magnetic properties of the molecules in this structure to the ones in the other structures, we will nontheless consider this structure for a direct comparison.

1. Symmetry of Saddle Deformations

The first aspect to be compared is the molecular geometry on the surface. From the STM topographis in fig. 3.26a-c, the densely-packed structure and the distorted staggered arrangement clearly show a saddle shape deformation of the Fe-TPyP molecules. The topography of the disordered adatom-mediated structure, in contrast only shows a weak hint of this deformation of the macrocycle. However, STM topographies in general do not purely reflect the geometry of the molecules but are a convolution with the electronic properties. To determine the molecular structure, AFM images are a more suitable choice. In fig. 3.26d-f, constant-height Δf maps of all three structures are depicted (compare to the corresponding sections for more details).

In case of the densely-packed structure (see fig. 3.26a,d) and the distorted staggered structure (see fig. 3.26b,e), the pyridyl legs are the molecular moities that protrude the most from the surface. This indicates a rather weak interaction with the substrate, as the favoured structure in gas phase exhibits completely orthogonal pyridyl legs. In the disordered adatom-mediated structure (see fig. 3.26c,f), in contrast, the pyridyl groups are much flatter and the upper pyrrole groups are the highest part of the molecule. This flattening of the pyridyl legs leads to much stronger hybridization of the macrocycle with the underlying Au(111) surface.

Moreover, there is a difference in the symmetry of the rotation of the pyridyl legs. Whereas the

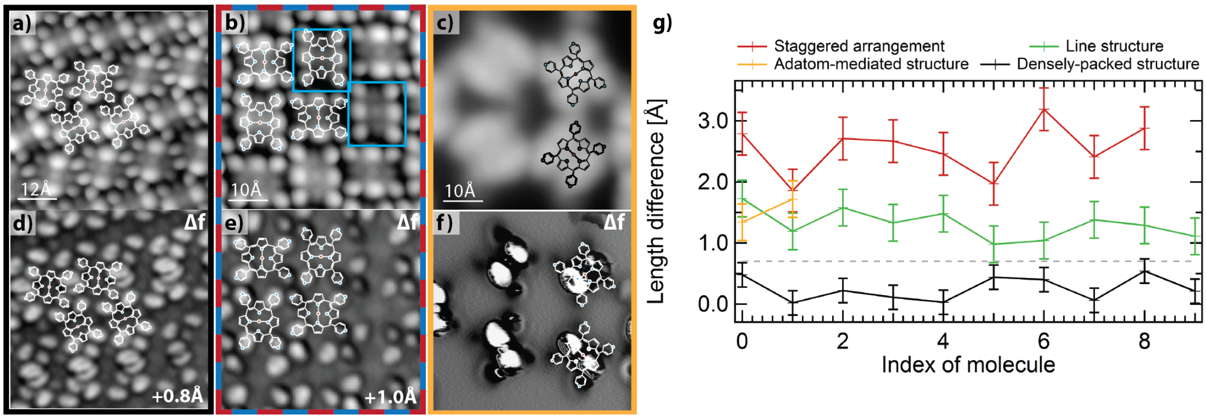

Figure 3.26. Constant-current topographies and constant-height Δf maps for **a,d)** the densely-packed structure; **b,e)** the distorted staggered structure; **c,f)** the disordered adatom-mediated structure. Whereas in the densely-packed structure and the distorted staggered structure, the pyridyl legs are the highest moiety, the molecules in the disordered adatom-mediated structure show a higher pyrrole group. Moreover, the maps indicate different symmetries of the rotational angles of the pyridyl legs between all structures. The blue boxes in b) indicate the type II molecules. STM topographies recorded at a) 0.23 V, 150 pA; b) 0.23 V, 160 pA; c) 0.84 V, 130 pA. **g)** Analysis of the length difference between opposing pyridyl groups of the molecules in the different structures. The grey dashed line corresponds to the maximal theoretical difference of 0.7 Å that is possible without considering intramolecular distortions.

map of the densely-packed structure (see fig. 3.26d) indicates equal rotational angles of all four pyridyl groups, the maps of the distorted staggered and the disordered adatom-mediated arrangements indicate that two diagonal pyridyl legs are rotated more strongly than the remaining two. Thus, there is a breaking of the mirror symmetry in the distorted staggered structure and the disordered adatom-mediated arrangement. Surprisingly, no difference was observable between the type I and type II species of the distorted staggered structure in the Δf maps (blue boxes in fig. 3.26e) mark the type II molecules). This indicates that only very small differences in the molecular structure that can not be resolved with AFM measurements, are responsible for the change of the molecular properties.

When analyzing the distance between opposing pyridyl groups, another discrepancy between the structures can be identified. An evaluation of the distance between the different pyridyl groups is shown in fig. 3.26g. Only minor differences between opposite pyridyl groups can be distinguished for the molecules in the densely-packed structure (black curve). For the molecules in the distorted staggered structure, on the contrary, the lower pyridyl groups of the molecules exhibit a larger distance than the upper ones (red curve). The grey dashed line at 0.7 Å indicates the maximum length difference than can be explained by different rotational angles of the pyridyl groups (see sec. C.1.1 for more details). As the experimentally determined length difference does exceed this value, the larger length difference indicates an intramolecular distortion of the molecular macrocycle.

A slightly smaller but non-negligible length difference is also observable for the distorted molecules in the line arrangement (green curve), as introduced in sec. C.1.1. Also the two left molecules in the adatom-mediated structure shown in fig. 3.26c exhibit different distances between the pyridyl groups along the different directions. For the two right molecules, the length difference could not be determined, as the flattening of the pyridyl groups for these molecules does not allow to precisely determine the position of all four pyridyl groups. Unfortunately, the lack of Δf maps of more molecules does not allow to get suffient statistics about the length difference for this structure. However, the two investigated molecules indicate that also the molecules in the adatom-mediated structure exhibit an intramolecular distortion.

2. Hybridization Effects Induced by Saddle Deformations

After the differences in the geometry of the molecules were analyzed, their influence on the electronic properties will be investigated in the following. In fig. 3.27a, the $\mathrm{d}I/\mathrm{d}V$ signals recorded in the center of Fe-TPyP molecules in the respective structures are compared. Whereas the energetic position of the HOMO resonance stays more or less constant for all different structures, the LUMO and LUMO+1 resonances, whose degeneracy is lifted by the saddle deformation of the macrocycle, vary by several hundreds of meV. As described in sec. B, the LUMO orbital is located at the organic macrocycle of the Fe-TPyP molecule with its main weight on the pyridyl legs (compare inset in fig. 3.27a, where a $\mathrm{d}I/\mathrm{d}V$ map at the energy of the LUMO resonance is exemplarily depicted for the densely-packed structure). A down-shifting of the LUMO towards the Fermi level therefore indicates a stronger hybridization of the organic macrocycle and especially the pyridyl endgroups with the underlying Au(111) substrate. Following the analysis of the adsorption geometries of the previous sections, the molecules in the densely-packed structure (black) and the distorted staggered arrangement (red, blue) both exhibit a geometry, where the pyridyl legs are the most protruding moiety. This elevates the porphin macrocycle from the substrate and minimizes hybridization effects. Moreover, the stronger rotation of the pyridyl legs with respect to the substrate also minimizes the orbital overlap on the pyridyl groups. The different rotational angles of the pyridyl groups in the distorted staggered structure might lead to slightly stronger hybridization effects, which might account for the down-shifting of the LUMO and LUMO+1 resonances. In contrast to the distorted staggered structure and densely-packed structure,

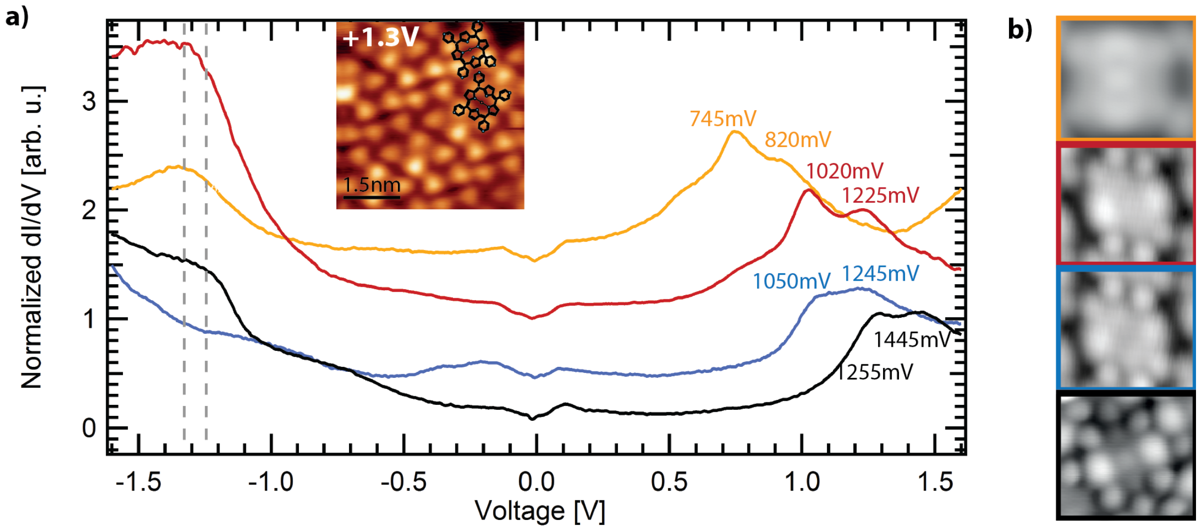

Figure 3.27. **a)** Shifting of the LUMO and LUMO+1 resonances for the three structures of Fe-TPyP. Black: the densely-packed structure, red and blue: the distorted staggered structure, and yellow: the disordered adatom-mediated structure. The spectra are normalized to their LUMO resonance and offset for clarity. The inset shows a dI/dV map of the LUMO resonance for the densely-packed structure, indicating that the LUMO is mainly localized on the organic macrocycle of the molecules. **b)** Changing topography of a single molecule of each of the structures. Although the overall appearance of the Fe-TPyP molecules is the same, with increasing hybridization, the topographies appear more blurry.

the pyridyl groups of the molecules in the disordered adatom-mediated structure (yellow) lie flatter on the substrate, which brings the macrocycle of the molecules closer to the surface. The enhanced hybridization of the porphin macrocycle and the stronger orbital overlap due to flatter pyridyl legs, hence induces a down-shifting of the LUMO and LUMO+1 towards E_F.

3. Magnetic Changes: Spin Crossover and Anisotropy Splitting

The changing of the molecular geometry does not only impact the electronic resonances of the molecules, but also goes along with changes in the magnetic properties. The magnetic ground state of a system is determined by the ligand field acting on the central magnetic atom. In general, in case of a stronger ligand field, a lower spin state is expected, as the ligand field induces a stronger splitting of the corresponding d levels such that the lower levels tend to be doubly occupied. For weaker ligand fields, in contrast, the system approaches the case of a free atom, where high-spin states are favoured. The same observation holds for the Fe-TPyP molecules in the different structures. Figure 3.28a shows the magnetic fingerprints in the dI/dV spectra of all four types of molecules. For all cases, the symmetric steps around the Fermi level correspond to the opening of an inelastic transport channel due to spin excitations. To understand the different signatures, the electron configurations of all four structures have to be compared.

Figure 3.28b shows the proposed d-level occupation of all structures. The left sketch corresponds to the level occupation in the densely-packed structure, as described in sec. B.3 and reported in [71]. Here, the d_{xy} and d_{xz} orbitals are doubly occupied, the d_{yz} and d_{z^2} orbitals bare one spin each, and the highest lying level, the $d_{x^2-y^2}$ remains unoccupied. The total spin of this electron configuration is $S = 1$, with a vanishing transverse anisotropy due to the almost degenerate d_{xz} and d_{yz} levels. If the molecular geometry is distorted, also the position of the adjacent N atoms that coordinate to the Fe center is changed, such that the D_{4h} symmetry is reduced to D_{2h}. As a consequence, the degeneracy between the d_{xz} and d_{yz} levels is lifted, which induces a transverse anisotropy component $E \neq 0$ to the system. This splitting of the spin eigenstates manifests itself in a splitting of the excitation step in the dI/dV spectra. Moreover, a downshifting of the d_{z^2} and $d_{x^2-y^2}$ orbitals will be observed, as the average Fe-N bond length will decrease due to the distortion, which weakens the influence of the ligand field. In case of these distortions being rather small, the system will still be in an intermediate $S = 1$ state, as is the case for the type I molecules of the distorted staggered structure (red). Interestingly, also in case of the molecules in the disordered adatom-mediated structure (yellow), the intramolecular distortion seems to be in a similar regime, as it is also described by a $S = 1$ state with very similar anisotropy parameters. If the Fe-N bond length is further increased, either by a stronger distortion or by dislocating the Fe atom into the surface plane, the energy level difference will become smaller than the spin-pairing energy and the system will undergo a spin crossover, with the $S = 2$ high-spin state constituting the new magnetic ground state. Although this elongation of the Fe-N bond length can not be resolved with AFM, this seems to be the origin of the spectral changes for the type II molecules in the distorted staggered arrangement (blue).

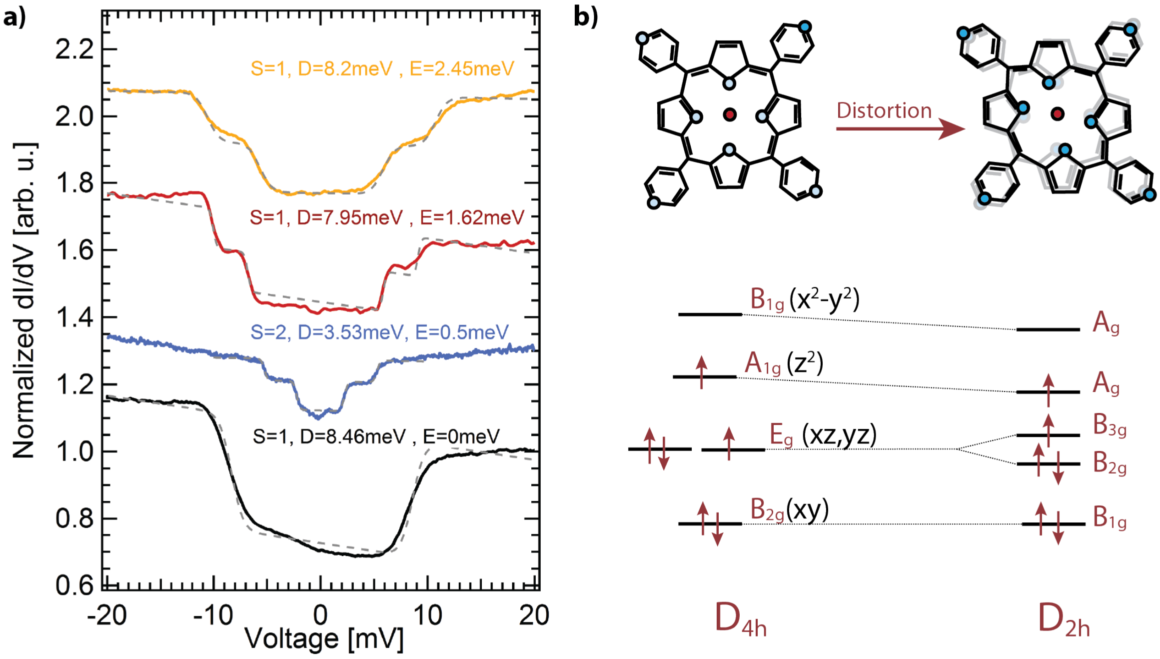

Figure 3.28. Comparison of the magnetic properties of all Fe-TPyP structures. **a)** dI/dV spectra at ±20 mV around E_F, exhibiting different numbers of steps symmetric around the Fermi level. The corresponding spin state assumed to fit the data (gray dashed lines) is given next to the graphs, as well as the resulting anisotropy parameters D and E. Fit performed with the program by Markus Ternes [99]. **b)** Proposed d-level occupation for the different magnetic ground states. The increased saddle shape distorts the ligand field, finally leading to a spin crossover. Feedback opened at yellow & black: 50 mV, 2 nA with $V_{mod} = 0.5$ mV; red & blue: 50 mV, 1 nA with $V_{mod} = 0.25$ mV, $B = 0.5T$, $T = 1.1$ K.

4. Intensity of Vibrational Signatures

Besides their magnetic ground state, another major difference between the molecular arrangements lies in the observation of vibrational excitations for some structures and the absence of the latter for others. In order to understand the cause of this effect, the minute changes in the energetic position of the resonances that mediate the virtual transitions have to be considered, namely the hybrid d_{z^2} and d_{yz} orbitals. Therefore, the dI/dV spectra in an energy window of −150 mV to 150 mV are shown both for the center of the molecule and for the ligand, respectively.

In the center of the molecules (fig. 3.29a), a V-shaped feature can be observed on all structures, which exhibits a symmetric lineshape with respect to the Fermi level. Moreover, all of the spectra show one or two steps at low bias voltages, which are attributed to spin excitations. However, only the yellow and red curves show a variety of steps at higher energies. For comparison, a spectrum has also been recorded on one of the non-metallated TPyP molecules, which can occasionally be found on the surface. In the corresponding spectrum shown in gray, neither peaks nor steps can be observed. To probe the localization of the corresponding features, spectra were also recorded on the upper pyrrole groups of the molecule, as shown in fig. 3.29b. Here, however, the lineshapes of the spectra recorded on the different structures show some differerences. In agreement to the spectra in the center of the molecules, also the spectra on the ligand show the low-energy spin excitations at the same energies. Apart from these innermost steps, the blue and the black spectra show a rather flat dI/dV curve at negative bias voltages. The yellow and red spectra, on the contrary, exhibit a step at around −84 mV. At positive bias voltages, the blue spectrum exhibits a single peak at 72 mV. The black spectrum shows a double resonance, with peaks at 70 mV and 115 mV. The yellow and red spectra also show two peaks, however, they are at 35 mV and 90 mV and hence shifted to lower energies (see grey dashed

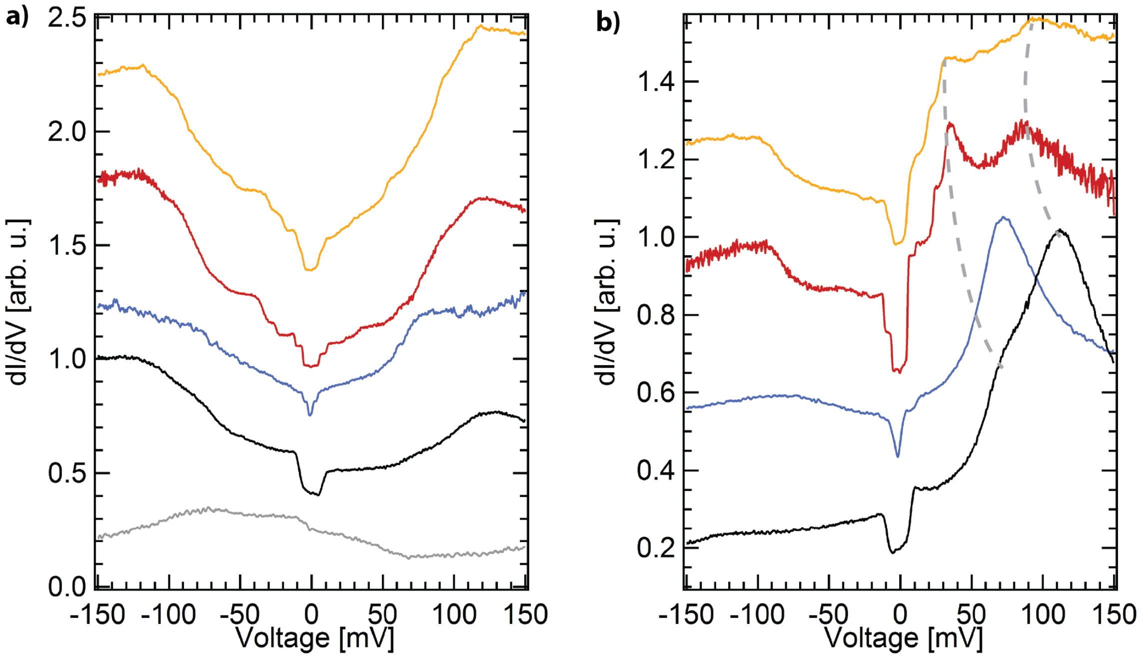

Figure 3.29. Comparison of the vibrational signatures **a)** in the center and **b)** on the ligand of the different molecular structures. Overall, the same spectral trends can be observed, with symmetric spectral shapes in the center, and more asymmetric lineshapes on the ligands. Feedback opened at yellow: 150 mV, 3 nA with $V_{\mathrm{mod}} = 1$ mV; red & blue: 200 mV, 2 nA with $V_{\mathrm{mod}} = 0.5$ mV, $B = 0.5T$, $T = 1.1$ K; black: 200 mV, 2 nA with $V_{\mathrm{mod}} = 1$ mV.

line). Moreover, the red and yellow spectra exhibit some pronounced steps at positve bias voltages.

From the HREELS data (see sec. C.3), the origin of the steps in the dI/dV spectra could be understood. However, only the yellow and red spectra exhibited fingerprints of vibrational excitations, whereas no steps were observable in the blue or black spectra. Furthermore, on the yellow and red spectra, the vibrational excitations were also observable on the upper pyrrole groups of the molecules. Here, however, the steps were visible exclusively at positive bias voltages.

In the center of the molecule, there are resonances both at around −130 mV and at 130 mV. On the ligand, on the contrary, peaks are only distinguishable at positive bias voltages. By comparing to recent studies of FeTPP on Au(111) [71], the peak at negative bias voltages, which is localized in the center of the molecule, is assigned to result from mainly the d_{z^2} orbital of the Fe atom. The resonance at positive bias voltages, which has a high density of states on the upper pyrrole groups is interpreted as a hybrid state between the unoccupied Fe d_{yz} orbital and ligand states. In relation to the molecular resonances, also the vibrational excitations on the ligand can only be discerned at positive bias polarity. To understand this correlation, the excitation mechanism of molecular vibrations has to be considered. For the excitation of molecular vibrations, one can differentiate between two scenarios. Either, the excitation occurs resonantly or non-resonantly (see sec. II.4). Non-resonant excitations occur, when the applied bias voltages lie well below the molecular resonances. The excitation of vibrations here is dominated by an impact scattering of the tunneling electron, which is independent of existing molecular resonances [42, 109]. Its contribution to the dI/dV signal is positive but typically very small [109], such that they are often not detected in spectroscopy. The excitation cross section of vibrations in the non-resonant regime can be strongly enhanced by the existence of molecular resonances close to the Fermi level, which allow for co-tunneling [42, 128–132]. The proximity of a molecular resonance leads to an increase of the dwell time of the electron in the molecule, giving it more time to interact with the vibrational modes of the molecule. As the excitation of molecular vibrations, in this case, is mediated via virtual excitations to the higher lying molecular resonances obeying Heisenberg's uncertainty principle, the energy alignment of the corresponding levels plays a crucial role for the observation of steps in the dI/dV signal [132, 133].

If, on the other hand, a molecular state lies within the transport window, the excitation process occurs resonantly. In contrast to the non-resonant excitation path, where the tunneling electron remains on the molecule only for very short times, the resonant process occurs in the ionic charge state of the molecule [132, 134]. Hence, the corresponding resonant vibronic excitations appear as peaks in the dI/dV signal, which can only be resolved in case of long lifetimes of the excited states.

In a simple transport picture, for non-resonant transport, the excitation of a molecular vibration should always result in a step in the dI/dV signal. However, interference effects can occur between the elastic and inelastic transport paths. More specifically, it has been shown that molecular vibrations change the density of states for the elastic path, which might lead to decreasing elastic contributions [109, 135]. As the total dI/dV signal is the sum of the elastic and inelastic contribution, the step intensity can vanish for certain vibrational modes [135] and might even lead to negative peaks and NDR effects in the signal [44, 109, 128, 135–138]. Although these effects might be able to explain the absence of certain vibrational modes on some of the molecular structures, it seems unlikely that all the vibrational signatures should have disappeared completely via these mechanisms for both the densely-packed structure and the type II molecule of the distorted structure.

Instead, to understand the different intensity of the vibrations in the Fe-TPyP molecules, the energy positions of the states that are involved in the virtual excitation processes have to be compared. In the center of the molecule, there are corresponding states at both bias polarites. Therefore, in the center of the molecule, the cross section to excite vibrations is enhanced at both bias polarities due to the presence of resonance. Hence, also the steps in the dI/dV signal can be observed at both bias polarities with almost equal intensity. On the ligand, however, there is no density of states available at negative bias voltages to mediate the virtual excitation process, as the states are too far away from the Fermi level. Therefore, vibrational modes are only enhanced at positive bias voltages.

Moreover, the energy position of the resonances also explains the absence of vibrational features on the blue and black spectra. As mentioned above, a shift of the positive bias resonances can be observed between the spectra, as indicated by the gray dashed lines in fig. 3.29b. Intriguingly, there is a connection between the energy position of this resonance and the intensity of molecular vibrations: for the yellow and red spectra, the energy of the resonances is lower than for the blue and black spectra. Following the framework of co-tunneling, a lower energy of the excited levels corresponds to a longer dwell time of the electron in the molecule. Therefore, also the cross section of the inelastic excitations increases, when the corresponding states shift to lower energy, which eventually leads to stronger inelastic features in the $\mathrm{d}I/\mathrm{d}V$ spectra.

Despite the fact that we were able to explain the intensity of the vibrational excitations solely by the energy position and localization of the involved resonances, more aspects usually have to be considered to explain the intensity of vibrational modes. Several studies have shown that the intensity of vibrations is also influenced by the symmetry of the orbitals of the molecule and the tip or the coupling of certain vibrational modes to the molecular orbitals [111, 139]. However, as we always study the same molecule on the same substrate, these other aspects that might influence the vibrational intensities basically remain unchanged. Hence, these parameters can be neglected in our considerations.

F. Annealed structure of FeTPyP

For all the different structures of Fe-TPyP that were shown in the previous sections, the sample was held at room temperature during the preparation process. In this section, the Fe-TPyP molecules were annealed to temperatures around 300 °C, where a modification of the topographic appearance of the molecules could be oberved. An image of the Fe-TPyP molecules on the Au(111) surface after annealing is depicted in fig. 3.30a, showing rather unordered islands of Fe-TPyP molecules. A close-up view of the molecules is shown in the inset of fig. 3.30b, indicating a flatter geometry of the

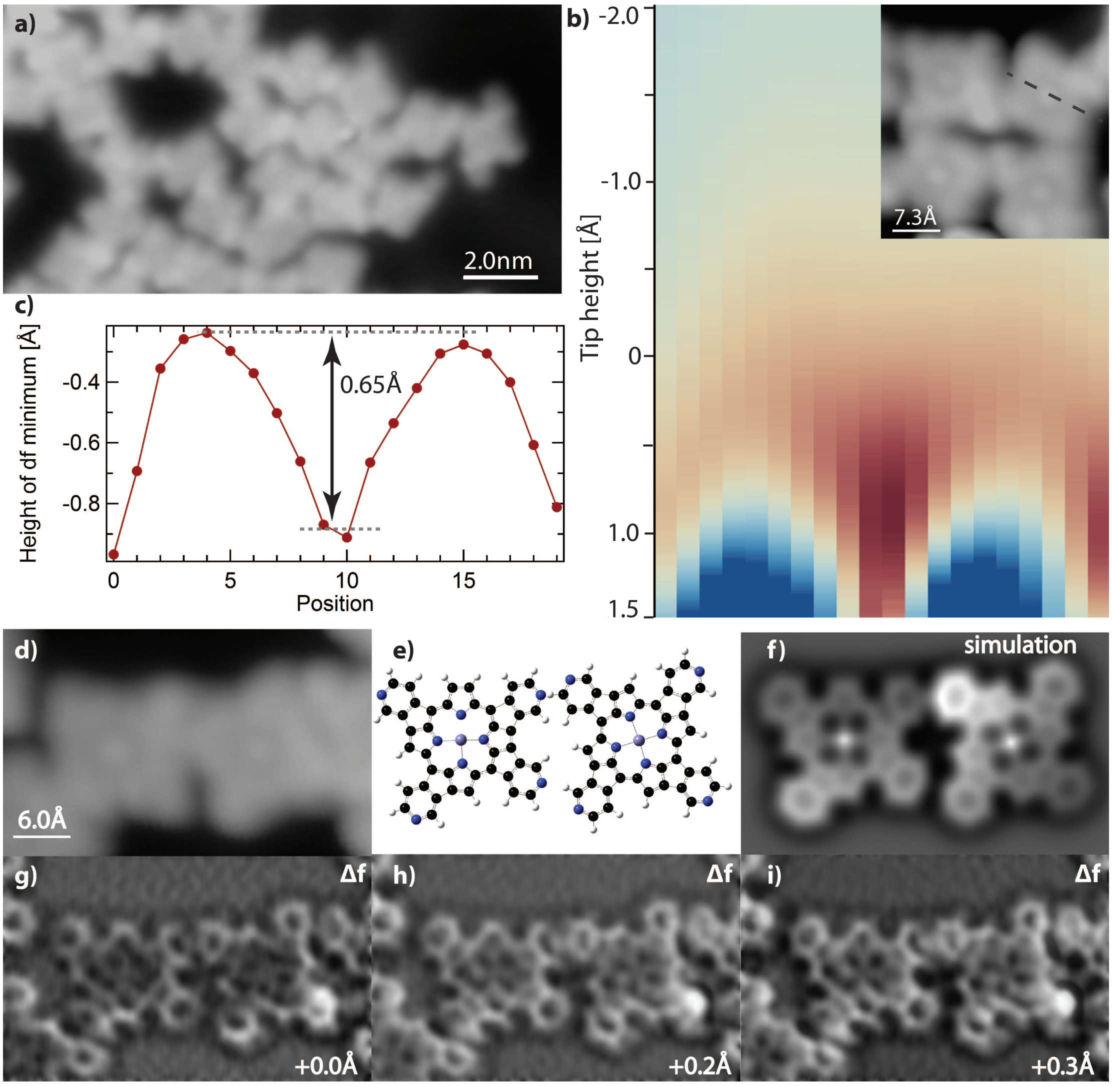

Figure 3.30. Adsorption structure of Fe-TPyP molecules after post-annealing the sample to 300 °C. **a)** Topography showing the random orientation of the Fe-TPyP molecules. **b)** Δf approach curves on various points along an Fe-TPyP molecule. **c)** Minima of the Δf curves in b). Despite the flat appearance of the molecule in STM and AFM images, the upper pyrroles are situated about 0.65 Å above the Fe center. **d)** Topography of two Fe-TPyP molecules. **e)** Structure model as assumed from the constant-height Δf maps recorded at different tip-sample distances in **g-i)**. To enhance the resolution, the Δf maps were post-treated by adding the Laplace-filtered image to the original map. **f)** Simulated Δf map based on the structure model in e). A good agreement between the simulation and the experimental maps can be observed.

molecules in contrast to the pronounced saddle shape that is visible in the STM topographies of the other structures. Morover, a distinguishable protrusion at the position of the Fe center is visible.

To analyze the molecular structure in terms of its saddle deformation, we recorded Δf approach curves on the Fe-TPyP molecules. Therefore, the tip was positioned on a molecule and the tip-sample distance was reduced until a minimum in the Δf curve was seen. This minimum indicates the distance at which repulsive forces between the tip and the molecule start to become non-neglegible. Hence, this distance is taken at as reference point to determine the height of the respective molecular group. One set of spectra recorded along the pyrrole groups of a molecule is shown in fig. 3.30b, with the determined minima of the Δf approach curves shown in fig. 3.30c. Despite the flat appearance of the molecules in the STM topographies, the Δf approach curves indicate the Fe center to be situated approx. 0.65 Å below the pyrrole groups, which might be explained by a lowering of the Fe atom into the surface plane as a result of the interaction with the surface. In the previous structures of Fe-TPyP, different properties were observed along the upper and lower pyrrole groups of the molecules, due to the saddle shape of the molecules (see Appendix B for corresponding Δf approach curves on the other structures of Fe-TPyP). For the annealed Fe-TPyP molecules, however, a similar height difference is obtained along both symmetry axis of the molecule, indicating the absence of a saddle-shape deformation.

To understand the intramolecular changes induces by the annealing, constant-height Δf maps were recorded on two molecules (see fig. 3.30g-i). The Δf maps support the interpretation that the molecules no longer exhibit a saddle shape. Moreover, the flat geometry of the molecules allows to resolve the structure of the carbon rings of the macrocycle and indicates that the molecular structure was strongly altered during the annealing process: in total eight C–H bonds were broken in each molecule and new C–C bonds have formed between the pyridyl rings and adjacent pyrrole groups (compare to structure model in fig. 3.30e). In the right molecule of the Δf maps, all pyridyl groups have bonded to the respective neighbouring pyrrole group on the right side. The left molecule, on the conrary, has a more asymmetric shape, as the upper pyrrole group has no pyridyl groups bound to it, whereas two new bonds were formed between the right pyrrole group and the two neighbouring pyridyl groups. From the topographic image, however, these structural differences between the two molecules can not be distinguished. In fig. 3.30f, a simulated[4] Δf map based on this structure model is depicted, showing a good agreement between the simulations and experimental findings.

1. Electronic properties of annealed FeTPyP

After strong modifications of the molecular structure were observed, their influence on the electronic and magnetic properties of Fe-TPyP has been investigated. Figure 3.31 shows $\mathrm{d}I/\mathrm{d}V$ spectra recorded on the annealed Fe-TPyP molecules. In fig. 3.31a, a spectrum recorded in the center of an Fe-TPyP molecule is shown. Apart from a resonance at approx. −200 mV, no further peaks can be distinguished. Even at positive bias voltages, where the previously investigated structures of Fe-TPyP exhibited pronounced LUMO resonances, no peaks can be observed. Only at voltages above 1.5 V, an onset of a peak can be seen. In fig. 3.31c and d, $\mathrm{d}I/\mathrm{d}V$ spectra are shown at different sites on an Fe-TPyP molecule. The largest contribution of the resonance at −200 mV can be observed in the center of the molecule. At the pyrrole groups (fig. 3.31c) and along the diagonal axis of the molecule (fig. 3.31d) some DOS at positive bias voltages can be seen at around 100 mV. Note that the spectra in fig. 3.31d on two opposing sites of the molecules are not the same, but a higher peak intensity is found in the red spectrum, corresponding to the lower left corner of the Fe-TPyP molecule. This asymmetry is also observable in $\mathrm{d}I/\mathrm{d}V$ maps (see fig. 3.31e) and might be attributed to an asymmetric geometry of

---

[4] The simulated images were obtained using the online tool provided by the group of P. Jelinek [87, 88].

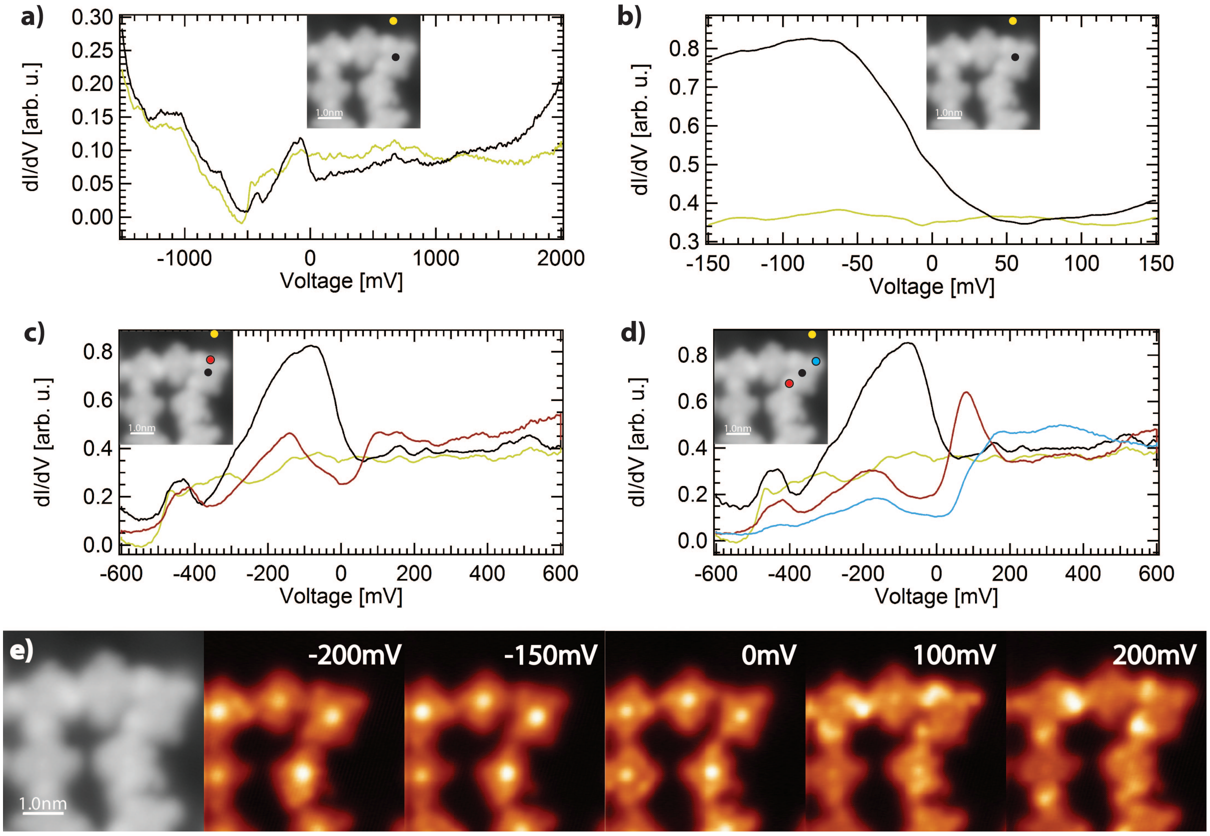

Figure 3.31. Electronic properties of Fe-TPyP molecules after post-annealing the sample to 300 °C. **a)** dI/dV spectrum recorded on Fe-TPyP (black) and a reference spectrum recorded on Au(111) (yellow). A pronounced resonance can be observed on the molecules right below the Fermi level. At positive bias voltages, the onset of a peak can be distinguished at above 1.5 eV. **b)** Zoom into the region around E_F, showing the absence of any inelastic features. **c)** dI/dV spectrum recorded in the center (black) and on one pyrrole group of the molecule (red). **d)** dI/dV spectrum recorded along the diagonal axis of an Fe-TPyP molecule. **e)** Constant-height dI/dV maps recorded on several molecules. Whereas all molecules exhibit a high DoS at negative bias voltages in the center, the dI/dV signal at positive bias voltages varies for the different molecules. For the recording of the maps, the tip was retracted by 1.5 Å from the setpoint of 500 pA, 200 mV with $V_\mathrm{mod} = 3$ mV.

this particular molecule. As described above, different bonding motifs are observed during the bond formation between the pyrrole groups and the pyridyl legs. Hence, these possible differences might explain the asymmetric distribution of the resonance at 100 mV across some molecules. Unfortunately, no Δf maps were recorded on this specific island, such that the identification of the molecular structure is not possible. The dI/dV maps recorded at negative bias voltages show a similar localization as for the previous structures, with its main contribution in the center of the molecule.

Moreover, in contrast to the previous structures of Fe-TPyP, no inelastic excitations of magnetic or vibrational nature can be observed on the annealed molecules (see fig. 3.31b). These differences can be explained by the formation of new bonds that alter the molecular orbitals. Therefore, both the magnetic properties and the vibrational modes are affected. Moreover, the flat adsorption geometry of the molecules increases the coupling with the substrate. The short lifetime of excited states hence leads to a quenching of inelastic signatures.

G. FeTPyP on Single-Layer MoS$_2$

In the previous sections, different adsorption structures of Fe-TPyP molecules were investigated on a Au(111) substrate. Depending on the preparation conditions, different structures emerged, with different electronic and magnetic properties. Moreover, depending on the energetic position and width of these electronic resonances with respect to the Fermi level, certain vibrational excitations were either observable in the $\mathrm{d}I/\mathrm{d}V$ spectra or smeared out for other structures. In this chapter, we want to investigate how the vibrational excitations of Fe-TPyP molecules are affected if the molecules adsorb on a decoupling layer of MoS$_2$, which is grown on the Au(111) substrate. Due to the decoupling layer, less overlap between the molecular orbitals and the surface can occur, and hence also the hybridization effects and lifetime broadening should be reduced. We thus expect to see narrow resonances that are higher in energy as compared to the Au(111) substrate, which, following the argument from above, should influence the intensity of the vibrational signals.

1. Preparation Conditions of Single-Layer MoS$_2$ on Au(111)

For the preparation, the general procedure described by S. Helveg, et al. [140] with some modifications in pressure and temperature was followed. To grow MoS$_2$ islands, molybdenum is evaporated for 40 to 80 minutes under H$_2$S atmosphere ($p = 1 \times 10^{-5}$ mbar) with the sample held at room temperature. After evaporation, the sample is annealed at 530 °C for 25 min still under H$_2$S atmosphere. Afterwards, the H$_2$S flow is stopped and the sample cooled down and transferred into the STM. In a second step, the Fe-TPyP molecules were evaporated onto the sample. Therefore, the sample had to be cooled down to below 150 K during evaporation, to assure that a part of the molecules stays on the MoS$_2$ substrate.

2. Properties of Single-Layer MoS$_2$

MoS$_2$ is a material from the family of transition-metal dichalcogenides (TMDC). These materials have gained a lot of attention in the scientific community in the last years, as they exhibit similar properties as graphene while they simultaneously exhibit a sizeable band gap [141]. Whereas bulk MoS$_2$ has an indirect band gap with the valence-band maximum (VBM) at the Γ point and the conduction-band minimum (CBM) between the Γ and K points, single-layer MoS$_2$ has both the VBM and the CBM at

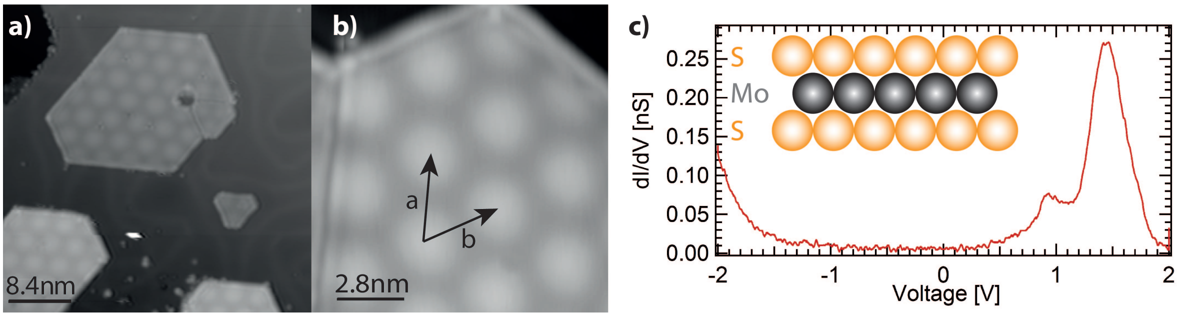

Figure 3.32. Single layer MoS$_2$ on Au(111). **a)** Topography showing the growth of multiple MoS$_2$ islands of different sizes on a Au(111) substrate. **b)** Close-up view of a MoS$_2$ island, showing the Moiré superstructure with its unit vectors $\vec{a}$ and $\vec{b}$. **c)** Characteristic spectrum on MoS$_2$, showing the band gap of approx. 1.9 V. Inset: Schematics of the triple-layer MoS$_2$ structure.

the K point [141].

The MoS_2 monolayer consists of a layer of molybdenum atoms, sandwiched between two sulfur layers (see inset of fig. 3.32c), which are bond via covalent ionic bonds [142, 143]. The topographic image of MoS_2 islands on Au(111) is shown in fig. 3.32a. Several islands of different sizes and apparent heights can be observed. The islands in the lower part of the image are about 2.3 Å higher than the islands in the upper part, which corresponds to an extra layer of Au underneath the MoS_2 island. The growth of these elevated islands goes along with a lifting of the herringbone reconstruction of the underlying Au(111) substrate [144]. Due to a lattice mismatch between the MoS_2 and the underlying Au(111) substrate, a Moiré superstructure with a periodicity of 3.3 nm emerges on all islands [142]. Moreover, the brighter stripe parallel to the edges of the island indicates one-dimensional metallic edge states that are characteristic for single-layer MoS_2 [145, 146]. The topmost island in fig. 3.32a has a darker depression on the right side of the islands, corresponding to Au vacancies underneath the intact MoS_2 layer [147]. On the lower edge of this defect, there is an additional line defect that arises from the structural domain boundary of differently oriented MoS_2 islands that meet during the growth process [144]. The different occuring defects of MoS_2 have been studied by W. Zhou, et al. [148]. Next to the described pit defect, which does not change the electronic structure of the intact MoS_2, there are defects in the MoS2 layer caused by molybdenum or sulfur vacancies in the internal structure of the MoS2, which induce a change of the electronic structure.

A typical $\mathrm{d}I/\mathrm{d}V$ spectrum on a MoS_2 island is shown in fig. 3.32c. It shows the aforementioned characteristic region within the band gap between −1 V and 0.5 V, with a very low conductance. At above 0.5 V, two peaks are visible, which correspond to single layer MoS_2 bands [141]. Spectra on MoS_2 are always taken as a reference spectrum to probe the quality of the tip.

3. Vibrational- and Spin Excitations of FeTPyP on Single-Layer MoS_2

Figure 3.33a shows the adsorption of Fe-TPyP molecules on MoS_2 islands and on Au(111). Due to the low temperatures during evaporation, the majority of the molecules is found isolated on the surface and with almost equal probability on MoS_2 and Au. On the first glance, the Fe-TPyP molecules seem to still exhibit a fourfold symmetry. Upon taking a closer look, however, also here the symmetry of the Fe-TPyP molecules is broken by the evolution of a saddle-shape deformation of the macrocycle. Due to the decoupling properties of the MoS_2 layer, spectroscopy on single molecules has proven to be difficult even at low bias voltages and small currents, as the molecules tend to desorb from the substrate and stick to the tip. Therefore, small islands of Fe-TPyP molecules, as shown in the inset of fig. 3.33a, were preferred for spectroscopy.

In fig. 3.33b, a typical $\mathrm{d}I/\mathrm{d}V$ spectrum in the range of −200 mV to 200 mV is shown on one of these small islands of Fe-TPyP molecules. It exhibits three pairs of symmetric steps around E_F: one pair of steps at ±11 mV, one pair at ±107 mV and one at ±135 mV. Morover, there is one shoulder at −60 mV, which is only observed at negative bias voltages. On MoS_2, all molecules show the same spectral features, independent of their position on the Moiré superstructure. By comparing to the findings of sec. B, sec. C and sec. D, the features in the $\mathrm{d}I/\mathrm{d}V$ spectrum can be identified. The steps at around ±11 mV are assigned to result from inelastic spin excitations. Due to the lower coupling strength between the molecule and the surface, it seems reasonable to assume a higher dihedral angle, with the pyridyl groups being strongly rotated. This would correspond to a flatter macrocycle. As described in sec. E, a flatter macrocycle favours an intermediate spin state. Therefore, the innermost step in the $\mathrm{d}I/\mathrm{d}V$ signal is assigned to a spin excitation from the $|0\rangle$ ground state of the $S = 1$ multiplett, to the degenerate $|\pm 1\rangle$ excited state. The corresponding axial anisotropy parameter was determined as D=11.2 meV with a vanishing transverse anisotropy E.

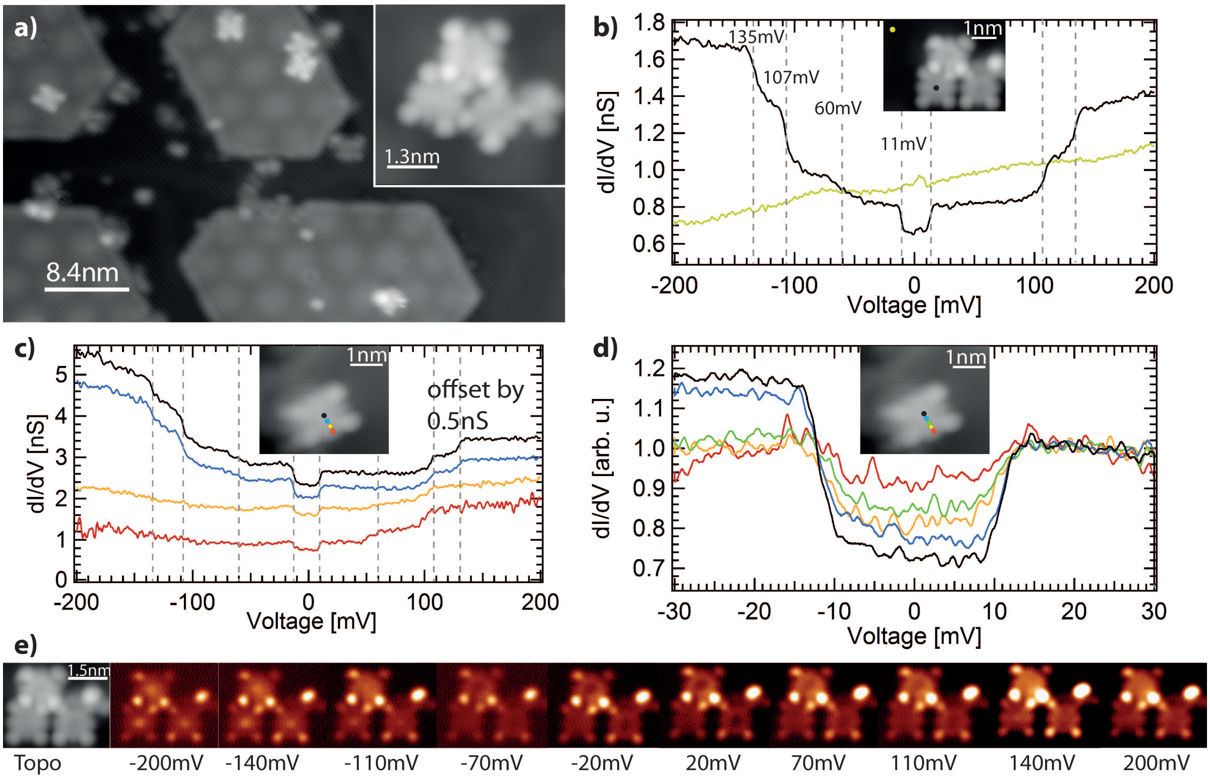

Figure 3.33. Fe-TPyP molecules on MoS$_2$ on Au(111). **a)** STM topography showing mostly single Fe-TPyP molecules on both MoS$_2$ and Au. Inset: in rare occasion, small islands of Fe-TPyP are formed. **b)** dI/dV spectrum recorded in the center of an Fe-TPyP molecule on MoS$_2$. Symmetric steps at ±11 mV, ±107 mV and ±135 mV can be observed, as well as a step at −60 mV. **c)** Spectra recorded along an Fe-TPyP molecule, showing the disappearance of the steps at higher negative bias voltages on the ligand of the molecule. **d)** Delocalization of spin excitations over the molecule. **e)** Constant-height dI/dV maps recorded on a small Fe-TPyP island on MoS$_2$. At negative bias voltages, a high differential conductance can be observed in the center of the molecule. For the recording of the maps, the tip was retracted by 1.5 Å from the setpoint of 10 pA, 200 mV with $V_{\mathrm{mod}} = 5$ mV.

The steps at higher energies on the other hand, can not be explained with magnetic excitations, but only by the excitations of vibrational degrees of freedom. In sec. C.3, we compared the steps positions in the dI/dV spectra to HREELS measurements performed on the Fe-TPyP molecuels on Au(111) and cross-checked with DFT calculations. For the distorted structure (sec. C) and the disordered adatom-mediated structure (sec. D), we identified vibrations in the dI/dV signal in the energy range between 19 meV to 115 meV. The lowest vibrational modes that were obervable on Au(111) can not be seen on MoS$_2$. Only the vibrations at 60 mV and 107 mV are observable on both structures (see tab. III). Instead, the Fe-TPyP molecules on MoS$_2$ exhibit another C−H wagging mode at 135 mV.

Figure 3.33c shows the evolution of the dI/dV spectra across the upper pyrrole group of an Fe-TPyP molecule. As in the case of Au(111), the spectra on the upper pyrrole group exhibit an asymmetric shape, with a vanishing step intensity of the vibrational modes at negative bias voltages. The intensity at positive bias voltages, in contrast, remains unchanged across the molecule. This behaviour is also observable in the dI/dV maps in fig. 3.33e. On the Au(111) surface, the asymmetric lineshape of the dI/dV signal on the ligand of the molecule and the intensity of the inelastic excitations was explained in terms of two different tunneling pathes through the molecule: the d$_{z^2}$ orbital in the center, which mainly contributes to transport at negative bias voltages and the d$_{yz}$ state on the lig-

Table III. Assignment of the peaks in the HREELS spectra to steps in the $\mathrm{d}I/\mathrm{d}V$ signal on MoS_2 and Au(111) (disordered adatom-mediated structure), together with their calculated energy from DFT calculations (b3pw91/genecp) for dihedral angles of 25° and 60°, respectively. All energies are given in meV. The symbols ν, δ, γ and τ denote stretching, in-plane wagging, out-of-plane wagging and torsion, respectively.

HREELS	**IETS (Au)**	**IETS (MoS_2)**	**DFT (25°/60°)**	**Mode**
16	21	-	23 / 18	symmetric buckling / asymmetric buckling
32	30.5	-	30 / 30	ν(Fe-N), Fe-tapping / ν(Pyrrole)
45	-	-	-	-
60	54	60	59 / 59	N-tapping / τ(Pyrrole)
72	69	-	-	-
78	-	-	82 / 83	δ(C-C-C) / γ(C-H)
88	90	-	92 / 93	γ(C-H) / δ(C-H)
100	104	107	109 / 108	γ(C-H) / δ(C-H)
122	115	-	114 / 115	δ(C-N / δ(C-H))
135	-	135	137 / 137	δ(C-H)
151	-	-	-	-

and, which predominantly contributed at positive bias voltages. In fig. 3.33c, the corresponding d orbitals, which were observable as peaks in the $\mathrm{d}I/\mathrm{d}V$ spectra in case of measurements on Au(111), can not be identified so easily. Instead, spectra in a broader energy range are necessary to observe possible resonances. A $\mathrm{d}I/\mathrm{d}V$ spectrum in the range of ±400 mV is depicted in fig. 3.34c in black, together with the corresponding spectrum on the ligand in red. A broad resonance can be observed at around -190 mV, which is only observable in the center of the Fe-TPyP molecule. This peak might correspond to the d_{z^2} state. On the positve bias side, however no such peak can be determined. The broad onset at positive bias voltages corresponds to a peak situated at 500 mV to 800 mV, depending on the molecule, which will be discussed in the next paragraph. As the varying energy position of this peak between different molecules did not affect the spectral shape around the Fermi level, it seems unlikely that it corresponds to the d_{yz} hybrid state, whose energetic position is expected to strongly influence the excitation of vibrations.

One possible explanation for the absence of the d_{yz} hybrid orbital in the $\mathrm{d}I/\mathrm{d}V$ spectra might be a weaker mixing between the d_{yz} Fe orbital and the ligand states. As the pure d_{yz} orbital typically couples rather weakly to the tip due the non-matching symmetries, the d_{yz} resonance would not be visible in the $\mathrm{d}I/\mathrm{d}V$ spectra. Moreover, a reduced mixing would also lead to a reduced PDOS on the pyrrole groups, which would also explain the low intensity of the spin excitations in the spectra (see fig. 3.33d).

To explain the observation of only higher-lying vibrational modes on MoS_2, the energy position of the corresponding resonances, which take part in the transport process has to be considered. As discussed in sec. E, the excitation cross-section of vibrations strongly depends on the proximity to an electronic state. As the lower coupling to the substrate shifts the molecular states to higher energies, also the vibrational excitations at higher energies become more likely. The lowest vibrational modes, on the other hand, become less probable, as the excitation cross section of the virtual excitations is inversely proportional to the energy difference between the vibrational modes and the corresponding electronic resonance. Thus, the decoupling nature of MoS_2 might account for the observation of the higher-energetic vibrational modes.

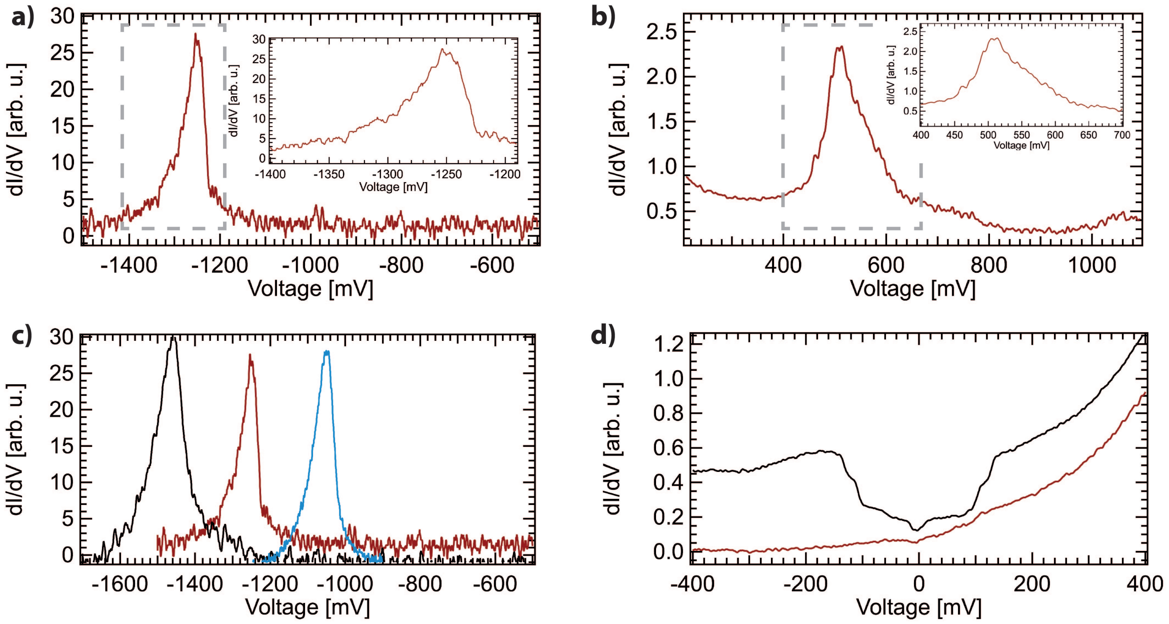

Figure 3.34. Electronic resonances of Fe-TPyP on MoS$_2$. **a,b)** HOMO and LUMO resonance of Fe-TPyP. The inset shows the asymmetric linshape of the peaks, with a sharp onset at lower absolute energies and a shoulder at higher absolute energies. **c)** Scattering of the HOMO position by several hundreds of meV for different molecules. The spectra were recorded in the constant-current mode at a) 5 pA and b) 100 pA with $V_{\mathrm{mod}} = 3$ mV and c) 5 pA to 10 pA with $V_{\mathrm{mod}} = 1$ mV to 3 mV. **d)** Constant-height spectra in the center (black) and on the ligand (red). Feedback opened at 10 pA 200 mV with $V_{\mathrm{mod}} = 3$ mV.

Vibronic Resonances on MoS$_2$

As just discussed for the vibrational excitations, the hybridization effects of metal substrates play an important role for the energetic position and shape of the molecular resonances. Screening from the substrate leads to shifting of the orbitals towards the Fermi level and the reduced lifetime induces a broadening of the corresponding peaks. The decoupling properties of MoS$_2$, on the other hand, can reduce these effects. Therefore, it is especially interesting to compare the frontier molecular orbitals of Fe-TPyP on Au(111) to the ones on MoS$_2$.

Due to the weak interaction of the Fe-TPyP molecules with the underlying substrate, it was difficult record the HOMO and LUMO resonances of the Fe-TPyP molecules. In the majority of cases, the molecule has switched position during the recording of the spectra, which mostly went along with a shift of the electronic resonances in the order of several 100 meV. Also between different molecules, the position of the HOMO and LUMO was different, as shown in fig. 3.34c for the measurement of the HOMO resonance on three different molecules. Nontheless, the average position of the HOMO of approx. −1.3 V is in agreement with the observed HOMO resonance on Au(111), whereas the LUMO resonance seems to have shifted from above 1 V to around 500 mV to 800 mV (only one spectrum shown in fig. 3.34b). The stronger shift of the energy position of the LUMO is in accordance to the observations on Au(111), where mostly the LUMO position experienced variations for the different structures. Despite the changing energetic positions of the HOMO and LUMO resonances in consecutive measurements, all of the recorded spectra show a similar line shape, with a rather sharp onset at small absolute energies and a slower fall-off towards larger absolute energies. Two exemplary spectra are depicted in fig. 3.34a,b for the HOMO and LUMO resonances at −1250 meV and 550 meV, respectively. The inset shows the described asymmetric peak shape. This asymmetric shape resembles the spectra of vibronic resonances, where an electronic peak is followed by a set of equidistant vibrational excitations. On metal surfaces, the spectra smear our by the short lifetimes of the corresponding vibronic states, with the damping occurring via the excitation of electron-hole pairs in the substrate by the long-range dipole field of the vibrating molecule [149, 150]. Therefore, the vibrational traces can no longer be identified, but rather vanish in the broad background and induce even larger broadenings [151, 152]. For other systems [45, 134, 153], the vibronic excitations were observable as distinct peaks in the $\mathrm{d}I/\mathrm{d}V$ signal, which made their identification unambiguous. For the measurements of Fe-TPyP on MoS$_2$, however, the rather small currents required to record the spectra do not allow for the necessary resolution to identify the underlying peaks in the shoulder of the resonance, despite the decoupling nature of the MoS$_2$ substrate. Therefore, unfortunately, it is not possible to compare the vibrational energies from the vibronic resonances to the step energies in the $\mathrm{d}I/\mathrm{d}V$ signal.

H. Summary and Conclusions

In this chapter, different arrangements of Fe-5,10,15,20-tetra-pyridyl-porphyrin (Fe-TPyP) molecules were investigated on a Au(111) substrate and on a sinlge layer of MoS$_2$. On Au(111), three different adsorption structures of Fe-TPyP could be observed that emerged under the same preparation conditions. By nc-AFM we showed that the molecules in one of the arrangements exhibited intramolecular distortions, which acted on the ligand field of the central Fe atom. Therefore, distinct magnetic properties were observed on the molecules in the different arrangements. Moreover, the different adsorption geometries also influenced the intensity of vibrational excitation that were very pronounced in some structures and absent in others. This difference in intensity has been explained by shifts of the electronic resonances around the Fermi level, which enhanced the excitation cross section for some of the arrangements.

The molecular structure was then modified by post-annealing the sample to 300 °C. Upon annealing, the breaking of some C-H bonds in the organic macrocycle enabled the formation of new intramolecular C-C bonds, such that the molecules adapt a flat structure. For these molecules, no signs of magnetic or vibrational excitations were found in the spectra and also the electronic resonances were shifted in comparison to the spectra on the other Fe-TPyP molecules.

Finally, the Fe-TPyP molecules were deposited on a decoupling MoS$_2$ layer, which was grown on the Au(111) surface. Here, spin- and vibrational excitations were identified in the $\mathrm{d}I/\mathrm{d}V$ spectra at energies that matched with the previous findings on Au(111). However, the vibrational modes at higher energies were more pronounced than on Au(111), which can be related to an upshifting of the electronic resonances and therefore different co-tunneling probabilities due to the decoupling properties of the MoS$_2$ layer.

CHAPTER IV

Shot Noise Measurements on Metallic Surfaces

"The noise is the signal" — There is no phrase more suited to express the idea of shot-noise measurements than the famous sentence by R. Landauer [154]. This approach, however, at first glance seems counterintuitive, as in scanning tunneling miscroscopy, typically only the DC component of the current signal is evaluated, *i.e.*, the mean current that is flowing under application of a certain bias voltage. Not only the STM topographies reflect the average current, but also scanning tunneling spectroscopy (STS) solely bases on the average current values. The average current value can be considered as the first-order moment of the probability distribution that describes the transmission of the electrons through the tunneling barrier (see fig. 4.1a). However, also the higher-order moments of the probability distribution contain important information. The second-order component, *i.e.*, the deviation of the measurement points from the mean of the distribution, is called variance. It is sketched in fig. 4.1a. In case of electron transport, it is often referred to as shot noise, and it contains complementary information about the electron-electron and electron-phonon interaction processes during the tunneling events. As these are not regarded in the average conductance value, a whole new field of physics can be accessed when analyzing the noise of the signal.

The importance of the variance to describe a signal can best be understood when comparing different signals. In fig. 4.1b and c, two exemplary random signals are depicted as a function of time. Both of these time traces are characterized by the same mean intensity of 100, however, their devia-

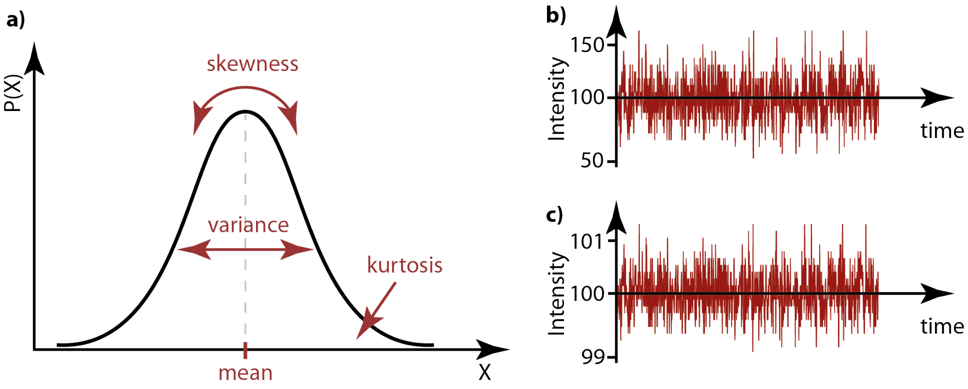

Figure 4.1. a) Different parameters characterizing a probability density distribution. The mean is the first order moment of the probability distribution, whereas the higher-order moments are the variance, the skewness, *i.e.*, the asymmetry of the curve, and the kurtosis, which characterizes the tails of the peak. **b,c)** Sketch of random signals as a function of time. Whereas the mean value of both time traces is the same, their variance, *i.e.*, their deviation from the mean value, is different.

tion from the mean value differs by an order of magnitude. If these were current traces, their shot-noise level would be very different, which would potentially give important information about internal interactions in the investigated system. Hence, it is sometimes not sufficient to look at the mean values of a measurement, but one also has to consider higher-order moments of a signal.

In the scientific transport community, shot-noise measurements have been performed already more than 20 years ago on many mesoscopic systems [155]. The first measurements showing the suppression of noise by highly transmitting channels were performed in 1995 and 1996 by M. Reznikov, et al. and A. Kumar, et al. for quantum point contacts [156, 157]. In the following years, a variety of physical phenomena has been studied, ranging from the observation of fractional charges in the quantum hall effect in 1997 [158, 159] to the study of Cooper-pair transport in superconductors with their corresponding quasi-particle charge of $2e$ in 2000 [160]. Shortly after, also the electron correlations of the Kondo regime gained more attention, which stimulated numerous shot-noise studies [161–163]. More recently, shot-noise measurements on a quantum dot have shown to be able to make a distinction between the SU(2) and SU(4) Kondo effect [164].

Besides the measurements on mesoscopic structures, the atomic scale transport properties have been studied for a variety of systems by means of mechanically controlled break junctions (MCBJ). Not only the shot-noise characteristics of normal metal contacts like Au and Ag have been examined [165, 166], but also more complex investigations were made, *e.g.*, on Al in the superconducting and normal state [167]. In 1998, E. Scheer, et al. combined STM and MCBJ measurements to relate the number of conduction channels in point contacts to the valence and orbital structure of the contacted atoms [168]. In 1999, H.E. van den Brom, et al. demonstrated the shot-noise suppression for atom-sized metallic Ag and Al contacts [169]. Additionally in 2013, first attempts were made to detect spin-polarized transport through Pt chains with shot noise [166], which however showed no experimental evidence. Furthermore, shot-noise measurements came into focus for IETS studies, after MCBJ measurements were used to detect vibration mode scattering in Au nanowires [170] and other atomic and molecular systems [165, 171–173].

There are also a handful of measurements on atomic contacts that were performed with the STM [174, 175], however, due to the requirements concerning the contact stability and large statistics to ensure reproducibility, much less research has been performed on this topic with STM compared to MCBJ. In a recent publication, the group of R. Berndt showed the suppression of shot noise due to spin-polarized transport through single Fe and Co atoms on a Au(111) surface for the first time [24, 176].

Despite the number of publications regarding shot noise, there are still a lot of open questions about electron correlations in single atoms and molecules. Therefore, in this chapter, the different working steps towards the implementation and testing of a shot-noise amplifier setup will be described. At first, the theoretical aspects of shot noise are introduced. Afterwards, the technical requirements of the high-frequency setup will elaborated. As the corresponding signals are extremely small (in the order of $100\,\mathrm{fA}/\sqrt{\mathrm{Hz}}$), the establishing of successful measurement conditions has proven to be rather challenging. Therefore, in the second part, the modifications that were necessary to obtain a running shot-noise setup will be depicted. Finally, to characterize the shot-noise setup, measurements were performed on Au adatoms, which are created by a Au-coated tip on a Au(111) substrate. As this system is well understood in terms of its transport properties [24, 170, 176], it is a suitable choice as a reference system.

A. Basic Concepts of Noise and Shot Noise

Before we go into detail about shot noise and other sources of noise, it is necessary to define how noise can be characterized. The most simple way to describe noise is by determining the Fourier transform of its time trace, referred to as the noise spectral density. In most cases, the square of the Fourier transform is considered, which is then called noise power spectral density. However, for some stochastic processes, the Fourier transform of the signal does not exist. Instead, the Fourier transform of the autocorrelation $\Phi_{\mathrm{yy}}(t)$ of the real time signal is then regarded, where the autocorrelation characterizes the correlation of a signal with itself after a time delay τ. For an arbitrary signal $y(t)$, the autocorrelation reads

$$\Phi_{\mathrm{yy}}(\tau) = \lim_{T\to\infty} \frac{1}{2T} \int_{-T}^{T} y(t)y(t+\tau)\mathrm{d}t. \tag{4.1}$$

The power spectral density of the signal can then be determined according to the Wiener-Khinchin theorem [177, 178] by the Fourier transform of the autocorrelation function

$$S_{\mathrm{yy}}(\omega) = \frac{1}{2\pi} \int_{-\infty}^{\infty} \Phi_{\mathrm{yy}}(\tau)e^{-i\omega t}\mathrm{d}t. \tag{4.2}$$

For functions whose Fourier transform is defined, which is generally the case for real-world signals, the calculation of the squared magnitude of the Fourier transform and the Fourier transform of the autocorrelation give the same result.

The power spectral density is typically expressed in units of $\mathrm{A}^2\,\mathrm{Hz}^{-1}$ or $\mathrm{V}^2\,\mathrm{Hz}^{-1}$, where the normalization to 1 Hz allows to give a consistent value of the noise signal, independent of the band width that is used during the measurement.

1. General Aspects of Shot Noise

The current flow in any conductor is a stochastic process, with the time between electrons fluctuating around an average value, *i.e.*, the DC current. The level of this fluctuation, known as the current noise, depends on several noise components, which will be elaborated in sec. 3 in more detail. The two most

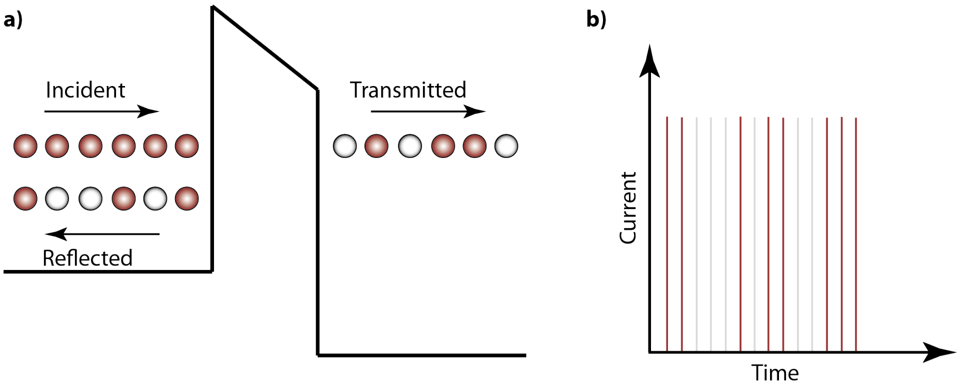

Figure 4.2. Sketch of the origin of shot noise. **a)** A regular beam of incident electrons splits into a reflected and a transmitted component, upon scattering at a finite potential barrier. **b)** The resulting current shows random fluctuations. Figure adapted from [179].

fundamental noise sources are Johnson-Nyquist noise, also known as thermal noise, and the shot noise. The thermal noise is an equilibrium noise, which arises from the random thermal motion of the electrons inside a conductor and is independent of any applied bias voltage. The second component, the shot noise, on the contrary, is transport related and arises due to the random outcome of the scattering processes of the electrons. This is schematically depicted in fig. 4.2a for a set of electrons scattering at a potential barrier. In case of a fully transmitting ($\tau = 1$) or fully closed ($\tau = 0$) barrier, all the electrons are transmitted or reflected, respectively. Hence, the resulting signal would show no current fluctuations. In case of a finite scattering probability, the beam of regularly incoming electron is split into a transmitted and a reflected component. As the scattering happens independently of the previous events, the transmitted electron beam, and hence the flowing current, will exhibit high current fluctuations, referred to as shot noise (see fig. 4.2b).

Since the first theoretical description of shot noise formulated by G. B. Lesovik and L. S. Levitov [180], a lot of effort has been made to get a better understanding of the non-equilibrium processes. One approach, the Landauer-Büttiker approach describes the transport in a quantum-mechanical scattering picture. Despite the fact that this description does not account for inelastic scattering, it is a suitable choice to understand the basic mechanism, as the suppression of noise for fully open and fully closed channels is captured.

2. Landauer-Büttiker Description of Shot Noise

The Landauer-Büttiker approach or Landauer approach is a scattering approach that relates the transport properties of a system to its scattering properties [181]. In this formalism, a quantum conductor is described as a scattering region, connected to two perfectly transmitting leads, as depicted in fig. 4.3. The leads act as electron reservoirs that obey the Fermi distribution and they constitute perfect sinks for the incoming electrons, independent of their respective energy. Due to the symmetry of the setup, the electron propagation can be separated into components perpendicular and parallel to the leads, referred to as transverse and longitudinal channels.

To describe the transport, the second-quantization formalism is used, which expresses the creation and annihilation of incoming electrons in the left lead in the transport channel τ_i by the operators $\hat{a}^\dagger_{\mathrm{L}n}$ and $\hat{a}_{\mathrm{L}n}$ and the outgoing electrons by $\hat{b}^\dagger_{\mathrm{L}n}$ and $\hat{b}_{\mathrm{L}n}$, respectively. Correspondingly, the

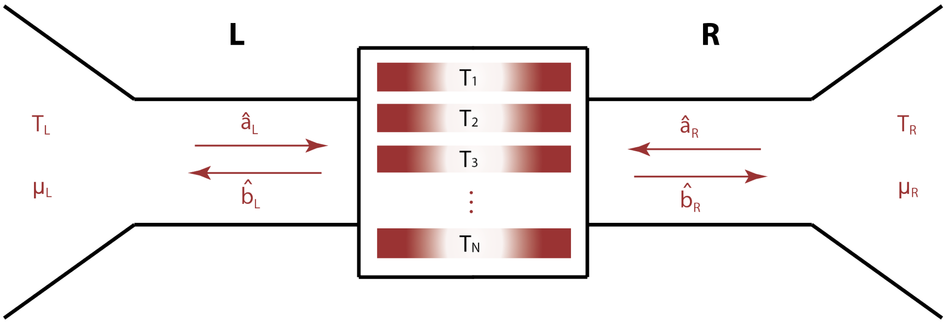

Figure 4.3. Schematics of the transport through a two-terminal conductor with a central scattering region. Several transport channels τ_i exist, which are connected with incoming states $\hat{a}_{\mathrm{R,L}}$ and outgoing states $\hat{b}_{\mathrm{R,L}}$ from the right and left lead, respectively. $T_{\mathrm{R,L}}$ and $\mu_{\mathrm{R,L}}$ denote the temperature and chemical potential in the right and left lead, respectively.

operators $\hat{a}^{\dagger}_{\mathrm{Rn}}$, $\hat{a}_{\mathrm{Rn}}$, $\hat{b}^{\dagger}_{\mathrm{Rn}}$ and $\hat{b}_{\mathrm{Rn}}$ account for the creation and annihilation of incoming and outgoing electrons in the right lead. The incoming states can be related to the outgoing states via a scattering matrix[1] $\mathscr{M}$

$$\begin{pmatrix} \hat{b}_{\mathrm{L1}} \\ \vdots \\ \hat{b}_{\mathrm{LN}} \\ \hat{b}_{\mathrm{R1}} \\ \vdots \\ \hat{b}_{\mathrm{RN}} \end{pmatrix} = \mathscr{M} \begin{pmatrix} \hat{a}_{\mathrm{L1}} \\ \vdots \\ \hat{a}_{\mathrm{LN}} \\ \hat{a}_{\mathrm{R1}} \\ \vdots \\ \hat{a}_{\mathrm{RN}} \end{pmatrix}. \tag{4.3}$$

The scattering matrix $\mathscr{M}$ in a reduced form is given by

$$\mathscr{M} = \begin{pmatrix} r_{\mathrm{N\times N}} & t'_{\mathrm{N\times N}} \\ t_{\mathrm{N\times N}} & r'_{\mathrm{N\times N}} \end{pmatrix}, \tag{4.4}$$

with the N×N on-diagonal matrices $r_{\mathrm{N\times N}}$ and $r'_{\mathrm{N\times N}}$ describing the reflected electron wave for the left and right leads, respectively. The off-diagonal blocks $t_{\mathrm{N\times N}}$ and $t'_{\mathrm{N\times N}}$, in contrast, account for the transmission of electrons through the central sample region. Due to flux conservation, the scattering matrix is unitary. Moreover, as in the presence of time-reversal symmetry $\mathscr{M}$ is symmetric, a diagonalization of the matrix is possible, allowing us to treat all transport channels τ_i individually. The total current is then a sum over all the contributions of the individual channels.

The resulting current[2] that flows in one quantum channel is the difference between the numbers of the incoming electrons and the outgoing electrons. Hence, the current in the lead $\alpha = \{\mathrm{R,L}\}$ in the transport channel n can be expressed as [155]

$$\hat{I}_{\alpha\mathrm{n}}(t) = \frac{2e}{2\pi\hbar}\sum_{n}\int \mathrm{d}E\,\mathrm{d}E'\, e^{i(E-E')t/\hbar}\left(\hat{a}^{\dagger}_{\alpha\mathrm{n}}(E)\hat{a}_{\alpha\mathrm{n}}(E') - \hat{b}^{\dagger}_{\alpha\mathrm{n}}(E)\hat{b}_{\alpha\mathrm{n}}(E')\right), \tag{4.5}$$

with $\hat{n}^{+}_{\alpha\mathrm{n}}(E) = \hat{a}^{\dagger}_{\alpha\mathrm{n}}(E)\hat{a}_{\alpha\mathrm{n}}(E)$ being the number operator, which determines the number of incident electrons at lead α. Accordingly, $\hat{n}^{-}_{\alpha\mathrm{n}}(E) = \hat{b}^{\dagger}_{\alpha\mathrm{n}}(E)\hat{b}_{\alpha\mathrm{n}}(E)$ accounts for the occupation number of the outgoing electrons. By making use of the scattering matrix $\mathscr{M}$ in eq. 4.3, we can express the current in terms of the incoming electrons $\hat{a}$ and $\hat{a}^{\dagger}$ only. For simplicity, only the region of the left lead is considered here

$$\hat{I}_{\mathrm{L}}(t) = \frac{2e}{2\pi\hbar}\sum_{\alpha\beta}\sum_{m,n}\int \mathrm{d}E\,\mathrm{d}E'\, e^{i(E-E')t/\hbar}\left(\hat{a}^{\dagger}_{\alpha\mathrm{m}}(E)A^{mn}_{\alpha\beta}(L;E,E')\hat{a}_{\beta\mathrm{n}}(E')\right), \tag{4.6}$$

with the matrix $A^{mn}_{\alpha\beta}(L;E,E')$ defined as $A^{mn}_{\alpha\beta}(L;E,E') = \delta_{mn}\delta_{\alpha L}\delta_{\beta L} - \sum_k \mathscr{M}^{\dagger}_{L\alpha;mk}(E)\mathscr{M}_{L\beta;kn}(E')$. The element $\mathscr{M}_{L\alpha;mk}(E)$ relates the operator $\hat{b}_{Lm}(E)$ of the outgoing state to $\hat{a}_{\alpha k}(E)$ of the incoming state, with α and β corresponding to the reservoirs, which can take the values L and R.

---

[1] For simplicity, the same dimensionality N is assumed for left and right leads. In the more general case of dimension N in the left and M in the right lead, the scattering matrices in eq. 4.4 have to be adjusted to $r_{\mathrm{N\times N}}$, $t'_{\mathrm{N\times M}}$, $t_{\mathrm{M\times N}}$ and $r'_{\mathrm{M\times M}}$.

[2] In this derivation, a factor of 2 accounting for spin-degenerate transport of electrons is already considered in the formulas.

Determination of the Average Current

From eq. 4.6, the average current $\langle I_\mathrm{L}\rangle$ can be derived. In thermal equilibrium, the statistical average of the product of the creation and annihilation operators can be expressed as

$$\langle \hat{a}^\dagger_{\alpha\mathrm{m}}(E)\hat{a}_{\beta\mathrm{n}}(E')\rangle = \delta_{\alpha\beta}\delta_{mn}\delta(E-E')f_\alpha(E), \tag{4.7}$$

with $f_\alpha(E)$ denoting the Fermi-Dirac distribution function. From the unitarity of the scattering matrix $\mathscr{M}$, one can deduce the relation

$$1-\sum_{mm}\mathscr{M}^\dagger_{LL;kk}\mathscr{M}_{LL;kk} = 1-\operatorname{Tr}\left[r^\dagger r\right] = \operatorname{Tr}\left[t^\dagger t\right]. \tag{4.8}$$

Combining eq. 4.8 with eq. 4.6 and eq. 4.7 leads to the expression

$$\langle I_\mathrm{L}\rangle = \frac{2e}{2\pi\hbar}\int \mathrm{d}E\ \operatorname{Tr}\left[t^\dagger(E)t(E)\right]\left[f_\mathrm{L}(E)-f_\mathrm{R}(E)\right], \tag{4.9}$$

with the matrix t corresponding to the off-diagonal elements of the scattering matrix $\mathscr{M}$ (see eq. 4.4). Neglecting the energy dependence of $t(E)$ on the scale of $k_\mathrm{B}T$ and eV, the expression can be simplified to

$$\langle I_\mathrm{L}\rangle = \frac{2e}{2\pi\hbar}\sum_{i=1}^{N}\operatorname{Tr}\left[t^\dagger t\right]\int \mathrm{d}E\left[f_\mathrm{L}(E)-f_\mathrm{R}(E)\right]. \tag{4.10}$$

For small temperatures and applied bias voltages, a conductance of

$$G = \frac{2e^2}{h}\sum_{i=1}^{N}\operatorname{Tr}\left[t^\dagger t\right] \tag{4.11}$$

can be obtained. To get to a more simplified expression for the conductance, the matrix $t^\dagger t$ can be diagonalized. Its eigen values $\tau_\mathrm{i}(E)$ correspond to the transmission probabilities of the eigen-channels. For the more general case of more than one conduction channel, the multi-channel generalization of the Landauer formula is obtained

$$G = \frac{2e^2}{h}\sum_{i=1}^{N}\tau_i. \tag{4.12}$$

The Landauer-Büttiker formalism hence expresses the total conductance G of a system as a superposition of the transmission probabilities τ_i of all channels of the system.

Calculation of the Current Fluctuations

Up to now, we have only considered the DC component of the current and conductance, respectively. However, we want to obtain an expression for the current fluctuations that occur due to the discreteness of charge. Following the Wiener-Khinchin theorem mentioned above, the noise power can be determined as the Fourier transform of the current-current autocorrelation function

$$S_\mathrm{I}(\omega) = 2\int_0^\infty \mathrm{d}t\, e^{i\omega t}\langle\delta I(t+t_0)\delta I(t)\rangle. \tag{4.13}$$

Using the relation $\delta\hat{I}_\alpha(t) = \hat{I}_\alpha(t) - \langle I_\alpha \rangle$, with $\langle I_\alpha \rangle$ denoting the average current, the current fluctuations can be expressed as

$$S_\mathrm{I}(\omega) = \frac{1}{2}\int_0^\infty \mathrm{d}t\, e^{i\omega t} \langle \delta\hat{I}_\alpha(t)\delta\hat{I}_\beta(0) + \delta\hat{I}_\beta(0)\delta\hat{I}_\alpha(t)\rangle. \qquad \mathbf{4.14}$$

Making use of the relation of eq. 4.6, $\delta\hat{I}(t)$ can be substituted by

$$\delta\hat{I}(t) = \frac{2e}{2\pi\hbar}\int \mathrm{d}E\mathrm{d}E' \sum_{\alpha\beta} A_{\alpha\beta}\left[\hat{a}_\alpha^\dagger(E)\hat{a}_\beta(E') - \langle \hat{a}_\alpha^\dagger(E)\hat{a}_\beta(E')\rangle\right] e^{i(E-E')t/\hbar}. \qquad \mathbf{4.15}$$

With this expression, the noise power yields [181]

$$S_\mathrm{I}(\omega) = \frac{2e^2}{h}\sum_{\alpha\beta}\int \mathrm{d}E A_{\alpha\beta}^2 \left[f_\alpha(E)\big(1 - f_\beta(E+\hbar\omega)\big) + f_\alpha(E+\hbar\omega)\big(1 - f_\beta(E)\big)\right]. \qquad \mathbf{4.16}$$

By considering only zero-frequency noise ($\omega \to 0$), the relation simplifies to

$$S_\mathrm{I} = \frac{2e^2}{h}\sum_{\alpha\beta}\int \mathrm{d}E A_{\alpha\beta}^2 \left[f_\alpha(E)\big(1 - f_\beta(E)\big) + f_\alpha(E)\big(1 - f_\beta(E)\big)\right]. \qquad \mathbf{4.17}$$

For the case of a two-terminal conductor, we get [155]

$$S_\mathrm{I} = \frac{2e^2}{h}\sum_{i=1}^{N}\int \mathrm{d}E \{\tau_i\left[f_\mathrm{L}\big(1-f_\mathrm{L}\big) + f_\mathrm{R}\big(1-f_\mathrm{R}\big)\right] + \tau_i[1-\tau_i]\big(f_\mathrm{L}-f_\mathrm{R}\big)^2\}, \qquad \mathbf{4.18}$$

by making use of the relation $A_{\alpha\beta}^{mn}(L;E,E') = \delta_{mn}\delta_{\alpha L}\delta_{\beta L} - \sum_k \mathcal{M}_{L\alpha;mk}^\dagger(E)\mathcal{M}_{L\beta;kn}(E')$. The first two terms in eq. 4.18 account for equilibrium noise, whereas the third term, which is second order in the distribution function, corresponds to the non-equlibrium shot noise. By neglecting the energy dependence of τ, the energy-dependent components in eq. 4.18 can be replaced by their values at the Fermi level. Under this assumption, the integration yields

$$S_\mathrm{I} = 2G_0 eV \coth\left(\frac{eV}{2k_\mathrm{B}T}\right)\sum_{i+1}^{N}\tau_i(1-\tau_i) + 4k_\mathrm{B}TG_0\sum_{i+1}^{N}\tau_i^2, \qquad \mathbf{4.19}$$

with G_0 denoting the quantum of conductance of $G_0 = \frac{2e^2}{h}$. This expression is known as the Lesovik-Levitov expression and gives a general equation for quantum noise. It is a complex function that depends on temperature and applied bias voltage and can no longer be easily devided into shot noise and thermal noise components. However, in the limit of small bias voltages $eV \ll k_\mathrm{B}T$, the noise is given by

$$S_\mathrm{I} = 4k_\mathrm{B}TG, \qquad \mathbf{4.20}$$

which corresponds to the thermal noise, whose characteristics will be described in more detail below. From the formula, on can see that the thermal noise does only depend on the conductance G and the electron temperature. In the opposite case of zero temperature and finite bias voltages, the noise is given by

$$S_\mathrm{I} = 2eG_0V\sum_{i=1}^{N}\tau_i(1-\tau_i). \tag{4.21}$$

This shot noise level does not only depend on the conductance, but also on the transmittivity of each transmission channel τ_i. A similar conductance for two channel compositions does hence not automatically generate the same noise level, as can be seen in a short example: both channel compositions $\tau_1 = 0.8, \tau_2 = 0.2$ and $\tau_1 = 0.5, \tau_2 = 0.5$ correspond to the same total conductance $G = 1G_0$, however they result in different shot noise levels of $S_\mathrm{I} = 2eG_0V \times 0.16$ and $S_\mathrm{I} = 2eG_0V \times 0.25$, respectively.

For the limit of $\tau_i \ll 1$ for all channels, the term $1-\tau_i \approx 1$ and the shot noise approaches its classical Poisson value

$$S_\mathrm{I} = 2eG_0V\sum_{i=1}^{N}\tau_i = 2eGV = 2eI, \tag{4.22}$$

which is also known as the full shot noise. Poisson statistics are typically used to describe events that are uncorrelated in time. Therefore, this approach only holds for small transmission probabilities, where the electrons are transmitted randomly and independently of each other. At higher transmission probabilities, the shot noise is suppressed with respect to its full value. The so-called Fano factor F is defined as the ratio between the actual shot noise and the Poisson noise. By comparing eq. 4.21 with eq. 4.22, the Fano factor F can be determined as

$$F = \frac{S_\mathrm{I}}{S_\mathrm{I,full}} = \frac{\sum_{i=1}^{N}\tau_i(1-\tau_i)}{\sum_{i=1}^{N}\tau_i}. \tag{4.23}$$

For electron transport, the Pauli principle is responsible for the suppression of shot noise. Two electrons with equal properties cannot tunnel into the same final state at the same time, which hence results in antibunching of electrons with identical spins. This leads to a reduction of the noise level, which explains why the noise power might be utilized to determine the degree of spin polarization of the electrons.

3. Additional Sources of Noise

Apart from the shot noise whose characteristics was explained in the previous part, any real physical system is exposed to other sources of noise. One fundamental contribution is the above mentioned thermal noise, however, there is also the so-called $1/f$ noise, which might predominate the signal at low measurement frequencies. Their origin as well as their frequency dependence will be described in the following.

Thermal Noise

The thermal noise or Johnson-Nyquist noise is an unavoidable source of noise at non-zero temperatures. It arises due to the thermal agitation of charge carriers inside electrical conductors. The resulting fluctuation of the occupation numbers induces current fluctuations, which are related to the

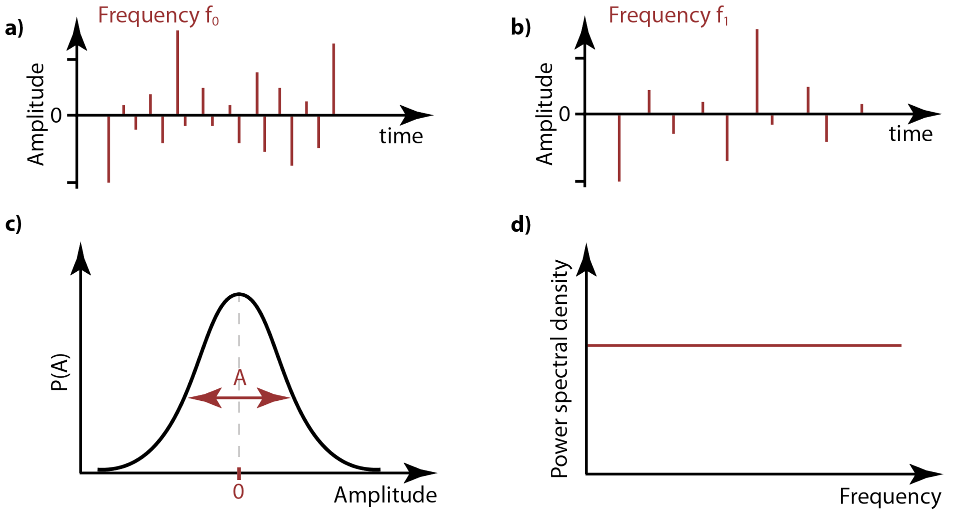

Figure 4.4. Origin of the spectral shape of white noise. **a)** Amplitude of a signal in time measured in regular intervals t_0, corresponding to a frequency f_0. The corresponding probability distribution of the amplitudes is depicted in **c)** with small amplitudes being more probable than large deviations. The FWHM of the distribution curve defines the noise amplitude A. **b)** The same probability distribution as in c) occurs for any arbitrarily chosen time interval t_1, which refers to a frequency f_1. **d)** As the noise amplitude A is the same for any frequency, the power spectral density as a function of frequency is constant.

conductance of the system via the fluctuation-dissipation theorem [182, 183]

$$S_\theta = 4 k_B T G, \tag{4.24}$$

with S_θ being the thermal noise, k_B the Boltzmann constant, T the temperature and G the system's conductance. Hence, the equilibrium current fluctuations S_θ contain the same information as can be obtained from investigations of the total conductance G of the system. This is in contrast to shot noise measurements, where internal electron-electron and electron-phonon interactions can only be determined from the current fluctuations. Thermal noise in ideal systems is white noise, *i.e.*, the power spectral density is constant throughout the entire frequency range. Hence, the trace of thermal noise in noise measurement would be a constant background level to the other noise sources, depending on the repective measurement temperature.

To understand the origin of a frequency-independent power spectral density, it is helpful to take a look at the probability distribution of the corresponding signal amplitude. Figure 4.4a shows the deviation of a signal from its mean amplitude 0 as a function of time. To evaluate the signal as a function of frequency, the deviation of the amplitude is evaluated at regular time intervals t_0, which correspond to a frequency f_0. The corresponding disribution of the amplitudes is shown in fig. 4.4c, and follows a Gaussian distribution, *i.e.*, small deviations from the mean value are more likely than large deviations. The FWHM of the amplitude distribution defines the noise amplitude A corresponding to the frequency f_0. In case of white noise, the very same Gaussian distribution with the same noise amplitude A is obtained when considering any other frequency of the signal, *i.e.*, by evaluating the amplitude deviation in any other time interval t_1, as shown in fig. 4.4b. Hence, as the noise amplitude is independent of the considered frequency, the power spectral density is constant, which is typically referred to as white noise.

$1/f$ -noise

Next to the thermal noise with its constant power spectral density, another noise source is the so-called $1/f$ noise, which shows a decaying noise amplitude with higher frequencies, proportional to $S_\mathrm{I} \sim 1/f^{\alpha}$. As visible light with this power spectrum appears pink, it is often referred to as pink noise. The first electronic $1/f$ noise was discovered in 1925 by J. B. Johnson [184] during the attempt to varify Schottky's theory of shot noise in vacuum tubes. There, he saw a deviation of the predicted constant noise level at low frequencies, which he termed flicker noise. Since then, $1/f$ noise was observed in the statistical fluctuations of many other systems, ranging from the fluctuation of human heart rates [185] to neuron activity in brains [186] up to intensity fluctuations in human voices [187]. However, almost a century after its discovery, the origin of pink noise is still not clear, and to date, there is no universal theory of $1/f$ noise. Therefore, even the most recent studies of $1/f$ noise in electronic devices tries to answer questions about the origin of pink noise, *e.g.*, if pink noise in graphene multilayers is a surface or volume effect [188].

As the amplitude of pink noise decreases with the frequency according to the relation $S_\mathrm{I} \sim 1/f^{\alpha}$, it vanishes in the thermal noise and amplifier noise background at higher frequencies. The corresponding frequency where $1/f$ noise vanishes in the noise floor is referred to as its corner frequency and can range from 10^2 Hz up to 10^6 Hz. On the other side of the spectrum at very low frequencies, no lower bound is known for pink noise in electronic devices. Even measurements in the range of 10^{-6} Hz, which took several weeks [189] did not show a plateau of the noise level. Therefore, the $1/f$ noise is not integrable, since the integral $\int_{-\infty}^{\infty} S(f)\mathrm{d}f = \infty$ diverges, as a result of the low frequency behaviour. However, this divergence violates Parsevals theorem, which states that the spectrum originating from any random process should be integrable. To date, the resulting paradoxon is still the focus of numerous studies [190–193].

Despite the lack of a universal theory of $1/f$ noise, there are concepts that explain the occurance of pink noise for each type of system indivually. For electronic compounds, it is widely accepted that the noise arises from intrinsic fluctuations of the resistance [194–196]. These fluctuations can have very different origins for the different materials. In semiconductors, for example, a thermally activated change of the number of charge carriers in the conductance and valence band might in some cases explain the occurance of pink noise. In metals, on the other hand, the thermal excitation of lattice defects might be the origin [197–199].

B. Technical Details of the Shot Noise Setup

The currents that typically flow in STM measurements are in the order of several pA to some nA. Since the average current value is already tiny, the detection of its fluctuation is technically extremely challenging. Moreover, as we have seen in sec. A.1, the existence of other noise sources such as $1/f$ noise requires measurements at high frequencies. Therefore, a complex technical setup has to be employed, which reduces the influence of external noise sources while being very sensitive to the noise signal of interest. Over the last years, various modifications were made at the combined STM and shot-noise setup to optimize the noise detection. In this section, the different components of the shot noise setup will be introduced.

1. Necessary Measurement Conditions to Detect Shot Noise

There are multiple noise sources present in real systems. Shot noise itself is temperature and frequency independent. The thermal noise and $1/f$ noise, on the other hand, depend on these parameters. To enable the detection of the desired shot-noise signal, the measurement conditions have to be adjusted such that the other noise sources can be disregarded.

The first prerequisite is to measure at high frequencies, where the amplitude of the $1/f$ noise has dropped below the noise floor of the thermal and amplifier noise (see fig. 4.5a). Typically, measurements in the order of 100 kHz are necessary to eliminate the $1/f$ noise signal. At high frequencies, however, the junction itself reduces the bandwidth of the measurements, as the combination of the junction resistance and its capacitance forms a low-pass filter. As this effect occurs in all the shot-noise measurements, it will be explained in detail in sec. 5. Another aspect of $1/f$ noise is that it is a resistance noise. Therefore, its noise power scales quadratically with the applied bias voltage, whereas shot noise increases linearly with the voltage. Hence, at high bias voltages, $1/f$ noise is likely to predominate the signal.

To account for the impact of thermal noise, another important condition is to measure at low temperatures to minimize thermal noise in all electronic components. Therefore, also the pre-amplifier of the noise setup is attached to one of cooling fingers of the STM (see fig. 4.6a), where it is cooled

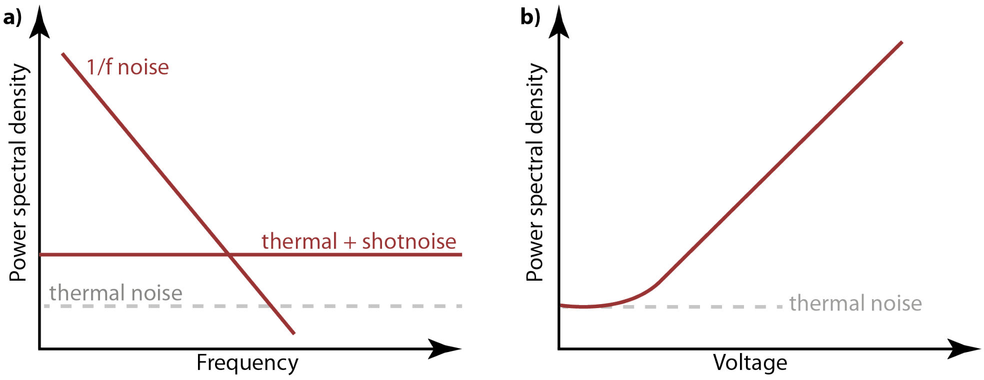

Figure 4.5. **a)** Sketch of the frequency dependence of the power spectral density of different noise sources. Whereas the amplitude of the $1/f$ noise decays at higher frequencies, both, the thermal noise and the shot noise are white, *i.e.*, they exhibit a constant power spectral density. **b)** Evolution of shot noise with increasing bias voltage. At higher voltages, a linear dependence can be observed, whereas at zero voltages, the constant background of the thermal noise predominates.

down to lHe-temperatures around 4.8 K. Moreover, the signal-carrying cables are guided through the lN cryostat, until they eventually are connected to a post-amplifier, which is stored outside of the UHV chamber. Furthermore, the positioning of the pre-amplifier next to the STM has the advantage that the cable length is minimized. Therefore, also the cable capacitances are reduced, and the signal loss up to the first amplifier is hence rather small. Despite those measures, there is a constant thermal noise background originating from all electronic components of the setup. To seperate this signal originating from thermal noise from the desired shot noise, the voltage dependence of the shot noise amplitude is exploited. Upon increase of the voltage, the power spectral density of the noise level increases linearly, as depicted in fig. 4.5b, whereas the thermal noise level is unaffected. Close to zero voltage, the total noise level does therefore not vanish, but it saturates at the value of the voltage-independent thermal noise.

2. Components of the Shot Noise Setup

The shot-noise setup used for the measurements in the next sections is shown in fig. 4.6. It was integrated into a conventional STM, whose general working principle has been described in more detail in sec. II.D. The most important pre-requisite for the detection of shot noise in the tunneling current is a set of amplifiers. The pre-amplifier is positioned inside the cryostat. To detect the noise signal,

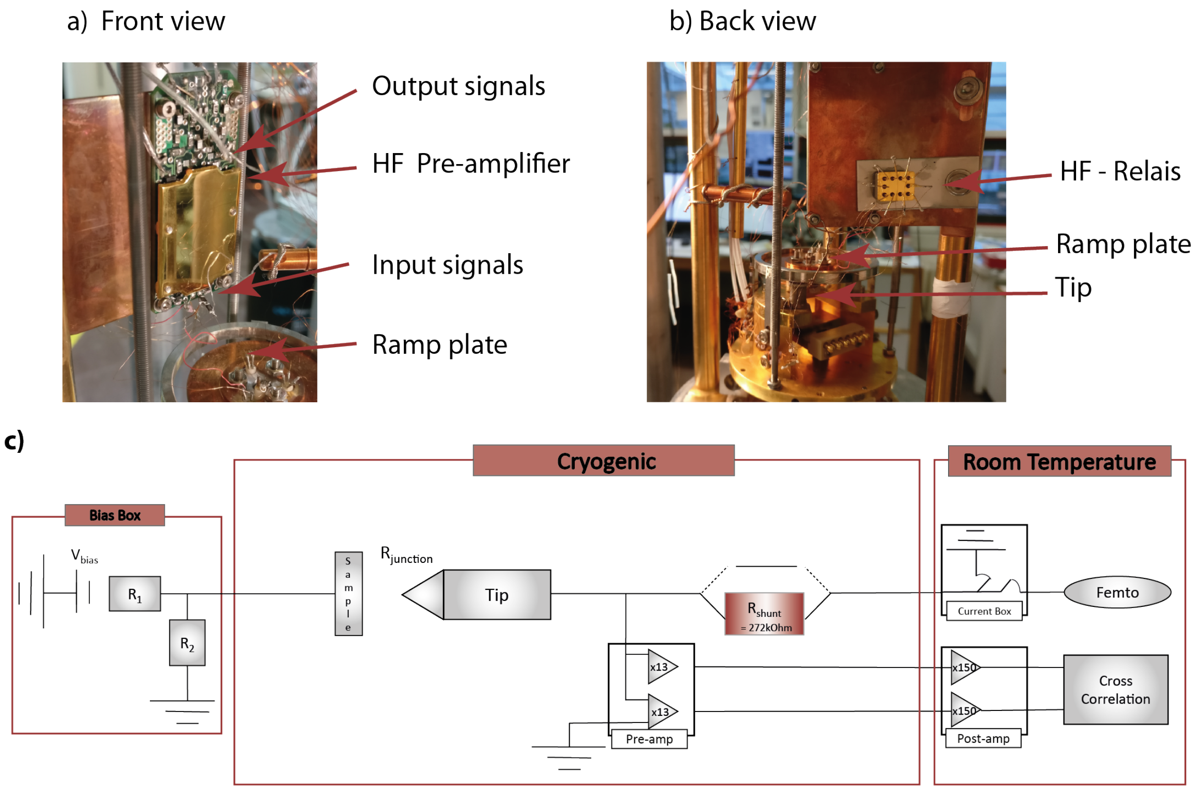

Figure 4.6. **a)** Back view and **b)** front view of the pre-amplifier. To minimize the length of the signal cables and to ensure optimized temperature conditions, the amplifier and the HF-relais are mounted onto a copper plate that is attached to one of the cooling fingers of the STM. **c)** Schematics of the final shot noise setup after modifications, with both input channels of the pre-amplifier connected to the tip. Moreover, the second shut resistance R_{Shunt} has been removed.

two parallel wires from the pre-amplifier input are attached to the STM tip, to record the fluctuations in the tunneling current. The pre-amplifier converts the current noise into a voltage signal and already amplifies it by a factor of approx. 13. The redundance of two pathes is necessary to perform a cross correlation later in the signal processing, which reduces the uncorrelated noise signals that are caught up during the signal transport. The pre-amplified signal is then enhanced by a factor of 150 in a post-amplifier, which is situated outside of the cryostat, before it can be processed via a cross correlation by a computer. For the conversion of the current noise into a voltage noise by the pre-amplifier, a shunt resistance R_{Shunt} has been integrated into the current path. For the value of the resistance, a compromise between the requirements of the shot noise and STM measurements had to be made, as a high resistance is needed for the voltage amplifier, which, however, is detrimental for normal STM measurements. Finally, a value of approx. $270\,\mathrm{k\Omega}$ has been chosen. Its exact value depends on its actual temperature during the measurements and strongly influences the conversion of current noise into a voltage signal. Therefore, to determine its exact magnitude, the tip has to be crashed into the surface with a specific bias voltage applied. From the current that flows through this resistance, its value can be accurately determined. To perform tip treatments at higher currents, HF-relais were installed (see fig. 4.6b) that allow to bypass the resistance.

As the current noise of the tunneling signal is several orders of magnitude smaller than the actual tunneling current, the system has to exhibit an extremly low noise level. Therefore, in addition to all the noise-reducing measures from the normal STM measurements like pneumatic feet, HF filters at the piezo cables and Eddy-current damped springs, special measures have to be taken in order to reduce external influences. The first adjustment for the shot-noise setup was the implementation of a custom-built bias-voltage box to supply the tunneling junction with the necessary bias voltage. It consists of a voltage source that exhibits a very low noise level, which, by a set of suitable resistors, can be controlled to generate 21 discrete voltage values ranging from $0\,\mathrm{mV}$, $\pm 20\,\mathrm{mV}$, …, $\pm 200\,\mathrm{mV}$ with low fluctuations. However, not only the path of the incoming bias voltage but also the outgoing current wires can transfer noise into the system. Therefore, a second grounding box was installed at the tip side, which automatically disconnects the current wire from the IV-converter (Femto) during the shot-noise measurements and connects it to ground.

During the first measurements, a parallelized setup was chosen, with the signal being recorded at both sides of the junction, *i.e.*, at the sample and the tip (see fig. 4.7). An unwanted stray capacitance at the sample holder itself in the order of several pF, however, lead to large signal losses, as it effec-

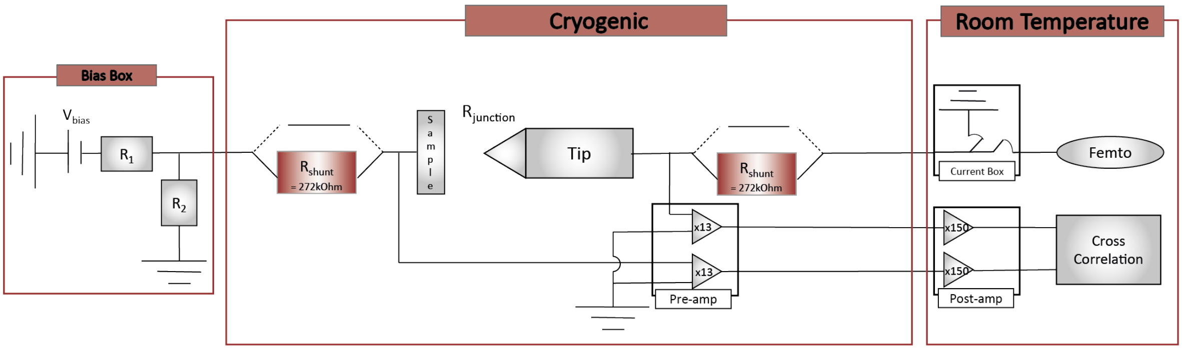

Figure 4.7. Schematics of the parallelized high-frequency setup. The so-called bias box supplies the tunneling junction with the necessary bias voltage, while minimizing voltage fluctuations. The pre-amplifier detects the current fluctuations at both the sample and the tip side as a voltage signal and amplifies the signal by a factor of approx. 13. The two signals are then amplified by a factor of 150 in a post-amplifier, before a cross correlation is performed to eliminate non-correlated noise.

tively acted as a direct high-pass shortcut to ground. The noise signal at the sample side was therefore not detectable anymore and measurements were only possible with one signal channel. As the occurance of the stray capacitance is difficult to avoid with the Createc sample holder design, in the next stage of optimization of the setup, both amplifier inputs were connected to the tip side. Moreover, the second resistance, which was initially included in the bias path, was therefore no longer necessary and has been removed.

3. Characteristics of the High-Frequency Amplifiers

The main constituents of the shot-noise setup are the HF pre- and post-amplifers. Both amplifiers feature very low input noise levels in the order of $2.5\,\mathrm{nV}/\sqrt{\mathrm{Hz}}$ for the post-amplifier and $0.8\,\mathrm{nV}/\sqrt{\mathrm{Hz}}$ to $4\,\mathrm{nV}/\sqrt{\mathrm{Hz}}$ for the pre-amplifier, depending on the respective frequency. As a pre-amplifier, the HFC 50B from Stahl-electronics is installed. It is optimized for frequencies in the range of 160 kHz to 50 MHz and suitable in a wide temperature range from 300 K to 4.2 K. Its high input impedance of 10 MΩ allows to detect signals from sources of high resistance, as is the case for the tunneling junction of an STM. The pre-amplifier is powered by the biasing unit of the RTA 50 post-amplifier. An automated feedback loop adjusts the supply currents of the seperate signal channels of the pre-amplifier in such a way that their amplification factors are matching. The original post-amplifier was optimized for a frequency range of 150 kHz to 50 MHz. By exchanging some input capacitances in the post-amplifier, its lower cutoff frequency could be reduced to 22 kHz, which enables measurements at lower frequencies. Moreover, the post-amplifier exhibits four different amplification steps, which can be fine-tuned by variable resistors to match exactly 10, 20, 50 and 150. To optain a maximal signal intensity, all measurements were performed with the highest amplification factor of 13 for the pre-amplifer and 150 of the post-amplifier, leading to a total amplification of the noise signal by approx. $13 \times 150 = 2010$ for each channel.

4. Two-Channel Cross Correlation

The shot-noise signal of samples is typically in the order of some $\mathrm{nV}/\sqrt{\mathrm{Hz}}$. As described above, the input noise of the pre- and post-amplifier exhibit noise in the same order of magnitude. Moreover, there

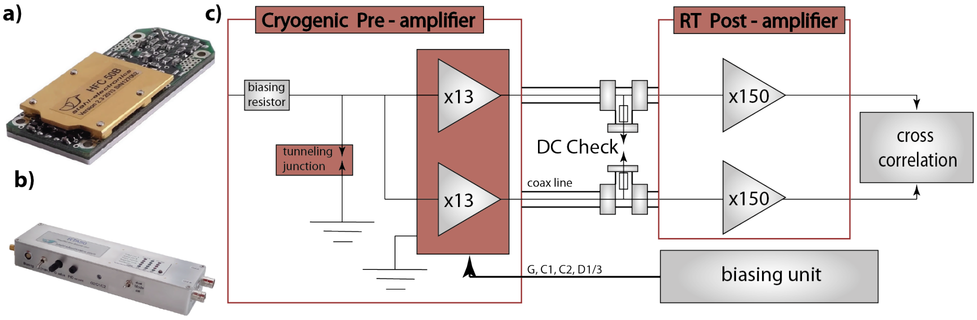

Figure 4.8. Post- and pre-amplifier used to detect shot noise. **a)** Image of the HFC 50B cryogenic amplifier from Stahl-electronics. **b)** Image of the RTA 50 combined post-amplifier and biasing unit. **c)** Sketch of the working principle of the biasing unit of the post-amplifier. By comparing the signal intensities of the amplified signal, the current supply of the corresponding channels of the pre-amplifier can be adjusted to obtain matching amplification factors in both channels. Scheme adapted from the Stahl-electronics manual.

are other non-negligible noise sources present in any system, such as $1/f$ noise. In order to detect such tiny shot-noise signals in an equally large noise background, a two-channel cross-correlation technique is typically implemented. Here, both channels measure the same correlated signal noise. Moreover, the cables also act as an antenna and pick up additional background noise. Due to their different cable lengths and pathes, this background noise is uncorrelated, such that the noise in the two channels exhibits a randomized phase shift. The signals of both channels $f(t)$ and $g(t)$ are then entering in the cross correlation

$$(f * g)(\tau) = \int_{-\infty}^{\infty} f^*(t) g(t+\tau) \mathrm{d}t, \qquad \textbf{4.25}$$

with τ corresponding to the time delay. The uncorrelated background noise exhibits a random phase in both channels and hence averages out over time. The noise signal from the sample, on the contrary, has a constant phase relation in both channels. Therefore, it does not cancel out over time. Unfortunately, the same holds for correlated noise that is picked up at both amplifiers, which is also not attenuated in the cross correlation. Therefore, background noise can be reduced by the cross correlation, but not fully eliminated.

5. Low-pass Effect of the Junction

A tunneling junction can be modelled by two components: a tunneling resistance $\mathrm{R_J}$ and a parallel capacitance. The combination of these two components leads to a frequency-dependent signal transmission. For the shot-noise signal, this means that only signals up to a certain cutoff frequency can pass the junction. All signals at higher frequencies will be strongly attenuated. For a conventional RC low-pass filter, the cutoff frequency can be determined by the relation $f = {}^1\!/_{2\pi RC}$, with R being the resistance and C the capacitance, respectively. This means that the cutoff frequency is inversely proportional to the corresponding resistance. A similar behaviour can also be observed in the tunneling junction. The higher the junction resistance $\mathrm{R_J}$, the lower is the cutoff frequency in the noise signal. For the measurements in the contact regime, the junction resistance is rather small (in the order of 10 kΩ to 20 kΩ) such that the signal is only cut off above several hundreds of kHz. In the tunneling regime, on the contrary, the junction resistance is by more than an order of magnitude larger (in the order of 0.5 MΩ to 1 MΩ), such that the signal attenuation starts already at below 100 kHz. At such low frequencies, however, the amplifer setup has not even reached its regime of full amplification. Therefore, a large part of the signal in the tunneling regime is not detected due to the combination of the junction low pass and the amplifier high pass.

C. First Results: Shot Noise on Au(111)

For the first shot-noise measurement, a test system was chosen that consists of a Au tip and a Au adatom created on a Au(111) surface. For Au-Au contacts, spin-degenerate transport is expected, with the main transport path being through the 6s orbital. For this system, reference data exists both from MCBJ measurements from M. Kumar, et al. [170] and from measurements with an STM-setup from A. Burtzlaff, et al. [24, 176], which confirm the suitability of the system in terms of stable and reproducible contacts. In these publications, the evolution of the Fano factor was shown as a function of the junction conductance, and it was confirmed that Au contacts behave as single-channel Landauer conductors. Therefore, it is a suitable reference system to calibrate our noise setup.

1. Recording of the Noise Signal

The most important pre-requisite to successfully detect shot noise are stable contacts. As the shot-noise level depends linearly on the current, an unstable tunnel resistance would lead to fluctuating noise levels. As the approach of the tip on a flat surface would allow for a variety of bonds, non-reproducible shot-noise values would be measured. Therefore, to ensure such stable and reproducible contacts between the tip and the sample, the creation of Au adatoms is essential. Adatoms are created by applying voltage pulses of −2 V with the tip indented into the surface by approx. 2 Å. By repeating this procedure, the tip can be conditioned to drop single atoms at every voltage pulse. Such creation of Au adatoms is depicted in fig. 4.9a for two single adatoms that are deposited on the surface. To garantuee the stable position of the adatoms and the stability of the tip, a series of tip approaches is performed onto the adatom. An exemplary approach curve is shown in fig. 4.9b. The jump in the current at 3.6 Å corresponds to the abrupt contact formation between the tip and the adatom. The current plateau that is reached indicates a stable contact, whose resistance can be determined from the applied bias voltage of 200 mV and the current of 698 nA as:

$$R = \frac{U}{I} = \frac{200\,\mathrm{mV}}{698\,\mathrm{nA}} = 286\,\mathrm{k}\Omega. \tag{4.26}$$

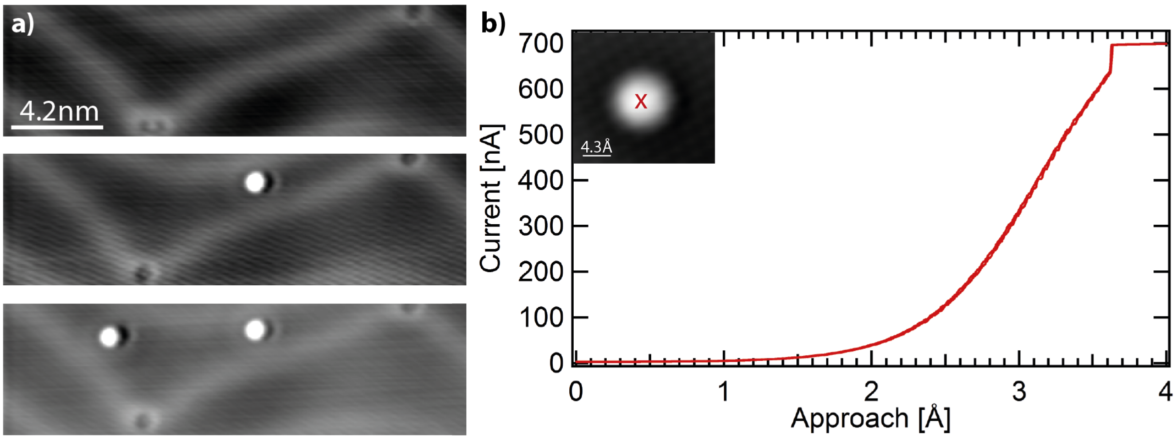

Figure 4.9. **a)** Subsequent creation of Au adatoms by applying voltage pulses of −2 V with the tip indented into the surface by approx. 2 Å. **b)** Approach curve on a Au adatom starting from a setpoint of 200 mV and 200 pA. The characteristic jump into contact can be observed at 3.6 Å, followed by the reaching of a current plateau. Both, the forward and backward curve are shwon and lie on top of each other.

Considering the built in shunt resistance[3] of $R_{\text{Shunt}} = 273\,\text{k}\Omega$, this corresponds to a junction conductance of around $1G_0$, with the quantum of conductance being defined as $G_0 = \frac{2e^2}{h} = {}^1/_{12.9\,\text{k}\Omega}$. Only if the resulting contact formation is reproducible, the shot-noise measurements were started.

To obtain information about a physical system from its shot noise, the current fluctuations have to be recorded at various DC currents, with the number and opening of the respective conduction channels being unchanged throughout this entire time. Therefore, the tip is brought into contact with the adatom. A defined bias voltage of 200 mV is applied and the DC current and the corresponding current fluctuations are recorded. The value of the DC current later allows to determine the junction resistance of the contact. Consecutively, the voltage is reduced in steps of 20 mV, such that the shot noise is recorded for 11 different voltage values until a value of 0 mV is reached. Thus, the total measurement time ranges in the order of 20 min for each contact. Afterwards, an STM image is recorded to confirm that the adatom position and the tip did not change during the contact formation. The measurement is then repeated for a different contact resistance. To optimize the measurement, a LabVIEW program was developed that automatically executed this entire measurement procedure at various distances (see Appendix A for a sketch of the LabVIEW structure and more information about the different measurement steps).

2. Noise Measurements on Au(111) Adatoms

During the data acquisition, the noise signal is recorded on two distinct pathes that collect the same noise signal. The cross correlation of these two channels is computed directly in the LabVIEW procedure. The cross-correlated voltage-noise signal that is acquired at one particular distance is shown in fig. 4.10a. Here, the tip was approached by 3.1 Å starting from a setpoint of 200 pA at 200 mV. In theory, the power spectral density (PSD) of shot noise should be frequency independent such that a constant noise plateau should be observable. In experiment, however, the band-pass characteristics of the pre- and post-amplifier leads to an onset of the noise signal only for frequencies above 10 kHz. In principle, the amplifiers are suitable for frequencies up to 50 MHz. Here, however, the above mentioned low-pass cutoff of the junction itself leads to the observable decrease of the signal amplitude already at frequencies above 100 kHz, as can be seen in fig. 4.10b.

The different traces in the graph correspond to the noise curves for the different applied bias voltages. In the tunneling regime (see fig. 4.10a), the noise level increases with the applied bias voltage. When the tip is brought into closer contact with the adatom (see fig. 4.10e), the increase of the noise level gets much smaller. Note that besides the signal amplitude, also the frequency of maximal signal of the noise curves changes for the different contact regimes. In the tunneling regime, the maximal amplitude is reached at 100 kHz as the large junction resistance reduces the low-pass filter cutoff frequency of the junction. In contact, this frequency is much higher, such that a constant plateau is reached between 180 kHz and 500 kHz. Within this frequency region, the noise level can be evaluated at any frequency with only a few percent deviation, as can be seen in fig. 4.10f. Figures 4.10c and g show a zoom into the region of the noise curves in b and f, where the noise amplitude has reached their respective maximum. To avoid the influence of the spikes in the noise curves, the noise level in the tunneling regime is considered at 125 kHz instead of 100 kHz. The seemingly larger fluctuations in fig. 4.10g originate from the smaller noise level close to the contact regime, which is much more sensitive to external influences. For further evaluation, the noise level was always evaluated at 260 kHz for the contact regime and at 125 kHz in tunnel.

---

[3] Note that the value of the shunt resistance changes with its temperature. The value of 273 kΩ corresponds to its resistance at lHe temperatures. As soon as the pre-amplifier is switched on, it is changing the temperature of the resistance, such that its value drops to 222.7 kΩ.

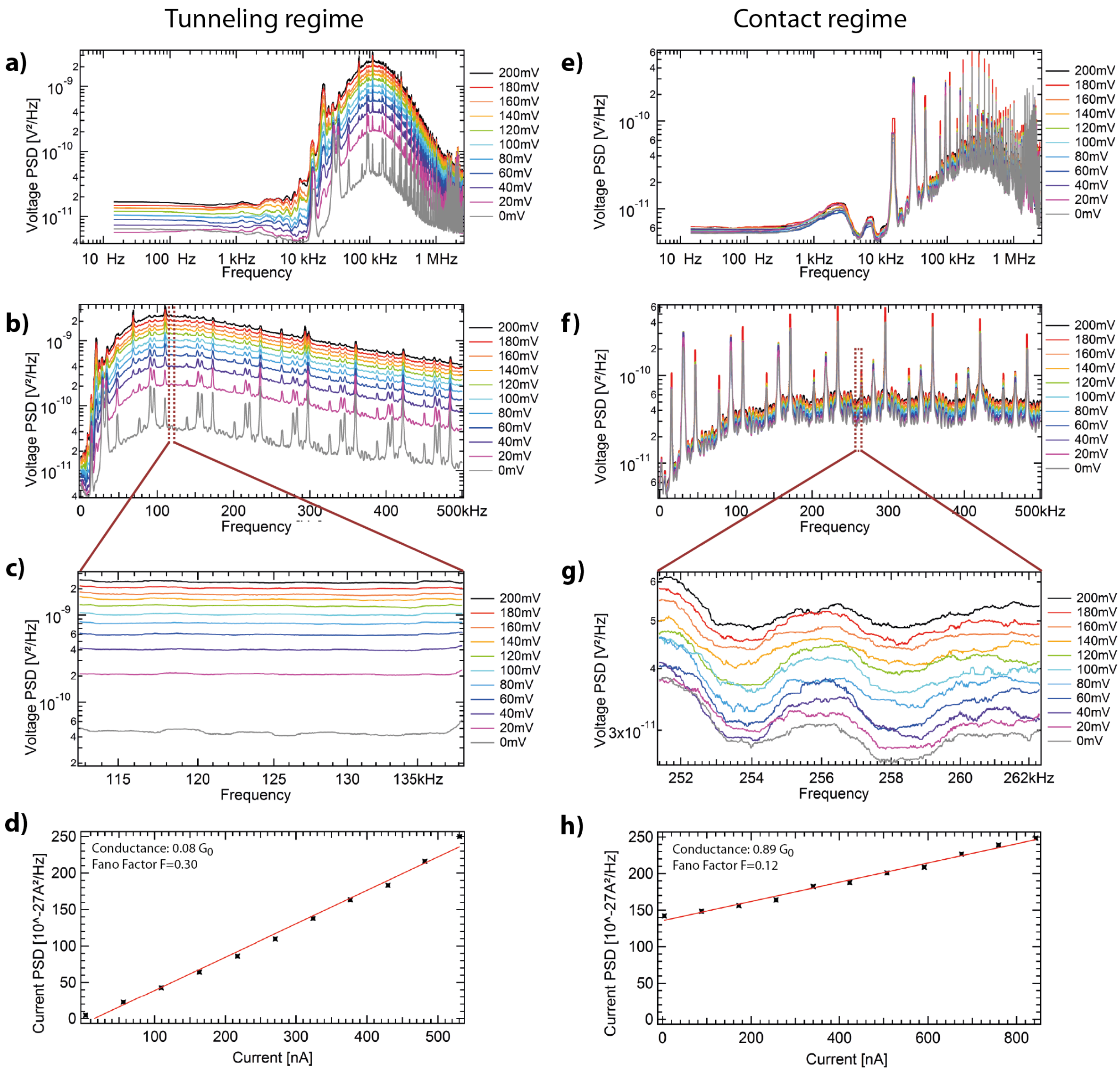

Figure 4.10. Shot noise measurements on Au adatoms: **a,b)** Voltage noise power spectral density recorded in the tunneling regime with $G = 0.08G_0$. The different traces correspond to the noise level recorded at different bias voltages between 0 mV and 200 mV. **c)** Zoom into the frequency region, where the noise level is maximal. **d)** Calculated current noise power spectral density as a function of DC current, evaluated at a frequency of 125 kHz. From the linear slope, a Fano factor of $F = 0.30$ can be determined. **e-h)** Corresponding voltage power spectral density and current PSD for a conductance of $0.89G_0$, with the resulting Fano factor amounting to $F = 0.12$.

In order to analyze the data in terms of their Fano factor, the noise data has to be converted from the measured voltage noise into the original current noise. This is done according to the relation

$$S_\mathrm{I} = \frac{S_\mathrm{U}}{2010^2 * ((^1/_{\mathrm{R_{Shunt}}}) + (^1/_{\mathrm{R_J}}))^{-2}}, \tag{4.27}$$

where S_I denotes the current noise density in units of A^2/Hz, S_U is the detected voltage noise density in V^2/Hz and $\mathrm{R_J}$ and $\mathrm{R_{Shunt}}$ denote the junction resistance and the built-in shunt resistance, respectively.

As described in Sec. B.3, the factor 2010^2 originates from the signal enhancement of each channel by the amplifier setup. The current noise density corresponding to the voltage noise densities in fig. 4.10c and g is depicted in fig. 4.10d and h, respectively. Here, the current noise levels have been calculated at a frequency of 125 kHz in the tunneling regime and a frequency of 260 kHz in the contact regime. According to the relation $S_I = 2eIF$, the shot noise is expected to increase linearly with the DC current, with the slope of the curve being proportional to the Fano factor F. This can indeed be observed for both measurements. In the tunneling regime ($0.08G_0$) in fig. 4.10d, a Fano factor of $F = 0.30$ has been determined. For the current noise close to the contact regime ($0.89G_0$) in fig. 4.10h, a Fano factor of $F = 0.12$ has been extracted.

Determination of the Fano Factor

The Fano factor has been evaluated for numerous contacts at different conductances. The corresponding evaluation is shown in fig. 4.11a, where the Fano factor is depicted as a function of conductance. The black line corresponds to the theoretical dependence, which is obtained from the definition of the Fano factor in case of spin-degenerate transport (compare to eq. 4.23 in sec. A for its derivation)

$$F = \frac{\sum_{i=1}^{N} \tau_i (1-\tau_i)}{\sum_{i=1}^{N} \tau_i}. \tag{4.28}$$

Two different contact regimes can be observed in the measurement data. A lot of data points are in the region between $0.8G_0$ and $1G_0$ and lie close to the theoretical curve. In the tunneling region below $0.2G_0$, another series of data points can be found, which, however, all lie well below the theoretical line. On the first glance, this might be associated with spin-polarized transport, where the Fano factor can exhibit lower values than for the case of two conduction channels (see red line in fig. 4.11b). However, in case of Au adatoms, spin-degenerate transport is expected. Instead, the lower noise level results from artefacts that occur in the tunneling regime. First of all, the preamplifier exhibits an input impedance of 10 MΩ. Therefore, the noise signal is only reliably detected for junction resistances well below 10 MΩ. In our measurements in the tunneling regime, however, the junction resistance often lies in the order of 1 MΩ, such that only about 90 % of the noise signal in the tunneling regime is actually detected. Another artefact that arises due to the large junction resistance is the low-pass cutoff of the junction itself. This effect is visualized in fig. 4.11c, where the Fano factor has been evaluated at different frequencies both for a measurement in the tunneling regime (black) and close to contact (red). Despite all the spikes in the spectra, the Fano factor in the contact regime exhibits a constant value between 180 kHz and 500 kHz (red region). At higher frequencies, the low-pass cutoff of the junction is damping the signal. At lower frequencies, on the contrary, the amplification characteristics of the amplifier setup is limiting the signal detection. In the tunneling regime, the cutoff frequency of the junction is shifted to lower values, such that the maximal signal intensity is reached already at around 100 kHz (gray region). Therefore, a large percentage in the order of 60 % to 80 % of the original signal is not detected. Due to both these effects, measurements in the tunneling regime do not yield reasonable results. Hence, only the data points at conductances above $0.7G_0$, as shown in fig. 4.11d, will be considered. The large error bars in fig. 4.11d (for clarity, they are shown in grey) of the conductance stem from the uncertainty of the magnitude of the shunt resistance. In the contact regime, where the junction resistance is in the order of 13 kΩ, a deviation of the value of R_{Shunt} of 1 kΩ already corresponds to an uncertainty of the conductance of approx. $0.1G_0$. However, the data points in the contact regime are in agreement with theoretical expectations. Hence the measurement on the Au adatoms indicate that the amplifier setup is sensitive to detect shot noise of single atoms.

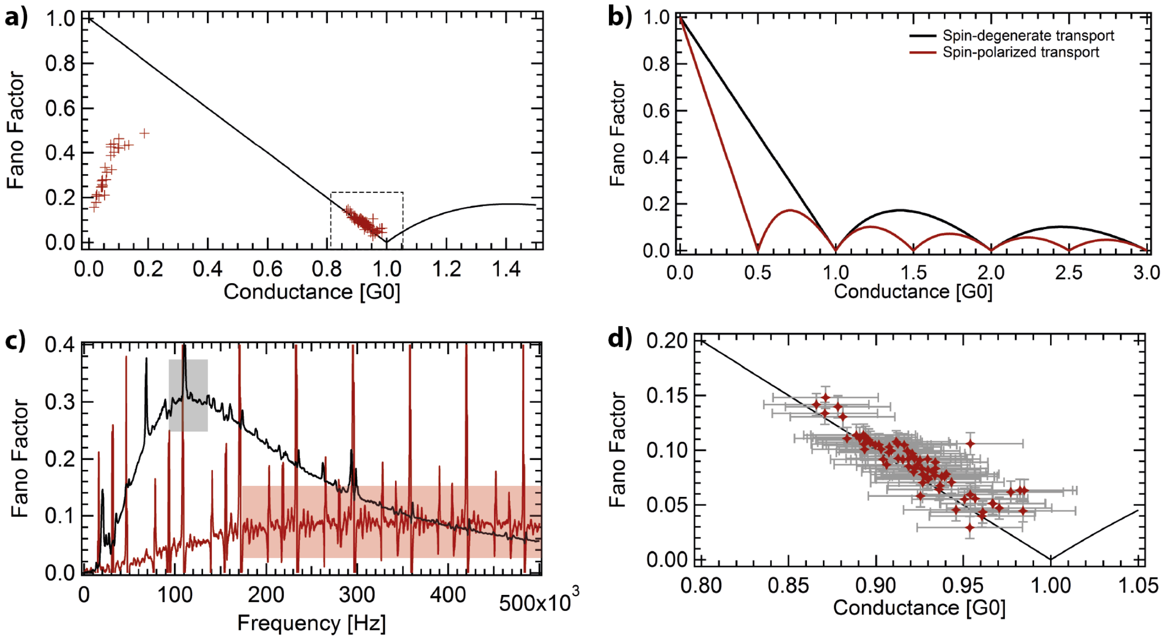

Figure 4.11. Shot noise measurements on Au(111). **a)** Evolution of the Fano factor depending on the junction conductance. At conductances above $0.8G_0$, the experimental data is in agreement with the theoretical curve, shown in black. For lower conductances, measurement artefacts lead to too low values for the Fano factor. **b)** Theoretical predictions of the Fano factor for spin-degenerate transport (black) and spin-polarized transport (red). **c)** Fano factor evaluated at different frequencies. At low frequencies, the amplification curve of the pre- and post-amplifier setup determines the onset frequency. At higher frequencies, the low-pass of the tunneling junction attenuates the signal. This effect is stronger for measurements in the tunneling regime, as the cutoff frequency is shifted to lower values. **d)** Measurement data from the gray square in a), where the data points from the tunneling regime were neglected.

3. The Influence of Thermal Noise

When we consider the voltage noise power spectral density in fig. 4.10c and g, a finite noise level is detected also at 0 mV bias voltage. As described before, the noise level at 0 mV bias voltage in theory should result from thermal noise only. The thermal voltage noise of a resistor is defined as $S_U = 4k_B TR$. In our setup, there are two resistors of importance: the junction resistance and the built-in shunt resistance $\mathrm{R_{Shunt}}$. Both resistances are in a parallel circuit with respect to the noise amplifier (see fig. 4.12a). Therefore, the two thermal noise levels can not just be added up to a total noise but instead, the noise level of the total resistance has to be considered, which yields

$$S_\theta\left(\mathrm{R_{Shunt}}+\mathrm{R_J}\right)=4k_B T R_{\text{total}}=4k_B T\left(\frac{1}{\mathrm{R_{Shunt}}}+\frac{1}{\mathrm{R_J}}\right)^{-1}. \qquad 4.29$$

As in the contact regime, the shunt resistance is around 20 times larger than the junction resistance, the $^1/_{\mathrm{R_{Shunt}}}$ term is neglegible, yielding a total thermal noise of

$$S_\theta\left(\mathrm{R_{Shunt}}+\mathrm{R_J}\right)=4k_B T R_{\text{total}}\approx 4k_B T\mathrm{R_J}. \qquad 4.30$$

This amounts to a voltage noise level in the order of $1.3\times10^{-11}\,\mathrm{V^2/Hz}$ at $1G_0$. Hence, in contact, the parallel circuit of the junction and the shunt resistance effectively eliminates the much larger thermal noise of the shunt resistance. Further away from the contact regime, the junction resistance is in the

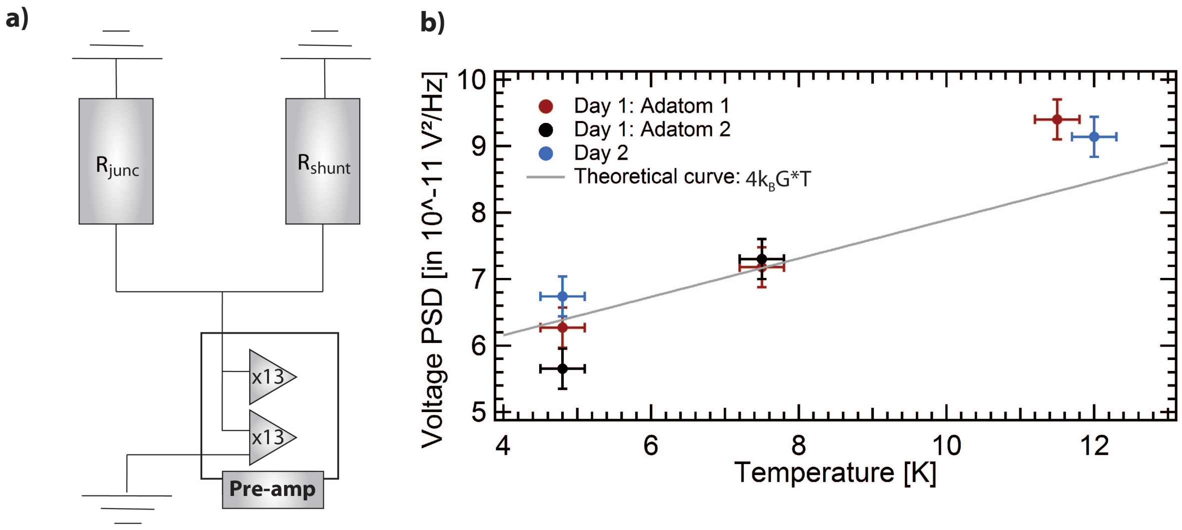

Figure 4.12. **a)** Circuit diagramm, showing the parallel wiring of the junction and the shunt resistance with respect to the pre-amplifier. Due to this assembly, the thermal noise levels of the junction resistance and shunt resistance can not just be added up, but the total resistance has to be considered first. **b)** Thermal noise level recorded on different adatoms at different STM temperatures. A clear linear increase of the recorded noise signal can be observed, in agreement with the theoretical curve, shown in grey. The slightly larger increase of the experimental noise can be attributed to a higher temperature of the tunneling junction.

same order of magnitude as the shunt resistance, or even larger. For a junction conductance of $0.08G_0$, the thermal noise amounts to $S_\theta\left(\mathrm{R_{Shunt}}+\mathrm{R_J}\right)=4k_\mathrm{B}T R_\mathrm{total}=4k_\mathrm{B}T\times 93\,\mathrm{k\Omega}=9.9\times10^{-11}\,\mathrm{V^2/Hz}$. Hence, a higher thermal noise background is expected for larger tunneling resistances.

When we compare the theoretically expected voltage noise levels with the experimental noise levels at 0 mV in fig. 4.10c and g, voltage noise levels in the order of $3\times10^{-11}\,\mathrm{V^2/Hz}$ in the contact regime and $4\times10^{-11}\,\mathrm{V^2/Hz}$ in the tunneling regime can be observed at 0 mV. Hence, the experimental noise level for the contact regime is slightly larger than the theoretically predicted thermal noise. The discrepancy can be explained by the input noise of the preamplifier, which is in the order of approx. $2\times10^{-11}\,\mathrm{V^2/Hz}$ and which has to be considered in addition to the thermal noise. For the tunneling regime, in contrast, the theoretical value is larger than the experimental value. However, as decribed above, in the tunneling regime only a fraction of the total noise signal is detected, such that the actual noise signal is by a factor of 2-3 larger than the detected value. Hence, the experimental value is in agreement with theory.

Despite the fact that the thermal voltage noise levels are of similar magnitude in both the tunneling and the contact regimes, their determined current noise levels strongly differ (see fig. 4.10d,h). To explain this discrepancy, the non-linear conversion factor from eq. 4.27 has to be considered. For the shot noise, the current fluctuations that exist in the junction are detected as voltage fluctuations in the amplifier. By employing eq. 4.27, the original current fluctuations that correspond to the detected voltage noise are extrapolated. In case of the thermal noise or the amplifier input noise, however, the signal already is a voltage noise. Hence, trying to extrapolate current fluctuations of this voltage noise does not yield any physical properties. Instead, it just results in an offset of the entire current noise level. Especially for the smaller junction resistance in the contact regime this leads to larger values of the current noise density at 0 mV (see fig. 4.10h), which, however, should not be mistaken to result from a real physical property. Despite of this artefact, the current noise data can be used without any reservations to characterize the transport properties, as only the slope of the current noise density with increasing current is of importance for the determination of the Fano factor.

Temperature-dependent Noise Measurements

In order to verify that our setup is indeed sensitive to thermal noise, the voltage noise level of the junction is recorded at different junction temperatures. Therefore, the junction is heated up by a lamp, which is directed at the STM through the windows of the cryostat. Here, different temperatures were achieved by varying the light intensity. The respective temperature change is then detected in a diode, which is attached at the bottom of the STM head. Hence, the actual junction temperature will be slightly higher than the detected STM temperature at the diode. The shunt resistance $\mathrm{R}_{\mathrm{Shunt}}$ and the noise preamplifier are mounted on a copper plate, which is well attached to a cooling finger of the STM. As they are at the backsite of the plate with respect to the light source, their temperature is expected to remain unaffected. Moreover, the stability of the temperature of the shunt resistance was checked by monitoring the tunneling current at a specific voltage that flows in a contact of a conductance of G_0. As the value of the shunt resistance changes with temperature, a thermal heating should be visible as changes in the respective tunneling current. During the temperature-dependent measurements, variations of the shunt resistance in the order of 2 kΩ were observable, which amounts to around 1 % of $\mathrm{R}_{\mathrm{Shunt}}$. For comparison, the value of the shunt resistance decreases from 273 kΩ to 222.7 kΩ as soon as the pre-amplifier is switched on, indicating a large response of its value to small temperature changes. Hence, the almost constant resistance in the temperature-dependent measurements indicates a constant resistance temperature, independent from the STM temperature.

Figure 4.12b shows the resulting voltage PSD acquired at 0 mV bias voltage for three different STM temperatures between 4.8 K and 12 K. The red and the black data points were acquired at the same measurement series but on different adatoms. For each data point, the thermal noise level was recorded eight times on the same adatom, with the adatom being contacted for each spectrum individually, to ensure the reproducibility of the contact formation. From those consecutive measurements, an average noise level was determined. This procedure was repeated on the same adatoms after the STM temperature was increased. To ensure the reproducibility, the temperature-dependent measurements were repeated in a different series with a different tip and adatom (blue data points). In between, the STM was cooled down to 4.8 K, again. For all three investigated adatoms, the noise level shows a clear linear increase with temperature. The grey curve in fig. 4.12b shows the theoretical thermal noise curve, according to the relation $S_\theta(T) = 4k_\mathrm{B}\mathrm{R}_\mathrm{J} \times T$. To account for the amplifier noise, it is offset by $5 \times 10^{-11}\,\mathrm{V}^2\,\mathrm{Hz}^{-1}$. The data points at 4.8 K and 7.5 K fall on this line. At 11.5 K, however, the experimental noise level is higher than the expected theoretical thermal noise of the junction. This deviation might be explained by the slightly higher junction temperature. Hence, the temperature-dependent noise analysis suggests that the high-frequency amplifier setup is suitable to detect changes in the thermal noise of the tunneling junction. As the termal noise is in the same order of magnitude as the shot noise, this test hence supports the previous conclusions of this amplifier setup being suitable to detect shot noise.

D. Conclusions

In this chapter, the steps towards developing and assembling a working shot-noise setup were presented. In the technical section, the main components of the employed setup were introduced. As shot-noise measurements require signal detection at high frequencies, a set of special amplifiers had to be included into a conventional STM setup. To collect the shot-noise signal on both sides of the junction, the first approach was to detect the signal at the tip and the sample side, and perform a cross correlation of the respective signals. Due to a stray capacitance at the sample holder, however, the signal on the sample side could not be detected. Therefore, the setup has been modified, such that both input channels of the pre-amplifier are connected to the tip side. With this assembly, test measurements were perfomed on single Au adatoms, which were created by indenting a Au-coated tip into the Au(111) surface. The creation of adatoms was necessary to guarantee stable and reproducible contacts. The shot-noise measurements on Au showed a linear decrease of the Fano factor with increasing conductance, in agreement with the theoretical predictions for spin-degenerate transport through a single conduction channel. As there are already publications on this system that showed the same results [24, 169, 170, 176], the measurements on Au indicate that our setup is indeed suitable to detect shot noise of atomic contacts.

Furthermore, to test the detection limit of the amplifiers, temperature-dependent measurements of the thermal noise level were performed. Therefore, the STM was heated up in two steps: first to 7.5 K and finally to 12 K by an external light source, such that the thermal noise of the junction would increase. Indeed, we could detect this linear increase of the junction noise with temperature, which confirms the achievement of the necessary noise resolution.

E. Outlook

The measurements on Au adatoms showed that the amplifier setup is fully functional. However, no new physical insights were obtained from these measurements. Therefore, in a next step, shot-noise measurements need to be performed on a new system. There are many systems that are potentially interesting for shot-noise measurements. As mentioned in the introduction, the shot-noise level allows to detect the effective charge e^* of the current-carrying particles of a system. Therefore, shot-noise measurements have been used to investigate fractional charges, Cooper-pair tunneling or spin-polarized transport. Another interesting aspect is the shot noise of Kondo systems. The Kondo effect describes a many-body effect, where the conduction electrons of a metal surface are scattered at a magnetic impurity [200, 201]. This scattering leads to the formation of a new many-body ground state, where the localized spin of the impurity is paired with the conduction electrons, such that a nonmagnetic Kondo singlet state is formed [202]. The transport through Kondo systems has mainly been studied for quantum dots, where a gating voltage allowed to shift the respective energy levels. From STM measurements, however, there is little experimental knowledge about the atomic-scale transport through Kondo impurities. Therefore, as a first new system, shot-noise measurements are performed on single cobalt atoms on a Au(111) surface. The properties of this system and the first preliminary results will be introduced in the following.

1. Properties of Co on Au(111)

Single Co atoms have already been studied on a Au(111) surface with STM by V. Madhavan, et al. in 2001 [203]. By means of STS measurements, they showed that cobalt exhibits characteristic Kondo resonances in the $\mathrm{d}I/\mathrm{d}V$ spectra. In STS measurements, a tunneling electron from the tip can have different tunneling pathes: **i**) it can directly tunnel into the unoccupied states of the Au surface or **ii**) it can tunnel into the Kondo resonance. Quantum interference between these two pathes leads to the emergence of so-called Fano line shapes[4] in the $\mathrm{d}I/\mathrm{d}V$ spectra, whose asymmetry can be expressed by the factor [204]

$$q = \frac{t_2}{2\pi V t_1}. \tag{4.31}$$

Here, V denotes the hybridization matrix element between the local singly-occupied orbital of the impurity and the continuum states of the sample. The parameters t_1 and t_2 are the tunneling probabilities into the substrate continuum and into the Kondo resonance, respectively. For $q \to \infty$, *i.e.*, pure tunneling into the Kondo resonance, the curve resembles a Lorentzian peak. For $q = 0$, *i.e.*, for direct tunneling into the continuum, it forms a Lorentzian dip. At intermediate values, asymmetric line shapes occur.

For the measurements of Co impurities on Au, V. Madhavan, et al. showed that the line shape of the Kondo resonance changes depending on the adsorption site of the Co atoms with respect to the Au surface reconstruction. This means that between different adsorption sites, the ratio between the tunneling probability through the Kondo state and the probability to tunnel directly into the substrate varies, which makes it a very interesting system also in terms of shot-noise measurements.

Cobalt exhibits an electron configuration of $[\mathrm{Ar}]4\mathrm{s}^2\,3\mathrm{d}^7$, such that it has a total spin of $S = {}^3\!/_2$ with, according to simple transport rules, three distinct transport pathes [168]. The Kondo effect partially screens the spin in the d-derived orbtitals. It is therefore interesting to investigate the interplay of the potentially three transport channels, as well as the above described interference due to direct tunneling into the continuum.

Shot-noise measurements on cobalt atoms on the Au(111) surface have recently been performed by A. Burtzlaff, et al. [24], where they measured a few Co contacts and found noise suppression as it is predicted for one spin-polarized transport channel. With the help of DFT calculations, they explain this observation by a symmetry filtering by the tip, which suppresses the transport through two of the three valence channels by more than two orders of magnitude, such that only one spin-polarized channel participates in the transport process. However, the impact of the different Fano line shapes of the Kondo resonance on the transport properties has not been studied so far, as A. Burtzlaff, et al. evaluated only 5 different contacts. To observe such a correlation, the shot noise of different Co atoms has to be evaluated in dependence of their corresponding Fano line shape and adsorption site.

2. First Shot-Noise Measurements on Cobalt Atoms

In order to obtain single Co atoms on the Au surface, Co has been deposited from a rod for 20 s at very low sample temperatures. An STM topography of the surface after Co deposition is shown in fig. 4.13. Most of the Co atoms lie well isolated on the surface, whereas some atoms can be found in dimers and trimers. In fig. 4.13c, three exemplary $\mathrm{d}I/\mathrm{d}V$ spectra are shown that were recorded on different Co atoms. Their respective position is indicated by the circles in fig. 4.13b. In agreement with observations of V. Madhavan, et al. [203], the Co atoms that lie in close proximity to the solitone lines of the herringbone reconstruction (blue spectrum) do not exhibit Kondo resonances. The atoms that lie in between the soliton lines either on the fcc or hcp site, in contrast, show a dip in the differential conductance right at the Fermi level (gray and red spectra).

To characterize the transport properties of the Co atoms, shot-noise measurements were performed on several Co atoms that are adsorbed on different areas of the Au(111) surface reconstruction. The corresponding plot of the Fano factor as a function of junction conductance is depicted in

---

[4] Note that the Fano line shape from the Kondo resonance and the Fano factor determined in shot-noise measurements are two independent parameters, despite both being named after the same physicist U. Fano.

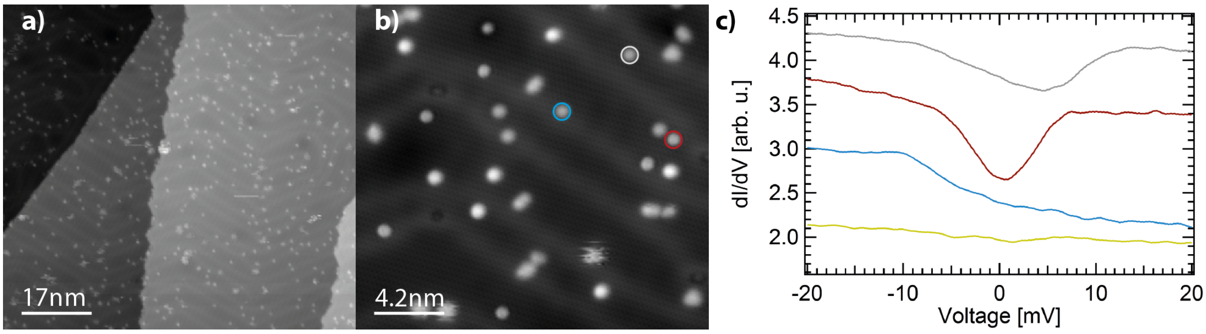

Figure 4.13. **a)** Topography of the Au(111) surface after deposition of Co. **b)** Close-up view of the sample, showing single Co atoms on different areas of the herringbone reconstruction. **c)** Different dI/dV spectra recorded on three different Co atoms that exhibit different Fano line shapes. The yellow spectrum corresponds to a reference spectrum recorded on the Au surface. Spectra are offset for clarity. Feedback opened at 50 mV, 0.5 nA with $V_{\mathrm{mod}} = 2$ mV.

fig. 4.14a. The red data points correspond to measurements on single Co atoms. In total, more than 125 measurements were evaluated on five different Co atoms. The black data points correspond to measurements on Au adatoms. By comparing the data on Au with the previously recorded data from the test measurements on Au adatoms, it seems that there is some more instability in the system, as the data points are slightly more scattered around the theoretically predicted line. Nontheless, the data on the Au adatoms is in agreement with the expectations for spin-degenerate transport. In the above-mentioned publication on shot noise on Co atoms [24], the data points on the Co atoms were all situated below the line of spin-degenerate transport, which indicates a certain degree of spin polarization. In our measurements, however, none of the data points falls into the spin-polarized region, but all the data points lie even above the theoretical line for spin-degenerate transport.

The occurance of such high Fano factors is rather complex to understand, as it indicates that more than one conduction channel participates in the transport process. These channels can be intrinsic to the system, such as the transport through several valence orbitals of the Co atom itself. By means of theoretical calculations, A. Burtzlaff, et al. determined a much lower transport probability through two of the valence channels in comparison to the third one. Following this argument, the option of more than one intrinsic transport path through the Co atom can be excluded.

However, also the transport through the Kondo impurity itself and the occuring quasiparticle scattering, might account for the higher noise level. There has been a multitude of theoretical publications that treat the transport through a Kondo system in a quantum dot geometry [162, 205–207]. From their transport analysis, they determine two components in the shot noise: a single-quasiparticle scattering, which leads to an effective charge $e^* = e$ of the quasiparticles and a two-quasiparticle scattering, which results from the interaction between the quasiparticles and which yields $e^* = 2e$. As both processes occur simultaneously, the shot noise analysis results in an average value of $e^* = 5e/3$ and hence leads to enhanced noise levels. However, these calculations have been performed for quantum-dot systems under special conditions, such as equal coupling to the right and left lead and the existence of particle-hole symmetry. These conditions can not be necessarily fulfilled in STM junctions. Therefore, it is not clear how the interaction between the quasiparticles would affect the shot noise in real STM measurements.

From the noise data itself, the origin of the number of channels can not be determined. Instead, a theoretical analysis is required to exclude certain options. If the Kondo system itself allows for two transport pathes, measurements on a different substrate that leads to a variation of the Kondo temperature might help to clarify this aspect. The Kondo temperature of Co on Au(111) is approx. 19 K

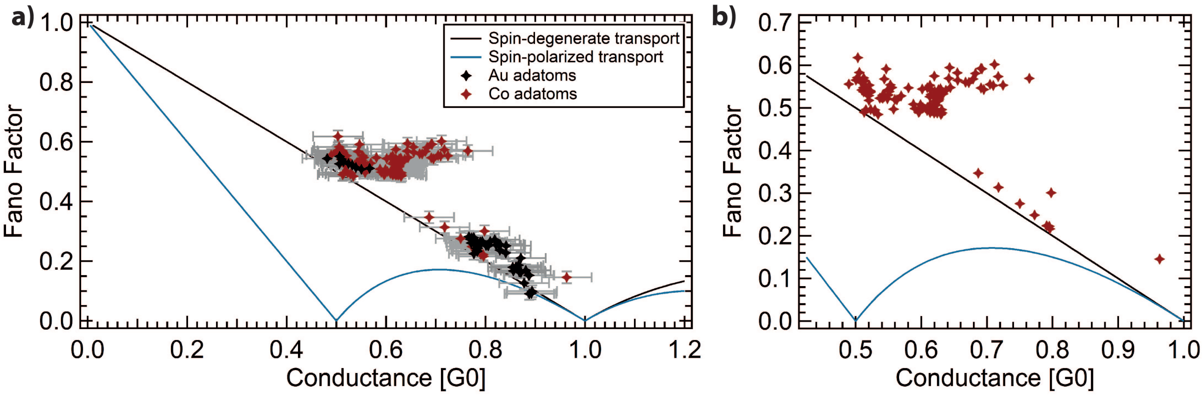

Figure 4.14. **a)** Fano factor in dependence of the junction conductance for measuremenets on cobalt atoms on the Au(111) surface (red measurement points). The black data points correspond to measurements on Au adatoms. The blue and black solid lines indicate the theoretical expectations for spin-polarized and spin-degenerate transport, respectively. For the evaluation, a resistance of $R_{\text{Shunt}} = 221\,\text{k}\Omega$ was assumed. **b)** Zoom into the region with the experimental data points. For sake of clarity, the error bars and the Au reference data points are omitted.

[203], which can be associated with an energy of $k_B \times T_K = 1.6\,\text{meV}$. With the highest typical voltages during the shot-noise measurements being around 12 mV to 16 mV, the transort primarily takes place at energies where Kondo correlations should be weak or absent. Cobalt atoms on Cu(100), in contrast, exhibit Kondo temperatures between 90 K to 200 K [208–211], which can be associated to an energy of 8 meV to 17 meV. Therefore, the shot noise measurements would take place at energies where Kondo correlations play a role.

All in all, more theoretical and experimental analysis is required to explain the discrepancy between the spin-polarized transport that is observed by A. Burtzlaff, et al. for single Co atoms on a Au(111) surface and our measurements on the same system that indicate transport through more than one conduction channel.

CHAPTER V

Summary and Conclusions

In this thesis, the properties of single atoms and molecules where studied with a scanning tunneling microscope by making two complementary approaches. In the first part, different arrangements of Fe-5,10,15,20-tetra-pyridyl-porphyrin (Fe-TPyP) molecules were investigated on a Au(111) substrate and on MoS_2. On Au(111), three different adsorption structures of Fe-TPyP could be observed that emerged under the same preparation conditions.

In the densely-packed structure, all molecules were found to exhibit the same properties. Within the second structure — the distorted structure — , two types of molecules could be distinguished. The third structure of Fe-TPyP on Au(111) was only obtained with one particular evaporator, indicating that during the evaporation procedure some other species was co-evaporated. In this structure, a more random distribution of the molecules was found, and no densely-packed islands were observable.

To understand the differences between the three structures of Fe-TPyP on Au(111), their geometry was analyzed by means of AFM measurements. From constant-height Δf maps recorded on all three structures, differences in their adsorption geometry could be identified. In the densely-packed structure, the pyridyl legs are the most protruding moiety, with all four pyridyl legs exhibiting a uniform dihedral angle. For the distorted staggered structure, two opposing pyridyl groups were rotated more strongly than the other two. Moreover, this asymmetric rotation of the pyridyl legs was accompanied by a distortion of the molecules. The same asymmetry of the rotational angles and distortion was observable on the disordered adatom-mediated structure. However Δf maps indicated that in this structure, the pyrrole groups are the highest molecular moiety and the pyridyl legs are more flattened, possibly due to the influence of the aforementioned coevapored species.

The different intramolecular geometries also affected the electronic properties. By analyzing the energetic position of the LUMO and LUMO+1 orbitals of all three structures, a changing hybridization with the substrate could be observed by their shift towards the Fermi level. The densely-packed structure has the energetically highest LUMO orbital and is hence interpreted as the most decoupled structure, in agreement to the findings from the structure analysis, as the more perpendicular pyridyl legs minimize the hybridization effects. The molecules in the distorted staggered structure exhibit asymmetrically rotated pyridyl groups, which slightly increases the interaction with the substrate and shifts the LUMO orbital towards the Fermi level. For the molecules in the disordered adatom-mediated structure, the flattening of all four pyridyl legs leads to the strongest hybridization effects, which results in the lowest LUMO orbital.

Furthermore, the geometric differences also determine the magnetic properties of the Fe-TPyP molecules. The molecules in the densely-packed structure exhibit no transverse anistropy, as the D_{4h} symmetry of the ligand field is still maintained. For the molecules in the distorted staggered structure, the symmetry of the ligand field is reduced to D_{2h} due to the asymmetric intramolecular distortions, which introduces a transverse magnetic anisotropy term due to the lifting of the degeneracy between the d_{xz} and d_{yz} orbitals. For the type II molecules of the distorted staggered structure, a spin crossover occured from the $S = 1$ intermediate-spin state to the $S = 2$ high-spin state. This transition to the high-spin state was explained by an elongation of the Fe-N bonds, which might originate from a stronger disortion of the molecules or a displacement of the Fe atom into the surface plane.

The final aspect that was compared for these structures was the observation of vibrational excitations. The type I molecules of the distorted staggered structure and the molecules in the disordered adatom-mediated structure exhibited a variety of higher-lying steps in the $\mathrm{d}I/\mathrm{d}V$ signal, which where attributed to vibrational excitations. This interpretation was confirmed by means of HREELS measurements. To explain the different intensities of the vibrational excitations four the different structures, their electronic levels have been compared. The proximity of electronic resonances to the Fermi level for two structures of Fe-TPyP leads to an enhanced excitation cross section. Therefore, vibrational steps can be observed in the corresponding $\mathrm{d}I/\mathrm{d}V$ spectra with high intensity. The shifting of these resonances away from E_F for the other two structures decreases this resonant contribution, which hence leads to the absence of vibrational excitations in the spectra.

After the minute structural differences between the molecules and their impact on the molecular properties was compared, another molecular structure of Fe-TPyP was studied. Here, however, the molecules were post-annealed on the Au(111) sample at around 300 °C, which led to major modifications in the molecular structure. Several intramolecular C-H bonds were broken and new C-C bonds have been formed between the pyridyl legs and the adjacent pyrrole groups. This led to a flat structure of the molecules. In this annealed structure, different electronic properties were oberved in comparison to the previously studied phases and no signs of magnetic or vibrational excitations were found in the spectra. This emphasized the importance of understanding the impact of changes in the molecular structure on the molecular properties.

Finally, to tune the coupling to the surface in a controlled way, the Fe-TPyP molecules were also investigated on a decoupling $\mathrm{MoS_2}$ layer, which was grown on Au(111). Here, the molecules also showed spin- and vibrational excitations that matched with the previous findings on Au(111). However, the vibrational excitations were more pronounced at higher energies, due to the up-shifting of the resonances.

In the second part of this thesis, a complementary approach was chosen to study the electron correlations within single atoms. In contrast to typical STM measurements, the information about a system is not obtained from the DC current but from the current fluctuations, *i.e.*, the shot noise of the system. In order to detect those fluctuations in the tunneling current, measurements at several hundreds of kHz are required, in order to assure that other noise sources such as the $1/f$ noise do not dominate the signal. Threrefore, a set of high-frequency amplifiers has been implemented into the STM. To examine the viability of the system, shot noise measurements were first performed on a test system, namely Au adatoms on a Au(111) surface, were the spin-degenerate transport is well understood. Our results were in agreement to literature, such that the test measurements confirm the functionality of the setup. Moreover, temperature-dependent measurements were perfomed, where the thermal noise of atomic contacts has been evaluated for different STM temperatures. As the thermal noise is in the same order of magnitude as the shot-noise level, an increase of the thermal noise with temperature confirmed that the setup exhibits the necessary sensitivity. Finally, preliminary results on cobalt adatoms on the Au(111) surface have been presented. Our experimental results indicate transport through more than one transport channel, which differs from previously published findings on the same system [24], where they report on transport through one spin-polarized channel. Further experimental and theoretical analysis is required to explain the contradicting findings.

The results presented in this thesis emphasize the importance of a proper understanding of the properties of single atoms and molecules on surfaces. As we have seen in the first part, minute changes in the adsorption geometry of a molecule can have an influence on its electronic and magnetic properties. Therefore, to ever built functional units out of single molecules, a detailed understanding of all the parameters that influence the molecular properties is essential. Moreover, the complex data of the shot-noise measurements on Co on Au(111) shows that even seemingly simple aspects such as the electron transport through single atoms is not fully understood. Therefore, more research is necessary to grasp the properties of nanoscopic systems.

APPENDIX A

Data Acquisition and Analysis for the Shot Noise Measurements

In chapt. IV.B, we already commented on the technical aspects of the measurements. Another challenge of shot-noise measurements is the data acquisition. As long measurement procedures have to be followed to acquire a single set of spectra, a complex LabVIEW procedure was developed. Its structure will be shortly introduced in the following.

The Measurement Procedure

For the determination of a Fano factor, consecutive series of shot-noise measurements have to be performed at different contact resistances and bias voltages. Therefore, within a LabVIEW procedure (see fig. A.1), the tip automatically moves to the desired adatom, whose coordinates are entered beforehand. The feedback is switched off and the tip is slowly approached by several Å up to a predefined value. Then, the external bias supply from the DSP boards is disabled and the bias box supplies the necessary bias voltage of 200 mV at a very low noise level. When the preparations are finished, a loop is executed, that first records the DC current that flows through the junction for a time span of 2 s. Its average value later allows to determine the junction resistance and monitor junction instabilities. Then, the current connection to the IV-converter is interrupted and noise spectra are recorded. This series of measuring the DC current and recording the noise spectra is repeated for each of the 21 bias voltages that can be supplied by the bias box (0 mV, ±20 mV, ..., ±200 mV). After this measurement set, where the tip has been in contact with the sample for approx. 20 min with the feedback disabled, the tip is slowly retracted and an STM image is recorded. Each of those measurement sets allows to determine the Fano factor for one specific junction resistance. Hence, the same measurement is automatically repeated for several junction resistances by consecutively approaching the tip.

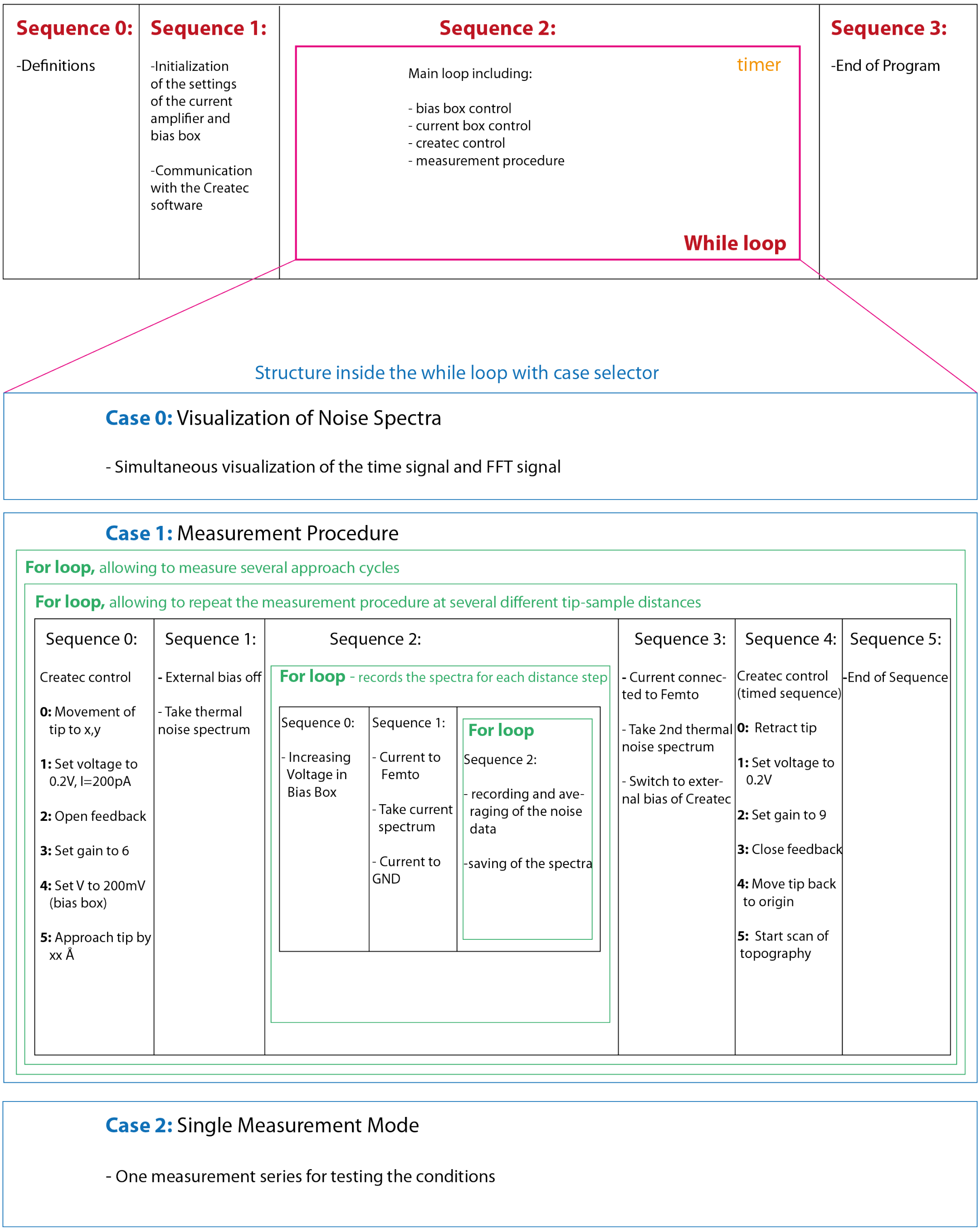

Figure A.1. Schematic structure of the LabVIEW Programm developed to automatically record the shot noise at various distances. The procedure consists of 4 parts. Upon starting of the program, the different ports (bias box, current box, connection to Createc electronics...) are initialized. Then, the measurement procedure is running in a while loop, allowing to switch between different cases. In **case 0**, the noise data is directly visualized in real time. This mode is useful to check the measurement conditions and look for noise sources, as a fast Fourier transform (FFT) signal is simultaneously displayed. In **case 2**, a single measurement run is executed, where the tip stays at the current position and noise spectra are recorded at one specific bias voltage. The spectrum is automatically saved into a subfolder. This mode allows to test the stability of the junction. **Case 1** is the actual measurement procedure, where noise spectra are recorded at different conductances in consecutive measurements. After the measurement at one distance is finished, a topographic image is automatically recorded to check the adatom position, before the measurement at the next distance starts.

APPENDIX B

Comparison of the Saddle Height of FeTPyP

In chapt. III.E, different structures of Fe-TPyP were compared and different rotational angles of their pyridyl legs accompanied by intramolecular distortions were found. Along with the changes in the orientation of the pyridyl legs, the strength of the saddle deformation is expected to change, as it is induced by the steric hindrance between the hydrogen atoms of the pyridyl legs and the pyrrole groups. Hence, the asymmetric rotation of the pyridyl moieties in the distorted staggered arrangement might influence the strength of the saddle shape. To characterize the strength of the saddle deformation, Δf approach curves were recorded. Therefore, the tip was positioned on different sites of the molecule and the tip-sample distance was reduced until a minimum in the Δf curve was seen. The minimum in the Δf curve indicates the distance at which repulsive forces between the tip and the molecule start to become non-neglegible. Therefore, it is taken at as reference point to determine the height of the re-

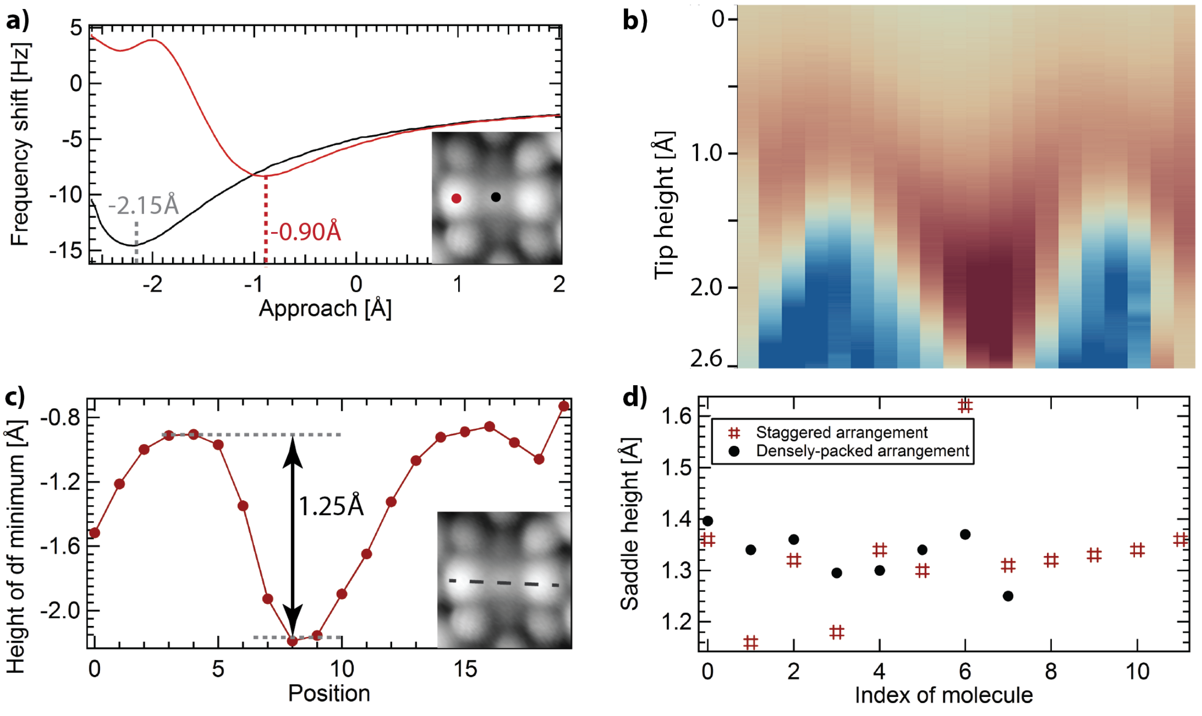

Figure B.1. Determination of the height of the saddle deformation. **a)** Δf approach curves recorded in the center (black) and on the upper pyrrole (red) of an Fe-TPyP molecule in the densely-packed structure. **b)** 20 approach spectra determined along the upper pyrroles of the molecule. **c)** Values of the determined minima of the Δf curves in c). A value of 1.25 Å was determined between the height of the upper pyrroles and the Fe center. **d)** Evaluation of the saddle height for several molecules in the densely-packed structure and the distorted staggered arrangement, showing similar saddle heights for both structures.

spective molecular moiety. Figure B.1a shows one of these Δf approach curves recorded in the center of an Fe-TPyP molecule in the densely-packed structure (black), with the gray dashed line indicating its minimum. Such curves where recorded on several locations across the molecule (see fig. B.1b). By determining the minima of the curves on all sites, an estimate of the height differences of the corresponding moieties can be determined. For the depicted set of spectra, the difference in the height of the upper pyrrole groups and the Fe center, *i.e.*, the saddle height, is around 1.25 Å (see fig. B.1c). This value was determined for several molecules in the densely-packed structure and the distorted staggered arrangement. As shown in fig. B.1d, the determined saddle heights for both structures are indistinguishable within the range of their variation.

However, when taking a closer look at some of these approach curves, a deviation of the increasing Δf signal is visible closely after the first minimum (see red curve in fig. B.1a, recorded on the upper pyrrole group). This second minimum might be indicating a deformation of the molecule upon tip approach. As this occured in a multitude of spectra especially on the ligand of the molecule, it might result from the flexibility of the pyrrole groups, which follow the attractive and repulsive potential of the tip, respectively. Hence, when approaching the tip, the pyrrole groups are attracted by the tip and lifted upwards. When the tip is approached further, the pyrrole groups start to bend down again, as the repulsive forces from the tip are increasing. This flexibility of the molecules makes it difficult to evaluate the determined distances in terms of the actual saddle height, as distortion effects can not be neglected. Therefore, no unambiguous information can be obtained from the Δf approach spectra.

References

1. Feynman, R. P. There's Plenty of Room at the Bottom. *Engineering and Science* **23,** 22–36 (1960).
2. Taniguchi, N. On the Basic Concept of "Nano-Technology". *Proc. Intl. Conf. Prod. Eng. Tokyo. Part II* (1974).
3. Von Hippel, A. Molecular Engineering. *Science* **123,** 315–317 (1956).
4. Aviram, A. & Ratner, M. A. Molecular Rectifiers. *Chem. Phys. Lett.* **29,** 277–283 (1974).
5. Drexler, K. E. Molecular Engineering: An Approach to the Development of General Capabilities for Molecular Manipulation. *P. Natl. Acad. Sci.* **78,** 5275–5278 (1981).
6. Drexler, K. E. *Engines of Creation: The Coming Era of Nanotechnology* (Anchor Books, New York, 1986).
7. Bumm, L. A. *et al.* Are Single Molecular Wires Conducting? *Science* **271,** 1705–1707 (1996).
8. Reed, M. A. Conductance of a Molecular Junction. *Science* **278,** 252–254 (1997).
9. Tans, S. J. *et al.* Individual Single-Wall Carbon Nanotubes as Quantum Wires. *Nature* **386,** 474–477 (1997).
10. Tans, S. J., Verschueren, A. R. M. & Dekker, C. Room-Temperature Transistor based on a Single Carbon Nanotube. *Nature* **393,** 49–52 (1998).
11. Green, J. E. *et al.* A 160-kilobit Molecular Electronic Memory Patterned at $10^1$1 Bits per Square Centimetre. *Nature* **445,** 414–417 (2007).
12. Song, H. *et al.* Observation of Molecular Orbital Gating. *Nature* **462,** 1039–1043 (2009).
13. Kudernac, T. *et al.* Electrically Driven Directional Motion of a Four-Wheeled Molecule on a Metal Surface. *Nature* **479,** 208–211 (2011).
14. Fuechsle, M. *et al.* A Single-Atom Transistor. *Nat. Nano* **7,** 242–246 (2012).
15. Kalff, F. E. *et al.* A Kilobyte Rewritable Atomic Memory. *Nat. Nano* **11,** 926–929 (2016).
16. Sauvage, J.-P., Stoddart, S. J. F. & Feringa, B. L. *The Nobel Prize in Chemistry* (2016).
17. Kroemer, H. *The Nobel Prize in Physics 2000; Quasi-Electric Fields and Band Offsets: Teaching Electrons New Tricks* (2000).
18. Jurow, M., Schuckman, A., Batteas, J. D. & Drain, C. M. *Porphyrins as Molecular Electronic Components of Functional Devices* (2010).
19. Binnig, G., Rohrer, H., Gerber, C. & Weibel, E. Surface Studies by Scanning Tunneling Microscopy. *Phys. Rev. Lett.* **49,** 57–61 (1982).
20. Binnig, G., Rohrer, H., Gerber, C. & Weibel, E. Tunneling through a Controllable Vacuum Gap. *Appl. Phys. Lett.* **40,** 178–180 (1982).
21. Stipe, B. C., Rezaei, M. A & Ho, W. Single-Molecule Vibrational Spectroscopy and Microscopy. *Science* **280,** 1732–1735 (1998).

22. Heinrich, A. J., Gupta, J. A., Lutz, C. P. & Eigler, D. M. Single-Atom Spin-Flip Spectroscopy. *Science* **306,** 466–469 (2004).
23. Shirato, N. *et al.* Elemental Fingerprinting of Materials with Sensitivity at the Atomic Limit. *Nano Lett.* **14,** 6499–6504 (2014).
24. Burtzlaff, A., Weismann, A., Brandbyge, M. & Berndt, R. Shot Noise as a Probe of Spin-Polarized Transport through Single Atoms. *Phys. Rev. Lett.* **114,** 016602 (2015).
25. Choi, T. *et al.* Atomic-scale Sensing of the Magnetic Dipolar Field from Single Atoms. *Nat. Nano* **12,** 420–424 (2017).
26. Tersoff, J. & Hamann, D. R. Theory and Application for the Scanning Tunneling Microscope. *Phys. Rev. Lett.* **50,** 1998–2001 (1983).
27. Bardeen, J. Tunnelling from a Many-Particle Point of View. *Phys. Rev. Lett.* **6,** 57–59 (1961).
28. Gross, L. *et al.* High-Resolution Molecular Orbital Imaging Using a p-Wave STM Tip. *Phys. Rev. Lett.* **107,** 0861011–0861014 (2011).
29. Lang, N. D. Spectroscopy of Single Atoms in the Scanning Tunneling Microscope. *Phys. Rev. B* **34,** 5947–5950 (1986).
30. Selloni, A., Carnevali, P., Tosatti, E. & Chen, C. D. Voltage-Dependent Scanning-Tunneling Microscopy of a Crystal Surface: Graphite. *Phys. Rev. B* **31,** 2602–2605 (1985).
31. Lorente, N. & Persson, M. Theory of Single Molecule Vibrational Spectroscopy and Microscopy. *Phys. Rev. Lett.* **85,** 2997–3000 (2000).
32. Feenstra, R. M., Stroscio, J. A. & Fein, A. P. Tunneling Spectroscopy of the Si(111)2 × 1 Surface. *Surf. Sci.* **181,** 295 –306 (1987).
33. Stroscio, J. A., Feenstra, R. M. & Fein, A. P. Electronic Structure of the Si(111)2 × 1 Surface by Scanning-Tunneling Microscopy. *Phys. Rev. Lett.* **57,** 2579–2582 (1986).
34. Ziegler, M., Néel, N., Sperl, A., Kröger, J. & Berndt, R. Local Density of States from Constant-Current Tunneling Spectra. *Phys. Rev. B* **80,** 125402 (2009).
35. *Application Notes 3: About Lock-In Amplifiers* Stanford Research Systems, Inc. (Sunnyvale, CA, USA, 2004).
36. Fernández-Torrente, I. *Local Spectroscopy of Bi-Molecular Assemblies: Screening, Charge Transfer, and Magnetism at the Molecular Scale,* PhD Thesis (Freie Universität Berlin, 2008).
37. Crispin, X. *et al.* Characterization of the Interface Dipole at Organic/ Metal Interfaces. *J. Am. Chem. Soc.* **124,** 8131–8141 (2002).
38. Ho, W. Single-Molecule Chemistry. *J. Chem. Phys.* **117,** 11033–11061 (2002).
39. Weinberg, W. H. Inelastic Electron Tunneling Spectroscopy: A Probe of the Vibrational Structure of Surface Species. *Annu. Rev. Phys. Chem.* **29,** 115–139 (1978).
40. Hansma, P. K. & Kirtley, J. Recent Advances in Inelastic Electron Tunneling Spectroscopy. *Acc. Chem. Res.* **11,** 440–445 (1978).
41. Gauyacq, J.-P., Lorente, N. & Novaes, F. D. Excitation of Local Magnetic Moments by Tunneling Electrons. *Prog. Surf. Sci.* **87,** 63–107 (2012).
42. Lorente, N. Mode Excitation Induced by the Scanning Tunnelling Microscope. *Appl. Phys. A* **78,** 799–806 (2004).

43. Galperin, M., Nitzan, A. & Ratner, M. A. Resonant Inelastic Tunneling in Molecular Junctions. *Phys. Rev. B* **73,** 045314 (2006).

44. Gaudioso, J., Lauhon, L. J. & Ho, W. Vibrationally Mediated Negative Differential Resistance in a Single Molecule. *Phys. Rev. Lett.* **85,** 1918–1921 (2000).

45. Franke, K. J. & Pascual, J. I. Effects of Electron–Vibration Coupling in Transport through Single Molecules. *J. Phys.: Condens. Matter* **24,** 394002 (2012).

46. Temirov, R. and Soubatch, S. and Lassise, A. and Tautz, F. S. Bonding and Vibrational Dynamics of a Large π-conjugated Molecule on a Metal Surface. *J. Phys.: Condens. Matter* **20,** 224010 (2008).

47. Franke, K. I., Schulze, G. & Pascual, J. I. Excitation of Jahn-Teller Active Modes during Electron Transport through Single C_{60} Molecules on Metal Surfaces. *J. Phys. Chem. Lett.* 500–504 (2010).

48. Liu, N., Pradhan, N. A. & Ho, W. Vibronic States in Single Molecules: C_{60} and C_{70} on Ultrathin Al_2O_3 Films. *J. Chem. Phys.* **120,** 11371–11375 (2004).

49. Frederiksen, T. *et al.* Dynamic Jahn-Teller Effect in Electronic Transport through Single C_{60} Molecules. *Phys. Rev. B: Condens. Matter* **78,** 233401 (2008).

50. Binnig, G., Quate, C. F. & Gerber, C. Atomic Force Microscope. *Phys. Rev. Lett.* **56,** 930–933 (1986).

51. Voigtländer, B. *Scanning Probe Microscopy* (Springer Berlin Heidelberg, 2015).

52. Giessibl, F. J. Forces and Frequency Shifts in Atomic-Resolution Dynamic-Force Microscopy. *Phys. Rev. B* **56,** 16010–16015 (1997).

53. Giessibl, F. J. Advances in Atomic Force Microscopy. *Rev. of Modern Phys.* **75,** 949–983 (2003).

54. Kopitzki, K. *Einführung in die Festkörperphysik* (Teubner Studienbücher Physik, Stuttgart, 1989).

55. Hamaker, H. C. The London—van der Waals Attraction between Spherical Particles. *Physica* **4,** 1058–1072 (1927).

56. Jones, J. E. On the Determination of Molecular Fields. —II. From the Equation of State of a Gas. *Proc. R. Soc. Lond. A. Math. Phys. Sci.* **106,** 463–477 (1924).

57. Umbach, T. R. *Magnetic and Electronic Properties of Supramolecular Architectures on Metal Surfaces,* PhD Thesis (Freie Universität Berlin, 2013).

58. Besocke, K. An Easily Operable Scanning Tunneling Microscope. *Surf. Sci.* **181,** 145 –153 (1987).

59. Giessibl, F. J. Advances in Atomic Force Microscopy. *Rev. Mod. Phys.* **75,** 949–983 (2003).

60. Horacas, I., R. Fernandez, J. M.G.-R., Colchero, J. & Baro, A. M. *Rev. Sci. Instrum.* **78** (2007).

61. Igor Pro. *WaveMetrics* **6.3.7.2.** (1988-2014).

62. Ruby, M. SpectraFox: A Free Open-Source Data Management and Analysis Tool for Scanning Probe Microscopy and Spectroscopy. *SoftwareX* **5,** 31–36 (2016).

63. Reinert, F., Nicolay, G., Schmidt, S., Ehm, D. & Hüfner, S. Direct Measurements of the L-Gap Surface States on the (111) Face of Noble Metals by Photoelectron Spectroscopy. *Phys. Rev. B* **63,** 1154151–1154157 (2001).

64. Kondo, J. Resistance Minimum in Dilute Magnetic Alloys. *Prog. Theor. Phys.* **32,** 37–49 (1964).

65. Gottfried, J. M. Surface Chemistry of Porphyrins and Phthalocyanines. *Surf. Sci. Rep.* **70,** 259–379 (2015).

66. Iancu, V., Schouteden, K., Li, Z. & Van Haesendonck, C. Electron-Phonon Coupling in Engineered Magnetic Molecules. *Chem. Commun.* 11359–11362 (2016).
67. Liu, B. *et al.* An Iron-Porphyrin Complex with Large Easy-Axis Magnetic Anisotropy on Metal Substrate. *ACS Nano* **11,** 11402–11408 (2017).
68. Wang, W. *et al.* Intramolecularly resolved Kondo Resonance of High-Spin Fe(II)-porphyrin adsorbed on Au(111). *Phys. Rev. B* **91,** 045440 (2015).
69. Auwärter, W. *et al.* Self-Assembly and Conformation of Tetrapyridyl-Porphyrin Molecules on Ag(111). *J. Chem. Phys.* **124,** 194708 (2006).
70. Auwärter, W. *et al.* Conformational Adaptation and Selective Adatom Capturing of Tetra-pyridyl-porphyrin Molecules on a Copper (111) Surface. *J. Am. Chem. Soc.* **129,** 11279–11285 (2007).
71. Rubio-Verdú, C. *et al.* Orbital-selective Spin Excitation of a Magnetic Porphyrin. *Communications Physics* **1,** 15 (2018).
72. Albrecht, F., Bischoff, F., Auwärter, W., Barth, J. V. & Repp, J. Direct Identification and Determination of Conformational Response in Adsorbed Individual Nonplanar Molecular Species Using Noncontact Atomic Force Microscopy. *Nano Lett.* 7703—7709 (2016).
73. Chen, X. *et al.* Conformational Adaptation and Manipulation of Manganese Tetra(4-Pyridyl)-Porphyrin Molecules on Cu(111). *J. Chem. Phys.* **146,** 092316 (2017).
74. Liao, M.-S. & Scheiner, S. Electronic Structure and Bonding in Metal Porphyrins, Metal=Fe, Co, Ni, Cu, Zn. *J. Chem. Phys.* **117,** 205–219 (2002).
75. Zhao, A. *et al.* Controlling the Kondo Effect of an Adsorbed Magnetic Ion Through Its Chemical Bonding. *Science* **309,** 1542–1544 (2005).
76. Zotti, L. *et al.* Ab-Initio Calculations and STM Observations on Tetrapyridyl and Fe(II)-Tetrapyridyl-Porphyrin Molecules on Ag(111). *Surf. Sci.* **601,** 2409–2414 (2007).
77. Zoldan, V. C., Faccio, R., Gao, C. & Pasa, A. A. Coupling of Cobalt–tetraphenylporphyrin Molecules to a Copper Nitride Layer. *J. Phys. Chem. C* **117,** 15984–15990 (2013).
78. Zhang, Q., Kuang, G., Pang, R., Shi, X. & Lin, N. Switching Molecular Kondo Effect via Supramolecular Interaction. *ACS Nano* **9,** 12521–12528 (2015).
79. Auwärter, W. *et al.* Controlled Metalation of Self-Assembled Porphyrin Nanoarrays in Two Dimensions. *Chem. Phys. Chem.* **8,** 250–254 (2007).
80. Jarvis, S. P. *et al.* Physisorption Controls the Conformation and Density of States of an Adsorbed Porphyrin. *J. Phys. Chem. C* **119,** 27982–27994 (2015).
81. Gatteschi, D., Sessoli, R. & Villain, J. *Molecular Nanomagnets* (Oxford University Press, 2006).
82. Auwärter, W. *et al.* Site-Specific Electronic and Geometric Interface Structure of Co-Tetraphenyl-Porphyrin Layers on Ag(111). *Phys. Rev. B* **81,** 245403 (2010).
83. Buchner, F. *et al.* Substrate-Mediated Phase Separation of Two Porphyrin Derivatives on Cu(111). *Chem. Eur. J.* **17,** 10226–10229 (2011).
84. Stark, M. *et al.* Coverage Dependent Disorder–Order Transition of 2H-Tetraphenylporphyrin on Cu(111). *Langmuir* **29,** 4104–4110 (2013).
85. Weber-Bargioni, A. *et al.* Visualizing the Frontier Orbitals of a Conformationally Adapted Metalloporphyrin. *Chem. Phys. Chem.* **9,** 89–94 (2008).
86. *Probe Particle Model, http://nanosurf.fzu.cz/ppr/* (accessed June, 2018).

87. Hapala, P., Temirov, R., Tautz, F. S. & Jelínek, P. Origin of High-Resolution IETS-STM Images of Organic Molecules with Functionalized Tips. *Phys. Rev. Lett.* **113,** 226101 (2014).

88. Hapala, P. *et al.* Mechanism of High-Resolution STM/AFM Imaging with Functionalized Tips. *Phys. Rev. B* **90,** 085421 (2014).

89. Reinert, F., Nicolay, G., Schmidt, S., Ehm, D. & Hüfner, S. Direct Measurements of the L-Gap Surface States on the (111) Face of Noble Metals by Photoelectron Spectroscopy. *Phys. Rev. B* **63,** 115415 (2001).

90. Lamoen, D. & Parrinello, M. Geometry and Electronic Structure of Porphyrins and Porphyrazines. *Chem. Phys. Lett.* **248,** 309–315 (1996).

91. Heinrich, B. W. *et al.* Change of the Magnetic Coupling of a Metal–Organic Complex with the Substrate by a Stepwise Ligand Reaction. *Nano Lett.* **13,** 4840–4843 (2013).

92. Heinrich, B. W., Braun, L., Pascual, J. I. & Franke, K. J. Tuning the Magnetic Anisotropy of Single Molecules. *Nano Lett.* **15,** 4024–4028 (2015).

93. Bernien, M. *et al.* Fe-Porphyrin Monolayers on Ferromagnetic Substrates: Electronic Structure and Magnetic Coupling Strength. *Phys. Rev. B* **76,** 214406 (2007).

94. Wende, H. *et al.* Substrate-induced Magnetic Ordering and Switching of Iron Porphyrin Molecules. *Nat. Mater.* **6,** 516–520 (2007).

95. Ohta, N., Arafune, R., Tsukahara, N., Kawai, M. & Takagi, N. Enhancement of Inelastic Electron Tunneling Conductance Caused by Electronic Decoupling in Iron Phthalocyanine Bilayer on Ag(111). *J. Phys. Chem. C* **117,** 21832–21837 (2013).

96. Vancoillie, S., Zhao, H., Tran, V. T., Hendrickx, M. F. A. & Pierloot, K. Multiconfigurational Second-Order Perturbation Theory Restricted Active Space (RASPT2) Studies on Mononuclear First-Row Transition-Metal Systems. *J. Chem. Theory Comput.* **7,** 3961–3977 (2011).

97. Liao, M.-S., Watts, J. D. & Huang, M.-J. Electronic Structure of Some Substituted Iron(II) Porphyrins. Are They Intermediate or High Spin? *J. Phys. Chem. A* **111,** 5927–5935 (2007).

98. Tanaka, K. *et al.* Electron Density Studies of Porphyrins and Phthalocyanines. IV. Electron Density Distribution in Crystals of (Meso-Tetraphenylporphinato) Iron(II). *J. Chem. Phys.* **84,** 6969–6978 (1986).

99. Markus Ternes. Spin Excitations and Correlations in Scanning Tunneling Spectroscopy. *New J. Phys.* **17,** 063016 (2015).

100. Stróżecka, A., Eiguren, A. & Pascual, J. I. Quasiparticle Interference around a Magnetic Impurity on a Surface with Strong Spin-Orbit Coupling. *Phys. Rev. Lett.* **107,** 186805 (2011).

101. Frisch, M. J. *et al.* Gaussian09 Revision D.01. Gaussian Inc. Wallingford CT 2009.

102. Anderson, P. W. Localized Magnetic States in Metals. *Phys. Rev.* **124,** 41–53 (1961).

103. Schrieffer, J. R. & Wolff, P. A. Relation between the Anderson and Kondo Hamiltonians. *Phys. Rev.* **149,** 491–492 (1966).

104. Bhandary, S. *et al.* Graphene as a Reversible Spin Manipulator of Molecular Magnets. *Phy. Rev. Lett.* **107,** 257202 (2011).

105. Bhandary, S. *et al.* Manipulation of Spin State of Iron Porphyrin by Chemisorption on Magnetic Substrates. *Phys. Rev. B* **88,** 024401 (2013).

106. Bhandary, S. *et al.* Correlated Electron Behavior of Metal-Organic Molecules: Insights from Density Functional Theory Combined with Many-Body Effects Using Exact Diagonalization. *Phys. Rev. B* **93,** 155158 (2016).
107. Baumann, S., Donati, F. & Stepanow, S. Origin of Perpendicular Magnetic Anisotropy and Large Orbital Moment in Fe Atoms on MgO. *Phys. Rev. Lett.* **115,** 237202 (2015).
108. Rau, I. G. *et al.* Reaching the Magnetic Anisotropy Limit of a 3d Metal Atom. *Science* **344,** 988–992 (2014).
109. Lorente, N. & Persson, M. Theory of Single Molecule Vibrational Spectroscopy and Microscopy. *Phys. Rev. Lett.* **85,** 2997–3000 (2000).
110. Lauhon, L. J. & Ho, W. Effects of Temperature and other Experimental Variables on Single Molecule Vibrational Spectroscopy with the Scanning Tunneling Microscope. *Rev. Sci. Instrum.* **72,** 216–223 (2001).
111. Lorente, N., Persson, M., Lauhon, L. J. & Ho, W. Symmetry Selection Rules for Vibrationally Inelastic Tunneling. *Phys. Rev. Lett.* **86,** 2593–2596 (2001).
112. Ahmadi, G. *Metal-Organic Networks and Metal-Porphyrins on Superconducting Pb(111): Structural, Electronic and Magnetic Properties,* PhD Thesis (Freie Universität Berlin, 2017).
113. Kuang, G. *et al.* Mechanically-Controlled Reversible Spin Crossover of Single Fe-Porphyrin Molecules. *ACS Nano* **11,** 6295–6300 (2017).
114. Chen, J., Reed, M. A., Rawlett, A. M. & Tour, J. M. Large On-Off Ratios and Negative Differential Resistance in a Molecular Electronic Device. *Science* **286,** 1550 (1999).
115. Grobis, M., Wachowiak, A., Yamachika, R. & Crommie, M. F. Tuning Negative Differential Resistance in a Molecular Film. *Appl. Phys. Lett.* **86,** 204102 (2005).
116. Wang, B. *et al.* Effects of Discrete Energy Levels on Single-Electron Tunneling in Coupled Metal Particles. *Appl. Phys. Lett.* **82,** 3767–3769 (2003).
117. Xue, Y. *et al.* Negative Differential Resistance in the Scanning-Tunneling Spectroscopy of Organic Molecules. *Phys. Rev. B* **59,** R7852–R7855 (1999).
118. Chen, L. *et al.* Mechanism for Negative Differential Resistance in Molecular Electronic Devices: Local Orbital Symmetry Matching. *Phys. Rev. Lett.* **99,** 146803 (2007).
119. Lyo, I.-W. & Avouris, P. Negative Differential Resistance on the Atomic Scale: Implications for Atomic Scale Devices. *Science* **245,** 1369 (1989).
120. Fernández-Torrente, I., Kreikemeyer-Lorenzo, D., Stróżecka, A., Franke, K. J. & Pascual, J. I. Gating the Charge State of Single Molecules by Local Electric Fields. *Phys. Rev. Lett.* **108,** 036801 (2012).
121. Warner, B. *et al.* Tunable Magnetoresistance in an Asymmetrically Coupled Single-Molecule Junction. *Nat. Nano* **10,** 259–263 (2015).
122. Pradhan, N. A., Liu, N., Silien, C. & Ho, W. Atomic Scale Conductance Induced by Single Impurity Charging. *Phys. Rev. Lett.* **94,** 076801 (2005).
123. Nazin, G. V., Qiu, X. H. & Ho, W. Charging and Interaction of Individual Impurities in a Monolayer Organic Crystal. *Phys. Rev. Lett.* **95,** 166103 (2005).
124. Liu, L., Dienel, T., Widmer, R. & Gröning, O. Interplay between Energy-Level Position and Charging Effect of Manganese Phthalocyanines on an Atomically Thin Insulator. *ACS Nano* **9,** 10125–10132 (2015).

125. Kocić, N. *et al.* Periodic Charging of Individual Molecules Coupled to the Motion of an Atomic Force Microscopy Tip. *Nano Lett.* **15,** 4406–4411 (2015).

126. Kocić, N., Decurtins, S., Liu, S.-X. & Repp, J. Forces from Periodic Charging of Adsorbed Molecules. *J. Chem. Phys.* **146,** 092327 (2017).

127. Prasongkit, J., Grigoriev, A., Ahuja, R. & Wendin, G. Interference Effects in Phtalocyanine Controlled by H-H Tautomerization: Potential Two-Terminal Unimolecular Electronic Switch. *Phys. Rev. B* **84,** 165437 (2011).

128. Persson, B. N. J. & Baratoff, A. Inelastic Electron Tunneling from a Metal Tip: The Contribution from Resonant Processes. *Phys. Rev. Lett.* **59,** 339–342 (1987).

129. Lauhon, L. J. & Ho, W. Single-Molecule Chemistry and Vibrational Spectroscopy: Pyridine and Benzene on Cu(001). *J. Phys. Chem. A* **104,** 2463–2467 (2000).

130. Pascual, J. I. *et al.* Adsorbate-Substrate Vibrational Modes of Benzene on Ag(110) Resolved with Scanning Tunneling Spectroscopy. *Phys. Rev. Lett.* **86,** 1050–1053 (2001).

131. Kim, Y., Komeda, T. & Kawai, M. Single-Molecule Reaction and Characterization by Vibrational Excitation. *Phys. Rev. Lett.* **89,** 126104 (2002).

132. Franke, K. J. & Pascual, J. I. Effects of Electron–Vibration Coupling in Transport through Single Molecules. *J. Phys.: Condens. Matter* **24,** 394002 (2012).

133. Pascual, J. I. Single Molecule Vibrationally Mediated Chemistry. *E. P. J. D* **35,** 327–340 (2005).

134. Qiu, X. H., Nazin, G. V. & Ho, W. Vibronic States in Single Molecule Electron Transport. *Phys. Rev. Lett.* **92,** 206102 (2004).

135. Ho, W. Single-Molecule Chemistry. *J. Chem. Phys.* **117,** 11033–11061 (2002).

136. Mingo, N. & Makoshi, K. Calculation of the Inelastic Scanning Tunneling Image of Acetylene on Cu(100). *Phys. Rev. Lett.* **84,** 3694–3697 (2000).

137. Hahn, J. R., Lee, H. J. & Ho, W. Electronic Resonance and Symmetry in Single-Molecule Inelastic Electron Tunneling. *Phys. Rev. Lett.* **85,** 1914–1917 (2000).

138. Gaudioso, J. & Ho, W. Steric Turnoff of Vibrationally Mediated Negative Differential Resistance in a Single Molecule. *Angew. Chem.* **113,** 4204–4206 (2001).

139. Pavliček, N., Swart, I., Niedenführ, J., Meyer, G. & Repp, J. Symmetry Dependence of Vibration-Assisted Tunneling. *Phys. Rev. Lett.* **110,** 136101 (2013).

140. Helveg, S. *et al.* Atomic-Scale Structure of Single-Layer MoS_2 Nanoclusters. *Phys. Rev. Lett.* **84,** 951–954 (2000).

141. Bruix, A. *et al.* Single-layer MoS_2 on Au(111): Band Gap Renormalization and Substrate Interaction. *Phys. Rev. B* **93,** 165422 (2016).

142. Sørensen, S. G., Füchtbauer, H. G., Tuxen, A. K., Walton, A. S. & Lauritsen, J. V. Structure and Electronic Properties of In Situ Synthesized Single-Layer MoS_2 on a Gold Surface. *ACS Nano* **8,** 6788–6796 (2014).

143. Sorkin, V., Pan, H., Shi, H., Quek, S. Y. & Zhang, Y. W. Nanoscale Transition Metal Dichalcogenides: Structures, Properties, and Applications. *Crit. Rev. Solid State Mater. Sci.* **39,** 319–367 (2014).

144. Grønborg, S. S. *et al.* Synthesis of Epitaxial Single-Layer MoS_2 on Au(111). *Langmuir* **31,** 9700–9706 (2015).

145. Zhang, C., Johnson, A., Hsu, C.-L., Li, L.-J. & Shih, C.-K. Direct Imaging of Band Profile in Single Layer MoS_2 on Graphite: Quasiparticle Energy Gap, Metallic Edge States, and Edge Band Bending. *Nano Lett.* **14,** 2443–2447 (2014).

146. Bollinger, M. V. *et al.* One-Dimensional Metallic Edge States in MoS_2. *Phys. Rev. Lett.* **87,** 196803 (2001).

147. Krane, N., Lotze, C., Läger, J. M., Reecht, G. & Franke, K. J. Electronic Structure and Luminescence of Quasi-Freestanding MoS_2 Nanopatches on Au(111). *Nano Lett.* **16,** 5163–5168 (2016).

148. Zhou, W. *et al.* Intrinsic Structural Defects in Monolayer Molybdenum Disulfide. *Nano Lett.* **13,** 2615–2622 (2013).

149. Persson, B. & Persson, M. Vibrational Lifetime for CO Adsorbed on Cu(100). *Solid State Commun.* **36,** 175–179 (1980).

150. Lorente, N., Rurali, R. & Tang, H. Single-Molecule Manipulation and Chemistry with the STM. *J. Phys.: Condens. Matter* **17,** S1049–S1074 (2005).

151. Repp, J., Meyer, G., Paavilainen, S., Olsson, F. E. & Persson, M. Scanning Tunneling Spectroscopy of Cl Vacancies in NaCl Films: Strong Electron-Phonon Coupling in Double-Barrier Tunneling Junctions. *Phys. Rev. Lett.* **95,** 225503 (2005).

152. Schulze, G., Franke, K. J. & Pascual, J. I. Resonant Heating and Substrate-Mediated Cooling of a Single C_{60} Molecule in a Tunnel Junction. *New J. Phys.* **10,** 065005 (2008).

153. Schulz, F. *et al.* Many-Body Transitions in a Single Molecule Visualized by Scanning Tunnelling Microscopy. *Nat. Phys.* **11,** 229 (2015).

154. Landauer, R. The Noise is the Signal. *Nature* **392,** 658 (1998).

155. Blanter, Y. & Büttiker, M. Shot Noise in Mesoscopic Conductors. *Phys. Rep.* **336,** 1–166 (2000).

156. Reznikov, M., Heiblum, M., Shtrikman, H. & Mahalu, D. Temporal Correlation of Electrons: Suppression of Shot Noise in a Ballistic Quantum Point Contact. *Phys. Rev. Lett.* **75,** 3340–3343 (1995).

157. Kumar, A., Saminadayar, L., Glattli, D. C., Jin, Y. & Etienne, B. Experimental Test of the Quantum Shot Noise Reduction Theory. *Phys. Rev. Lett.* **76,** 2778–2781 (1996).

158. De Picciotto, R. *et al.* Direct Observation of a Fractional Charge. *Nature* **389,** 162–164 (1997).

159. Saminadayar, L., Glattli, D. C., Jin, Y. & Etienne, B. Observation of the e/3 Fractionally Charged Laughlin Quasiparticle. en. *Phys. Rev. Lett.* **79,** 2526–2529 (1997).

160. Jehl, X., Sanquer, M., Calemczuk, R. & Mailly, D. Detection of Doubled Shot Noise in Short Normal-Metal/ Superconductor Junctions. *Nature* **405,** 50–53 (2000).

161. Sakano, R., Fujii, T. & Oguri, A. Kondo Crossover in Shot Noise of a Single Quantum Dot with Orbital Degeneracy. *Phys. Rev. B* **83,** 075440 (2011).

162. Zarchin, O., Zaffalon, M., Heiblum, M., Mahalu, D. & Umansky, V. Two-electron Bunching in Transport Through a Quantum Dot Induced by Kondo Correlations. *Phys. Rev. B* **77,** 241303 (2008).

163. Kubo, T., Tokura, Y. & Tarucha, S. Kondo Effects and Shot Noise Enhancement in a Laterally Coupled Double Quantum Dot. *Phys. Rev. B* **83,** 115310 (2011).

164. Ferrier, M. *et al.* Universality of Non-Equilibrium Fluctuations in Strongly Correlated Quantum Liquids. en. *Nat. Phys.* **12,** 230–235 (2016).

165. Chen, R., Wheeler, P. J., Di Ventra, M. & Natelson, D. Enhanced Noise at High Bias in Atomic-Scale Au Break Junctions. *Sci. Rep.* **4,** 4221 (2014).

166. Kumar, M. *et al.* Shot Noise and Magnetism of Pt Atomic Chains: Accumulation of Points at the Boundary. en. *Phys. Rev. B* **88,** 245431 (2013).

167. Cron, R., Goffman, M. F., Esteve, D. & Urbina, C. Multiple-Charge-Quanta Shot Noise in Superconducting Atomic Contacts. en. *Phys. Rev. Lett.* **86,** 4104–4107 (2001).

168. Scheer, E. *et al.* The Signature of Chemical Valence in the Electrical Conduction through a Single-Atom Contact. *Nature* **394,** 154–157 (1998).

169. Van den Brom, H. E. & van Ruitenbeek, J. M. Quantum Suppression of Shot Noise in Atom-Size Metallic Contacts. en. *Phys. Rev. Lett.* **82,** 1526–1529 (1999).

170. Kumar, M., Avriller, R., Yeyati, A. L. & van Ruitenbeek, J. M. Detection of Vibration-Mode Scattering in Electronic Shot Noise. *Phys. Rev. Lett.* **108,** 146602 (2012).

171. Avriller, R. & Levy Yeyati, A. Electron-Phonon Interaction and Full Counting Statistics in Molecular Junctions. en. *Phys. Rev. B* **80,** 041309 (2009).

172. Schmidt, T. L. & Komnik, A. Charge Transfer Statistics of a Molecular Quantum Dot with a Vibrational Degree of Freedom. en. *Phys. Rev. B* **80,** 041307 (2009).

173. Haupt, F., Novotný, T. & Belzig, W. Phonon-Assisted Current Noise in Molecular Junctions. en. *Phys. Rev. Lett.* **103,** 136601 (2009).

174. Birk, H., de Jong, M. J. M. & Schönenberger, C. Shot-Noise Suppression in the Single-Electron Tunneling Regime. en. *Phys. Rev. Lett.* **75,** 1610–1613 (1995).

175. Herz, M. *et al.* Fundamental Quantum Noise Mapping with Runnelling microscopes tested at Surface Structures of Subatomic Lateral Size. *Nanoscale* **5,** 9978–9983 (20 2013).

176. Burtzlaff, A., Schneider, N. L., Weismann, A. & Berndt, R. Shot Noise from Single Atom Contacts in a Scanning Tunneling Microscope. *Present challenges in surface science, a special issue in honour of Dietrich Menzel* **643,** 10–12 (2016).

177. Wiener, N. Generalized Harmonic Analysis. en. *Acta Math.* **55,** 117–258 (1930).

178. Khintchine, A. Korrelationstheorie der stationären stochastischen Prozesse. *Mathematische Annalen* **109,** 604–615 (1934).

179. Kumar, M. *A Study of Electron Scattering through Noise Spectroscopy* PhD Thesis (Universiteit Leiden, Netherlands, 2012).

180. Levitov, L. S. & Lesovik, G. B. Charge Distribution in Quantum Shot Noise. *ZhETF Pisma Redaktsiiu* **58,** 225 (1993).

181. Büttiker, M. Scattering Theory of Current and Intensity Noise Correlations in Conductors and Wave Guides. en. *Phys. Rev. B* **46,** 12485–12507 (1992).

182. Nyquist, H. Thermal Agitation of Electric Charge in Conductors. en. *Phys. Rev.* **32,** 110–113 (1928).

183. Callen, H. B. & Welton, T. A. Irreversibility and Generalized Noise. en. *Phys. Rev.* **83,** 34–40 (1951).

184. Johnson, J. B. The Schottky Effect in Low Frequency Circuits. en. *Phys. Rev.* **26,** 71–85 (1925).

185. M. Kobayashi & T. Musha. 1/f Fluctuation of Heartbeat Period. *IEEE Trans. Biomed. Eng.* **BME-29,** 456–457 (1982).

186. Novikov, E., Novikov, A., Shannahoff-Khalsa, D., Schwartz, B. & Wright, J. Scale-similar Activity in the Brain. en. *Phys. Rev. E* **56,** R2387–R2389 (1997).

187. Voss, R. F. & Clarke, J. "1/f noise" in Music: Music from 1/f Noise. *J. Acoust. Soc. Am.* **63,** 258–263 (1978).

188. Liu, G., Rumyantsev, S., Shur, M. S. & Balandin, A. A. Origin of 1/f Noise in Graphene Multilayers: Surface vs. Volume. *Appl. Phys. Lett.* **102,** 093111 (2013).

189. Kleinpenning, T. G. M. & de Kuijper, A. H. Relation between Variance and Sample Duration of 1/f Noise Signals. *J. Appl. Phys.* **63,** 43–45 (1988).

190. Niemann, M., Kantz, H. & Barkai, E. Fluctuations of 1/f Noise and the Low-Frequency Cutoff Paradox. en. *Phys. Rev. Lett.* **110,** 140603 (2013).

191. Rodríguez, M. A. Class of Perfect 1/f Noise and the Low-Frequency Cutoff Paradox. en. *Phys. Rev. E* **92,** 012112 (2015).

192. Diaz, S. A. & Di Ventra, M. The Role of Measurement Time on the Universal Crossover from 1/f to non- 1/f Noise Behavior. en. *J. Comput. Electron.* **14,** 203–208 (2015).

193. Yadav, A. C., Ramaswamy, R. & Dhar, D. General Mechanism for the 1/f Noise. en. *Phys. Rev. E* **96,** 022215 (2017).

194. Voss, R. F. & Clarke, J. Flicker 1/f Noise: Equilibrium Temperature and Resistance Fluctuations. *Phys. Rev. B* **13,** 556–573 (2 1976).

195. Weissman, M. B. 1/f Noise and other Slow, Nonexponential Kinetics in Condensed Matter. en. *Rev. of Modern Phys.* **60,** 537–571 (1988).

196. Kogan, S. *Electronic Noise and Fluctuations in Solids* (Cambridge [England] ; New York, NY, USA : Cambridge University Press, 1996).

197. Dutta, P., Dimon, P. & Horn, P. M. Energy Scales for Noise Processes in Metals. en. *Phys. Rev. Lett.* **43,** 646–649 (1979).

198. Dutta, P. & Horn, P. M. Low-frequency Fluctuations in Solids: 1/f Noise. *Rev. Mod. Phys.* **53,** 497–516 (3 1981).

199. Pelz, J. & Clarke, J. Dependence of 1/f Noise on Defects Induced in Copper Films by Electron Irradiation. en. *Phys. Rev. Lett.* **55,** 738–741 (1985).

200. Kondo, J. Resistance Minimum in Dilute Magnetic Alloys. *Prog. Theor. Phys.* **32,** 37–49 (1964).

201. Hewson, A. C. *The Kondo Problem to Heavy Fermions* (Cambridge University Press, 1997).

202. Ternes, M., Heinrich, A. J. & Schneider, W.-D. Spectroscopic Manifestations of the Kondo Effect on Single Adatoms. *J. Phys.: Condens. Matter* **21,** 053001 (2009).

203. Madhavan, V., Chen, W., Jamneala, T., Crommie, M. F. & Wingreen, N. S. Local spectroscopy of a Kondo impurity: Co on Au(111). *Phys. Rev. B* **64,** 165412 (2001).

204. Plihal, M. & Gadzuk, J. W. Nonequilibrium Theory of Scanning Tunneling Spectroscopy via Adsorbate Resonances: Nonmagnetic and Kondo impurities. *Phys. Rev. B* **63,** 085404 (2001).

205. Meir, Y. & Golub, A. Shot Noise through a Quantum Dot in the Kondo Regime. *Phys. Rev. Lett.* **88,** 116802 (2002).

206. Sela, E., Oreg, Y., von Oppen, F. & Koch, J. Fractional Shot Noise in the Kondo Regime. *Phys. Rev. Lett.* **97,** 086601 (2006).

207. Vitushinsky, P., Clerk, A. A. & Le Hur, K. Effects of Fermi Liquid Interactions on the Shot Noise of an SU(N) Kondo Quantum Dot. *Phys. Rev. Lett.* **100,** 036603 (2008).

208. Knorr, N., Schneider, M. A., Diekhöner, L., Wahl, P. & Kern, K. Kondo Effect of Single Co Adatoms on Cu Surfaces. *Phys. Rev. Lett.* **88,** 096804 (2002).

209. Choi, D.-J., Rastei, M. V., Simon, P. & Limot, L. Conductance-Driven Change of the Kondo Effect in a Single Cobalt Atom. *Phys. Rev. Lett.* **108,** 266803 (2012).

210. Choi, D.-J. *et al.* Kondo Resonance of a Co Atom Exchange Coupled to a Ferromagnetic Tip. *Nano Lett.* **16,** 6298–6302 (2016).

211. Choi, D.-J., Abufager, P., Limot, L. & Lorente, N. From tunneling to contact in a magnetic atom: The non-equilibrium Kondo effect. *J. Chem. Phys.* **146,** 092309 (2017).

List of Publications

Publications Related to this Thesis

- D. Rolf, C. Lotze, C. Czekelius, B. W. Heinrich, and K. J. Franke: *Visualizing Intramolecular Distortions as the Origin of Transverse Magnetic Anisotropy*, J. Phys. Chem. Lett., (**2018**), 9 (22), pp 6563–6567
- A. Stein, D. Rolf, C. Lotze, C. Czekelius, K. J. Franke and P. Tegeder: *Electronic Structure of an Iron-Porphyrin Derivative on Au(111)*, J. Phys.: Condens. Matter **31** 044002, (**2018**)

Non-Related Publications

- N. Hatter, B. W. Heinrich, D. Rolf, and K. J. Franke: *Scaling of Yu-Shiba-Rusinov energies in the weak-coupling Kondo regime*, Nat. Comm. 8, (**2017**)
- P. Stoll, M. Bernien, D. Rolf, F. Nickel, Q. Xu, C. Hartmann, T. R. Umbach, J. Kopprasch, J. N. Ladenthin, E. Schierle, E. Weschke, C. Czekelius, W. Kuch, and K. J. Franke: *Magnetic anisotropy in surface-supported single-ion lanthanide complexes*, Phys. Rev. B 94, 224426 (**2016**)
- M. Bernien, D. Wiedemann, C. F. Hermanns, A. Krüger, D. Rolf, W. Kroener, P. Müller, A. Grohmann, and W. Kuch: *Spin Crossover in a Vacuum-Deposited Submonolayer of a Molecular Iron(II) Complex*, J. Phys. Chem. Lett. 3, 3431 (**2012**)

Conference Contributions

2015

- Student-organized workshop of the International Max Planck Research School (IMPRS) "Functional Interfaces in Physics and Chemistry: From Micro to Macro", Tegernsee, Germany, 09.02.-13.02.2015
  - Poster contribution: *Silicene as a Substrate for Manganese-Phthalocyanine Molecules*
- DPG Spring meeting of the condensed matter section, Berlin, Germany, 15.03.-20.03.2015
  - Poster contribution: *Inelastic Excitations in Rare-Earth-Based Metal-Organic Complexes*
- 598th WE-Heraeus Seminar: "Frontiers in Scanning Probe Microscopy", Bad Honnef, Germany, 02.11. - 05.11.2015
  - Poster contribution: *Origin of Inelastic Excitations in Rare-Earth-Based Metal-Organic Complexes*

2016

- DPG Spring meeting of the condensed matter section, Regensburg, Germany, 06.03.-11.03.2016
  - Oral presentation: *Inelastic Excitations in Rare-Earth-Based Metal-Organic Complexes*
- Workshop "Spins on Surfaces", San Sebastián, Spain, 05.09.-09.09.2016

2017

- DPG Spring meeting of the condensed matter section, Dresden, Germany, 20.03.-24.03.2017
  - Poster contribution: *Inelastic Excitations on Fe-TPyP on Au(111)*
- 654th WE-Heraeus Seminar: "Topical Insights into Nanoscience using Scanning Probes", Bad Honnef, Germany, 19.11. - 23.11.2017
  - Poster contribution: *Inelastic Spin- and Vibrational Excitations of Fe-TPyP on Au(111)*

2018

- DPG Spring meeting of the condensed matter section, Berlin, Germany, 12.03.-16.03.2018
  - Oral contribution: *Inelastic Spin- and Vibrational Excitations on FeTPyP on Au(111)*

Acknowledgement

Despite all the work we put in on our own, like almost everything in life, this PhD would not have been possible without the help of many people. First of all, I want to thank Katharina for allowing me to be part of this group for the last years. You literally always have the door open to support us in any way that you can without ever giving us the feeling that you have more important things to do (although most of the time, you actually do have a whole list of things to do). I really appreciate the way you treat us as equals, respected our opinions and never made us feel like a question is too stupid to be asked. This created a really nice and productive atmosphere in this group, and made going to work so enjoyable.

Among the people that supported me the most are many former members of the group who tought me so much in the beginning of my PhD. Special thanks goes to Nino, who is not only a former collegue but also became a good friend, who has been a great mental support throughout the more stressful times. I also want to thank Paul and Gelavizh, who worked with me for the first months in the lab and answered a lot of questions with great pacience. Special thanks also goes to Ben for lots of fruitful discussions. Moreover, I want to thank Micha, for being so quick in implementing all his special features into his software 'Spectrafox'. I am also thankful for the successful collaboration with Arnulf Stein, Friedrich Maaß and Petra Tegeder from the University of Heidelberg.

No one deserves more gratitude than Chris for all his support in the lab. Although his to-do lists are getting longer and longer, he does not hesitate to take his time to fix computer bugs and look for grounding issues. It has been really nice to work with you for the last years and I hope I was able to acquire a tiny bit of the incredible amount of technical understanding you have. I also want to thank Sergey, who I was working with during his Masters. Although we keep telling you that your singing is annoying, I am sure that I am really going to miss hearing it all day long.

Knowing that the shot-noise project that I have been working on for so long is in good hands with you, Idan, is a great relief. It has been a pleasure to work with you for the last weeks and I wish you good luck with the project in the future. Moreover, I want to thank you and Asieh, for sharing an office with me. I really enjoyed the time, and I wish the international politicians could see an iranian, an israeli and a german sitting peacefully in the same office ...=). Moreover, I want to thank all the other members of the AG Franke: Eva, Gaël, Jannik, Laëtitia, Nils, Nils (you can decide on your own, which of the Nils' is which), Olof and Rika. I really appreciate the nice atmosphere that always existed in the group and which made all the social activities like 'coffee club' and 'volleyball club' a lot of fun. Special thanks also goes to Birgit, who is responsible for all the paper work 'behind the scenes'.

Eventually, I want to thank my family and friends for all their support throughout the years. Answering the delicate question of "and what is it good for?" every once in a while helped me realize how much I really loved what I was doing all day long (although it might eventually not be good for anything in real life). Last but not least, my greatest gratitude goes to Jannik, who is always there for me with all the encouragement and support in the world.

Selbstständigkeitserklärung

Hiermit erkläre ich, dass ich die vorliegende Arbeit selbständig und nur unter Verwendung der angegebenen Literatur und Hilfsmittel angefertigt habe. Zudem versichere ich, dass diese Arbeit in keinem früheren Promotionsverfahren eingereicht und dort angenommen oder für ungenügend befunden wurde.

Berlin, 30. Oktober 2018